UNIVERSITÀ DEGLI STUDI DI MILANO

DOTTORATO DI RICERCA IN SCIENZE DELLA TERRA

Ciclo XXXII

DIPARTIMENTO DI SCIENZE DELLA TERRA

STUDY OF THE GEOLOGICAL EVOLUTION AND STRUCTURAL PATTERNS AT DIFFERENT SCALES CHARACTERISING THE TRES VÍRGENES REGION (MEXICO) TO EVALUATE THE GEOTHERMAL ENERGY POTENTIAL

04/A2 – GEO/03

CLAUDIA PELLICIOLI

GIANLUCA GROPPELLI

MICHELE ZUCALI

COORDINATORE DEL DOTTORATO

FERNANDO CAMARA ARTIGAS

Structure of the Thesis

This PhD Thesis is presented as a series of published or submitted scientific papers, illustrated in Chapters 3 to 7. The contribution of the PhD candidate and co-authors are set forth as indicated in each specific paper.

Funding

The PhD research was sponsored by CeMIE Geo (*Centro Mexicano de Innovación en Energía Geotérmica*) through the project P15 of SENER-CONACyT (grant number 207032), awarded to Professor José Luis Macías from UNAM (*Universidad Nacional Autónoma de México*), and by *Italgas s.p.a.* through the project (grant number CIG 648306172D), awarded to former CNR-IDPA (now CNR-IGAG, *Consiglio Nazionale delle Ricerche – Istituto di Geologia Ambientale e Geoingegneria,* sezione di Milano).

Abstract

Faults play a fundamental role in sustaining fluid circulation across volcanic-geothermal regions, where volcanic rocks commonly exhibit low porosity and permeability. In fact, most of geothermal resources production is often connected to faults and fault zones. Thus, a precise knowledge of deformational patterns is of paramount importance to extend the assessment of the geothermal potential to areas surrounding a producing field, and to find strategies to enhance energy production. Increasing electrical energy production and using geothermal energy to desalinate seawater have recently become main concerns of the Mexican authorities with regards to the Tres Vírgenes region (Baja California, Mexico), where the Las Tres Vírgenes geothermal field represents the only producing zone across the Baja California peninsula, which nowadays struggles with energy and water supplies due to the recent growth of tourism. The herein presented PhD research places into this scenario, by means of the CeMIE Geo project P15 of SENER-CONACyT, which was appointed by the Mexican authorities to UNAM (*Universidad Nacional Autónoma de México*) and sponsored this Thesis.

In order to evaluate the geothermal prospectivity of areas surrounding the currently producing Las Tres Vírgenes field and the role of structural patterns affecting the Tres Vírgenes region in sustaining hydrothermal fluid migration a multi-disciplinary approach has been deployed, including a wide range of methodologies and receiving contributions from several branches of the Earth Sciences. Five studies have been performed, whose results are presented in this Thesis under the form of papers published or submitted to dedicated ISI-Journals:

1) A geological study on La Reforma caldera complex, resulting in a 1:50,000 scale geological map produced with modern survey methodologies and representing an important contribution concerning the geological evolution of the Tres Vírgenes region and the Quaternary volcanic processes linked to the exploitation of geothermal resources in the Las Tres Vírgenes field.

2) The investigation of the structural patterns affecting the Tres Vírgenes region, by coupling observations at the meso- (field data) and micro-scales (image analysis of fault-related micro-fractures and veins), resulting in a structural model for the Tres Vírgenes region. This structural model highlights the strong control of regional-scale strike-slip oblique structures linked to the Gulf of California on Quaternary volcanic processes and the interplay between regional and volcanic structures in exhuming the Cretaceous basement throughout the region.

3) The assessment at the micro-scale of geometrical and chronological relationships between faulting and multiple fluid circulation events depositing mineralization along fault planes, providing further

support to the proposed structural model and resulting in a deeper understanding of fault-related mechanisms across the Tres Vírgenes region. Fractal statistics applied to fault-related deformation patterns indicates and quantifies the self-similarity (fractal charcter) of regional structures at the scale of the Tres Vírgenes region, possibly extending to this sector of the Gulf of California.

4) Multi-scale petrographic and geochemical investigations, determining the composition, origin and temperature of fluids circulating and depositing calcite along regional faults. The integration of different techniques working at different scales defines a novel methodology, which was for the first time applied in a volcanic-geothermal setting in this Thesis. Fluids circulating along regional faults at different temperatures and redox conditions display a geothermal-hydrothermal component and reach maximum temperatures (100°C) in proximity of the Tres Vírgenes feeding system, acting as the heating source for the hydrothermal fluids and defining the areas where fault-sustained hydrothermal circulation is more likely to occur.

5) The quantification of physical properties of undeformed and faulted volcanic rocks through triaxial tests, X-ray computerized tomography (CT) and coupled permeability simulations, suggesting the highly unlikeliness of vertical and lateral fluid migration through the exposed undeformed Quaternary volcanic rocks in the areas surrounding the Las Tres Vírgenes field. The estimate of along- and across-fault fluid flow potential, and of changes in the interconnected pore space and fault-permeability once these volcanic rocks are involved within regional damage zones, confirms the role of regional structures in focusing hydrothermal fluid circulation across the Tres Vírgenes region.

The novel and quantitative findings of the several studies constituting this Thesis bear multifaceted implications: of regional and industry-related importance concerning modelling of fluid flow through the Tres Vírgenes and other geothermal regions worldwide, and more far-reaching concerning upper-crustal deformation processes in volcanic and non-volcanic settings.

Chapter 1
Introduction

The Tres Vírgenes volcanic-geothermal region is located within the Santa Rosalía basin, on the eastern side of the Baja California peninsula (Mexico) facing the Gulf of California, 30 km north-west of the Santa Rosalía town (Fig. 1.1). It includes La Reforma, Sierra Aguajito and Tres Vírgenes volcanic complexes, representing the only example across the Gulf of California of Quaternary silicic volcanism associated to geothermal energy production (Las Tres Vírgenes geothermal field, LTV), conducted by CFE (*Comisión Federal de Electricidad*) since the early 1980s. Tectonics and volcanism across the Baja California peninsula and in the Santa Rosalía basin are strongly affected by large-scale geodynamic processes linked to the Gulf of California opening, whose complex and controversial evolution is still matter of debate. Recently, the Baja California peninsula has been struggling to keep the pace of an increasing demand in electricity and potable water linked to the rapid tourism growth over the last decades. As a consequence, Mexican authorities have been actively working to enhance electricity production in the Tres Vírgenes region by optimizing the exploitation of geothermal resources and considering the use geothermal energy to desalinate seawater to compensate the scarcity of annual rainfalls typical of the Baja California peninsula desert climate. In this scenario, several projects sponsored by the Mexican authorities have focused on extending the assessment of geothermal prospectivity beyond the currently active LTV, to include the nearby La Reforma and Sierra Aguajito volcanic complexes. Among these, the CeMIE Geo project P15 of SENER-CONACyT awarded to UNAM (*Universidad Nacional Autónoma de México*) is the one which the present PhD research activity has benefited from, by means of financial support and of scientific collaboration with Professor José Luis Macías that resulted in co-authoring of some of the papers included in this Thesis. In line with the main scopes of the CeMIE Geo project and in the context of the multifaceted collaboration with the UNAM University, the specific objectives of the herein presented PhD research activity consist in: building a structural model of the Tres Vírgenes region (1) and demonstrating and quantifying the dominant role played by structures in controlling hydrothermal fluids migration paths (2).

Figure 1.1 Location of the Baja California peninsula and of the Santa Rosalìa town, Mexico.

Despite the CeMIE Geo project included the study of both La Reforma and Sierra Aguajito volcanic complexes, complications and delays arisen during field surveys and subsequent collaboration with UNAM researchers hampered reconstructing a robust stratigraphic and evolutionary record for the Sierra Aguajito volcanic complex. As a result, the originally planned 1:50,000 scale geological map of the Sierra Aguajito volcanic complex could not be delivered as part of this PhD Thesis. This however did not prevent reaching the above-mentioned objectives of the Thesis, as the collection of data regarding structures and hydrothermal fluid circulation spanned across an area covering and surrounding both complexes. Also, the originally planned integration of field data and research elaboration results with well bore data, by means of a 3D subsurface model of the Tres Vírgenes region, could not be performed due to the failed delivery of well bore data by CFE, notwithstanding the existing agreements regarding confidential data disclosure to UNAM.

Following the Methodologies chapter (Chapter 2), this PhD Thesis will illustrate the main outcomes of the research under the form of scientific papers (published or submitted to dedicated ISI-Journals) in separate chapters (Chapters 3 to 7). These will be recalled and summarized in the Concluding remarks chapter (Chapter 8), where their relevance for the objectives of this Thesis will be highlighted. Chapter 3 (Paper I: *Geology of La Reforma caldera complex, Baja California, Mexico; Journal of Maps, 2019*) will present La Reforma caldera complex 1:50,000 scale geological map, including structures mapped

during 2016-2017 field surveys. These structures will be discussed in terms of attitude, kinematics, throw, nature and orientation in respect to the active stress field in Chapter 4 (Paper II: *Control of regional structures on the evolution of Pleistocene La Reforma caldera complex: implications on caldera collapse and resurgence; GSA Bulletin, submitted*). Chapter 4 will also address regional control on the evolution of La Reforma caldera complex (including caldera collapse and resurgence processes), the interplay between regional and volcanic structures and the link between identified structures and mapped hydrothermal alteration. Chapter 5 (Paper III: *Kinematics and deformation patters from micro-structural and image analysis on fault-rock samples in volcanic regions: the example of the Tres Vírgenes active geothermal region, Baja California (Mexico); Journal of Structural Geology, submitted*) will couple macro-scale structural analysis results (Chapter 4) with micro-structural and image analyses on fault-rock samples, aimed to define faults architecture and characteristics, fluid flow mechanisms and to test the structural model illustrated in Chapter 4. Chapter 6 (Paper IV: *Insights on fluid origin from multi-scale petrographic and geochemical investigation of fault-related calcites in volcanic-geothermal regions (Tres Vírgenes area, Baja California, Mexico); Journal of Volcanology and Geothermal Research, submitted*) will analyse calcite phases precipitated along regional fault planes following fluid circulation events recognised in Chapter 5, to gain insights regarding the origin, temperature and redox conditions of circulating fluids. This will be performed by means of a novel methodology applied for the first time to a volcanic-geothermal setting, using multiple techniques operating at different scales, which include: X-ray diffraction, petrography, cathodoluminescence, oxygen and carbon stable isotopes, electron microprobe and laser ablation inductively coupled plasma mass spectrometry (LA-ICP-MS). Chapter 7 (Paper V: *Determination of porosity and permeability of undeformed and faulted volcanic rocks and related challenges: a case study on the Tres Vírgenes geothermal region (Baja California, Mexico); Engineering Geology, submitted*) will determine the petrophysical properties of undeformed and faulted volcanic rocks by means of triaxial, X-ray computerized tomography (CT) and permeability simulation tests. Fault-permeability along micro-fracture sets identified in Chapter 5 and sometimes sealed by mineral precipitation following fluid circulation events illustrated in Chapter 6 will be compared with the one of undeformed rocks. This allows closing the loop and drawing conclusions on fluid flow migration processes and pathways across the Tres Vírgenes area.

Chapter 2
Methodologies

The research activity was divided into two parts: fieldwork activity and processing of collected data.

2.1 Fieldwork activity

A premise should be done regarding the logistically difficult, extreme and remote character of the study area, lying several kilometres from the nearest inhabited area, the town of Santa Rosalía (Fig. 2.1). Most of the study area lacks roads and the access is feasible only from the sea or from few and scarcely traced mountain paths. Field surveys were thus supervised by local guides (UMA and Ecoturismo Borrego Cimarrón, Bonfil, Baja California Sur) employed by UNAM researchers, who also took care of all logistic aspects of fieldtrips. Fieldwork was performed during five separate field campaigns (from 2014 to 2017), two of which (2016-2017) conducted in the context of this PhD research. Data collected during 2016-2017 campaigns were merged and integrated with those of previous surveys for the purposes of this PhD research activity. The main aims of fieldwork were geological mapping, structural data collection and sample gathering for laboratory analyses.

2.1.1 The study area

The area covered by 2014-2017 field surveys extends for about 400 km^2 inside the Santa Rosalía basin and includes La Reforma and Sierra Aguajito complexes and surrounding areas, lying 5 to 40 kilometres north-west of the Santa Rosalía town (Fig. 2.1). The Santa Rosalía basin is a NW-SE trending half graben basin developed from oblique divergence following Cenozoic subduction ceasing between the Farallon and North America plates (Ferrari et al., 2018). La Reforma caldera complex marks the onset of Quaternary siliciclastic volcanism inside the basin (1.35 Ma, Garcia-Sánchez et al., 2019), followed by Sierra Aguajito (1.17 Ma, Schmitt et al., 2006) and Tres Vírgenes (Holocene, Avellán et al., 2018) volcanic complexes. Quaternary volcanic products, mainly consisting of several rhyolitic ignimbrites intercalated with basaltic to andesitic and dacitic lava flows, lie above several local PDCs (pyroclastic density currents), pillow lavas and hyaloclastites representing early submarine volcanic activity. Below and interfingered with these submarine deposits are, from oldest to youngest:

i) crystalline Cretaceous plutonic rocks (*Batholites Peninsulares*, Gastil, 1975; Schmidt, 1975; McLean, 1988) intruded into the Early Cretaceous supra-crustal volcanic and sedimentary sequence; ii) the Comondù Group (12-30 Ma, Umhoefer et al., 2001) composed of red siltstones, sandstones and conglomerates and interlayered with the Santa Lucia formation (19.25 Ma, Garduño-Monroy et al., 1993; Garcia-Sánchez et al., 2019) deposited in an arc-forearc setting linked to the Farallon-Guadalupe and North America plates subduction and possibly extending through the Gulf of California early rifting phases (Umhoefer et al., 2001; Ferrari et al., 2018; Garcia-Sánchez et al., 2019); iii) the sedimentary Formation of the Santa Rosalía basin (Pliocene-middle Pleistocene, Garcia-Sánchez et al., 2019) representing marine sedimentation coeval to scattered volcanic activity occurred inside the Santa Rosalía basin. Exploration activities in the region conducted by CFE (*Comisión Federal de Electricidad*) since the early 1980s culminated in the establishment of the Las Tres Vìrgenes geothermal field (LTV) in 1988, currently counting a dozen of wells (producing and injectors, Fig. 2.1) and exhibiting a 10 MWe operating net capacity (Gutierrez-Negrin et al., 2010).

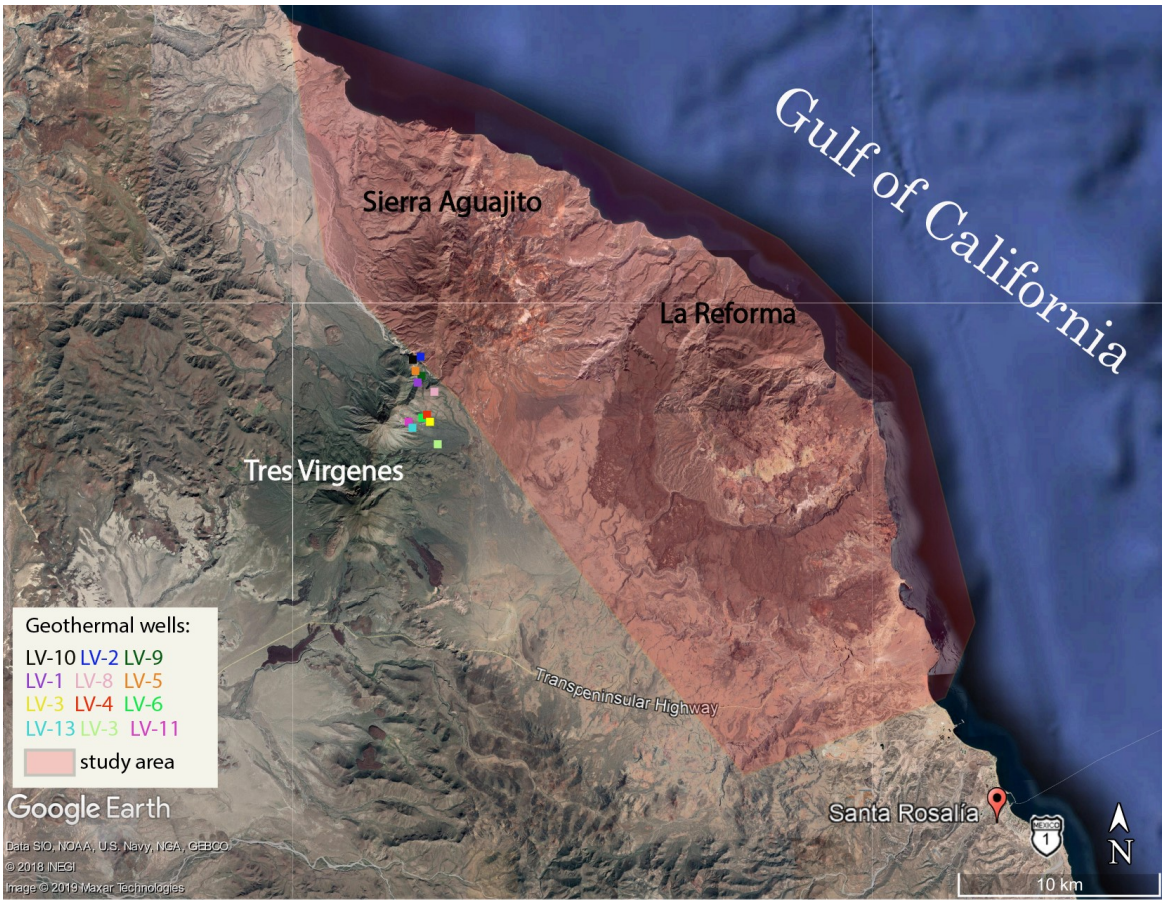

Figure 2.1 Location and extension of the study area (shaded in red colour) covered by 2014-2017 field campaigns. To notice the only carriageable road (Transpeninsular Highway 1) and the location of the Las Tres Vìrgenes geothermal wells.

2.1.2 Geological mapping

A geologic map provides information about both past and present-day processes affecting a region of the Earth. Results of geological mapping are products (maps) that can be used for many different purposes, including: assessing ground-water quality and contamination risks; predicting earthquake, volcano, and landslide hazards; characterizing energy and mineral resources and their extraction costs; waste repository siting; land management and land-use planning; general education (Soller, 2004). These are all purposes that directly concern the study area, which is a quickly developing region where the recent growth of tourism (Arango-Galván et al., 2015) and derived issues concerning water and energy supply strongly influence land management and land-use decisions, and where the exploitation of geothermal energy plays a rather important and strategic role for the local economy.

Geological mapping in the study area was preceded by literature review, analysis of satellite images (including ESRI and Google images) and of a 25 m pixel-size digital elevation model (DEM) and derived morphological features. Geological field survey was carried out at 1:25,000 scale using INEGI topographic maps and iGIS ® software on iPad mini equipped with Google Earth images. The adopted methodology for geological mapping was based on lithostratigraphic units, representing the best applicable approach in the field for volcanic regions (Groppelli and Viereck-Goette, 2010; Groppelli and Martì-Molist, 2013; Martì et al., 2018). This allowed the definition of several formations, mainly based on the stratigraphic position and lithology of the recognized units. In the case of La Reforma caldera complex, units of lower rank (members) were furtherly identified based on lithological criteria, together with six litosomes (Wheeler and Mallory, 1953; Pasquarè et al., 1992), which allowed to characterize volcanic deposits based on their morphology, vent location and product distribution. Furthermore, in order to summarize the evolution of La Reforma caldera complex the previously defined lithostratigraphic units were grouped into three main phases: pre-, syn- and post-caldera. If geology of La Reforma caldera complex was defined to a high detail and results published (Paper I, Chapter 3), the geological characterization of the Sierra Aguajito volcanic complex is still at an incipient stage, due to complications and delays arisen during fieldwork (i.e. some key areas could not be reached) that resulted in an incomplete and debatable stratigraphic record supporting multiple evolution scenarios.

2.1.3 Structural mapping

Structural mapping, meant as the mapping of structures directly linked to (i.e. syn-sedimentary) or modifying (i.e. tectonic) the original depositional characteristics of rock successions, has to be part of the geological map production process. Faults form in response to several and often interfering geologic and natural processes (i.e. tectonic, volcanic and mechanical processes) and only a detailed

study of these features can directly address issues linked to their formation and propagation inside rock masses. Good geological maps cannot lack faults, as these are the expression of the large-scale processes acting on Earth, they are often sites of seismic and volcanic activity and mineralization, or where other important natural resources (i.e. water) commonly focus. Any land-use planning activity and any production of hazard and risk maps cannot forget faults and their impact on landscape morphology, natural processes and human activities.

Structural mapping in the study area was coupled with geological mapping activity and was thus performed at the same scale (1:25,000) and in the same area covered by geological surveys (Fig. 2.1). The main measured elements included: faults, fractures, veins, dykes, folds and mineralization. In few cases bedding was also measured for evaluating regional tilting and resurgence processes (i.e. La Reforma) affecting the region. Attitude (dip inclination, dip direction, strike), kinematics and throw (where applicable) were measured with a geological compass and stored in an iPad mini equipped with iGIS ® and Lambert ® software, also providing the exact location for all collected measurements. Kinematics of faults were deduced in the field, either based on well-preserved kinematic indicators (i.e. striae and slickensides) or based on visible offsets and/or in analogy with similarly oriented and dipping structures of certain kinematics, where preservation conditions of kinematic indicators were bad.

2.1.4 Sample collection

Sample collection for petrographic and geochemical analyses and for radiometric dating usually supports the production of geological maps. Petrographic and geochemical analyses can help correlations among volcanic deposits and determination of the composition and source of magma, and they are often used for defining the evolution phases of volcanic complexes. Radiometric dating is easily performed in volcanic settings, due to the large abundance of minerals containing U, Pb, Th and Ar elements. It also represents a useful tool to temporally constrain lithostratigraphic units and to distinguish volcanic products that span over a small geological time interval (i.e. hundreds of years for lava flows). Besides from petrographic and geochemical analyses and radiometric dating, sample collection can also be performed for a variety of other purposes or specific studies, whose results often are presented in thematic maps.

Samples for petrographic and geochemical characterization and for absolute radiometric dating were collected across the study area by UNAM researchers, who conducted the analyses in the Morelia and Mexico City laboratories. This information is partially included in La Reforma caldera complex 1:50,000 scale geological map (Chapter 3), but is not part of this Thesis. In addition, and in line with the specific purposes of this Thesis, a total of 22 samples were collected across the study area (Fig.

2.2, Table 2.1) and analysed with different techniques at different scales, as detailed in Paragraph 2.2.2. They all represent volcanic rocks: mainly ignimbrites or local PDCs, andesitic and basaltic lava flows and intrusions. The collected samples divide into two main categories: undeformed and faulted rock samples (Fig. 2.2). Undeformed rock samples (labelled protoliths) were collected away from structures or deformation zones and are thus representative of petrographic and physical properties intrinsic to the lithotype. Faulted rock samples (labelled fault-rocks) represent the same protoliths but collected along shear and deformation zones, that often modify their original petrographic and physical characteristics. In the case of fault-rock samples, the direction of shear was marked in the field with a felt-tip pen in order to prepare thin sections perpendicular to the shear direction, where the best chance of observing kinematic indicators and micro-structures commonly is. The location of the structures along which fault-rock samples were collected is reported in Figure 2.2, whilst detailed information regarding structures characteristics and nature (i.e. tectonic or volcanic) is illustrated in Chapter 4.

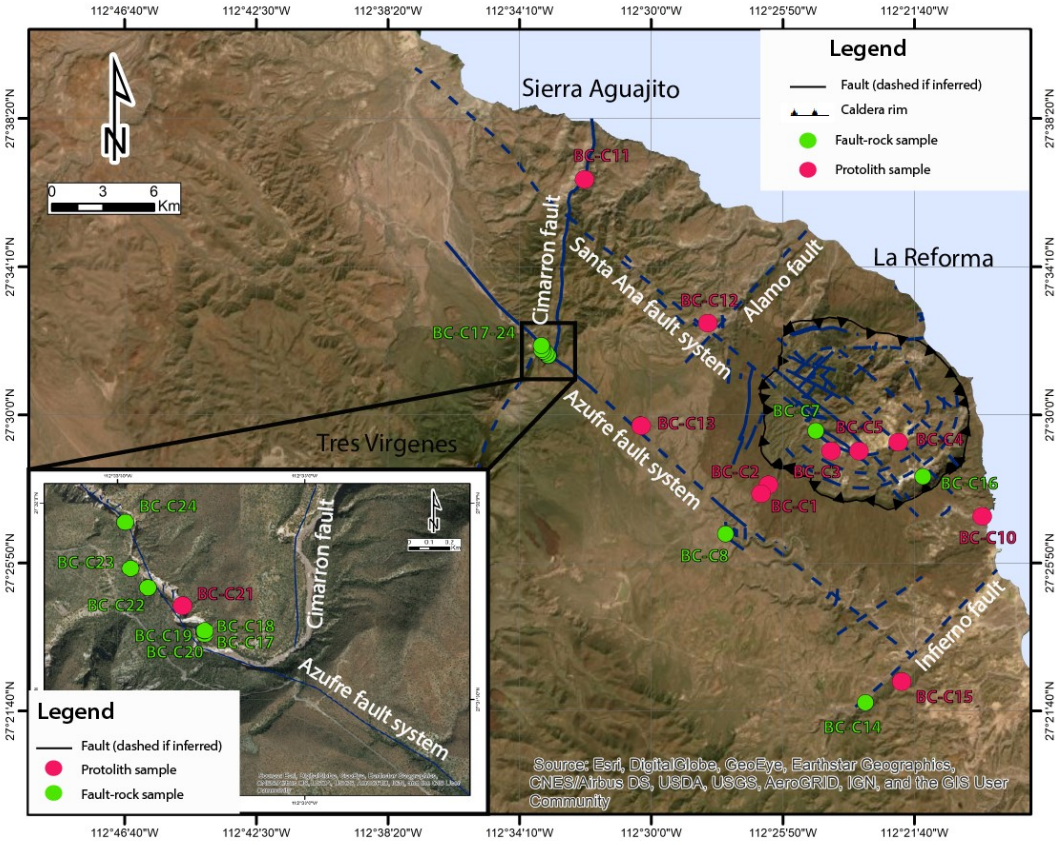

Figure 2.2 Location of the 22 samples (protolith and fault-rock samples) collected and analysed in this Thesis.

2.2 Data processing

This paragraph describes all methods and software used for processing field-data, performing analyses on collected samples and elaborating results.

2.2.1 Processing of field data

Processing of data collected in the field included: i) the production of a 1:50,000 scale geological map for La Reforma caldera complex (Chapter 3); ii) the plotting and interpretation of collected structural data to define a structural model for the Tres Vírgenes region (Chapter 4); iii) the production of geological cross sections through La Reforma caldera complex (Chapter 4) to summarize and illustrate the interplay between regional and volcanic processes across La Reforma caldera complex. For the above-mentioned reasons, no geological map and geological cross- sections could be produced for the Sierra Aguajito volcanic complex.

2.2.1.1 La Reforma caldera complex 1:50,000 scale geological map

La Reforma caldera complex geological map represents the first and fundamental step of this Thesis, on which all following work, interpretations and analyses are hinged. Geological boundaries, structures and polygons were digitized directly from field paper maps using ArcGIS ESRI ® (for Desktop 10.2.1.3497 version, by ESRI Inc.). Google Earth Pro was used to infer geology and prolongation of structures in those areas that were inaccessible in the field (i.e. ravines or steep slopes). Polygons summarize lithostratigraphic units defined in the field, whilst lines and symbols indicate morphological and structural lineaments (including buried caldera rims, crater rim, pit crater rim, faults, dykes and marine terraces) and structural features (vents location, attitude of mapped units). The chosen topographic contouring is 50 m. The colour scale of the lithostratigraphic units is based on different shadings of the same colour for formations belonging to the same evolutionary phase (pre-, syn- and post-caldera): brown shades for pre-caldera units; red shades for syn-caldera units; green shades for post-caldera units. Blue and light-blue shades were used to represent units providing the basement for Quaternary volcanism through the study area. All colour shades combinations (C,M,Y,K) were derived from the *Chromatic Handbook for the printing of geological maps* of the Geological Survey of Italy (Pignone and Accardi, 2002). In addition to the map and legends, a stratigraphic scheme was inserted, showing the relationships between the different units and summarizing their position according to La Reforma caldera complex evolution phases. Also, a 3D view of the complex

produced with the ArcScene software ® (ArcGIS 10.2.1) highlights the present-day morphology resulting from resurgence processes. Two map insets (1:20,000 scale) were added for those areas where the 1:50,000 scale could not provide sufficient detail (i.e. deeply incised fluvial valleys). A geographical scheme, placed on the top left corner of the map page and produced with CorelDraw X6 software ®, indicates the location of La Reforma caldera complex within the Mexican Baja California peninsula. Following digital cartography production, the map was edited and improved for publication purposes using Adobe Illustrator 6.0 ® software. The map, accompanied by a short article (Paper I), was published on the Journal of Maps (Taylor & Francis) in 2019 and is illustrated in Chapter 3.

2.2.1.2 Structural model of the Tres Vírgenes region

The main aim of analysing structural data collected in the field was to provide a structural model for the study area, able to resume the processes responsible for the upper crustal volume deformation and to highlight the interplay between structures formed in response to different geological processes (i.e. regional and volcanic). Actually, the study area displays quite a complicated structural character, deriving from its collocation inside a complex and actively deforming tectonic setting (Gulf of California). For this reason, it is generally difficult to distinguish regional from volcanic structures in the field based on their orientation and on cross-cutting relationships with lithostratigraphic units. As a result, most of the interpretation was performed following fieldwork activity, by plotting and analysing collected structural measurements and focusing on those sites where elements and morphologies were best exposed. Despite collected during the 2014-2017 field campaigns, structural data regarding the Sierra Aguajito volcanic complex were not processed, due to the lack of a robust geological base able to support any interpretation. Most of the structural measurements plotted and analysed in this Thesis thus relate to areas within or surrounding La Reforma caldera complex. Exceptions include two large-scale structures of regional importance, the Azufre and Cimarron fault systems (Fig. 2.2), which bound (Azufre fault system) or dissect (Cimarron fault) the Sierra Aguajito volcanic complex. These were included in the performed structural analysis as of key importance for the reconstruction of the regional deformation patterns characterising the Tres Vírgenes region. Structural data collected in the field were firstly loaded into ArcGIS ESRI ® (for Desktop 10.2.1.3497 version, by ESRI Inc.). Then they were sorted and divided into 'structural sites' for plotting and interpretation purposes, according to their intra- or extra-caldera location and their belonging to the most meaningful and prominent structures identified in the field. Plotting of sorted data was performed with the Stereonet software ® (2016 version by R.W. Allmendiger). Inside each identified structural site structures were furtherly subdivided based on their nature (i.e. faults, fractures, veins, dykes) and kinematics (i.e. normal fault, reverse fault, oblique fault; when applicable). As the production of La Reforma caldera complex

geological map (Paper I) and the analysis of structural data proceeded toe-to-toe, mapped structures were included in the map.

2.2.1.3 Geologic cross-sections through La Reforma caldera complex

Geologic cross-sections represent an easy way to visualize vertically the geometries of rock successions and their deformation caused by geological processes (i.e. tectonics, volcanism, slope movements). In order to summarize the outcomes of geological and structural studies performed across La Reforma caldera complex and in surrounding areas, two NW-SE and NE-SW trending geological cross-sections were traced with the ArcGIS ESRI ® software (for Desktop 10.2.1.3497 version, by ESRI Inc.) through La Reforma caldera complex. This helped to understand the role exerted by the identified structures in the evolution of La Reforma caldera complex, allowing discussing issues like geometries characterising caldera collapse and resurgence processes, and the exhumation and consequent exposure of Cretaceous basement inside the caldera depression.

The structural model of the study area and the geological cross-sections through La Reforma caldera complex are included in Paper II, that discusses regional control on the evolution of La Reforma caldera complex (Chapter 4). This paper was submitted to the Geological Society of America (GSA) Bulletin in June 2019.

2.2.2 Analyses performed on collected samples and elaboration of results

Not all 22 collected samples could undergo planned analyses, mainly due to issues arisen during the preparation stage (i.e. sample breakage or loss during coring and cutting). Along with Figure 2.2, Table 2.1 summarizes information regarding the location of the samples, and illustrates the performed analyses. Detailed description of the samples (i.e. lithology, mineralogical composition, age) is included in the dedicated papers and chapters (Papers I to V in Chapters 3 to 7).

Table 2.1 List of analysed samples and type of performed test/analysis

		TYPE OF ANALYSIS PERFORMED											
Sample – Coordinates	**Lithology – Sample type**	**Thin section**	**Micro-structural**	**Image analysis**	**Fractal statistics**	**X-ray diffraction**	**Petrogr and Cathodolum**	**Electron microprobe**	**Laser abl ICP-MS***	**Stabe isotopes**	**Triaxial tests**	**X-ray (CT)**	**Permeab simulation**
BC-C1 112°26'31.867"W 27°27'47.435"N	Ignimbrite – protolith (La Reforma ignimbrite [a])	✓	-	-	-	-	-	-	-	-	✓	✓	✓
BC-C2 112°26'17.661"W 27°28'2.841"N	Ignimbrite – protolith (Los Balcones ignimbrite [a])	✓	-	-	-	-	-	-	-	-	✓	✓	✓
BC-C3 112°24'19.277"W 27°28'59.324"N	Ignimbrite – protolith (Punta Arena ignimbrite [a])	✓	-	-	-	-	-	-	-	-	✓	✓	✓
BC-C4 112°22'9.845"W 27°29'16.127"N	Altered ignimbrite – protolith (Punta Arena ignimbrite [a])	✓	SAMPLE LOST DURING CORING OPERATIONS										
BC-C5 112°23'26.094"W 27°28'58.396"N	Altered ignimbrite – protolith (Punta Arena ignimbrite [a])	-	-	-	-	✓	-	-	-	-	-	-	-
BC-C7 112°24'47.588"W 27°29'33.192"N	Altered ignimbrite – fault-rock (Punta Arena ignimbrite [a])	✓	✓	-	-	✓	-	-	-	-	-	✓	✓
BC-C8 112°27'38.085"W 27°26'39.097"N	Ignimbrite – fault-rock (Los Balcones ignimbrite [a])	✓	✓	-	-	-	-	-	-	-	-	-	-
BC-C10 112°19'30.949"W 27°27'9.618"N	Ignimbrite – protolith (Cueva Amarilla ignimbrite [a])	SAMPLE LOST DURING THIN SECTION PREPARATION AND CORING OPERATIONS											
BC-C11 112°32'7.548"W 27°36'38.825"N	Pliocene PDC – protolith (unnamed)	✓	SAMPLE LOST DURING CORING OPERATIONS										
BC-C12 112°28'11.835"W 27°32'36.312"N	Ignimbrite – protolith (Carrizo ignimbrite [a])	✓	-	-	-	-	-	-	-	-	✓	✓	✓
BC-C13 112°30'21.793"W 27°29'44.131"N	Ignimbrite – protolith (Aguajito ignimbrite [a])	✓	-	-	-	-	-	-	-	-	✓	✓	✓

BC-C14 112°23'12.894"W 27°21'54.19"N	Lava flow – fault-rock (Santa Lucia fm. [a])	✓	✓	✓	✓	-	✓	✓	✓	✓	-	✓	✓
BC-C15 112°22'5.636"W 27°22'32.183"N	Ignimbrite – protolith (La Reforma ignimbrite [a])	✓	-	-	-	-	-	-	-	-	✓	✓	✓
BC-C16 112°21'23.773"W 27°28'15.673"N	Intrusion – fault-rock (Cueva del Diablo fm. [a])	✓	✓	✓	✓	-	-	-	-	-	-	✓	✓
BC-C17 112°33'15.934"W 27°31'39.999"N	Ignimbrite – fault-rock (Aguajito ignimbrite [a])	✓	✓	✓	✓	-	-	-	-	-	-	✓	✓
BC-C18 112°33'16.026"W 27°31'40.064"N	Ignimbrite – fault-rock (Aguajito ignimbrite [a])	✓	✓	✓	✓	-	-	-	-	-	-	✓	✓
BC-C19 112°33'16.075"W 27°31'40.553"N	Ignimbrite – fault-rock (Aguajito ignimbrite [a])	✓	✓	✓	✓	-	-	-	-	-	-	✓	✓
BC-C20 112°33'16.007"W 27°31'40.571"N	Ignimbrite – fault-rock (Aguajito ignimbrite [a])	✓	✓	✓	✓	-	-	-	-	-	-	✓	✓
BC-C21 112°33'19.514"W 27°31'44.525"N	Altered ignimbrite – protolith (Aguajito ignimbrite [a])	-	-	-	-	✓	-	-	-	-	-	-	-
BC-C22 112°33'24.864"W 27°31'47.133"N	Ignimbrite – fault-rock (Aguajito ignimbrite [a])	✓	✓	✓	✓	-	-	-	-	-	-	✓	✓
BC-C23 112°33'27.842"W 27°31'50.046"N	Ignimbrite – fault-rock (Aguajito ignimbrite [a])	✓	✓	✓	✓	-	-	✓	-	-	-	✓	✓
BC-C24 112°33'28.869"W 27°31'57.057"N	Pliocene PDC – fault-rock (unnamed)	✓	✓	✓	✓	-	✓	✓	✓	✓	-	✓	✓

[a] : for detailed description of the lithostratigraphic units see Paper I in Chapter 3.

* Laser abl ICP-MS : laser ablation inductively coupled plasma mass spectrometry.

2.2.2.1 Thin sections preparation

Thin section observation at the optical microscope represents the basis for any geological investigation at the millimetre to sub-millimetre scale, including the mineralogical and petrographic characterization of rocks that usually represents the starting point for any geological study.

For what concerns this Thesis, prepared thin sections (Table 2.1) not only provided the base for lithological and petrographic descriptions, but also represented the material directly inspected during micro-structural and image analyses, and by cathodoluminescence, electron microprobe and laser ablation inductively coupled plasma mass spectrometry (LA-ICP-MS) instruments. Standard 28 x 47 mm thin sections were prepared for most samples, whilst specific polished thin sections about 100 μm thick were instead prepared for samples BC-C14 and BC-C24 undergoing LA-ICP-MS analysis. Following manual cut with a metal saw working with water, the roughly 23 x 41 x 10 mm resulting rock slice was impregnated with blue dimethyl resin to highlight open porosity. The rock slice was then thinned to a thickness variable for different samples (around 30-50 μm), in function of the cohesive characteristics. No thin sections were prepared for samples BC-C5 and BC-C21, representing a duplicate sample of BC-C7 and BC-C13 respectively, and specifically collected for X-ray diffractometric analysis purposes. Sample BC-C10 was lost during cutting operations preceding thin section preparation due to its loose character.

2.2.2.2 Micro-structural and image analyses

Coupling of meso- and micro-structural investigations is a commonly used methodology for understanding the mega- to meso-scale structures evolution in a variety of volcanic settings (Taylor et al., 1994; Sibson, 1996; Van Wyk de Vries et al., 1998; Lagmay et al., 2005; Norini et al., 2006; Holoham et al., 2008; Cembrano et al., 2009; Nkono et al., 2009; Lavallée et al., 2014). In this Thesis, micro-structural and image analyses (micro-scale) followed and were coupled with structural analysis of field data (meso-scale) in order to: i) gain a better picture on fault-related deformation patterns considering the often encountered bad preservation conditions of fault kinematic indicators, common in volcanic settings (i.e. Norini et al., 2016); ii) discern among the different mechanisms (regional or volcanic) that generated the structures observed in the study area, exhibiting a structurally complicated character; iii) reconstruct the timing of structures marked by specific products of volcanic or tectonic activity (i.e. fluid circulation and related high-temperature mineralization vs pure brittle deformation under shear regimes). Following the identification of the mineral assemblage constituting the samples, 11 standard thin sections of fault-rock samples (Table 2.1) were carefully investigated for micro-structural elements (i.e. micro-fractures, veins and sigmoids) with the Axioskop Pol Routine

Microscope (transmitted and reflected light) by Carl Zeiss Microscopy ® at the Earth Sciences Department "Ardito Desio" of Milan University. The chronology between faulted-related deformation and fluid circulation events was identified, when possible. Image analysis followed micro-structural observations, and was performed on photos taken with the Axioskop Pol Routine Microscope on which the previously identified structural elements were manually re-traced. These photos were processed with the Fiji (Fiji Is Just ImageJ) © software, an open-source image processing package that allowed gathering the following data: i) total number of elements; ii) total area covered by elements; iii) elements average size; iiii) single elements length and angles formed with a set direction. The set direction was the projection of the shear direction (marked in the field) on thin sections. Measurements performed by the Fiji © software in local units were converted to millimetres for each sample based on the scale of the photo derived from the optical microscope. Not all samples that underwent micro-structural study were subject to image analysis: sample BC-C7 could not undergo image analysis due to the lack of orientation with respect to the shear zone, whilst sample BC-C8 due to the lack of micro-structures. Image analysis was therefore performed on 9 fault-rock standard thin sections (Table 2.1). Resulting angles formed by micro-structural elements with the projection of the shear direction were interpreted according to the well-known Riedel model (Riedel, 1929; Tchalenko and Ambraseys, 1970), and plotted in un-weighted and length-weighted rose diagrams (Nixon et al., 2001). Micro-structures length frequency distributions were also plotted. The ratio between the micro-structural elements smallest measured length and the minimum length of the investigated structure was also estimated in order to gain information on the extent reached by deformation at the micro-scale.

2.2.2.3 Fractal statistics

Fractal geometry is a branch of mathematics that identifies and quantifies how the geometry of patterns repeats from one size to another (Barton and La Pointe, 1995). Several are the examples in nature of shapes and geometries rather similar to fractals (i.e. geomorphological coast profiles, ice crystal geometries, leaves and flowers structures), including those resulting from geological processes. Actually, one of the most studied subjects over the last 20 years is the fractal nature of faults. Quantitative analysis of fault-zone characteristics has so far represented a growing research field, aimed at providing statistically-based predictions beyond the scale of observation (Barton and La Pointe, 1995; Cowie et al., 1996; Turcotte, 1997; Cello et al., 2000). Fractal statistics and the determination of fractal dimensions are the most commonly performed operations to test whether the analysed fault or fracture patterns display a self-similarity in the growth process, that could imply a universal faulting mechanism (Hatton et al., 1994) and a generalized deformation trend over a certain region. As part of the PhD research activity, the length distributions of micro-fractures identified

during image analysis performed on 9 fault-rock samples underwent simple fractal statistics calculations (Mandelbrot, 1983). This was done with the purpose of testing whether regional fault patterns identified across the study area resulted from a self-similarity in deformation processes affecting this sector of the Gulf of California, as already suggested by field observations and results of analyses performed at the meso-scale. The fractal dimension (D) was determined for each of the analysed samples by approximation to the "a" coefficient of the linear regression line (y=ax+b) fitting: the ratio between the sample maximum micro-fracture length and the cumulative length of a certain length interval (1/s), on the X axis, versus the frequency of micro-fractures falling within a certain length interval (N(s)), on the Y axis, in a log-log plot.

Results of micro-structural and image analysis and of fractal statistics are included in Paper III (Chapter 5), submitted to the Journal of Structural Geology in August 2019.

2.2.2.4 X-ray diffraction

X-ray diffraction represents a non-destructive powerful tool to identify minerals in rocks and soils, routinely applied to geological, mineralogical, pedological, chemical and forensic investigations (Hanawalt et al., 1938; Périnet, 1964; Eberl, 2003; Harris et al., 2008). This technique is also able to investigate clay particles, frequently too small to be recognised by classical optical crystallographic methods (Carrol, 1970; Brown, 1982). For these reasons, X-ray diffraction was chosen to investigate the unknown mineralogy of hydrothermal alteration phases developed within ignimbrites collected in proximity of some of the mapped faults (Table 2.1, Fig. 2.2). Samples BC-C5, BC-C7 and BC-C21 were manually reduced to powders, which were analysed with the high-resolution X-ray powder diffractometer Panalytical X' pert Pro at 40 kV and 40mA at the Department of Earth Sciences "Ardito Desio" of Milan University. Results were plotted by the XPert software in graphs displaying the peaks and relative abundance of the identified mineral phases.

2.2.2.5 Petrographic and cathodoluminescence analyses

Standard petrographic and cathodoluminescence analyses were performed on the only two fault-rock samples (BC-C24 and BC-C14, Table 2.1) displaying considerable amounts of calcite under various forms, that were identified during mineralogical characterization preceding micro-structural analysis. In this Thesis, in addition to describing the mineral assemblage of rocks, petrographic analysis also focused on distinguishing and describing the structure and chronology of the different identified calcite phases linked to circulation events along the fault planes. Petrographic analysis was performed on 4 thin sections with the polarized transmitted and reflected light Axioskop Pol Routine Microscope by

Carl Zeiss Microscopy ® at the Department of Earth Sciences "Ardito Desio" of Milan University. Cathodoluminescence analysis followed petrographic analysis and was aimed to detect eventual luminescence of the calcite phases, activated and quenched by the concentration of Mn^{2+} and Fe^{2+} within the calcite crystals, respectively (Machel, 1985; Barnaby and Rimstidt, 1989). As manganese can be incorporated in calcite crystal lattice only when reduced, cathodoluminescence is a routinely deployed technique on carbonates (Richter et al., 2003) to provide information on diagenetic features, calcite cement phases, replacement reactions, pore water chemistry and redox conditions during calcite precipitation (Machel, 1985; Budd et al., 2000) and to investigate grain provenance and diagenetic cement phases in clastic sedimentary rocks (Richter et al., 2003). This technique has also been successfully applied in volcanic-hydrothermal settings and along deformation zones by Benedicto et al. (2008), Barker et al. (2009) and Uysal et al. (2011). In the case of this Thesis, the use of cathodoluminescence was specifically aimed to derive information regarding the redox conditions and the origin of the calcite-precipitating fluids. Cathodoluminescence analysis was performed using a luminoscope Cambridge Image Technology Limited (CITL), Cambridge, UK, at the Department of Earth Sciences "Ardito Desio" of Milan University. Photos of calcite luminescent and non-luminescent phases were taken with a camera assembled on the luminoscope and used as the basis for following analyses (electron microprobe and LA-ICP-MS) performed to define their chemical composition.

2.2.2.6 Electron microprobe

The electron microprobe technique allows characterising silicate minerals and metal oxides (Sweatman et al., 1969; Paquette et al., 1990) and is often combined with cathodoluminescence in the case of calcite to investigate the Fe and Mn content of luminescent and non-luminescent calcite phases (Paquette et al., 1990; Pagel et al., 2000). For this purpose, previously identified and mapped spots representing luminescent and non-luminescent calcite phases in samples BC-C14 and BC-C24 were investigated with a 5 μm wide electron beam generated by the JEOL 8200 Super Probe of the Electron Microprobe Laboratory of the Department of Earth Sciences "Ardito Desio" of Milan University. Results obtained in percentages of mass and oxides were converted to ppm and plotted in graphs for each of the analysed spots. The Mn and Fe content of points analysed with the electron microprobe was compared with their luminescent or non-luminescent character, in order to gain information on the redox conditions of fluids precipitating calcite along BC-C24 and BC-C14 fault planes.

2.2.2.7 Laser ablation inductively coupled plasma mass spectrometry (LA-ICP-MS)

The laser ablation inductively coupled plasma mass spectrometry (LA-ICP-MS) technique is routinely applied in several contexts (i.e. environmental, geology, nuclear, clinical, life-science, pharmaceutical)

and to a variety of materials (i.e. semiconductors, various inorganic materials including metals, oxides, nanoparticles, foods, organic molecules like proteins, minerals; Bolea-Fernandez et al., 2015; Sakai, 2015) to detect minor and trace element (including rare earths elements, REE) abundances. In the case of calcite this technique is often coupled with the electron microprobe technique, and provides REE patterns and anomalies that are useful to typify fluids of different origin, to investigate equilibrium/dis-equilibrium conditions of the fluid-rock system, as well as to determine REE fractionation and partition coefficients of complexing species (Bau, 1991; Bau and Möller, 1992; Bau, 1996; Bau and Dulski, 1999; Möller et al., 2004; Uysal et al., 2007 and 2011; Benedicto et al., 2008; Della Porta et al., 2015). For these reasons the LA-ICP-MS technique was used on samples BC-C14 and BC-C24. The objective was to determine the origin (i.e., marine, meteoric, hydrothermal) of fluids circulating and precipitating calcite along faults and to verify the potential of faults in sustaining hydrothermal fluid circulation across the study area. The LA-ICP-MS analysis was performed on the specifically prepared 100 µm thick and polished thin sections at the IGG-CNR (*Istituto di Geoscienze e Georisorse - Consiglio Nazionale delle Ricerche*) of Pavia. The used instrument couples an Eximer Laser 193nm ArF (GeoLas200 Microlas) with a Triple Quadrupole (8900 QQQ from Agilent). The Agilent 9800 QQQ Triple Quadrupole allows obtaining precision and accuracy better than 5% and 10%, respectively. Photos of BC-C24 and BC-C14 standard thin sections displaying luminescent and non-luminescent calcite phases and photos taken in parallel and crossed polarizers with the Axioskop Pol Routine Microscope by Carl Zeiss Microscopy ® were used to position the 50 µm wide laser beam on the targeted spots during the LA-ICP-MS analysis. Photos of the 100 µm thick polished thin sections, taken under reflected light with the Zeiss Axioscope A.1 microscope (combined for transmitted and reflected light observations) by Carl Zeiss Microscopy ® at the Department of Earth Sciences "Ardito Desio" of Milan University, were also used during LA-ICP-MS analysis. Data reduction was performed using the Glitter software package (van Achterbergh et al., 2001) and results of the LA-ICP-MS analysis were exported in Excel sheets. Average REE abundances of the two analysed samples were compared, and Y/Ho, Zr/Hf and Sm/Nd ratios calculated to derive information on the marine or non-marine origin of fluids precipitating calcite. Siliciclastic contamination by volcanic material and metal contamination by anthropic source was inferred based on Zr, U, Th, Cu, Zn, Ni and Cr concentrations. REE and Yttrium (REY=REE + Y) concentrations measured by the LA-ICP-MS for samples BC-C24 and BC-C14 were normalized to shale (PAAS) and chondrite (C1-chondrite) values using Evensen et al. (1978), Bau and Dulski (1999), Möller (2002) and Piper and Bau (2013) equations, plotted in Excel and compared with trends displayed by calcite precipitated in a variety of geological settings (i.e. marine, hydrothermal, geothermal, meteoric, fluvial, fault-zone, altered crust). Enrichment and depletion trends of Light Rare Earths Elements (LREE), Middle Rare Earths Elements

(MREE) and Heavy Rare Earths Elements (HREE), along with Ce, La, Gd and Eu anomalies were computed on shale- and chondrite-normalized values based on Lawrence et al. (2006) geometric calculation method. The Ce anomaly was used to derive further indication on the redox state of calcite-precipitating fluids based on its polarity, as commonly performed in both marine (Bau and Dulski, 1999; Möller, 2000; Möller et al., 2003) and hydrothermal settings (Barrat et al., 2000), and on fault-related calcite phases (Pili et al., 2002). Ce and Eu anomalies were additionally used to constrain calcite precipitation temperatures (Bau and Möller, 1992; Yamagutchi et al., 2011). These were then compared with palaeotemperatures estimated based on stable isotope values ($\delta^{18}O$) determined on the same calcite phases.

2.2.2.8 Oxygen and carbon stable isotopes

Delta values of hydrogen (δD), oxygen ($\delta^{18}O$) and carbon ($\delta^{13}C$) are routinely measured in sedimentary geology (Arthur et al., 1983), as they can provide information on fluid origin (hydrogen and carbon, Hoefs, 1980; Sharp, 2007), calcite precipitation temperature (oxygen, McCrea 1950; Epstein et al., 1953; Craig, 1965; Tarutani et al., 1969; Hoefs, 1980; Kim and O'Neil, 1997; Sharp, 2007; Coplen 2007), as well as insights on diagenesis, palaeoclimatology and palaeoceanography (Hudson and Anderson 1989; Lajtha and Michener, 1994; Hiatt and Pufhal, 2014). For the same purposes they have been recently used in geothermal-volcanic contexts (Barker et al., 2009; Uysal et al., 2009; Liotta et al., 2010) and on fault-related calcite phases (Travè et al., 1998; Boles and Grivetti, 2000; Pili et al., 2002; Benedicto et al., 2008; Liotta et al., 2010). Despite some indications on temperature and origin of calcite precipitating fluids were provided by LA-ICP-MS analysis on samples BC-C24 and BC-C14, carbon and oxygen stable isotopes determinations were also performed. This choice derived from the possible contamination of REE patterns and resulting anomalies measured by the LA-ICP-MS technique by siliciclastic volcanic material hosting the calcite. Carbon and oxygen stable isotopes on fault-precipitated calcite were thus performed to independently infer precipitation palaeotemperatures (oxygen) and to obtain confirmation on the origin of fluids (carbon) suggested by LA-ICP-MS analysis. Carbonate powders were manually extracted from samples BC-C24 and BC-C14 with a micro-drill and reacted with > 99% orthophosphoric acid at 70°C before the analysis with the automated carbonate preparation device (Gasbench II) and the Thermo Fischer Scientific Delta V Advantage continuous flow isotopic ratio mass spectrometer (IRMS) at the Department of Earth Sciences "Ardito Desio" of Milan University. The resulting carbon and oxygen isotopic compositions were expressed in the conventional delta notation calibrated to the Vienna Pee-Dee Belemnite (V-PDB) scale by the international standards IAEA 603 and NBS-18. Output results were normalized using the two point linear normalization (Paul et al., 2007). $\delta^{13}C$ and $\delta^{18}O$ isotopic

values for different calcite phases were compared with published values for different geological settings and plotted in Excel. Palaeotemperatures were then derived from $\delta^{18}O$ isotopic values based on $\delta^{18}O$ isotopic value of spring waters in the Tres Vírgenes region (Portugal et al., 2000; Hinojosa et al., 2005) and on the application of different published equations (Craig, 1965; O'Neil et al., 1969; Coplen et al., 1983; Kim and O'Neil, 1997; Mulitza et al., 2003; Sharp, 2007; Coplen, 2007). $\delta^{13}C$ values of the CO_2 indicative of the isotopic signature of the Dissolved Inorganic Carbon (DIC) of the fluids precipitating calcite were also derived based on Panichi and Tongiorgi (1976) and Romanek et al. (1992) equations using the previously computed $\delta^{18}O$-derived palaeotemperatures as input parameters, due to the scarcity of data regarding the Tres Vírgenes geothermal waters characterization (Birkle et al., 2016). Differently from what performed during the electron microprobe and LA-ICP-MS analyses, luminescent and non-luminescent calcite phases of samples BC-C24 and BC-C14 phases could not be properly separated during manual micro-drilling preceding stable isotopes determinations, due to their sub-millimetre scale. For the same reason only one (non-luminescent) calcite phase among the several identified could be analysed in sample BC-C14. As a result, the derived isotopic signature and palaeotemperatures do often refer either to a mixture of luminescent and non-luminescent calcite phases (BC-C24) or only to some of the identified calcite phases (BC-C14).

Results of X-ray diffraction, petrographic and cathodoluminescence analyses, electron microprobe, LA-ICP-MS and carbon and oxygen stable isotopes analyses are included in Paper IV (Chapter 6), submitted to the Journal of Volcanology and Geothermal Research in September 2019.

2.2.2.9 Porosity and permeability determinations in the triaxial cell

The determination of porosity and permeability in standard (Carpenter et al., 1986; Pan et al., 2015) or specifically designed (Monfared et al., 2011) triaxial cells is a consolidated methodology used on a variety of natural (i.e. rocks) and artificial materials. Protolith samples (Table 2.1) underwent porosity and permeability determinations through collocation inside the automatic Wikeham Farrance triaxial system fitted with an automatic volume change device and hydromatic devices for pressure control at Department of Earth and Environmental Sciences of Milano-Bicocca University. The main aim of determining porosity and permeability of protolith rocks was to evaluate the potential of having vertical and/or lateral flow of hydrothermal fluids through the formations mapped across the study area. Fault-rock samples could not be tested with this methodology, as they could not be collocated inside the Wikeham Farrance triaxial cell, which only allows tests on cores of specific shape (cylindrical) and dimensions. Before their collocation in the triaxial cell, protolith samples underwent coring and cutting operations to isolate a 37 mm diameter and variably (46 to 75 mm) long core.

During these preparatory operations samples BC-C4, BC-C10 and BC-C11 broke into pieces too small to be placed inside the triaxial cell and their porosity and permeability could thus not be determined. Following sample collocation, the triaxial cell was filled with distilled water and protolith samples were left until the highest possible saturation degree was reached. The achievement of saturated conditions was generally difficult, and CO_2 flushing of samples was used in some cases to favour air escape from tight pores before filling the triaxial cell with water. Following saturation, interconnected (or effective) porosity of samples was computed by knowing the sample volume, dry and wet weights (prior and following saturation), based on the standard test procedure by IRMS (1972) using the following equation (Eq. 1):

$$\Phi_i = V_v / V_T \tag{1}$$

where Φ_i is interconnected porosity, V_v is the volume of voids and V_T is the total volume. Following saturation, the interconnected pores are filled by water and V_v thus represents the volume of water. V_T instead represents the sum of the volume of water (V_v) and the volume or the solid (or dry volume of the sample prior to saturation). All volumes were back-calculated from measured dry and wet weights and from densities. Under saturated conditions, a top to bottom (or vice versa) flow of distilled water was then induced inside the core, by applying a delta pressure between the sample top and bottom. The water flow was measured at regular time intervals (30 seconds) by an automatic volume change device connected to the triaxial system. Hydraulic conductivity was determined based on the recorded volume variations by means of the Darcy equation (Eq. 2):

$$Hc = Q \cdot 10^{-2} / 60 \cdot i \cdot \delta t \cdot A_C \tag{2}$$

where Q is the volume variation (cm^3) measured by the volume change device during the δt time interval, i is the idraulic gradient, or the ratio between the applied hydraulic load and the height of the core, and A_C the core section (cm^2). Permeability was calculated from hydraulic conductivity (Hc) by taking into consideration the fluid (distilled water) density (997 kg/m^3) and viscosity ($8.9 \cdot 10^{-4}$ Pa.s) and g (9.8 m/s^2). Both interconnected porosity and hydraulic conductivity derived using the triaxial system were determined under unconfined conditions, representative of the surface to near-surface conditions at which all samples were collected, and without reaching sample failure.

2.2.2.10 Porosity determination through X-ray computerized tomography (CT)

High resolution X-ray computerized tomography (CT) is a technique ideally suited to a wide range of geological investigations, as it is a non-destructive and relatively quick method to produce images that closely match serial sections through an object (Ketcham and Carlson, 2001; Fusi and Marinez-Martinez, 2013) of either homogeneous (i.e. artificial material like concrete) or heterogeneous (i.e. magmatic and sedimentary rocks) texture. It is commonly used for porosity and pore space geometry characterization with resolutions from 5 to 650 μm in several rock types, including volcanic rocks (Pola et al., 2014; Pola et al., 2016) like the one analysed in this Thesis. Both protolith and fault-rock samples (Table 2.1) were analysed with the X-ray (CT) technique, for comparison purposes with the triaxial system results in the case of protoliths, and to obtain novel porosity estimates in the case of fault-rock samples. The X-ray (CT) technique thus allowed to overcome the limitations affecting the triaxial system. X-ray (CT) images were acquired with the GE-D600 medical CT hybrid scanner and a Bir/Actis 130/150 Micro CT/DR system at the Department of Earth and Environmental Sciences of Milano-Bicocca University. With this technique, X-rays passing through the sample, that rotates during the acquisition, are collected by a detector that transforms them into light radiations, collected by a 12 bit digital camera sending images to a computer where they are processed and visualized as grey scale images that reconstruct the internal structure of samples based on the distribution of the X-ray linear absorption coefficient deduced from the projection of X-rays through a sample (Ohtani et al., 2000). The same resolution (voxel size = 0.026 mm) was used in the x, y and z directions and a variable number of slices (between 900 and 2600) was obtained, depending on sample dimensions. X-ray (CT) images were processed with the Thermo Scientific ™ Avizo ™ Software 9, which allowed estimating total and interconnected (or effective) porosity by applying interactive thresholds that isolated the 3D total and pore space volume for each sample. Interconnected pores were distinguished from isolated pores based on the evidence that interconnected pores are seen by the Avizo software as a single large pore displaying a rather high 3D pore volume. Interconnected and isolated pore 3D volume distributions were then plotted in Excel and interconnected porosity of protoliths determined with the X-ray (CT) technique was compared with estimates obtained from the triaxial system. In the case of samples BC-C14, BC-C16 and BC-C24, displaying significant amounts of minerals precipitated into fault-related micro-fractures following fluid circulation, porosity associated with the pore space filled by these minerals was separately calculated. Open porosity left in these samples following fluid circulation (actual conditions) and porosity associated with the pore space filled by mineral precipitation were summed to estimate the original porosity of fault-rock samples before any

fluid circulation occurred (pre-sealing conditions). The decrease in interconnected porosity following mineral precipitation was then determined.

2.2.2.11 Permeability simulations with the Avizo XLab extension

Permeability simulations (or fluid flow models) represent the most commonly used tool for describing the behaviour and properties of fluids circulating through rock masses and along crustal structures, in both the hydrocarbon and geothermal industries (Younker et al., 1982; Clauser and Villinger, 1990; Muraoka et al., 1998; Furuya et al., 2000; Bellani et al., 2004). These models have a crucial role for assessing successive exploration or exploitation strategies (Barbier, 2000 and references therein; O'Sullivan et al., 2001; Liotta et al., 2010) and use a variety of data inputs and formats. Given that porosity of fault-rock samples was estimated through the tomography technique, for continuity purposes fault-rock permeability was determined based on the same X-ray (CT) images. The same software (Avizo™) was thus used to perform permeability simulations. A trial version of the Avizo XLab extension was requested to Thermo Scientific ™ and installed on the CPU of the X-ray (CT) laboratory of the Department of Earth and Environmental Sciences of Milano-Bicocca University. This extension was chosen as specifically designed to provide numerical simulation capabilities to calculate physical properties of materials from the 3D images of a sample. In addition to fault-rock samples, permeability simulation were also performed on protoliths (Table 2.1), based on the same extension module and software. Permeability simulations allowed to overcome the limitations of the triaxial system preventing hydraulic conductivity measurements on fault-rock samples and to investigate the along-fault and cross-fault fluid flow potential across the study area. Furthermore, novel permeability values were obtained on protoliths, that could be compared with those resulting from the triaxial system. The algorithm chosen to estimate permeability with the Avizo XLab extension suite is the *Absolute Permeability Experiment Simulation*, based on Stokes equations resolution and simulating an experiment along the x, y and z axes. The boundary conditions for this algorithm imply the following: no slip conditions at fluid-solid interfaces; the isolation of the sample from outside allowing no flow out of the system; the user can choose two among the following three conditions, the third being estimated from the chosen two: input pressure, output pressure, flow rate. In this study the input and output pressures were set at 130 and 100 kPa respectively, while the flow rate left free to be computed by the software. The chosen pressure values imply a delta pressure of 30 kPa, comparable with the hydraulic load applied inside the triaxial cell and representative of surface or near-surface conditions. Fluid viscosity during the simulation was set at 0.001 Pa.s, representing the viscosity of water. The input volume for the *Absolute Permeability Experiment Simulation* was the 3D pore space volume extracted by the Avizo software during porosity calculations. The *Axis Connectivity Tool* algorithm

was used before any permeability simulation to remove isolated void spaces and speed up computer calculations. A maximum number of 50 slices was used to optimize the computation time, even though additional simulations with a different number of slices were performed in order to investigate the presence of a size effect (Alarcon-Ruiz et al., 2010) and outputs were compared. Permeability was determined in the x, y and z directions for fault-rock samples in order to evaluate both the along-fault and cross-fault permeability, whilst only along one direction (z) for protolith samples, the same tested inside the triaxial cell. As in the case of porosity, protolith permeability derived from X-ray (CT) images through simulation was compared with the one obtained from inducing a fluid flow through the sample inside the triaxial cell. Analogously to porosity estimation, double permeability simulations were performed on samples BC-C14, BC-C16 and BC-C24: a first simulation for the actual conditions and a second one for the pre-sealing conditions.

2.2.2.12 Porosity-permeability relationships

The identification of porosity vs permeability relationships is common practice in sedimentary geology (i.e., sandstone and carbonate rocks) for permeability predictions, mostly linked to hydrocarbon exploration and exploitation purposes. Rather scarce are instead published porosity-permeability relationships for volcanic rocks (i.e. unconventional hydrocarbon reservoirs or geothermal reservoirs), despite few attempts have been recently done by using simplified relationships (Costa, 2006). In order to search for a porosity-permeability relationship for the study area, and to improve the number of case studies regarding volcanic and ignimbrite rocks in particular, porosity-permeability relationships were extrapolated for protolith and fault-rock samples, based on values obtained with the triaxial system and the X-ray (CT) and Avizo XLab permeability simulation techniques. Porosity and permeability were plotted one against the other in Excel on linear plots, and the equations were extrapolated by fitting the data with simple regression lines. Two equations were derived: i) one for protoliths based on triaxial tests results; ii) one for fault-rocks based on X-ray (CT) and coupled Avizo XLab permeability simulations conducted in the along-fault flowing direction.

Results of porosity and permeability testing inside the triaxial cell, X-ray (CT) and permeability simulations are included in Paper V (Chapter 7), submitted to the Engineering Geology Journal in September 2019.

2.3 References

Alarcon-Ruiz, L., Brocato, M., Dal Pont, S., & Feraille, A. (2010). Size effect in concrete intrinsic permeability measurements. Transport in porous media, 85(2), 541-564.

Arango-Galván, C., Prol-Ledesma, R. M., Torres-Vera, M. A., 2015. Geothermal prospects in the Baja California peninsula. Geothermics, 55, 39-57.

Arthur, M., Anderson, T., Kaplan, I., Veizer, J., Land, L., 1983. Stable Isotopes in Sedimentary Geology, SEPM Short Course No 10. SEPM.

Avellán, D. R., Macías, J. L., Arce, J. L., Jiménez-Haro, A., Saucedo-Girón, R., Garduño-Monroy, V. H., Sosa-Ceballos, G., Bernal, J. P., Lopez-Loera, H., Cisneros, G., Layer, P. W., Garcia-Sanchez, L., Reyes-Aguston, G., Rocha, V.S., Rangel, E., 2018. Eruptive chronology and tectonic context of the late Pleistocene Tres Vírgenes volcanic complex, Baja California Sur (México). Journal of Volcanology and Geothermal Research, 360, 100-125.

Barbier, E., 2002. Geothermal energy technology and current status: an overview. Renewable and sustainable energy reviews, 6, 3-65.

Barker, S. L., Bennett, V. C., Cox, S. F., Norman, M. D., Gagan, M. K., 2009. Sm–Nd, Sr, C and O isotope systematics in hydrothermal calcite–fluorite veins: implications for fluid–rock reaction and geochronology. Chemical Geology, 268, 58-66.

Barnaby, R. J., Rimstidt, J. D., 1989. Redox conditions of calcite cementation interpreted from Mn and Fe contents of authigenic calcites. Geological Society of America Bulletin, 101, 795-804.

Barrat, J. A., Boulegue, J., Tiercelin, J. J., Lesourd, M., 2000. Strontium isotopes and rare-earth element geochemistry of hydrothermal carbonate deposits from Lake Tanganyika, East Africa. Geochimica et Cosmochimica Acta, 64, 287-298.

Barton, C. C., Larsen, E., 1985. Fractal geometry of two-dimensional fracture networks at Yucca Mountain, southwestern Nevada.

Bau, M., 1991. Rare-earth element mobility during hydrothermal and metamorphic fluid-rock interaction and the significance of the oxidation state of europium. Chemical Geology, 93, 219-230.

Bau, M., 1996. Controls on the fractionation of isovalent trace elements in magmatic and aqueous systems: evidence from Y/Ho, Zr/Hf, and lanthanide tetrad effect. Contributions to Mineralogy and Petrology, 123, 323-333.

Bau, M., Dulski, P., 1999. Comparing yttrium and rare earths in hydrothermal fluids from the Mid-Atlantic Ridge: implications for Y and REE behaviour during near-vent mixing and for the Y/Ho ratio of Proterozoic seawater. Chemical Geology, 155, 77-90.

Bau, M., Möller, P., 1992. Rare earth element fractionation in metamorphogenic hydrothermal calcite, magnesite and siderite. Mineralogy and Petrology, 45, 231-246.

Bellani, S., Brogi, A., Lazzarotto, A., Liotta, D., Ranalli, G., 2004. Heat flow, deep temperatures and extensional structures in the Larderello Geothermal Field (Italy): constraints on geothermal fluid flow. Journal of Volcanology and Geothermal Research, 132, 15-29.

Benedicto, A., Plagnes, V., Vergély, P., Flotté, N., Schultz, R. A., 2008. Fault and fluid interaction in a rifted margin: integrated study of calcite-sealed fault-related structures (southern Corinth margin). Geological Society, London, Special Publications, 299, 257-275.

Birkle, P., Marín, E. P., Pinti, D. L., Castro, M. C., 2016. Origin and evolution of geothermal fluids from Las Tres Vírgenes and Cerro Prieto fields, Mexico–Co-genetic volcanic activity and paleoclimatic constraints. Applied geochemistry, 65, 36-53.

Bolea-Fernandez, E., Van Malderen, S.J.M., Balcaen, L., Vanhaecke, F., 2015. Direct strontium isotopic analysis of solid samples by LA-ICP-MS/MS. Application note 5991-6409EN. Agilent Technologies.

Boles, J. R., Grivetti, M., 2000. Calcite cementation along the Refugio/Carneros fault, Coastal California: a link between deformation, fluid movement and fluid–rock interaction at a basin margin. Journal of Geochemical Exploration, 69, 313-316.

Brown, G., 1982. Crystal structures of clay minerals and their X-ray identification, Vol. 5. The Mineralogical Society of Great Britain and Ireland.

Budd, D. A., Hammes, U., Ward, W. B., 2000. Cathodoluminescence in calcite cements: new insights on Pb and Zn sensitizing, Mn activation, and Fe quenching at low trace-element concentrations. Journal of Sedimentary Research, 70, 217-226.

Carpenter, G. W., Stephenson, R. W., 1986. Permeability testing in the triaxial cell. Geotechnical Testing Journal, 9, 3-9.

Carroll, D., 1970. Clay minerals: a guide to their X-ray identification, Vol. 126. Geological Society of America.

Cello, G., Gambini, R., Mazzoli, S., Read, A., Tondi, E., Zucconi, V., 2000. Fault zone characteristics and scaling properties of the Val d'Agri Fault System (Southern Apennines, Italy). Journal of Geodynamics, 29, 293-307.

Cembrano, J., Lara, L., 2009. The link between volcanism and tectonics in the southern volcanic zone of the Chilean Andes: a review. Tectonophysics, 471, 96-113.

Clauser, C., Villinger, H., 1990. Analysis of conductive and convective heat transfer in a sedimentary basin, demonstrated for the Rheingraben. Geophysical Journal International, 100, 393-414.

Coplen, T. B., Kendall, C., Hopple, J., 1983. Intercomparison of stable isotope reference samples. Nature 302, 236–238.

Coplen, T. B., 2007. Calibration of the calcite–water oxygen-isotope geothermometer at Devils Hole, Nevada, a natural laboratory. Geochimica et Cosmochimica Acta, 71, 3948-3957.

Costa, A., 2006. Permeability-porosity relationship: A reexamination of the Kozeny-Carman equation based on a fractal pore-space geometry assumption. Geophysical research letters, 33.

Cowie, P. A., Knipe, R. J., Main, I. G., 1996. Scaling laws for fault and fracture populations—analyses and applications. Journal of Structural Geology. Special Issue, 18.

Craig, H., 1965. Measurement of oxygen isotope paleotemperatures, p. 162–182. Tongiorgi, E. ed., Stable Isotopes in Oceanographic Studies and Paleotemperatures. Consiglio Nazionale Delle Ricerche, Spoleto, Italy.

Della Porta, G., Webb, G. E., McDonald, I., 2015. REE patterns of microbial carbonate and cements from Sinemurian (Lower Jurassic) siliceous sponge mounds (Djebel Bou Dahar, High Atlas, Morocco). Chemical Geology, 400, 65-86.

Eberl, D. D., 2003. User guide to RockJock-A program for determining quantitative mineralogy from X-ray diffraction data, US Geological Survey, N.2003-78.

Epstein, S., Mayeda, T., 1953. Variation of O-18 content of water from natural sources. Geochim. Cosmochim. Acta 4, 213–224.

Evensen, N. M., Hamilton, P. J., O'nions, R.K., 1978. Rare-earth abundances in chondritic meteorites. Geochimica et Cosmochimica Acta, 42, 1199-1212.

Ferrari, L., Orozco-Esquivel, T., Bryan, S. E., Lopez-Martinez, M., Silva-Fragoso, A., 2018. Cenozoic magmatism and extension in western Mexico: Linking the Sierra Madre Occidental silicic large igneous province and the Comondú Group with the Gulf of California rift. Earth-Science Reviews, 183, 115-152.

Furuya, S., Aoki, M., Gotoh, H., Takenaka, T., 2000. Takigami geothermal system, northeastern Kyushu, Japan. Geothermics, 29, 191-211.

Fusi, N., Martinez-Martinez, J., 2013. Mercury porosimetry as a tool for improving quality of micro-CT images in low porosity carbonate rocks. Engineering Geology, 166, 272-282.

García-Sánchez, L., Macías, J.L., Sulpizio, R., Osorio-Ocampo, L.S., Pellicioli, C., Pola, A., Avellán, D., Cisneros, G., García, F., Ocampo-Díaz, Y.Z.E, Lira-Beltran, R.M., Saucedo, R., Sánchez-Nuñez, J.M., Arce, J.L., Corona-Chávez, P., Reyes-Augustin, G., Cardona, M., Layer, P.W., Benowitz, J., Solari, L., Groppelli, G., 2019. Geology of La Reforma caldera complex, Baja California, Mexico. Journal of Maps, 15, 487-498.

Garduño-Monroy, V. H., Vargas-Ledezma, H., Campos-Enriquez, J.O., 1993. Preliminary geologic studies of Sierra El Aguajito (Baja California, Mexico): a resurgent-type caldera. Journal of Volcanology and Geothermal Research, 59, 47-58.

Gastil, R. G., Phillips, R. P., Allison, E.C., 1975. Reconnaissance geology of the state of Baja California (Vol. 140). Geological Society of America.

Groppelli, G., Molist, J. M., 2013. Volcanic Stratigraphy-State of the art. Ciências da Terra/Earth Sciences Journal, 18.

Groppelli, G., Viereck-Goette, L., (Eds.), 2010. Stratigraphy and geology of volcanic areas, Vol. 464. Geological Society of America.

Gutiérrez-Negrín, L. C., Maya-González, R., Quijano-León, J.L., 2010. Current status of geothermics in Mexico. In Proceedings World Geothermal Congress 2010, Bali, Indonesia, 25-29 April 2010, pp. 25-29.

Hanawalt, J. D., Rinn, H. W., Frevel, L. K., 1938. Chemical analysis by X-ray diffraction. Industrial & Engineering Chemistry Analytical Edition, 10, 457-512.

Harris, W, White, G. N., Ulery, A. L., Drees, L. R., 2008. X-ray diffraction techniques for soil mineral identification. Methods of soil analysis. Part, 5, 81-115.

Hatton, C. G., Main, I. G., Meredith, P. G., 1994. Non-universal scaling of fracture length and opening displacement. Nature, 367, 160.

Hiatt, E. E., Pufahl, P. K., 2014. Cathodoluminescence petrography of carbonate rocks: a review of applications for understanding diagenesis, reservoir quality and pore system evolution. Short Course, 45, 75-96.

Hinojosa, E. T., Verma, M. P., Partida, E. G., 2005. Geochemical Characteristics of Reservoir Fluids in the Las Tres Virgenes, BCS, Mexico. In Proceedings of World Geothermal Congress 2005 Antalya, Turkey, 24–29 April 2005, p. 11.

Hoefs, J., 1980. Stable isotope geochemistry (Vol. 9, No. 1980). Berlin: springer.

Holohan, E. P., de Vries, B. V. W., Troll, V. R., 2008. Analogue models of caldera collapse in strike-slip tectonic regimes. Bulletin of Volcanology, 70, 773-796.

Hudson, J. D., Anderson, T.F., 1989. Ocean temperatures and isotopic compositions through time. Transactions of the Royal Society of Edinburgh: Earth Sciences, 80, 183-192.

Ketcham, R. A., Carlson, W. D., 2001. Acquisition, optimization and interpretation of X-ray computed tomographic imagery: applications to the geosciences. Computers & Geosciences, 27, 381-400.

Kim, S.T., O'Neil, J.R., 1997. Equilibrium and nonequilibrium oxygen isotope effects in synthetic carbonates. Geochimica et Cosmochimica Acta 61, 3461–3475.

Lagmay, A. M. F., Tengonciang, A. M. P., Uy, H. S., 2005. Structural setting of the Bicol Basin and kinematic analysis of fractures on Mayon Volcano, Philippines. Journal of Volcanology and Geothermal Research, 144, 23-36.

Lajtha, K., Michener, R. H., 1994. Stable Isotopes in Ecology and Environmental Science. Blackwell publishing Ltd, printed in Singapore.

Lavallée, Y., Hirose, T., Kendrick, J. E., De Angelis, S., Petrakova, L., Hornby, A. J., Dingwell, D. B., 2014. A frictional law for volcanic ash gouge. Earth and Planetary Science Letters, 400, 177-183.

Lawrence, M. G., Greig, A., Collerson, K. D., Kamber, B.S., 2006. Rare earth element and yttrium variability in South East Queensland waterways. Aquatic Geochemistry, 12, 39-72.

Liotta, D., Ruggieri, G., Brogi, A., Fulignati, P., Dini, A., Nardini, I., 2010. Migration of geothermal fluids in extensional terrains: the ore deposits of the Boccheggiano-Montieri area (southern Tuscany, Italy). International Journal of Earth Sciences, 99, 623-644.

Machel, H. G., 1985. Cathodoluminescence in calcite and dolomite and its chemical interpretation. Volume 12, number 4. Published by Geoscience Canada in 1985.

Mandelbrot, B. B., 1983. The fractal geometry of nature. Vol. 173, p. 51. New York: WH freeman.

Martí, J., Groppelli, G., da Silveira, A. B., 2018. Volcanic stratigraphy: A review. Journal of Volcanology and Geothermal Research, 357, 68-91.

McCrea J. M., 1950. On the isotopic chemistry of carbonates and a paleotemperatures scale. Journal of Chemical Physics, 18, 163–171.

McLean, H., 1988. Reconnaissance geologic map of the Loreto and part of the San Javier quadrangles, Baja California Sur, Mexico. U.S. Geological Survey Miscellaneous Field Studies Map, Report No. MF-2000, p. 10, 1 mapa, escala 1:50,000.

Möller, P., 2000. Rare earth elements and yttrium as geochemical indicators of the source of mineral and thermal waters. In Hydrogeology of crystalline rocks, pp. 227-246. Springer, Dordrecht.

Möller, P., 2002. Rare earth elements and yttrium in geothermal fluids. Water Science and Technology Library, 40, 97-125.

Möller, P., Dulski, P., Morteani, G., 2003. Partitioning of rare earth elements, yttrium, and some major elements among source rocks, liquid and vapor of Larderello-Travale geothermal field, Tuscany (Central Italy). Geochimica et Cosmochimica Acta, 67, 171-183.

Möller, P., Dulski, P., Savascin, Y., Conrad, M., 2004. Rare earth elements, yttrium and Pb isotope ratios in thermal spring and well waters of West Anatolia, Turkey: a hydrochemical study of their origin. Chemical Geology, 206, 97-118.

Monfared, M., Delage, P., Sulem, J., Mohajerani, M., Tang, A. M., De Laure, E., 2011. A new hollow cylinder triaxial cell to study the behavior of geo-materials with low permeability. International Journal of Rock Mechanics and Mining Sciences, 48, 637-649.

Mulitza S., Donner B., Fischer G., Paul A., Patzold J., Ruhlemann C. Segl M., 2003. The South Atlantic oxygen isotope record of planktic foraminifera. In The South Atlantic in the Late Quaternary: Reconstruction of Material budgets and Current Systems, eds. G. Wefer, S. Mulitza and V. Ratmeyer. Springer-Verlag, Berlin, pp. 121–142.

Muraoka, H., Uchida, T., Sasada, M., Yagi, M., Akaku, K., Sasaki, M., Yasukawa, K., Miyazaki, S., Doi, N., Saito, S., Sato, K., Tanaka, S., 1998. Deep geothermal resources survey program: igneous, metamorphic and hydrothermal processes in a well encountering 500 C at 3729 m depth, Kakkonda, Japan. Geothermics, 27, 507-534.

Nixon, C. W., Sanderson, D. J., Bull, J. M., 2011. Deformation within a strike-slip fault network at Westward Ho!, Devon UK: Domino vs conjugate faulting. Journal of Structural Geology, 33, 833-843.

Nkono, C., Féménias, O., Demaiffe, D., 2009. Geodynamic framework of large volcanic fields highlighted by SRTM DEMs: Method evaluation and perspectives exampled on three areas from the Cameroon Volcanic Line. Journal of volcanology and geothermal research, 187, 13-25.

Norini, G., Groppelli, G., Lagmay, A. M. F., Capra, L., 2006. Recent left-oblique slip faulting in the central eastern Trans-Mexican Volcanic Belt: Seismic hazard and geodynamic implications. Tectonics, 25.

Ohtani, T., Nakashima, Y., & Muraoka, H. (2000). Three-dimensional miarolitic cavity distribution in the Kakkonda granite from borehole WD-1a using X-ray computerized tomography. Engineering Geology, 56(1-2), 1-9.

O'Neil J. R., Clayton R. N. Mayeda T. K., 1969. Oxygen isotope fractionation in divalent metal carbonates. Journal of Chemical Physics, 51, 5547–5558.

O'Sullivan, M. J., Pruess, K., Lippmann, M. J., 2001. State of the art of geothermal reservoir simulation. Geothermics, 30, 395-429.

Pagel, M., Barbin, V., Blanc, P., Ohnenstetter, D., 2000. Cathodoluminescence in geosciences: an introduction. In Cathodoluminescence in Geosciences (pp. 1-21). Springer, Berlin, Heidelberg.

Pan, Z., Ma, Y., Connell, L. D., Down, D. I., Camilleri, M., 2015. Measuring anisotropic permeability using a cubic shale sample in a triaxial cell. Journal of Natural Gas Science and Engineering, 26, 336-344.

Panichi, C., Tongiorgi, E., 1976. Carbon isotopic composition of CO_2 from springs, fumaroles, mofettes and travertines of central and southern Italy: a preliminary prospection method of geothermal area. Proceedings 2nd UN Symosium on the Develop and Use of Geothermal Energy, 20– 29 May 1975, San Francisco, U.S.A., pp. 815– 825.

Paquette, J., Reeder, R.J., 1990. New type of compositional zoning in calcite: Insights into crystal-growth mechanisms. Geology, 18, 1244.

Pasquarè, G., Abbate, E., Castiglioni, G. B., Merenda, L., Mutti, E., Ortolani, F., Sassi, F. P., 1992. Guida al rilevamento e all'informatizzazione della Carta Geologica d'Italia alla scala 1: 50.000. Quaderni SGN, serie III, 1, 203.

Paul, D., Skrzypek, G., Fórizs, I., 2007. Normalization of measured stable isotopic compositions to isotope reference scales–a review. Rapid Communications in Mass Spectrometry: An International Journal Devoted to the Rapid Dissemination of Up-to-the-Minute Research in Mass Spectrometry, 21, 3006-3014.

Périnet, G., 1964. Determination par diffraction X de la temperature de cuisson dun ossement calcine. Application au materiel prehistorique. Comptes Rendus Hebdomadaires De Seances De l'academie Des Sciences, 258, 4115.

Pignone, R., Accardi, N., 2002. Cromatic handbook for the printing of the geological maps. Geological Map of Italy CARG Project, Geological Survey of Italy, Cathographic State Bureau.

Pili, E., Poitrasson, F., Gratier, J. P., 2002. Carbon–oxygen isotope and trace element constraints on how fluids percolate faulted limestones from the San Andreas Fault system: partitioning of fluid sources and pathways. Chemical Geology, 190, 231-250.

Piper, D. Z., and Bau, M., 2013. Normalized rare earth elements in water, sediments, and wine: identifying sources and environmental redox conditions. American Journal of Analytical Chemistry, 4, 69-83.

Pola, A., Crosta, G. B., Fusi, N., Castellanza, R., 2014. General characterization of the mechanical behaviour of different volcanic rocks with respect to alteration. Engineering geology, 169, 1-13.

Pola, A., Martínez-Martínez, J., Macías, J. L., Fusi, N., Crosta, G., Garduño-Monroy, V. H., Núñez-Hurtado, J. A., 2016. Geomechanical characterization of the Miocene Cuitzeo ignimbrites, Michoacán, Central Mexico. Engineering geology, 214, 79-93.

Portugal, E., Birkle, P., Tello, E., Tello, M., 2000. Hydrochemical–isotopic and hydrogeological conceptual model of the Las Tres Vırgenes geothermal field, Baja California Sur, México. Journal of Volcanology and Geothermal Research, 101, 223-244.

Richter, D. K., Götte, T., Götze, J., Neuser, R.D., 2003. Progress in application of cathodoluminescence (CL) in sedimentary petrology. Mineralogy and Petrology, 79, 127-166.

Riedel, W., 1929. Zur Mechanik geologischer Brucherscheinungen ein Beitrag zum Problem der Fiederspatten. Zentbl. Miner. Geol. Palaont. Abt., 354-368.

Romanek, C. S., Grossman, E. L., Morse, J. W., 1992. Carbon isotopic fractionation in synthetic aragonite and calcite: effects of temperature and precipitation rate. Geochimica et cosmochimica acta, 56, 419-430.

Sakai, K., 2015. Routine soil analysis using an Agilent 8800 ICP-QQQ. Application note 5991-6409EN. Agilent Technologies.

Schmidt, E. K., 1975. Plate tectonics, volcanic petrology, and ore formation in the Santa Rosalía area, Baja California, Mexico. Master Degree Thesis, Department of Geosciences, University of Arizona, 1975.

Schmitt, A. K., Stockli, D. F., Hausback, B. P., 2006. Eruption and magma crystallization ages of Las Tres Vírgenes (Baja California) constrained by combined 230Th/238U and (U–Th)/He dating of zircon. Journal of Volcanology and Geothermal Research, 158, 281-295.

Sharp Z., 2007. Principles of Stable Isotope Geochemistry. Pearson Prentice Hall, Upper Saddle River, New Jersey.

Sibson, R. H., 1996. Structural permeability of fluid-driven fault-fracture meshes. Journal of Structural Geology, 18, 1031-1042.

Soller, D. R., 2004. Introduction to Geologic Mapping. McGraw-Hill Yearbook of Science & Technology, 128-130.

Sweatman, T. R., Long, J.V.P., 1969. Quantitative electron-probe microanalysis of rock-forming minerals. Journal of Petrology, 10, 332-379.

Tarutani T., Clayton R. N., Mayeda T. K., 1969. The effect of polymorphism and magnesium substitution on oxygen isotope fractionation between calcium carbonate and water. Geochimica et Cosmochimica Acta 33, 987–996.

Taylor, B., Crook, K., Sinton, J., 1994. Extensional transform zones and oblique spreading centers. Journal of Geophysical Research: Solid Earth, 99, 19707-19718.

Tchalenko, J. S., & Ambraseys, N. N., 1970. Structural analysis of the Dasht-e Bayaz (Iran) earthquake fractures. Geological Society of America Bulletin, 81, 41-60.

Travé, A., Calvet, F., Soler, A., Labaume, P., 1998. Fracturing and fluid migration during Palaeogene compression and Neogene extension in the Catalan Coastal Ranges, Spain. Sedimentology, 45, 1063-1082.

Turcotte, D. L., 1997. Fractals and chaos in geology and geophysics. Cambridge university press.

Umhoefer, P. J., Dorsey, R. J., Willsey, S., Mayer, L., Renne, P., 2001. Stratigraphy and geochronology of the Comondu Group near Loreto, Baja California Sur, Mexico. Sedimentary Geology, 144, 125-147.

Uysal, I. T., Feng, Y. X., Zhao, J. X., Isik, V., Nuriel, P., Golding, S. D., 2009. Hydrothermal CO_2 degassing in seismically active zones during the late Quaternary. Chemical Geology, 265, 442-454.

Uysal, I. T., Feng, Y. X., Zhao, J. X., Bolhar, R., Işik, V., Baublys, K. A., Yago, A., Golding, S. D., 2011. Seismic cycles recorded in late Quaternary calcite veins: geochronological, geochemical and microstructural evidence. Earth and Planetary Science Letters, 303, 84-96.

Uysal, I. T., Zhao, J. X., Golding, S. D., Lawrence, M. G., Glikson, M., Collerson, K. D., 2007. Sm–Nd dating and rare- earth element tracing of calcite: implications for fluid-flow events in the Bowen Basin, Australia. Chemical Geology, 238, 63-71.

van Achterbergh, E., Ryan, C. G., and Griffin, W. L., 2001. GLITTER user's manual: on-line interactive data reduction for the LA-ICP-MS microprobe. GEMOC Version, 4, 72.

Van Wyk de Vries, B., Merle, O., 1998. Extension induced by volcanic loading in regional strike-slip zones. Geology, 26, 983-986.

Wheeler, H. E., Mallory, V. S., 1953. Designation of stratigraphic units. AAPG Bulletin, 37, 2407-2421.

Yamaguchi, A., Cox, S. F., Kimura, G., Okamoto, S. Y., 2011. Dynamic changes in fluid redox state associated with episodic fault rupture along a megasplay fault in a subduction zone. Earth and Planetary Science Letters, 302(3-4), 369-377.

Younker, L. W., Kasameyer, P. W., Tewhey, J. D., 1982. Geological, geophysical, and thermal characteristics of the Salton Sea Geothermal Field, California. Journal of Volcanology and Geothermal Research, 12, 221-258.

Chapter 3

Paper I

Geology of La Reforma caldera complex, Baja California, Mexico

L. García Sánchez [a], J.L. Macías [b], R. Sulpizio [c, e], L.S. Osorio-Ocampo [a], C. Pellicioli [c, d], A. Pola [f], D.R. Avellan [g],G. Cisneros [b], F. García [b], Y.Z.E. Ocampo-Díaz [h], R.M. Lira-Beltran [a], R. Saucedo [i], J.M. Sánchez-Núñez [j], J.L. Arce [k],P. Corona-Chávez [l], G. Reyes-Agustin [b], M. Cardona [b], P.W. Layer [m], J. Benowitz [m], L. Solari [n] and G. Groppelli [c].

[a] Posgrado en Ciencias de la Tierra, Instituto de Geofísica, Universidad Nacional Autónoma de México, Ciudad de México, México;
[b] Instituto de Geofísica, Universidad Nacional Autónoma de México, Morelia, México;
[c] Istituto per la Dinamica dei Processi Ambientali, sezione di Milano, C.N.R., Milano, Italia;
[d] Dipartimento di Scienze della Terra "Ardito Desio", Università degli Studi di Milano, Milano, Italia;
[e] Dipartimento di Scienze della Terra e Geoambientali, Università degli Studi di Bari "Aldo Moro", Bari, Italia;
[f] Escuela Nacional de Estudios Superiores, Unidad Morelia, Universidad Nacional Autónoma de México, Morelia, México;
[g] Cátedra CONACYT – Instituto de Geofísica, Universidad Nacional Autónoma de México, Morelia, México;
[h] Área de Ciencias de la Tierra, Facultad de Ingeniería, Univeridad Autónoma de San Luis Potosí, San Luis Potosí, México;
[i] Instituto de Geología, Universidad Autónoma de San Luis Potosí, San Luis Potosí, México;
[j] Centro Interdisciplinario de Investigaciones y Estudios sobre Medio Ambiente y Desarrollo, Instituto Politécnico Nacional, Ciudad de México, México;
[k] Instituto de Geología, Universidad Nacional Autónoma de México, Ciudad de México, México;
[l] Instituto de Investigaciones en Ciencias de la Tierra, Universidad Michoacana de San Nicolás de Hidalgo, Morelia, México;
[m] Geophysical Institute, University of Alaska at Fairbanks, Fairbanks, USA;
[n] Centro de Geociencias, Universidad Nacional Autónoma de México, Juriquilla, México.

PUBLISHED IN THE JOURNAL OF MAPS (Open Access), 2019, VOL. 15, NO. 2, 487-498, DOI: 10.1080/17445647.2019.1612287.

Field mapping and collection of geological data: *L. García Sánchez, S. Osorio-Ocampo,* ***C. Pellicioli***.
Collection of structural data reported in the geological map: ***C. Pellicioli****, G. Groppelli*.
Supervision of fieldwork activities: *G. Groppelli, J.L. Macías, R. Sulpizio*.
Editing and digital cartography production (digitalization of geological and structural features, production of map insets, legends, 3D view, scheme of stratigraphic relationships and map layout): ***C. Pellicioli***.
Palaeogeographic reconstructions and sedimentological studies on the sedimentary basement: *Y.Z.E. Ocampo-Díaz, R.M. Lira-Beltran*.
Radiometric geochronology determinations: *P.W. Layer, L. Solari*.
Discoutinuous attendance to fieldtrips and/or any additional scientific contribution to the CeMIE Geo project (evaluated at the discrection of the coordinator of the project, *J.L. Macías*): *A. Pola, D.R. Avellan, G. Cisneros, F. García, R. Saucedo, J.M. Sánchez-Núñez, J.L. Arce, P. Corona-Chávez, G. Reyes-Agustin, M. Cardona, J. Benowitz.*
Manuscript writing: *R. Sulpizio, J.L. Macías, G. Groppelli,* ***C. Pellicioli****.*

Journal of Maps

Taylor & Francis
Taylor & Francis Group

ISSN: (Print) 1744-5647 (Online) Journal homepage: https://www.tandfonline.com/loi/tjom20

Geology of La Reforma caldera complex, Baja California, Mexico

L. García Sánchez, J.L. Macías, R. Sulpizio, L.S. Osorio-Ocampo, C. Pellicioli, A. Pola, D.R. Avellan, G. Cisneros, F. García, Y.Z.E. Ocampo-Díaz, R.M. Lira-Beltran, R. Saucedo, J.M. Sánchez-Núñez, J.L. Arce, P. Corona-Chávez, G. Reyes-Agustin, M. Cardona, P.W. Layer, J. Benowitz, L. Solari & G. Groppelli

To cite this article: L. García Sánchez, J.L. Macías, R. Sulpizio, L.S. Osorio-Ocampo, C. Pellicioli, A. Pola, D.R. Avellan, G. Cisneros, F. García, Y.Z.E. Ocampo-Díaz, R.M. Lira-Beltran, R. Saucedo, J.M. Sánchez-Núñez, J.L. Arce, P. Corona-Chávez, G. Reyes-Agustin, M. Cardona, P.W. Layer, J. Benowitz, L. Solari & G. Groppelli (2019) Geology of La Reforma caldera complex, Baja California, Mexico, Journal of Maps, 15:2, 487-498, DOI: 10.1080/17445647.2019.1612287

To link to this article: https://doi.org/10.1080/17445647.2019.1612287

JOURNAL OF MAPS
2019, VOL. 15, NO. 2, 487–498
https://doi.org/10.1080/17445647.2019.1612287

Taylor & Francis
Taylor & Francis Group

Science

OPEN ACCESS Check for updates

Geology of La Reforma caldera complex, Baja California, Mexico

L. García Sánchez[a], J.L. Macías [b], R. Sulpizio[c,e], L.S. Osorio-Ocampo[a], C. Pellicioli[c,d], A. Pola[f], D.R. Avellan[g], G. Cisneros[b], F. García[b], Y.Z.E. Ocampo-Díaz[h], R.M. Lira-Beltran[a], R. Saucedo[i], J.M. Sánchez-Núñez[j], J.L. Arce[k], P. Corona-Chávez[l], G. Reyes-Agustin[b], M. Cardona[b], P.W. Layer[m], J. Benowitz[m], L. Solari[n] and G. Groppelli [c]

[a]Posgrado en Ciencias de la Tierra, Instituto de Geofísica, Universidad Nacional Autónoma de México, Ciudad de México, México; [b]Instituto de Geofísica, Universidad Nacional Autónoma de México, Morelia, México; [c]Istituto per la Dinamica dei Processi Ambientali, sezione di Milano, C.N.R., Milano, Italia; [d]Dipartimento di Scienze della Terra "Ardito Desio", Università degli Studi di Milano, Milano, Italia; [e]Dipartimento di Scienze della Terra e Geoambientali, Università degli Studi di Bari "Aldo Moro", Bari, Italia; [f]Escuela Nacional de Estudios Superiores, Unidad Morelia, Universidad Nacional Autónoma de México, Morelia, México; [g]Cátedra CONACYT – Instituto de Geofísica, Universidad Nacional Autónoma de México, Morelia, México; [h]Área de Ciencias de la Tierra, Facultad de Ingeniería, Univeridad Autónoma de San Luis Potosí, San Luis Potosí, México; [i]Instituto de Geología, Universidad Autónoma de San Luis Potosí, San Luis Potosí, México; [j]Centro Interdisciplinario de Investigaciones y Estudios sobre Medio Ambiente y Desarrollo, Instituto Politécnico Nacional, Ciudad de México, México; [k]Instituto de Geología, Universidad Nacional Autónoma de México, Ciudad de México, México; [l]Instituto de Investigaciones en Ciencias de la Tierra, Universidad Michoacana de San Nicolás de Hidalgo, Morelia, México; [m]Geophysical Institute, University of Alaska at Fairbanks, Fairbanks, USA; [n]Centro de Geociencias, Universidad Nacional Autónoma de México, Juriquilla, México

ABSTRACT

A new geological map at 1:50,000 scale of La Reforma Caldera Complex has been produced applying modern survey methodologies to volcanic areas. This map aims to represent a reliable and objective tool to understand the geological evolution of the region. La Reforma Caldera Complex is a Pleistocene nested caldera located in the central part of the Baja California peninsula, Mexico. The twelve formations defined within the Quaternary volcanic record were grouped into three phases (pre-caldera, caldera, and post-caldera). The pre-caldera phase (>1.35 Ma) is characterized by scattered eruptions, mostly occurred in submarine environment. The caldera phase (1.35–0.96 Ma) groups several distinct explosive and effusive eruptions that formed the present-day caldera depression. The post caldera phase includes scattered effusive eruptions (ended at 0.28 Ma) and resurgence, characterized by several hundred meters of uplift of the central block within the caldera depression.

ARTICLE HISTORY
Received 3 December 2018
Revised 16 April 2019
Accepted 24 April 2019

KEYWORDS
Geology; stratigraphy; caldera complex; Pleistocene volcanism; ignimbrites; geothermal resources

1. Introduction and previous studies

Geological maps have to be objective and detailed because they represent a fundamental tool to understand the geological evolution of a given area, and, when mapping is conducted at relatively high scale, they provide a sound basis for detailed studies aimed at assessment of natural hazards, and exploitation of geothermal potential and/or ore deposits. For this reason, within the project CEMIE GEO (Centro Mexicano de Innovación en Energía Geotérmica), which involves different sites in Mexican Quaternary volcanic districts, we surveyed La Refoma Caldera Complex area and produced a new geological map at 1:50,000 scale Main Map.

La Reforma Caldera Complex is located in the central part of the Baja California peninsula, 35 km to the NW of the town of Santa Rosalía (Demant, 1984). Along with the Aguajito Caldera (Garduño-Monroy, Vargas-Ledezma, & Campos-Enriquez, 1993) and the Tres Vírgenes volcanic complex (Avellán et al., 2018) La Reforma caldera complex represents a manifestation of the Quaternary volcanism in the central part of the Baja California (Figure 1). The first geological contributions in the region focused on the Plio-Pleistocene sedimentary rocks of the Santa Rosalía Basin (Ortlieb, 1978; Ortlieb & Colleta, 1984; Wilson, 1948; Wilson & Rocha, 1955) because of the exploitation of copper and manganese minerals. Wilson and Rocha (1955) provided a detail geological map of the Santa Rosalía area, but did not include La Reforma range, located to the northwest. Schmidt (1975) published the first geological map of the Sierra La Reforma that was interpreted as a complex system of uplifted tectonic blocks. One of these blocks was made of crystalline granodioritic rocks dated by the Author at 91.2 ± 2.1 Ma by K-Ar method. Demant and Ortlieb (1981) recognized the Sierra La Reforma as a resurgent caldera, and Demant (1984) presented a regional geological map of Santa Rosalía with a mineral and petrological characterization that included La Reforma caldera. In 1982, the National Power Company (Comisión Federal de Electricidad = CFE) began geological and geophysical

CONTACT G. Groppelli gianluca.groppelli@cnr.it, gianluca.groppelli@unimi.it Istituto per la Dinamica dei Processi Ambientali, sezione di Milano, C.N.R., Milano, Italia

Supplemental data for this article can be accessed https://doi.org/10.1080/17445647.2019.1612287.

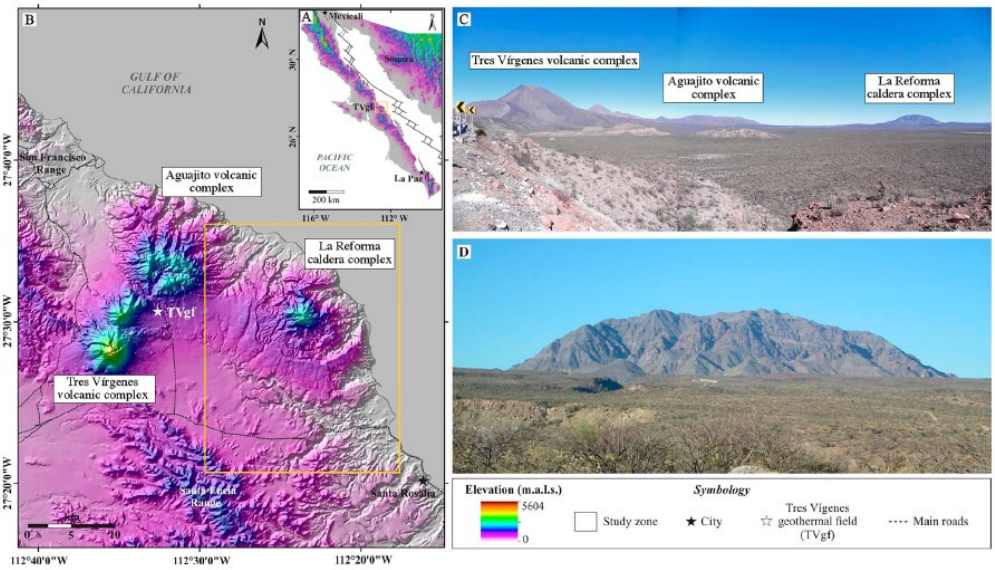

Figure 1. (A) Tectonic setting of the Gulf of California in northwestern Mexico with the location of the study area (box) and Tres Vírgenes geothermal field (TVgf). (B) Shaded relief map of the study area that displays the location of the Tres Vírgenes volcanic complex (TVVC), the Tres Vírgenes geothermal field (TVgf), the El Aguajito volcanic complex and La Reforma caldera complex, (C) Panoramic view from the south of the TVVC, El Aguajito volcanic complex and La Reforma caldera. (D) Close up view from the southwest of La Reforma caldera in the background (resurgent area) and gentle slopes formed by lava flows in the foreground.

prospecting in the Tres Vírgenes area (southwest of La Reforma) for geothermal exploration (e.g. Lira, González, & Arellano, 1997; Lira, Ramirez, Herrera, & Vargas, 1983) followed by its exploitation in 1986. The CFE survey involved other prospecting areas as El Aguajito (Garduño-Monroy et al., 1993) and set the basis for new studies of Tres Vírgenes (Capra, Macıas, Espındola, & Siebe, 1998; Sawlan et al., 1981; Schmitt, Stockli, & Hausback, 2006; Schmitt, Stockli, Niedermann, Lovera, & Hausback, 2010) with the updated geology of the Tres Vírgenes volcanic complex (Avellán et al., 2018; Macías et al., 2012). Schmitt et al. (2006) dated the age of La Reforma (1.3 Ma) and Aguajito ignimbrites (1.2 Ma) with the U-Pb method in zircon, with the aim of understanding the general evolution of the Quaternary volcanic centres northwest of Santa Rosalia.

Despite these efforts, no detailed studies of La Refoma were carried out to produce a comprehensive volcanological map and evolution of the caldera. The CEMIE GEO project, a Mexican initiative to carry out modern geothermal studies, allowed to perform new investigations of La Reforma caldera, aimed at understanding its geothermal potential.

Here, we present the first contribution of this project with the revised geology and stratigraphy of La Reforma caldera complex that was assisted by $^{40}Ar/^{39}Ar$ and U-Pb geochronology (Table 1) from previous studies and new data from the PhD work of García-Sánchez (2019). This new map will set the basis for modern studies in the area, which will be helpful to future prospecting for ore deposits and geothermal potential areas, as well as paleogeographic reconstructions of marine depositional systems and mineralization.

2. Methods

The geological map, here presented at 1:50,000 scale, has been surveyed at 1:25,000 scale in a logistically difficult area due to the absence of any roads and access feasible only by the coastline and a few mountain pathways (Figure 2).

The fieldwork was preceded by critical review of existing literature for the studied area, along with analyses of satellite images (including ESRI and Google images) and of a 25 m pixel-sized digital elevation model (DEM) and its derived morphological features (slope aspect, shaded relief, 3D visualization, etc.).

The geological survey, carried out during 5 field campaigns (from 2014 to 2017), has been realized using INEGI topographic map and iGIS® software on iPad mini equipped with Google Earth images. Geological survey was carried out on lithostratigraphic basis, which allowed for the definition of various formations. Indeed, lithostratigraphic units are the only ones easily recognizable in the field because of their lithology and stratigraphic position (Groppelli & Martì-Molist, 2013; Groppelli & Viereck-Goette, 2010; Martí, Groppelli, & da Silveira, 2018; Salvador,

Table 1. Summary of age determinations from selected samples of La Reforma caldera complex.

Sample	Coordinates		Altitude (m)	Lithostratigraphic unit	Age (Ma) error 1 σ	Method	Material dated	MSWD
	Longitude	Latitude						
RF-102	358009	3050519	612	Plutonic rocks	97.8 ± 1.5	U/Pb	zircons	–
RF-5A	360207	3046366	157	Santa Lucia formation	19.25 ± 0.08	$^{40}Ar/^{39}Ar^{2}$	Whole rock	–
RF-47	367168	3037565	160	Cueva Amarilla ignimbrite	2.4 ± 1.5	U/Pb	zircons	–
RF-53F	354423	3046366	250	Carrizo ignimbrite	1.89 ± 0.27	$^{40}Ar/^{39}Ar^{2}$	Whole rock	2.58
RF-26D	365319	3033781	319	Contrabando formation	1.47 ± 0.08	$^{40}Ar/^{39}Ar^{2}$	Plagioclase	0.41
RF-51	369626	3037573	1	Punta Candeleros formation (pillow lavas)	1.42 ± 0.05	$^{40}Ar/^{39}Ar^{2}$	Whole rock	1.35
RF-65	358751	3051407	6	Punta Candeleros formation (lava dome)	1.36 ± 0.06	$^{40}Ar/^{39}Ar^{2}$	Whole rock	0.46
RF-18	355645	3036623	257	Los Balcones ignimbrite	1.35 ± 0.02	$^{40}Ar/^{39}Ar^{2}$	Whole rock	0.86
RF-88	363593	3041869	719	Cerro la Reforma formation	1.27 ± 0.02	$^{40}Ar/^{39}Ar^{2}$	Whole rock	0.57
RF-16A	357090	3038486	367	La Reforma ignimbrite	1.29 ± 0.02	$^{40}Ar/^{39}Ar^{2}$	Whole rock	1.08
RF-12	357200	3037510	394	Mesa el Yaqui formation	1.18 ± 0.46	$^{40}Ar/^{39}Ar^{2}$	Whole rock	0.16
BH00R41	–	–	–	Aguajito ignimbrite (Schmitt et al., 2006)U/Pb	1.17 ± 0.07	U/Pb	zircons	1.3
RF-122	366559	3045415	14	Punta Arena ignimbrite	0.96 ± 0.21	$^{40}Ar/^{39}Ar^{2}$	Whole rock	2.6
RF-26I	365319	3033781	319	Cueva del Diablo formation	0.46 ± 0.08	$^{40}Ar/^{39}Ar^{2}$	Whole rock	0.71
RF-41A	368029	3043132	33	Cueva del Diablo formation	0.28 ± 0.05	$^{40}Ar/^{39}Ar^{2}$	Whole rock	0.44

The analyses were performed at: (1) Laboratory of Isotopic Studies of the Centro de Geociencias of the UNAM, Juriquilla, and (2) Geochronology Laboratory at the University of Alaska, Fairbanks. Further details on age determinations are given in García-Sánchez (2019).

1994). In addition to the stratigraphic position, we used abrupt change in lithology, presence of palaeosols, or intercalation of marine sediment to define formations.

For the pre-Quaternary basement units (Figure 3), we adopted the published regional stratigraphic framework (Bryan, Orozco-Esquivel, Ferrari, & Lopez-Martinez, 2014; Conly, Brenan, Bellon, & Scott, 2005; Ferrari, Orozco-Esquivel, Bryan, López-Martínez, & Silva-Fragoso, 2018; Hausback, 1984; Kimbrough et al., 2001; McLean, 1988; Sawlan & Smith, 1984; Schmidt, 1975; Umhoefer, Dorsey, Willsey, Mayer, & Renne, 2001). For the Quaternary volcanics, we have defined twelve formations (Table 2). The youngest one (Cueva del Diablo formation) includes lithostratigraphic units of lower rank, members, as the lithological properties allow distinguishing them from the adjacent part of the formation (Salvador, 1994). Moreover, six different lithosomes (Pasquarè et al., 1992; Wheeler & Mallory, 1953) provide additional details to the stratigraphic succession of the Cueva del Diablo formation, based on their morphology, vent location and product distribution (Table 3).

In order to summarize the volcanic succession, we have identified three main phases (pre-caldera, caldera and post-caldera) on the basis of the relationships of the deposits with the caldera evolution. Moreover, we have grouped all the pre-Quaternary rocks into a 'sedimentary and igneous basement' unit.

During field mapping, we have collected samples for petrographic and geochemical analyses and age determination of rocks. Petrographic data allowed for a better characterization of the lithostratigraphic units, whereas radiometric data allowed constraining formations and lithosomes, thus helping reconstruct the evolutionary phases of La Reforma caldera.

All the field data have been stored in a geodatabase, using iGIS software in the field and then ArcGis® platform during the preparation of the geological map.

The colour scale chosen for representation of lithostratigraphic units on the map follows the three evolutionary phases: pre- (brown shaded), syn- (red shaded) and post-(green shaded) caldera phases. A scale of light blue was used to represent the sedimentary and igneous basement units, whereas blue colour was used for the Cretaceous basement (granitoids) in order to highlight its location. This was important in order to highlight the resurgence of the central part of the caldera. Regarding symbols, we have marked crater rims, pit crater rims, caldera rim, bedding attitude, marine terraces and faults. Dykes have been marked by lines too. Insets at 1:20,000 scale highlight the detailed stratigraphic succession in two deep fluvial valleys to the west and south-west.

In addition to the legend, we have included the following elements into the map: (1) an inset showing the geographic location of the mapped area, (2) a stratigraphic scheme to illustrate the relationships among

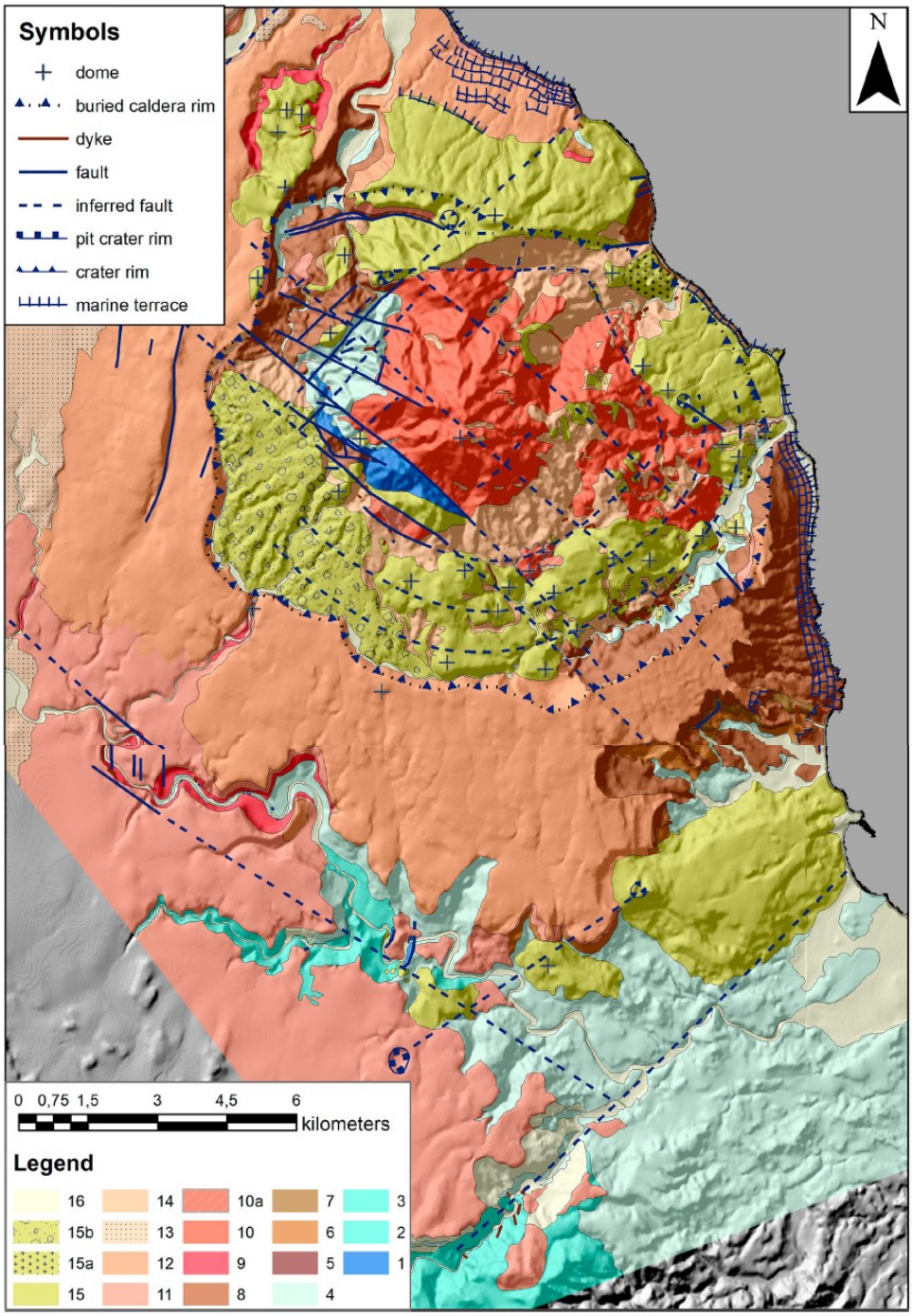

Figure 2. Geological map on a shaded topography (INEGI data). Numbers refer to the lithostratigraphic units described in Table 2, except (16) Recent alluvial deposits.

Table 2. Description of the lithostratigraphic units (group, formation and member) identified within La Reforma caldera complex.

Formation	Acronym	Description	Location	Geochemistry	Interpretation and notes
Post-caldera phase					
Cueva del Diablo formation	15	Scoria cones and domes sometimes associated with limited lava flows (Figures 4(c) and 5(c)). Lava flows are usually thin (2–5 m) and alternated to scoriae. Dikes and small sub-intrusive bodies are also present (Figure 6(a and b)). Lavas display large variability in texture (from aphyric to porphyritic, with phenocrysts of pl, px, and Fe-Ti oxides).	The formation crops out both inside and outside the caldera	Mainly basaltic-andesitic and andesitic lavas. Locally rhyolitic lavas	This formation includes all the deposits formed after the caldera phase. The volcanic activity is scattered and low volume respect the previous phase. Inside the caldera depression usually the centres are located along the ring faults. It is possible to identify several lithosomes (see Table 3).
Arroyo Grande member	15b	Sands to gravels deposits made of lavas and plutonic rocks with interbedded three thin (<1 m) white fallout deposits (Figure 6 (c)). The deposits are matrix supported, partially loose, and coarsely stratified (0.5–1 m) with parallel and lenticular shapes. The total thickness is up to 50 m.	Western side of the caldera depression		The deposits form alluvial fans within the western part of the caldera depression probably due to the dismantling of the resurgent block.
Caldera phase					
Punta Arena ignimbrite	14	White loose pyroclastic deposit, made of grey and white pumices, lava and scoria lithics (red and grey) in abundant ashy matrix. Matrix is generally whitish to yellowish in colour, but it becomes light-green when hydrothermalised (Figure 5(c and d)). It is locally fairly well-consolidated due to hydrothermal alteration. Locally abundant shells (mainly bivalves) are present, mixed into the deposit. Lag breccias made of abundant heterolithologic lithic blocks are present around Cerro la Reforma. The thickness varies from few meters to more than 200 m because of the irregular paleo-topography at the time of deposition.	This ignimbrite crops out only inside the caldera depression	White pumices are trachydacitic, while the grey ones are dacitic.	This ignimbrite represents the last event caldera-forming partially filling the paleo-depression formed during the previous caldera collapses. It was deposited in subaqueous environment and affected locally by hydrothermal circulation. Age: 0.96 ± 0.21 Ma.
Aguajito ignimbrite	13	Not welded, light-brown pyroclastic deposit with white pumice and loose crystals of pl at the bottom, overlain by light-pink to light-purple, lithic-rich ignimbrite. Welded at top, with brown fiammes, lithics (granite, lavas), ash-rich matrix, and loose crystals of pl, amph and px. The total thickness is up to 40 m.	This ignimbrite, belonging from the Aguajito Volcanic Complex, crops out only along the western sector outside La Reforma caldera depression.	Rhyolite	This ignimbrite represents one of the main volcanic events of the close Aguajito Volcanic Complex. Age: 1.17 ± 0.07 Ma (Schmitt et al., 2006).
Mesa El Yaqui formation	12	Blocky lava flow succession, dark-grey in colour, associated with few scoria layers. Aphyric to porphyritic lavas with phenocrysts of pl, ol, px and Fe-Ti oxides. The thickness varies from 3 to 20 m.	These lava flows cover most of the external slopes of the caldera depression, and locally also of its inner walls.	The lavas are basaltic-andesite in composition.	This formation represents an effusive period during the caldera-forming phase, when most of the caldera depression was already formed. Age: 1.18 ± 0.46 Ma.
La Reforma ignimbrite	11	Pyroclastic deposits consisting of basal welded, reddish bed overlain by various welded brownish to dark-grey deposits (Figure 5(b)). Welded deposits contain black fiamme pumice and accidental lithics (lavas). Loose crystals of pl and px occur in ashy matrix. The thickness is up to 40 m.	This formation crops out in limited areas inside the caldera depression and widely outside the caldera.	Rhyolite	This ignimbrite represents one of the main events caldera-forming and responsible of most present caldera morphology. Age: 1.29 ± 0.02 Ma.
Cerro La Reforma formation	10	Succession of thick lava flows (up to 10 m) associated with minor pyroclastic deposits (Figure 5(d)). The formation comprises also lava domes along caldera rims (in map n. 10a). Lavas are porphyritic with phenocrysts of pl, px and Fe-Ti oxides. Xenocrysts of qtz and sedimentary xenoliths are also present. The thickness is more than 400 m because the base is always not visible.	This formation crops out only in the central part of the caldera depression (resurgence block). The original depositional surface appears tilted to SE.	The lavas are dacitic in composition.	This formation represents the first lava flow filling of the caldera depression, later tilted during the resurgence. Age: 1.27 ± 0.02 Ma.
Los Balcones ignimbrite	9	Grey welded pyroclastic deposit made of light-grey pumice and dark grey fiamme, with abundant lithics (grey, black and white lavas) (Figures 4(c) and 5(a and b)). Abundant loose crystals of pl and minor px in greyish ash-rich matrix. The thickness is up to 30 m.	This ignimbrite crops out outside the caldera depression, mainly along deep valleys.	Rhyolite	This ignimbrite represents the first known event caldera-forming. Age: 1.35 ± 0.02 Ma.

(*Continued*)

Table 2. Continued.

Formation	Acronym	Description	Location	Geochemistry	Interpretation and notes
Pre-caldera phase					
Punta Candeleros formation	8	Hyaloclastites, pillow lavas and lava domes with columnar jointing (Figure 4(a and b)). Lava texture varies from aphyric to porphyritic with phenocrysts of pl and px.	This formation crops out widely in the NW and SE sectors of the caldera depression, both inside and outside.	Lava composition varies from basaltic-andesite to andesite with minor trachy-dacite.	The formation includes effusive episodes, mainly submarine, affecting the area immediately before the onset of the caldera phase. Age: 1.42 ± 0.05 Ma (pillow lavas); 1.36 ± 0.06 Ma (lava dome).
Contrabando formation	7	Stratified, light-yellow pyroclastic deposit made of white and grey pumices (Figure 4(a)). Loose crystals of pl and px occur in yellowish ash-rich matrix. The thickness is up to 15 m.	This formation crops out only in the SE area along the external slopes of the caldera depression.	ND	The formation represents one of the scattered explosive events affecting the area before the caldera phase. The source area is unknown due the scarce outcrops. Age: 1.47 ± 0.08 Ma.
Carrizo ignimbrite	(not mappable)	Red welded pyroclastic deposit containing yellow and grey pumices and abundant lithics (green or grey lavas and black scoriae) (Figures 4(c) and 5(a)). Abundant loose crystals of pl in reddish ash-rich matrix. The thickness is up to 10 m.	This ignimbrite crops out only in limited areas along deep valleys all around the caldera depression.	Rhyolite	The formation represents one of the scattered explosive events affecting the area before the caldera phase. The source area is unknown due the scarce outcrops. Due to the reduce thickness and few outcrops, this formation is not mappable at the present scale. Age: 1.89 ± 0.27 Ma.
Cueva Amarilla ignimbrite	6	Greenish grey pyroclastic deposit with white pumice at bottom and black scoriae at top (Figure 4(a and c)). Loose crystals of pl and px occur in greenish ash-rich matrix. The thickness is up to 30 m.	This ignimbrite crops out in the S and N sector along the external slopes of the caldera depression.	ND	The formation represents one of the scattered explosive events affecting the area before the caldera phase. The source area is unknown due the scarce outcrops. Age: 2.4 ± 1.5 Ma.
Mesa de Enmedio ignimbrite	5	Light-grey pyroclastic deposit made of pumices (10–50 cm long). Loose crystals of pl and px occur in yellow ashy matrix. The thickness is up to 5 m.	This formation crops out only close to the Punta Arena	ND	The formation represents one of the scattered explosive events affecting the area before the caldera phase. The source area is unknown due the scarce outcrops.
Sedimentary Formation of the Santa Rosalia basin	4	Siltstones, sandstones and isolated conglomerates (Figure 4(c)) with interlayered several volcanic deposits (ignimbrites, pillow lavas, hyaloclastites, and reworked volcanics, see # 5, 6, 7, and 8). Brownish siltstones (up to 30 m thick) at base, overlain by fossiliferous sandstones and conglomerates (5–20 m thick). Fossils mainly consist of bivalves (*Pectinidae*) and well-preserved oysters and sea urchins.	This formation crops out mainly along the coast and deep valleys south of the caldera depression. Inside the caldera, it crops out in the resurgent block and locally at the base of the caldera inner walls.		This formation, known also as *Formación sedimentaria de la cuenca de Santa Rosalia*, Auct. (Ortlieb & Colleta, 1984; Wilson, 1948), represents the marine sedimentation, during which coeval scattered volcanic activities happened. The Santa Rosalia basin is a tectonic depression due to the opening of the California Gulf. Age: Pliocene-Middle Pleistocene (Ortlieb & Colleta, 1984).
Sedimentary and igneous basement					
Santa Lucia formation	3	Lava flows and domes, associated with dikes. Lavas with aphyric to porphyritic texture and phenocrysts of pl and px and amph. The formation, interlayered with the Comondú Group (see n. 2), is up to 80 m thick.	This formation crops out only in the south margin of the map.	Lavas are andesitic to basaltic in composition.	Andesite-dominated arc lava suites erupted when the Gulf region was affected by oblique-subduction of the Farallon-Guadalupe plate under the North America plate along the western margin of Baja California (Conly et al., 2005). Age: 19.25 ± 0.08 Ma.
Comondú Group	2	Red sandstones, siltstones and conglomerates interlayered with lavas (Santa Lucia Formation, see n. 3) (Figure 3(b)). The thickness is up to 100 m, but the base is always not visible.	This group crops out only in the south margin of the map and some deep valleys.		Volcanic and sedimentary unit deposited in an arc-forearc context linked to the Farallon-Guadalupe and North America plates subduction, possibly extending through the Gulf early rifting phases (Ferrari et al., 2013, 2018; Umhoefer et al., 2001). Age: 30–12 Ma (Umhoefer et al., 2001).
Plutonic rocks	1	Several crystalline intrusive bodies (Figure 3(a)). Holocrystalline rock with 3–4 mm sized phenocrysts of Kfs, pl, qz, amph and bio. Some associated aplitic dikes are present. The thickness is variable (from 8 to more than 50 m) and the base is always not visible.	These rocks crop out inside the caldera depression (western margin of the resurgent block) and outside along Yaqui canyon.	The intrusive rocks are granodioritic in composition.	Also known as *Batholites Peninsulares*, (Gastil, 1975; McLean, 1988; Schmidt, 1975) these rocks represent a voluminous batholith intruded into the Early Cretaceous supra-crustal volcanic and sedimentary sequence. Intrusions occur as small sheet and diapirs or as a combination of large nested intrusive centres and smaller isolated intrusions (Kimbrough et al., 2001). Age: 97.8 ± 1.5 Ma.

Table 3. Description of the lithosomes recognized inside the Cueva del Diablo formation (Post-caldera phase).

Lithosomatic unit	Acronym	Description	Interpretation and notes
Punta Prieta scoria cones	L6	Scoria cones associated with a thin lava flow (max. 5 m thick) extending eastward up to the sea. No evidences of marine terraces.	Small scoria cones that produced limited lava flows cropping out in the eastern sector of La Reforma Caldera. These represent the most recent volcanic event of La Reforma caldera complex. Age: 0.28 ± 0.05 Ma.
Cerro Colorado scoria cone	L5	Low-volume products aligned pit craters and scoria cones, except for the easternmost lava flow that extends up to the coastline. No evidences of marine terraces. The easternmost lava flow field is a complex 'aa' morphology with superimposed flows reaching a maximum thickness of 50 m.	NE-SW striking aligned pit craters and scoria cones, cropping out outside the caldera depression (south). The easternmost cone is associated with a large lava flow extending up to the coastline. Age: 0.46 ± 0.08 Ma.
Punta El Gato stratocone	L4	Scoria cone associated with a short lava flow. The lava flow surface is smoothed by erosion. Lava flow thickness is up to 10 m.	Short lava flow cropping out outside the caldera depression (north).
Punta Gorda stratocone	L3	Eroded scoria cone associated with a lava flow extending up to the coastline. The lava flow surface is smoothed by erosion. Lava flow thickness is up to 10 m. No evidences of marine terraces.	Lava flow cropping out outside the caldera depression (north) and extending up to the coastline.
Morro de las Palmas dome	L2	Small-volume rhyolitic domes cropping out along the northern side of La Palma river. Presence of thick lava flows, with a maximum thickness of 40 m.	Rhyolitic domes cropping out outside the caldera depression (north) forming a small dome field.
Las Minitas dome	L1	Domes associated with thick (more than 20 m) tabular lava flows displaying columnar joints.	Thick tabular lava flows and domes covering the Punta Arena Ignimbrite and cropping out inside the caldera depression (north).

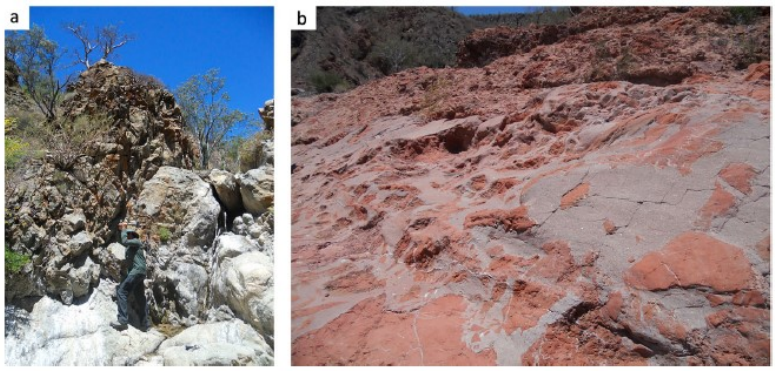

Figure 3. View of representative outcrops from the sedimentary and igneous basement of La Reforma caldera complex. (a) Granitoid basement from central part of La Reforma caldera complex; (b) Reddish fluvial conglomerate (Comondú Group).

lithostratigraphic units, fundamental to understand the volcanic succession and the evolution of the caldera complex, and (3) a 3D view of the mapped area reporting a simplified geology in order to visualize the relationships between morphology of the caldera complex, resurgence phenomena and the volcanological evolution.

3. Evolution of La Reforma caldera complex

The geological map (Figure 2) highlights how La Reforma caldera complex developed over a basement made of igneous (granitoids) rocks (Peninsular Ranges Batholith, Gastil, 1975), volcaniclastic and sedimentary rocks (Comondú Group, Bryan et al., 2014; Hausback, 1984; López, García, & Arellano, 1995; Sawlan, 1991; Sawlan & Smith, 1984; Umhoefer et al., 2001) with interbedded lava flow, ignimbrites, and domes (Santa Lucia formation, Garduño-Monroy et al., 1993).

The pre-caldera volcanic activity developed in a shallow water, marine basin, as suggested by the occurrence of siltstones and fossiliferous sandstones (Sedimentary Formation of the Santa Rosalia basin) interbedded with volcanic units. The pre-caldera activity is characterized by both explosive and effusive eruptions, with emplacement of pyroclastic density currents (PDCs; Mesa de Enmedio and Cueva Amarilla ignimbrites), volcaniclastics (Contrabando formation), pillow lavas and domes (Punta Candeleros formation). Only one subaerial ignimbrite is exposed at El Carrizo canyon, SW of the caldera rim (Carrizo ignimbrite). The pre-caldera activity probably built up a stratovolcano, whose remnants are today exposed on the SE and NE parts of the caldera complex, and along the sea cliffs in the Punta Gorda area.

The onset of La Reforma caldera started with the eruption of Los Balcones ignimbrite, nowadays not

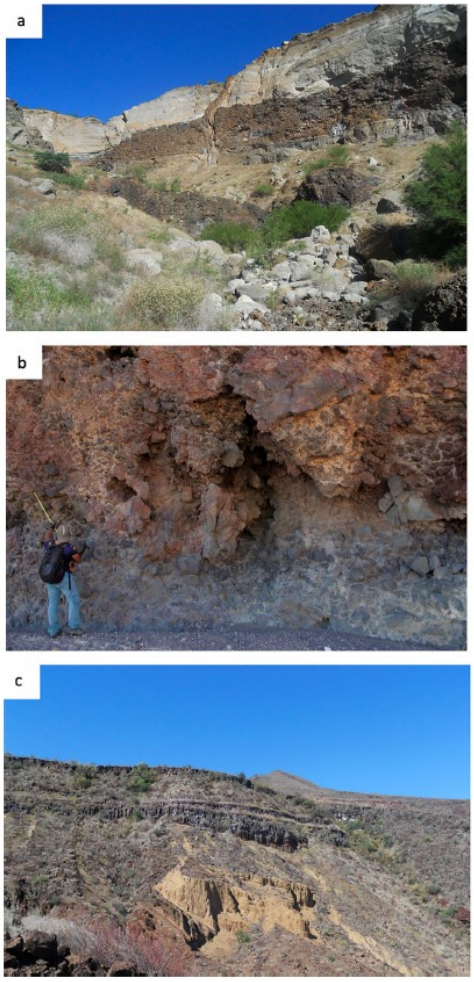

Figure 4. View of representative outcrops from the pre-caldera phase of La Reforma caldera complex. (a) Cueva Amarilla ignimbrite, Contrabando formation and Punta Candeleros formation from the Canada La Cueva Amarilla area; (b) Massive hyaloclastitic lava (≤7 m) composed of grey to red angular blocks supported by a matrix of altered yellow glass. (c) from bottom to top Sedimentary Formation of the Santa Rosalia Basin, Cueva Amarilla ignimbrite, Carrizo ignimbrite and Los Balcones ignimbrite topped by post-caldera lava flows (Cueva del Diablo formation) (Punta el Gato area).

exposed within the caldera, but only visible in the Arroyo Grande and El Carrizo canyons, to the SW of the caldera rim, and La Palma canyon to the north. The caldera depression was filled by lava flows alternating with scoriae, with a thickness of more than 400 m (Cerro La Reforma formation). La Reforma ignimbrite marks the second caldera-forming eruption, which enlarged the initial caldera depression. The deposits of La Reforma ignimbrite are extensively exposed outside the caldera rims to the S and SW, whereas they crop out sporadically within the caldera in the northern, eastern and southern parts. The eruptive activity resumed with the emplacement of widespread, thin lava flows, probably erupted along fissures parallel to the caldera-forming ring faults, and composing the Mesa El Yaqui formation. The geographical distribution of these lava flows (bordering almost all the caldera rims), suggests they were accompanied by resurgence of the central block of the caldera, which prevented most of the intrusion of feeding dykes within the caldera depression. After the emplacement of Mesa El Yaqui formation, La Reforma stratigraphic succession is characterized by the occurrence of Aguajito ignimbrite, likely deriving from the nearby Aguajito volcanic complex (Garduño-Monroy et al., 1993; Schmitt et al., 2006). The Aguajto ignimbrite deposits are well exposed to the west, but they have been never reported within La Reforma caldera. The Punta Arena ignimbrite is the last eruption of the caldera phase, and it extensively crops out only within the caldera, where it fills up topographic depressions with thickness of up to 200 m. Thin horizontal stratification and the occurrence of marine shells within the deposits testify for the subaqueous deposition of this formation.

The Cueva del Diablo formation contains the post-caldera deposits (Table 3), dominated by the evidence of effusive activity along the ring faults and faults bordering the central resurgent block (Las Minitas dome, Morro de las Palmas dome, Punta Gorda stratocone, Punta El Gato stratocone, Punta Prieta scoria cones). Only a few eruptive centres occur outside the caldera rims, and are located along NE-SW tectonic alignments (Cerro Colorado scoria cone). It is during this phase that the resurgence culminated to the present-day status, with the exposure of the plutonic rocks of the Peninsular Ranges Batholith in the SW part of the resurgent block. The uplift of the central part of the resurgent block determined the closure of the drainages to the E, with the formation of a small sedimentary basin in the western part of the caldera. This morphological barrier was likely responsible for the deposition of the volcaniclastic sediments of the Arroyo Grande member.

The magmatic driven resurgence of the central block of the caldera was accompanied by a regional uplift of the entire complex, in the order of more than 100 m, as testified by several marine terraces visible on the marine cliffs to the east (Figure 7). This regional uplift has been also responsible of the emersion of the whole caldera complex, as it is visible today.

4. Conclusions

The new geological map of La Reforma caldera complex represents an accurate and updated basis for understanding the geological evolution of this part of

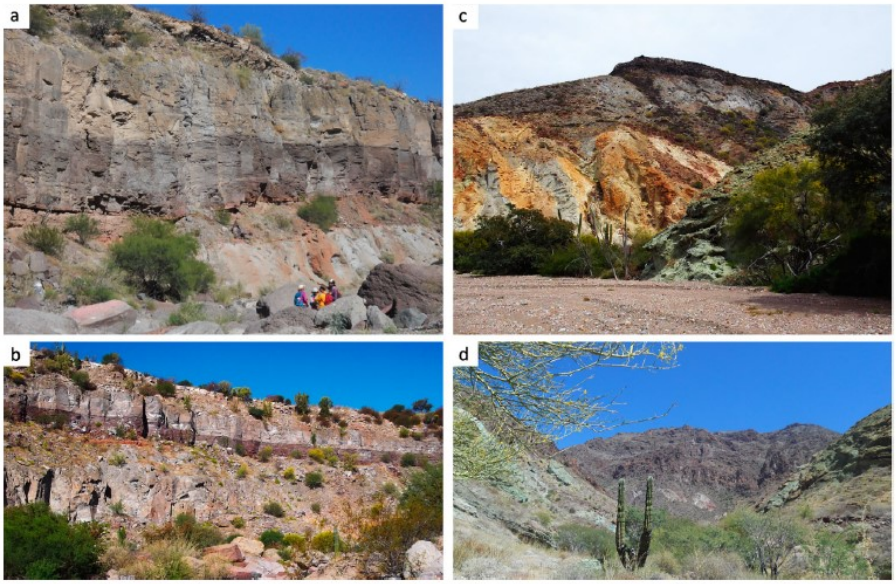

Figure 5. View of representative outcrops from the caldera phase of La Reforma caldera complex. (a) Los Balcones greyish ignimbrite on top of the Carrizo reddish ignimbrite in the Yaqui canyon area; (b) La Reforma ignimbrite (grey and red basal facies) on top of the Los Balcones ignimbrite; (c) Punta Arena ignimbrite, locally displaying yellowish and greenish hydrothermal alteration topped by post-caldera lava flows in the Cerro La Cueva del Diablo area; (d) View of Cerro La Reforma formation.

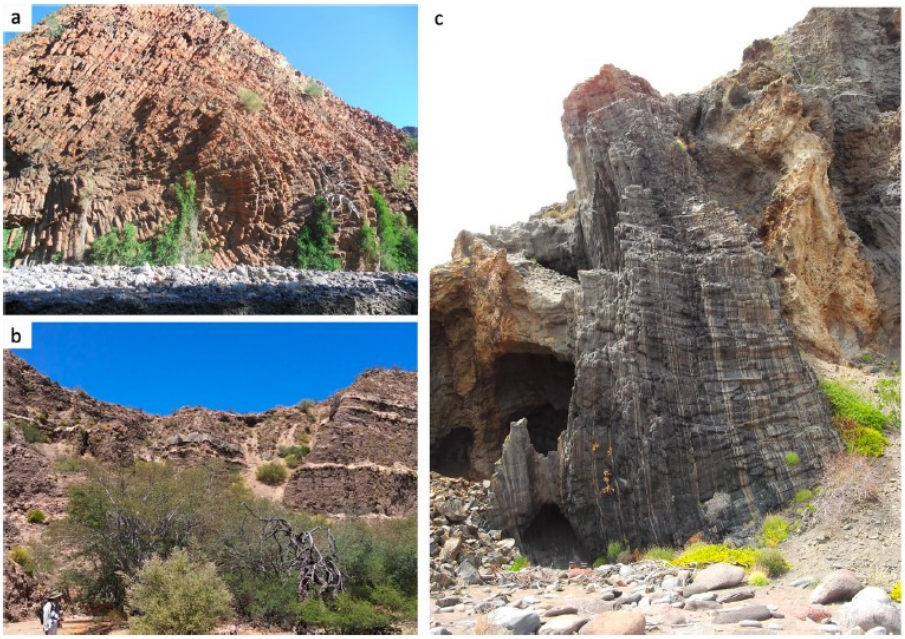

Figure 6. View of representative outcrops from the post-caldera phase of La Reforma caldera complex. (a) Intrusion with cooling joints from the Cueva Del Diablo formation; (b) View of the Arroyo Grande member in the Arroyo Grande canyon area; (c) Layered intrusion.

Figure 7. View of representative outcrops displaying Quaternary morphologies of La Reforma caldera complex. (a) Several orders of marine terraces along the coast (Punta El Contrabando and Punta Candeleros); (b) Marine terraces along the northern coast (Punta El Gato).

Baja California (Figure 2). The map has relevance for the comprehension of the Pleistocene volcanism in the area as it provides new insights into the inception of volcanism in this part of the peninsula. The content of the map includes a new stratigraphic reconstruction of La Reforma pre-caldera, syn-caldera, and post-caldera activity and their timing. This information will provide support to understand the evolution of the Santa Rosalia Basin and the interaction between marine sedimentation and submarine and subaerial volcanism. The geological map of La Reforma caldera complex also represents an invaluable contribution towards the knowledge of the territory and the exploitation of natural resources.

Software

Geological boundaries, structural features and polygons were digitized from field paper maps using ArcGIS ESRI (10.2.1 for Desktop, 10.2.1.3497 version), often with the aid of Google Earth Pro. The regional setting scheme (on the upper left corner of the map page) was constructed and edited by using CorelDraw X6. The 3D scene (on the bottom of the map page) was edited using ArcScene (ArcGIS 10.2.1). The map was produced by using ArcGIS ESRI and the final editing page was performed in Adobe Illustrator 6.0.

Acknowledgements

This study was funded by Grant 207032 of the Centro Mexicano de Innovación en Energía Geotérmica (CeMIE Geo) projects P15 to J.L. Macías. *Italgas S.p.a.* funds issued by CNR-IDPA (Milan) sponsored C. Pellicioli in her PhD research activity. We thank F. Mendiola for her technical support during the laboratory analyses of this study, and V.H. Garduño, A. Jiménez, H. Cepeda, and P. Pacheco for their observations during fieldwork in Baja. All field campaigns were made possible thanks to the kind assistance of UMA and Ecoturismo Borrego Cimarrón, Bonfil, B.C.S personnel guides, especially of F. Romero (El Borrego). Thanks for the comments made by reviewers (H. Apps, G. Giordano and M. Sacchi) and by the associated editor (A. Merschat) to the map and manuscript.

Disclosure statement

No potential conflict of interest was reported by the authors.

Funding

This work was supported by CeMIE Geo [grant number 207032]; Consiglio Nazionale delle Ricerche - Italgas [grant number CIG 648306172D].

ORCID

J.L. Macías http://orcid.org/0000-0002-2494-9849
G. Groppelli http://orcid.org/0000-0003-4660-2288

References

Avellán, D. R., Macías, J. L., Arce, J. L., Jiménez-Haro, A., Saucedo-Girón, R., Garduño-Monroy, V. H., & Layer, P. W. (2018). Eruptive chronology and tectonic context of the late Pleistocene Tres Vírgenes volcanic complex,

Baja California Sur (México). *Journal of Volcanology and Geothermal Research*. doi:10.1016/j.jvolgeores.2018.06.012

Bryan, S. E., Orozco-Esquivel, T., Ferrari, L., & Lopez-Martinez, M. (2014). Pulling apart the mid to late Cenozoic magmatic record of the Gulf of California: Is there a Comondú arc? *Geological Society, London, Special Publications*, *385*(1), 389–407.

Capra, L., Macıas, J. L., Espındola, J. M., & Siebe, C. (1998). Holocene plinian eruption of La Virgen volcano, Baja California, Mexico. *Journal of Volcanology and Geothermal Research*, *80*(3), 239–266.

Conly, A. G., Brenan, J. M., Bellon, H., & Scott, S. D. (2005). Arc to rift transitional volcanism in the Santa Rosalia region, Baja California Sur, Mexico. *Journal of Volcanology and Geothermal Research*, *142*(3), 303–341.

Demant, A. (1984). The Reforma caldera, Santa Rosalia area, Baja California. A volcanical, petrographical and mineralogical study. In V. Malpica-Cruz, S. Celis-Gutierrez, J. Guerrero-García, & L. Ortilieb (Eds.), *Neotectonics and sea level variations in the Gulf of California area, Symposium (Hermosillo, Son. April)* (pp. 21–23).

Demant, A., & Ortlieb, L. (1981). Plio-Pleistocene volcanotectonic evolution of la Reforma caldera, Baja California, Mexico. *Tectonophysics*, *71*, p. 194.

Ferrari, L., López-Martínez, M., Orozco-Esquivel, T., Bryan, S. E., Duque-Trujillo, J., Lonsdale, P., & Solari, L. (2013). Late Oligocene to Middle Miocene rifting and synextensional magmatism in the southwestern Sierra Madre Occidental, Mexico: The beginning of the Gulf of California rift. *Geosphere*, *9*(5), 1161–1200.

Ferrari, L., Orozco-Esquivel, T., Bryan, S. E., López-Martínez, M., & Silva-Fragoso, A. (2018). Cenozoic magmatism and extension in western Mexico: Linking the Sierra Madre Occidental silicic large igneous province and the Comondú Group with the Gulf of California rift. *Earth-Science Reviews*, *183*, 115–152.

García-Sánchez, L. (2019). *Origen y evolución de la Caldera de La Reforma, Baja California Sur: Estudio vulcanológico, petrológico, geoquímico e isotópico* (UNAM, Ph Dissertation).

Garduño-Monroy, V. H., Vargas-Ledezma, H., & Campos-Enriquez, J. O. (1993). Preliminary geologic studies of Sierra El aguajito (Baja California, Mexico): A resurgent-type caldera. *Journal of Volcanology and Geothermal Research*, *59*, 47–58.

Gastil, R. G. (1975). Reconnaissance geology of the state of Baja California. The Geological Society of America, Inc. *Memoir*, *40*, 139–143.

Groppelli, G., & Martì-Molist, J. (2013). Volcanic stratigraphy-state of the art. *Ciências da Terra/Earth Sciences Journal*, *18*, 99–104.

Groppelli, G., & Viereck-Goette, L. (2010). Introduction. In G. Groppelli & L. Viereck-Goette (Eds.), *Stratigraphy and geology of volcanic areas* (Vol. 464, pp. V–VII). Boulder, CO: Geological Society of America.

Hausback, B. P. (1984). Cenozoic volcanic and tectonic evolution of Baja California Sur, Mexico. In V. A. Frizzel Jr. (Ed.), *Geology of the Baja California Peninsula* (pp. 219–236). SEPM Pacific Section, Special Publication 39.

Kimbrough, D. L., Smith, D. P., Mahoney, J. B., Moore, T. E., Grove, M., Gastil, R. G., … Fanning, C. M. (2001). Forearc-basin sedimentary response to rapid Late Cretaceous batholith emplacement in the Peninsular Ranges of southern and Baja California. *Geology*, *29*(6), 491–494. doi:10.1130/0091-7613(2001)029<0491:FBSRTR>2.0.CO;2

Lira, H. H., Ramirez, S. G., Herrera, F. J. J., & Vargas, H. (1983). Estudio geologico a semidetalle de la zona geotérmica de las Tres Vírgenes, B.C.S., Intern. Rep. 30/83, Gerencia de Proyectos Geotermoelectricos-CFE (Mexico).

Lira, H. H., González, M. L., & Arellano, F. G. (1997). Actualización del modelo conceptual del Campo Geotérmico de Tres Vírgenes, Baja California Sur. Technical Report, RE-12/97, Gerencia de Proyectos Geotermoeléctricos, Comisión Federal de Electricidad, 26.

López, H. A., García, G. H., & Arellano, F. G. (1995). *Geothermal exploration at Las Tres Vírgenes, BCS, Mexico*. Proceedings of the World Geothermal Congress (pp. 707–712).

Macías, J. L., Arce, J. L., Garduño, V. H., Avellán, D. R., García, L., Reyes, G., … Navarrete, J. A. (2012). Estudio de estratigrafía y geología del Complejo Volcánico Tres Vírgenes. [Informe Final DEX-DGL-TV-17-11]. *Comisión Federal de Electricidad*, 104 pp.

Martí, J., Groppelli, G., & da Silveira, A. B. (2018). Volcanic stratigraphy: A review. *Journal of Volcanology and Geothermal Research*, *357*, 68–91.

McLean, H. (1988). *Reconnaissance geologic map of the Loreto and part of the San Javier quadrangles, Baja California Sur, Mexico*. U.S. Geological Survey Miscellaneous Field Studies Map, Report No. MF-2000 (p. 10), 1 mapa, escala 1:50,000.

Ortlieb, L. (1978). Reconocimiento de las terrazas marinas cuaternarias en la parte central de Baja California. *Universidad Nacional Autónoma de México. Instituto de Geología*, *2*(2), 200–211.

Ortlieb, L., & Colleta, B. (1984). Síntesis cronoestratigráfica sobre el Neogeno y el Cuaternario marino de la cuenca de Santa Rosalía, Baja Clifornia Sur. In V. Malpica-Cruz, S. Celiz-Gutiérrez, J. Guerrero-García, & L. Ortlieb (Eds.), *Neotectonics a sea level variations in the Gulf of California area, a symposium (Hermosillo, Son., April 21–23)* (pp. 241–268). México, DF: Universidad Nacional Autónoma de México, Instituto de Geología.

Pasquarè, G., Abate, E., Castiglioni, G. B., Merenda, M., Mutti, E., Ortolani, F., … Sassi, F. P. (1992). *Carta geologica d'Italia 1:50.000 Guida al Rilevamento*. Quaderni serie III (Vol. 1, p. 203).

Salvador, A. (1994). *International stratigraphic guide: A guide to stratigraphic classification, terminology, and procedure (No. 30)*. Boulder, CO: Geological Society of America.

Sawlan, M. G. (1991). Magmatic evolution of the Gulf of California rift. In J. P. Dauphin & B. R. Simoneit.

Sawlan, M. G., Ortlieb, L., & Roldan, O. (1981). *Late Cenozoic volcanism in the Tres Vírgenes area*. Proceedings of the Geology of Northwestern Mexico and Southern Arizona Congress (pp. 309–319), Universidad Nacional Autónoma de México, Hermosillo, Sonora, México.

Sawlan, M. G., & Smith, J. G. (1984). *Petrologic characteristics, age and tectonic setting of Neogene volcanic rocks in northern Baja California Sur, Mexico*.

Schmidt, E. K. (1975). *Plate tectonics, volcanic petrology, and ore formation in the Santa Rosalía area, Baja California*. Mexico: The University of Arizona.

Schmitt, A. K., Stockli, D. F., & Hausback, B. P. (2006). Eruption and magma crystallization ages of Las Tres Vírgenes (Baja California) constrained by combined

230Th/238U and (U-Th)/He dating of zircon. *Journal of Volcanology and Geothermal Research*, *158*, 281–295. doi:10.1016/j.jvolgeores.2006.07.005

Schmitt, A. K., Stockli, D. F., Niedermann, S., Lovera, O. M., & Hausback, B. P. (2010). Eruption ages of Las Tres Vírgenes volcano (Baja California): A tale of two helium isotopes. *Quaternary Geochronology*, *5*(5), 503–511.

Umhoefer, P. J., Dorsey, R. J., Willsey, S., Mayer, L., & Renne, P. (2001). Stratigraphy and geochronology of the Comondu Group near Loreto, Baja California Sur, Mexico. *Sedimentary Geology*, *144*(1–2), 125–147.

Wheeler, H. E., & Mallory, V. S. (1953). Designation of stratigraphic units. *AAPG Bulletin*, *37*(10), 2407–2421.

Wilson, I. F. (1948). Buried topography, initial structures, and sedimentation in Santa Rosalia area, Baja California, Mexico. *American Association of Petroleum Geologists Bulletin*, *32*, 1762–1807.

Wilson, I. F., & Rocha, V. S., (1955). Geology and mineral deposits of the Boleo copper district, Baja California, Mexico. Geological Survey Special Paper, 273. Washington, DC: U.S. Government Publishing Office, 140 pp.

Geology of La Reforma caldera complex, Baja California, Mexico

García Sánchez, L.[1], Macías, J.L.[2], Sulpizio, R.[3,6], Osorio-Ocampo, L.S.[1], Pellicioli, C.[3,4], Pola, A.[5], Avellán, D.R.[7], Cisneros, G.[2], García, F.[2], Ocampo-Díaz, Y.Z.E.[8], Lira-Beltran, R.M.[1], Saucedo, R.[9], Sánchez-Núñez, J.M.[10], Arce, J.L.[11], Corona-Chávez, P.[12], Reyes-Agustin, G.[2], Cardona, M.[2], Layer, P.W.[13], Benowitz, J.[13], Solari, L.[14] and Groppelli G.[3]

[1] Posgrado en Ciencias de la Tierra, Instituto de Geofísica, Universidad Nacional Autónoma de México, Ciudad de México, México
[2] Instituto de Geofísica, Universidad Nacional Autónoma de México, Morelia, Michoacán, México
[3] Istituto per la Dinamica dei Processi Ambientali, sezione di Milano, C.N.R., Milano, Italia
[4] Dipartimento di Scienze della Terra "Ardito Desio", Università degli Studi di Milano, Milano, Italia
[5] Dipartimento di Scienze della Terra e Geoambientali, Università degli Studi di Bari "Aldo Moro", Bari, Italia
[6] Escuela Nacional de Estudios Superiores, Unidad Morelia, Universidad Nacional Autónoma de México, Morelia, Michoacán, México
[7] Cátedra CONACYT - Instituto de Geofísica, Universidad Nacional Autónoma de México, Morelia, Michoacán, México
[8] Area de Ciencias de la Tierra, Facultad de Ingeniería, Universidad Autónoma de San Luis Potosí, San Luis Potosí, México
[9] Instituto de Geología, Universidad Autónoma de San Luis Potosí, San Luis Potosí, México
[10] Centro Interdisciplinario de Investigaciones y Estudios sobre Medio ambiente y Desarrollo, Ciudad de México, México
[11] Instituto de Geología, Universidad Nacional Autónoma de México, Ciudad de México, México
[12] Instituto de Investigaciones en Ciencias de la Tierra, Universidad Michoacana de San Nicolás de Hidalgo, Morelia, Michoacán, México
[13] Geophysical Institute, University of Alaska at Fairbanks, Fairbanks, USA
[14] Centro de Geociencias, Universidad Nacional Autonoma de Mexico, Junquilla, Queretaro, Mexico

Coordinator of the project: Macías, J.L.
Heads of field survey: Groppelli G., Macías, J.L., Sulpizio, R.
PhD students: García Sánchez, L., Osorio-Ocampo, L.S., Pellicioli, C., Lira-Beltran, R.M.
Sedimentary basement stratigraphy: Ocampo-Díaz, Y.Z.E., Lira-Beltran, R.M.
Radiometric geochronology: Layer, P. W., Solari, L.
Editing and digital cartography production: Pellicioli, C.

Coordinate System:
Projection: UTM (zone 12N); Datum: WGS84

0 Kilometers 4
1:50,000

Legend

Recent debris flow deposits (16) and Alluvial, talus and marine-marginal deposits (17): Massive, heterolithologic gravel deposits sometimes supported by a sandy matrix (16). Sands, pebbles and cobbles derived from volcanic and plutonic rocks with interlayered silty and sandy lenses. Silty-to-sandy matrix locally abundant. Located along seasonal water courses, at base of slopes, and along coast (17).

Cueva del Diablo formation (15): Up to 50-m thick lava flows, domes, and scoria cones sometimes associated with dikes and intrusive bodies (15a). Lavas display large variability in both composition (mainly basaltic-andesitic and andesitic, and minor rhyolitic) and texture (from aphyric to porphyritic, with phenocrysts of pl, px, and Fe-Ti oxides). Several lithosomes (vents and related lava flows and domes) can be identified within the formation: L1 Las Mintas dome; L2 Morro del las Palmas dome; L3 Punta Gorda stratocone; L4 Punta El Gato stratocone; L5 Cerro Colorado scoria cone (age: 0.46 Ma); L6 Punta Prieta scoria cones (age: 0.28 Ma).
Arroyo Grande member (15b): Up to 50-m thick alluvial deposits made of sandy to gravelly (lavas and plutonic rocks) lenticular to stratified deposits. These thin (<1 m) white fall deposits interbed the alluvial succession. The deposits form alluvial fans within the eastern part of the caldera depression.

Punta Arena ignimbrite (14): Up to 200 m thick, white loose pyroclastic deposit, made of grey and white pumices, lava and scoria lithics (red and grey) in ashy matrix. Lithic blocks are locally abundant (leg breccias). Matrix is generally whitish to yellowish in colour, but it becomes light-green when hydrothermalised. It is locally fairly well-consolidated due to hydrothermal alteration. White pumice is trachydacitic, grey pumice is dacitic. Age: 0.96 Ma

Aguajito ignimbrite (13): Up to 40-m thick, non-welded, light-brown pyroclastic deposit with white pumice and loose crystals of pl at the bottom, overlain by light-pink to light-purple, lithic-rich ignimbrite. Welded at top, with brown fiammes, lithics (granite, lavas), ash-rich matrix, and loose crystals of pl, amph and px. Rhyolite. Age: 1.17 Ma.

Mesa El Yaqui formation (12): 3- to 20-m thick, dark-grey lava flow succession generally covering slopes external to caldera. Aphyric to porphyritic lavas of basaltic-andesitic composition with phenocrysts of pl, ol, px and Fe-Ti oxides. Age: 1.18 Ma.

La Reforma ignimbrite (11): Up to 40-m thick pyroclastic deposits, consisting of basal welded, reddish bed overlain by various welded brownish to dark-grey deposits. Welded deposit contains black fiamme pumice and accidental lithics (lavas). Loose crystals of pl and px occur in ashy matrix. Rhyolite. Age: 1.29 Ma

Cerro La Reforma formation (10): Succession of thick lava flows (up to 10 m) and minor pyroclastic deposits cropping out in central part of caldera. It comprises also lava domes along caldera rims (10a). Porphyritic lavas of dacitic composition, with phenocrysts of pl, px and Fe-Ti oxides. Xenocrysts of qtz and sedimentary xenoliths are also present. Age: 1.27 Ma.

Los Balcones ignimbrite (9): Up to 30-m thick, grey welded pyroclastic deposit made of light-grey pumice and dark-grey fiamme, with abundant lithics (grey, black and white lavas). Abundant loose crystals of pl and minor px in greyish ash-rich matrix. Rhyolite. Age: 1.35 Ma.

Punta Candeleros formation (8): Hyaloclastites, pillow lavas and lava domes with columnar jointing emplaced in submarine settings. Composition is mainly basaltic-andesitic to andesitic with minor trachy-dacitic lavas. Texture varies from aphyric to porphyritic with phenocrysts of pl, px. Age: 1.42 Ma (pillow lavas); 1.36 Ma (lava dome).

Contrabando formation (7): Up to 15 m thick, stratified, light yellow pyroclastic deposit made of white and grey pumice. Loose crystals of pl and px occur in yellowish ash-rich matrix. Age: 1.47 Ma.

Carrizo ignimbrite *(not mappable)*: Up to 10-m thick, red welded pyroclastic deposit containing yellow and grey pumice and abundant lithics (green or grey lavas and black scorias). Abundant loose crystals of pl in reddish ash-rich matrix. Rhyolite. Age: 1.89 Ma.

Cueva Amarilla ignimbrite (6): Up to 30-m thick, greenish grey pyroclastic deposit with white pumice at bottom and black scoriae at top. Loose crystals of pl and px occur in greenish ash-rich matrix. Age: 2.4 Ma.

Mesa de en Enmedio ignimbrite (5): Up to 5-m thick, light-grey pyroclastic deposit made of pumices (10-50 cm long). Loose crystals of pl and px occur in yellow ashy matrix.

Sedimentary Formation of the Santa Rosalía basin (*Formación sedimentaria de la cuenca de Santa Rosalía*, Auct.) (4): Mainly brownish siltstones (up to 30 m thick) at base, overlain by fossiliferous sandstones and conglomerates (5-20 m thick). Fossils mainly consist of bivalves (Pectinidae) and well-preserved oysters and sea urchins. Several interlayered ignimbrites (cf. units 5, 6 and 7). Pliocene-Middle Pleistocene.

Santa Lucía formation (3): Up to 80-m thick lava flows and domes, associated with dikes. Andesitic and basaltic lava, aphyric to porphyritic texture with phenocrysts of pl and px. Age: 19.25 Ma.

Comondú Group (2): Red sandstones, siltstones and conglomerates interlayered with lavas (Santa Lucía Formation). Up to 100-m thick. Age: 12-30 Ma.

Plutonic rocks (*Batholithes Peninsulares*, Auct), (1): Several crystalline intrusive bodies cropping out along the Yaqui canyon (up to 8-m thick) and near Cerro La Reforma (up to 50 m thick - base not visible). Holocrystalline granodiorite, with 3-4 mm sized Kfs, pl, qa, amph and bio phenocrysts. Associated aplitic dikes. Age: 97.9 Ma.

- Dome
- Bedding attitude
- Buried caldera rim
- Crater rim
- Pit crater rim
- Fault (dashed if inferred)
- Dyke
- Marine terrace
- Contour line: 50 m
- Scoria cone and proximal fallout deposit (the background color corresponds to the formation color)

Scheme of stratigraphic relationships

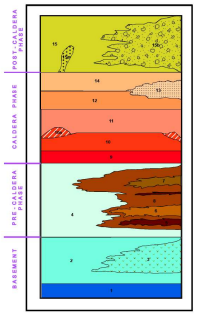

3D view of La Reforma caldera complex

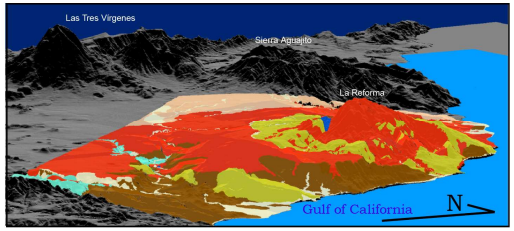

Chapter 4

Paper II

Control of regional structures on the evolution of Pleistocene La Reforma caldera complex: implications on caldera collapse and resurgence

C. Pellicioli [a, b], *G. Groppelli* [b], *J.L. Macías* [c] *and R. Sulpizio* [b, d].

[a] Dipartimento di Scienze della Terra "Ardito Desio", Università degli Studi di Milano, Milano, Italia;
[b] Istituto per la Dinamica dei Processi Ambientali, sezione di Milano, Consiglio Nazionale delle Ricerche, Milano, Italia;
[c] Instituto de Geofísica, Universidad Nacional Autónoma de México, Morelia, Michoacán, México;
[d] Dipartimento di Scienze della Terra e Geoambientali, Università degli Studi di Bari "Aldo Moro", Bari, Italia.

SUBMITTED TO THE GEOLOGICAL SOCIETY OF AMERICA® BULLETIN IN JUNE 2019, REF: TRACKING NUMBER B35390.

Collection of structural data in the field: ***C. Pellicioli****, G. Groppelli.*

Plotting, analysis and interpretation of structural data: ***C. Pellicioli.***

Reconstruction of La Reforma caldera complex evolution: ***C. Pellicioli*** (under the supervision of *G. Groppelli and R. Sulpizio*).

Coordinator of the project and main beneficiary of the funds used for PhD work: *J.L. Macías.*

Manuscript writing: ***C. Pellicioli.***

THE GEOLOGICAL SOCIETY OF AMERICA®

BULLETIN

E: gsab@geosociety.org
W: geosociety.org/gsa
T: @geosociety

Control of regional structures on the evolution of Pleistocene La Reforma caldera complex: implications on caldera collapse and resurgence

Tracking no: B35390

Authors:
Claudia Pellicioli (Università degli Studi di Milano), Gianluca Groppelli (University of Milano), José Luis Macìas (UNAM), and Roberto Sulpizio (Dipartimento di Scienze della Terra e Geoambientali)

Abstract:
La Reforma caldera complex lies on the western side of the Gulf of California, Mexico. It is the oldest of three Pleistocene-to-present day active calc-alkaline volcanic complexes in the Santa Rosalía basin, that hosts the currently producing Las Tres Vírgenes geothermal field. The whole area is affected by the complex regional setting related to the Gulf of California opening and evolution. This study is part of the CEMIE Geo project (awarded to UNAM) aimed to improve the geological knowledge of La Reforma and Sierra Aguajito volcanic complexes for geothermal exploitation purposes and discusses the control of regional structures on the evolution of La Reforma caldera complex. Results highlighted that regional structures are responsible for La Reforma caldera trap-door collapse geometry and the asymmetrical shape of its uniformly-dipping layers resurgent block, bounded by volcanic structures only to the SE. Resurgence inside La Reforma caldera complex is quite pronounced, as consisting of at least 840 m of vertical uplift and causing the uplift of Cretaceous basement up to altitudes of about 600 m a.s.l. inside the caldera depression. Further implications of this study include that geothermal potential throughout the Tres Vírgenes area is maximum where several sets of structures interact or in accommodation zones, despite individual regional or volcanic structures can represent sites of pervasive hydrothermal circulation. This work represents a good case study of regionally-driven caldera collapse and resurgence processes, that need to be unravelled prior than making any assessment on hydrothermal circulation in geothermally active regions.

4.1 Abstract

La Reforma caldera complex lies on the western side of the Gulf of California, Mexico. It is the oldest of three Pleistocene-to-present day active calc-alkaline volcanic complexes in the Santa Rosalía basin, that hosts the currently producing Las Tres Vírgenes geothermal field. The whole area is affected by the complex regional setting related to the Gulf of California opening and evolution. This study is part of the CeMIE Geo project (awarded to UNAM) aimed to improve the geological knowledge of La Reforma and Sierra Aguajito volcanic complexes for geothermal exploitation purposes and discusses the control of regional structures on the evolution of La Reforma caldera complex. Results highlighted that regional structures are responsible for La Reforma caldera trap-door collapse geometry and the asymmetrical shape of its uniformly-dipping layers resurgent block, bounded by volcanic structures only to the SE. Resurgence inside La Reforma caldera complex is quite pronounced, as consisting of at least 840 m of vertical uplift and causing the uplift of Cretaceous basement up to altitudes of about 600 m a.s.l. inside the caldera depression. Further implications of this study include that geothermal potential throughout the Tres Vígenes area is maximum where several sets of structures interact or in accommodation zones, despite individual regional or volcanic structures can represent sites of pervasive hydrothermal circulation. This work represents a good case study of regionally-driven caldera collapse and resurgence processes, that need to be unravelled prior than making any assessment on hydrothermal circulation in geothermally active regions.

Keywords: *regional tectonics, caldera collapse, resurgence, geothermal*.

4.2 Introduction

Caldera-forming processes are among the most catastrophic events affecting the Earth dynamics. They imply withdrawal of tens to hundreds of km^3 of magma from the subsurface, shaping the surrounding territory with thick volcanic deposits and modifying the crust structure through collapse of the magma chamber(s) and volcanic feeding system. Also the post caldera dynamics includes outstanding processes, like block resurgence and establishment of large-scale fluid circulation that may originate geothermal fields. Because of the unique structural and volcanological setting that characterizes each volcano, also the processes driving to caldera-forming eruptions and subsequent structural collapse are various and far to be satisfactorily understood. Follows the need to improve the number of case studies

of caldera-forming events worldwide, in order to increase the available data sets in different geodynamics and volcanic settings. This is particularly true when considering the interaction of the volcanic-driven processes with regional tectonics and stress distribution, which add complexity to the processes driving the structural collapse (Cole et al., 2005; Acocella, 2007). Besides the shape of the shallow magma chamber, geometry and location of ring faults may be controlled by regional stress and pre-existing structures (Cole et al., 2005; Acocella, 2007). Furthermore, ring faults and regional structures act jointly in driving magma up to surface during post-caldera volcanic phases and control fluid circulation during inter-eruptive phases (Norini et al., 2015). Therefore, if we aim to understand caldera processes and evolution (including collapse and resurgence processes) and to assess calderas geothermal potential, we first need unravelling the reciprocal relationships between regional and volcanic structures.

In the light of this, this paper aims to present results of a newly-performed structural study across La Reforma caldera complex (Baja California, Mexico) and to address the role of regional structures in magma trapping and rise, their interplay with volcanic structures linked to caldera collapse and resurgence, and the nature of structures controlling caldera resurgence. La Reforma caldera complex belongs to the Quaternary volcanic activity of Santa Rosalía area, hosting the only-known Quaternary silicic polygenetic centres in the whole Gulf of California (Schmidt, 1975; Sawlan and Smith, 1984; Conly et al., 2005; Gutiérrez-Negrín, 2015). These are La Reforma (2.4 Ma, García-Sánchez et al., 2019), Sierra Aguajito (1.17 Ma, Schmitt et al. 2006) and Tres Vírgenes (including three volcanoes aligned along a NNE trend: El Viejo–El Partido, 300 ka; El Azufre, 173-128 ka and La Vírgen, 112-22 ka according to Avellán et al., 2018 or last eruption in 1746 according to López A.C. et al., 1993). The present study frames into the CeMIE Geo (Centro Mexicano de Innovación en Energía Geotérmica) project P15 of SENER-CONACyT awarded to UNAM (Universidad National Autónoma de México, Instituto de Geofísica, Morelia, Michoacán, México) and focused on improving the geological knowledge of La Reforma and Sierra Aguajito volcanic complexes for exploitation purposes linked to the currently producing Las Tres Vírgenes geothermal field (10 MW installed running capacity, Gutiérrez-Negrín, 2015, Fig. 4.1A). Despite geothermal and volcanic activity throughout the region shifted over time from La Reforma to the Tres Vírgenes volcanic complex (where they currently focus), a good understanding on La Reforma fossil geothermal system is in fact fundamental to fully capture mechanisms that drive hydrothermal fluids circulation across the Santa Rosalía region. A series of geological field surveys between 2015-2017 allowed to compile a detailed stratigraphy of La Reforma caldera complex, summarized by García-Sánchez et al. (2019) 1:50,000 geological map. In parallel, we performed a series of structural field surveys, whose results are herein presented and summarized in a structural map, that allowed to capture the link between regional structures and La

Reforma caldera complex main evolutionary stages, with implications regarding geothermal processes. The structural contribution of this study is of particular relevance when considering that, despite López H. A. et al. (1989) and López A.C. et al. (1993) stressed the importance of faults acting as main pathways for hydrothermal fluids circulation and ore mineralization across the Santa Rosalía region, no detailed study on its volcano-tectonic setting is available so far. Results of this work could contribute to any activity concerning current production enhancement or future geothermal exploration and also be applied to analogue geological settings, either along the Gulf of California or globally.

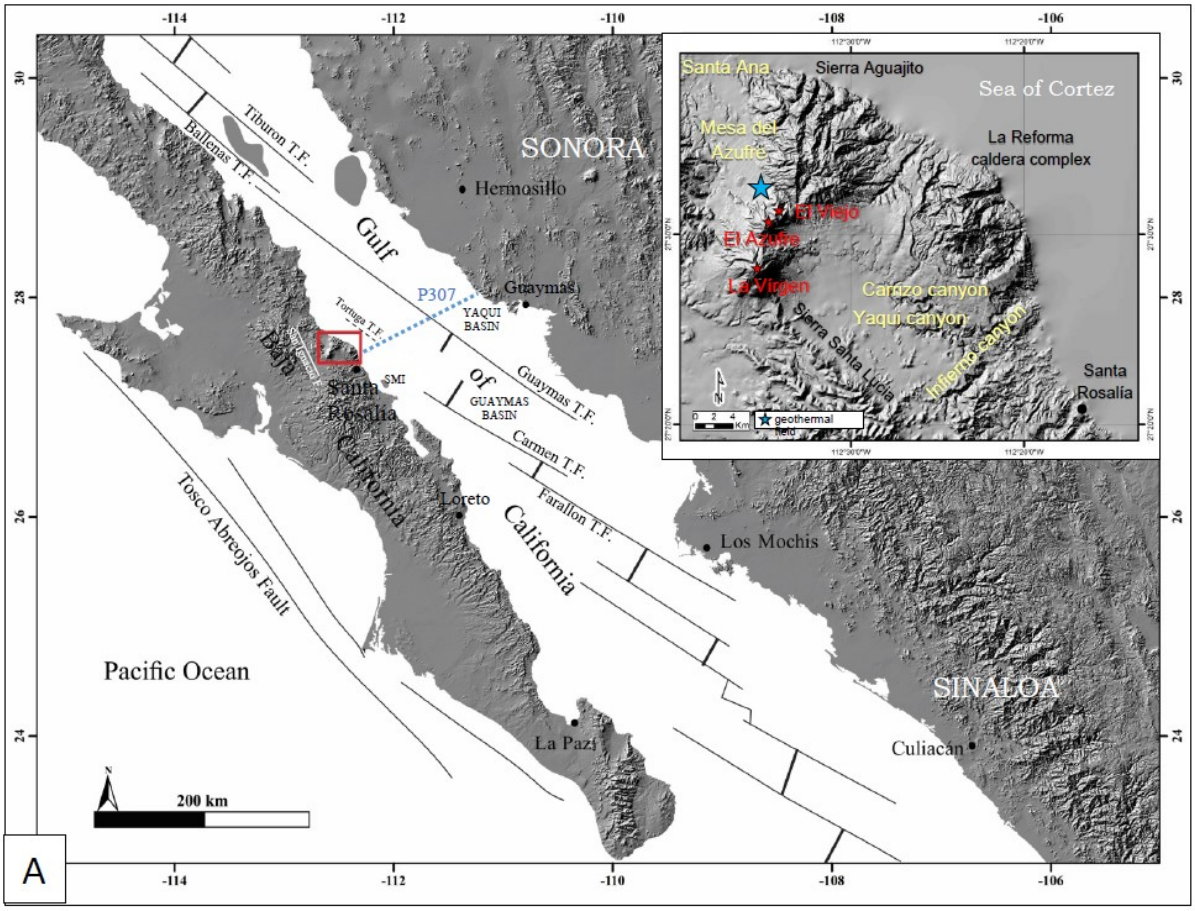

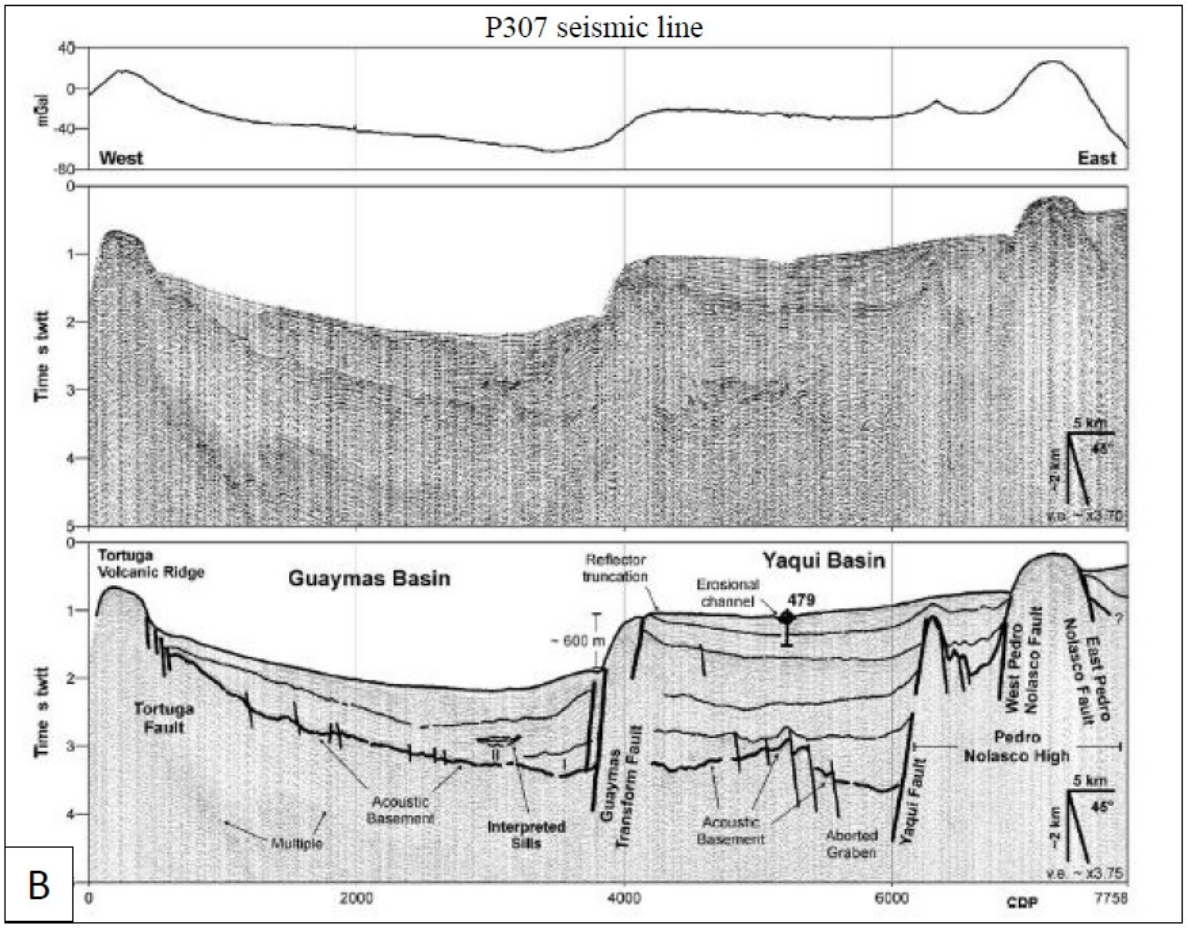

Figure 4.1 Location of La Reforma caldera complex (a) and detail of seismic line P307 across the Yaqui and northern Guaymas basins in the central Gulf of California (modified after Fenby and Gastil, 1991 and Arágon-Arreola et al., 2015). Shaded DEM, imagery source: INEGI.

4.3 Regional geological setting

La Reforma caldera complex lies on the eastern side of the Sea of Cortez, a 90 to 220 km wide marginal sea (also known as Gulf of California) separating the Baja California peninsula from mainland Mexico and representing one of the world best studied cases where a subduction convergent margin switched into an obliquely divergent plate boundary with no collision (Ferrari et al., 2018). In detail, subduction ceasing between the Farallon and North American plates in Tertiary times caused the transfer of the modern Baja California peninsula from the North American to the Pacific plate. At the same time, the region has been involved in the modern Gulf of California orthogonal and oblique-rifting (Stock and Hodges, 1989; Fletcher et al., 2007) phases. The complex and controversial evolution of the Gulf of California region (whose main steps are summarized in Table 4.1) has recently been reviewed by Ferrari et al. (2013, 2018), who identified a long-lasting extension process starting at

the end of Eocene and leading to the Gulf of California rifting, in opposition to traditional models that collocate the onset of Gulf-associated extension only after subduction ceasing (12.3 Ma, Atwater and Stock, 1998) and first production of sea-floor oceanic crust in the early Pliocene (Atwater and Severinghaus, 1989; Lonsdale, 1991). The Santa Rosalía basin is a NW-SE trending half-graben basin bounded by NE dipping and NW-SE trending faults (Aragón-Arreola et al., 2005, seismic line P307 in Fig. 4.1B), where marine incursion occurred about 8 Ma (Conly et al., 2005). It is bordered by the Sierra Santa Lucia on the W and most likely by the San Marcos Island offshore on the E (SMI in Fig. 4.1A, Conly et al., 2005), while northern and southern limits are difficult to identify as buried under Quaternary volcanic products (Conly et al., 2005). Slope morphology in the offshore part of the Santa Rosalía basin is marked by mass transport processes along faults and by depressions developed perpendicularly to the coastline, that suggest active faulting and erosion processes (Nava-Sanchez et al., 2001). The dominant style of active faulting inside the Santa Rosalía basin since 3.5 Ma ago stress reorganization (Table 4.1) is normal right-lateral oblique slip. Local direction of extension is approximately E-W and the maximum horizontal stress is roughly N-S aligned (Wong and Munguía, 2006; Antayhua-Vera et al., 2015). Faults recognised within this basin by López H. A. (1998), Portugal et al. (2000), Conly et al. (2005), Verma et al. (2006), Wong and Munguía (2006), Barragán et al. (2010), Macías and Jimenez (2012, 2013), Antayhua-Vera et al. (2015) and Avellán et al. (2018), principally strike: NW-SE, to generate a series of steps falling to the NE (*Bonfil*, *Mezquital*, *La Virgen*, *El Volcan*, *El Viejo*, *El Partido*, *El Azufre* or *Reforma Fault*); NE-SW (*Los volcanes alignment*, *El Alamo*) and N-S (*Las Viboras*, *El Colapso*, *El Cimarron*).

Table 4.1 Summary of main evolution steps of the Gulf of California region.

Phase/Process/Structures	Location/Province	Age	Reference
Wide-scale and generalised extension – spatially continuous large structures	Gulf of California and Mexican Basin and Range	Eocene- middle Miocene, prior to Farallon plate subduction end	Ferrari et al. (2013, 2018), Mark et al. (2012).
Focusing of extension and volcanism with large magnitude crustal thinning – pure orthogonal rifting (proto-gulf)	Gulf of California	19 - 16 Ma	Bryan et al. (2014), Ferrari et al. (2018).
Pure strike-slip deformation	West of Baja California peninsula – Tosco Abreojos Fault		
Plate convergence cease	Farallon plate subduction zone	13 - 12 Ma	Ferrari et al. (2018)
Right-lateral transtension and oblique rifting onset	Gulf of California	12 Ma / 6 Ma	Fletcher et al. (2007) / Stock and Hodges (1989)

Production of new oceanic crust	southern Gulf of California (i.e. Guaymas basin)	Early Pliocene	Atwater and Severinghaus (1989), Fuis and Kohler (1984), Lonsdale (1991), Ness et al. (1991).
Transform plate boundary between Pacific and North American plates	Gulf of California	3.5 Ma	Lonsdale (1991), Ness (1991).
45° clockwise rotation of minimum horizontal stress from NE-SW to E-W and 45° counter-clockwise rotation of fault directions			Angelier et al. (1981), Aragón-Arreola et al. (2005), Atwater (1970), Ortlieb et al (1989), Umhoefer et al. (2002), Zanchi (1994).
Offshore and onshore pull-apart basins bordered by NW-SE trending dextral strike-slip faults (partly gulf-inherited)			Angelier et al. (1981), Zanchi (1994).
Production of new oceanic crust	northern Gulf of California (i.e. Upper and Lower Delfin basins)	1 Ma	Martín-Barajas et al. (2013), Persaud et al. (2003).

4.4 La Reforma caldera complex

La Reforma is a 10 km wide and 1200 m high Pleistocene resurgent (Demant and Ortlieb, 1981; Hausback et al., 2000; García-Sánchez et al., 2019) caldera complex, covering an approximate area of 300 km^2 inside the Santa Rosalía basin, NW of the Santa Rosalía town (Mulegé municipality of northern Baja California Sur, Fig. 4.1A). Recent geological studies within the CEMIE Geo project, led to identify three evolution phases inside La Reforma caldera complex (pre, -syn, and post-caldera, García-Sánchez et al., 2019), illustrated in Table 4.2, Figs. 4.2A and B. The quaternary volcanic succession lies on plutonic rocks (Wilson and Rocha 1955) belonging to the crystalline Late Cretaceous to Eocene batholith of the *Laramide arc belt* (also known as *Great Baja California batholith*, Schmidt, 1975; McLean, 1988 or *Peninsular Range Batholith*, Kimbrough et al., 2001; Kimbrough et al., 2014) and the overlying Oligocene to middle Miocene volcani-clastic deposits of the Comondù Group (Hausback, 1984; Sawlan and Smith, 1984; Sawlan, 1991,; López H. A. et al., 1995; Umhoefer et al., 2001; Conly et al., 2005; Bryan et al. 2014), interlayered with andesitic and basaltic lava flows, domes and associated dykes (Santa Lucia formation, Garduño-Monroy et al. 1993; Conly et al., 2005; García-Sánchez et al., 2019).

Table 4.2 Stratigraphy of La Reforma caldera complex.

PHASE	Lithostratigraphic units	Age
POST – CALDERA	**15 - Cueva del Diablo formation** and related **intrusions**	Pleistocene [a]
	15b - Arroyo Grande member	-
	Lithosomes: **l6 - Punta Prieta scoria cones**	0.28 ± 0.05 Ma [a]
	Lithosomes: **l5 - Cerro Colorado scoria cone**	0.46 ± 0.08 Ma [a]
	Lithosomes: **l4 - Punta El Gato stratocone**	-
	Lithosomes: **l3 - Punta Gorda stratocone**	-
	Lithosomes: **l2 - Morro de Las Palmas dome**	-
	Lithosomes: **l1 - Las Minitas dome**	-
SYN – CALDERA	**14 - Punta Arena ignimbrite**	0.96 ± 0.21 Ma [a]
	13 - Aguajito ignimbrite*	1.17 ± 0.07 Ma [b]
	12 - Mesa El Yaqui formation	1.18 ± 0.46 Ma [a]
	11 - La Reforma ignimbrite	1.29 ± 0.02 Ma [a]
	10 - Cerro La Reforma formation	1.27 ± 0.02 Ma [a]
	9 - Los Balcones ignimbrite	1.35 ± 0.02 Ma [a]
PRE – CALDERA	**8 - Punta Candeleros formation**	1.42 ± 0.05 Ma [a]; 1.36 ± 0.06 Ma [a]
	7 - Contrabando formation	1.47 ± 0.08 Ma [a]
	Carrizo ignimbrite (not mappable)	1.89 ± 0.27 Ma [a]
	6 - Cueva Amarilla ignimbrite	2.4 ± 1.5 Ma [a]
	5 - Mesa de Enmedio ignimbrite	-
	4 - Sedimentary Formation of the Santa Rosalía basin	Pliocene – Middle Pleistocene [c, d, e]
BASEMENT	**2 - Comondù Group / 3 - Santa Lucia formation**	30-12 Ma [f]; 24-12 Ma [e]; / 19.25 ± 0.08 Ma [a]; 12 Ma [e].
	1 - Great Baja California or **Peninsular Range Batholith**	91.2 ± 2.0 Ma [g]; 94 ± 2 Ma [h]; 91.5 ± 1.5 Ma [i]; 92.5 ± 1.5 Ma [i]; 92.4 ± 1.6 Ma [i]; 97.8 ± 1.5 Ma [a].

(*) Erupted by neighbouring Sierra Aguajito volcanic centre

[a] García-Sánchez et al. (2019);

[b] Schmitt et al. (2006);

[c] Ortlieb and Colletta (1984);

[d] Holt et al. (2000);

[e] Conly et al. (2005);

[f] Hausback (1984); Sawlan and Smith (1984); Umhoefer et al. (2001); Bryan et al. (2014);

[g] Schmidt (1975);

[h] McLean (1988);

[i] Kimbrough et al. (2001).

The pre-caldera phase activity probably built a stratovolcano, whose remnants are today exposed on the SE and NE parts of the caldera complex, and emplaced widespread ignimbrites, settled in submarine environment and interlayered with the Pliocene to middle Pleistocene sedimentary Formation of the Santa Rosalía basin (Table 4.2, Ortlieb and Colletta, 1984; Holt et al., 2000; Conly et al., 2005; García-Sánchez et al., 2019). The present-day observable E-W slightly elongated caldera depression, whose rim scarp reaches a height of 500 m a.s.l. in the S and NW sectors and less of 100 m a.s.l. in the NE sector, has formed during multiphase collapse, started with the Los Balcones ignimbrite eruption, and followed by at least two other caldera forming eruptions (La Reforma and Punta Arena ignimbrites). Interposed between the explosive eruptions are some lava flows, domes and scoriae cones partially filling the caldera or covering its external slopes (Cerro La Reforma and Mesa El Yaqui formations, García-Sánchez et al., 2019). Younger than most of La Reforma syn-caldera phase products is the Aguajito ignimbrite (Schmitt et al., 2006), erupted by neighbouring Sierra Aguajito volcanic centre (Garduño-Monroy et al., 1993).

During the post-caldera phase, several intra- and extra-caldera basaltic-andesitic and andesitic lava flows, domes, scoria cones and intrusive bodies (Cueva del Diablo formation) emplaced, together with a large alluvial fan (Arroyo Grande member, García-Sánchez et al., 2019). Worth of note inside La Reforma caldera complex is also the presence of several orders of Pleistocene wave-cut marine terraces, easily visible along the northern and eastern flanks, that testify a more than 100 m vertical tectonic uplift recently affecting the eastern coast of the Baja California peninsula (Demant and Ortlieb, 1981; Mayer and Vincent, 1999).

A

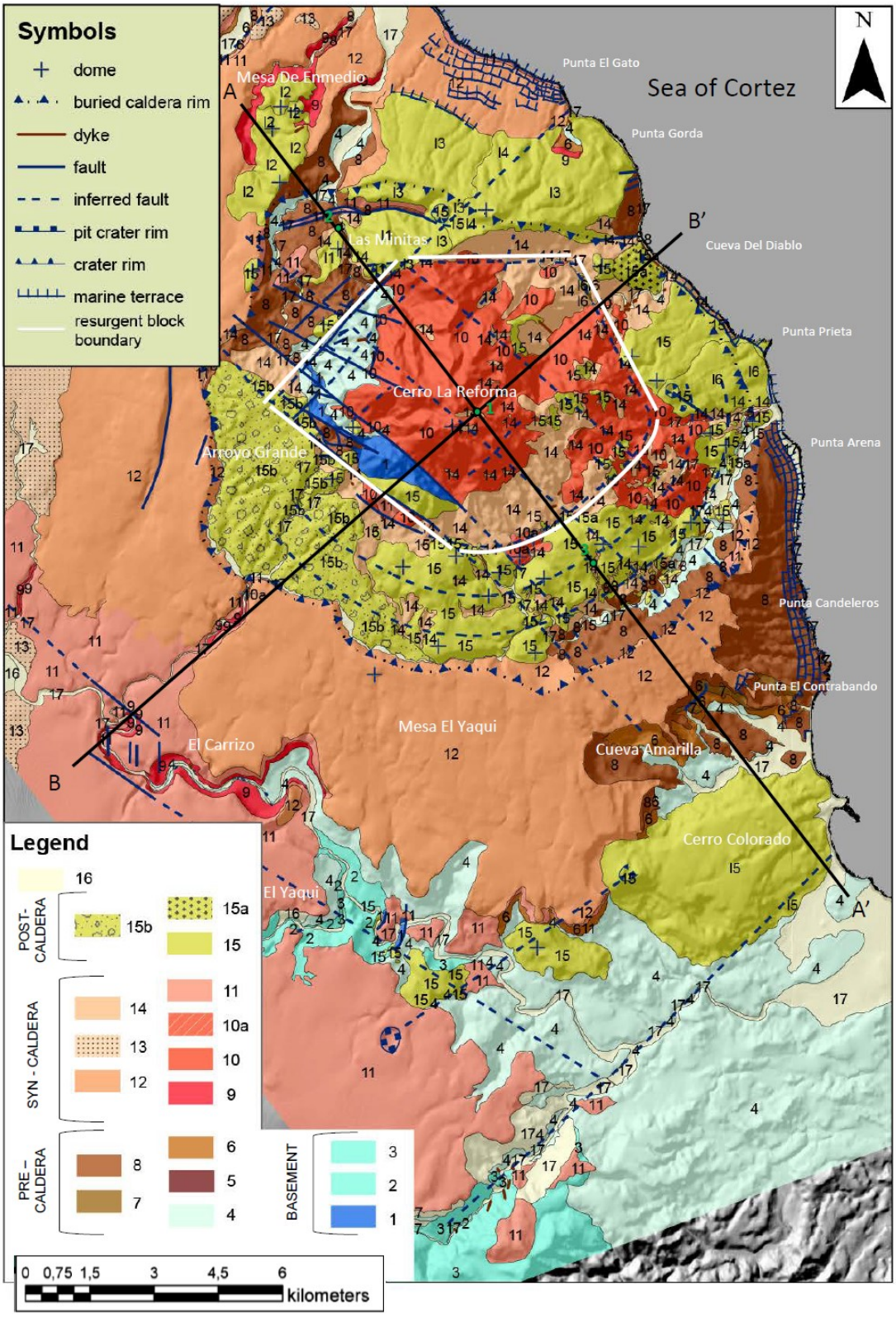
Symbols
dome
buried caldera rim
dyke
fault
inferred fault
pit crater rim
crater rim
marine terrace
resurgent block boundary
N
Sea of Cortez
Punta El Gato
Mesa De Enmedio
Punta Gorda
Las Minitas
Cueva Del Diablo
Punta Prieta
Cerro La Reforma
Arroyo Grande
Punta Arena
Punta Candeleros
Punta El Contrabando
Mesa El Yaqui
El Carrizo
Cueva Amarilla
Cerro Colorado
El Yaqui
A
A'
B
B'
Legend
POST-CALDERA
SYN - CALDERA
PRE – CALDERA
BASEMENT
16
15b
15a
15
14
13
12
11
10a
10
9
8
7
6
5
4
3
2
1
0 0,75 1,5 3 4,5 6
kilometers

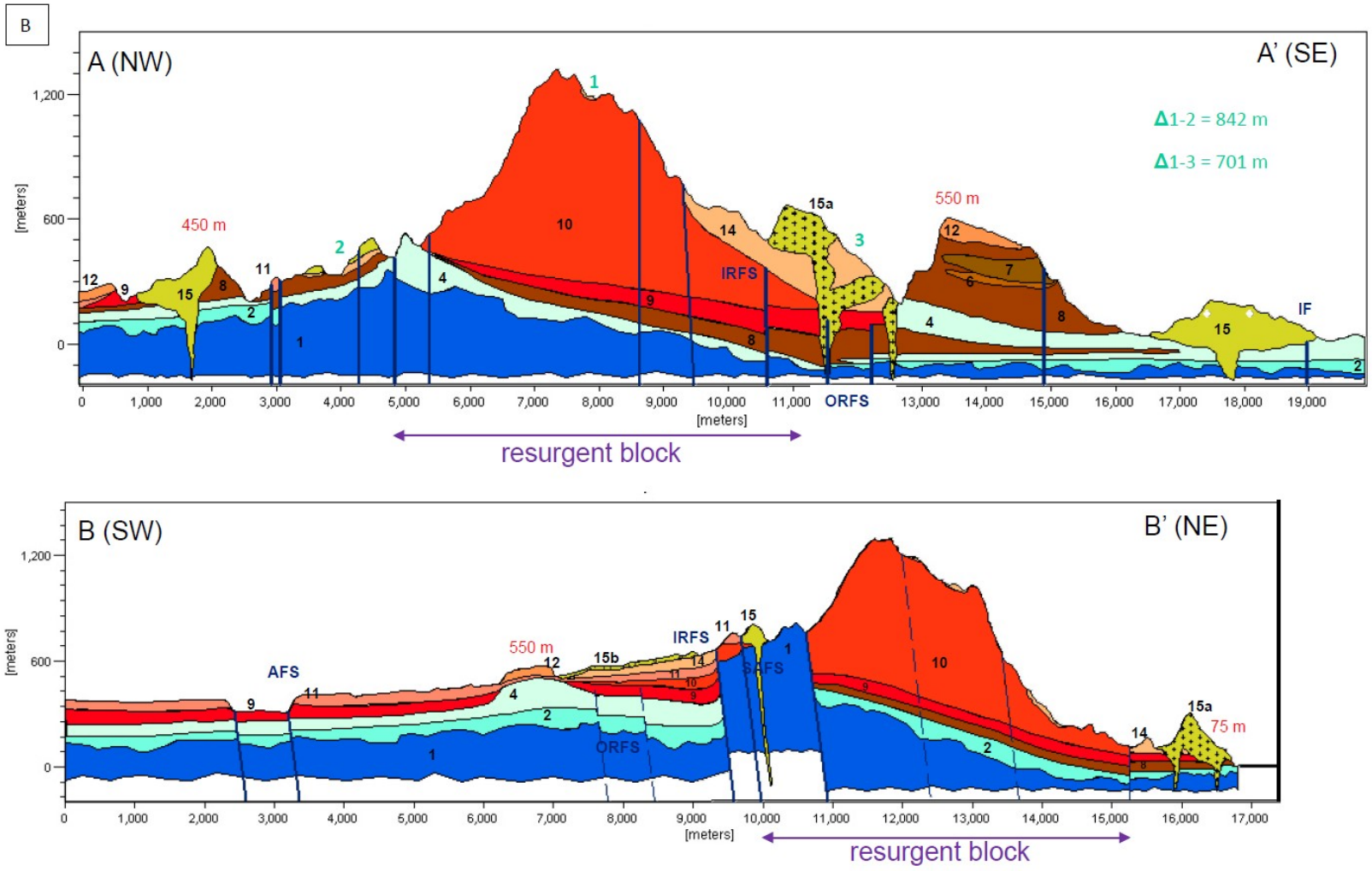

Figure 4.2 Geological map (a) of the study area (modified after García-Sanchez et al., 2019) and geological cross sections (b). Legend geology: provided in Table 4.1. Legend faults: IRFS: inner ring fault system; IF: Infierno fault; AFS: Azufre fault system; ORFS: outer ring fault systems; SAFS: Santa Ana fault system. Vertical exaggeration factor: 2,32. Points 1, 2 ad 3 in Figure 4.2A and cross section AA' indicate altitudes used to estimate caldera resurgence.

4.5 Survey area, data collection and methodology

The present study is based on a complete revision of La Reforma caldera complex geology and evolution performed by García-Sánchez et al. (2019) and summarized in a 1:50,000 scale geological map, that includes most of the structures discussed in the present paper. Structures were mapped at the 1:25,000 scale during several field surveys conducted between 2015 and 2017 over an approximate area of 500 km^2, inside the Santa Rosalía basin. The survey area is bounded by the Santa Ana bay to the north and the Infierno canyon to the south, and by the Sea of Cortez to the east. From N to S, the Mesa del Azufre plain, Tres Vírgenes volcanic complex and Carrizo and Yaqui canyons delimit the study area to the west (Fig. 4.1A). Faults, fractures, veins and mineralization represent the main structural elements measured in the field. Exact location, together with data regarding attitude (dip, inclination, dip direction, strike), kinematics and throw (where applicable), and filling (for fractures and veins) collected in the field were stored in an Ipad equipped with Igis and Lambert software ®. Due to bad preservation of striae, slickensides and other kinematic indicators on fault planes, faults kinematics was often deduced in the field based on visible offsets or in analogy with similarly oriented and dipping structures, analogously to what performed by Norini et al. (2006) in the Trans-Mexican volcanic belt. Collected data were uploaded into ArcGIS (10.2.1 for Desktop version, by ESRI Inc.), sorted by region of interest, plotted and interpreted with the aid of Stereonet software (2016 version, by R. W. Allmendiger). The reasons and criteria used to identify regions of interest are explained in the Results chapter.

4.6 Results

In this section, we present results of the structural study carried out within and around La Reforma caldera complex. Being La Reforma caldera complex located in a tectonically active area, it is often quite hard to distinguish between regional fault systems and volcano-tectonic structures related to caldera collapse and resurgence merely based on spatial orientation and cross-cut units. We therefore described the most meaningful and prominent structures encountered outside and inside the caldera depression, by selecting those sites where structural elements and morphologies are best exposed: the Azufre, Carrizo, Yaqui, southern Cimarron and Infierno canyons and the western external caldera slopes (Fig. 4.3); the Santa Ana bay, the gold and lead mine sites and the western and eastern intra-caldera sectors (Figs. 4.4A and 4.6). The analysis of dykes and intrusion patterns is also included in

order to investigate the interaction between regional and local stresses, as well as to infer magmatic pressure regimes linked to different evolution stages of La Reforma caldera complex.

4.6.1 Structures outside the caldera depression

4.6.1.1 The Azufre fault system

The more than 30 km long NW-SE (305-345°) striking Azufre fault system (AFS, Fig. 4.3) is the most significant structure running outside La Reforma caldera depression. It dissects the whole study area, from the Azufre to the Infierno canyons (García-Sánchez et al. 2019, Figs. 4.1A and 4.3) and marks the limit between Sierra Aguajito and Tres Vírgenes volcanic complexes. It represents a prominent transtensive fault system, whose right-lateral-normal kinematics was indicated in the field (plot *a* Fig. 4.3) by slickensides and other kinematic indicators and by the right-lateral displacement of the left-lateral (Garduño-Monroy et al., 1993) Cimarron fault system (CFS, Fig. 4.3). The AFS transtensive kinematics is also confirmed by previous studies (Portugal et al., 2000; Verma et al., 2006; Wong and Munguía, 2006; Barragán et al., 2010; Antayhua-Vera et al., 2015; Avellán et al., 2018). Most of the structural data related to the AFS were collected along the Azufre (plots *a* to *e* Fig. 4.3), Carrizo (plots *f* to *i* Fig. 4.3) and Yaqui canyons (plots *j* and *k* Fig. 4.3). Along the Azufre canyon are the best exposures of the AFS main fault zone (plot *a* Fig. 4.3). Here the nearly vertical (85° dip) AFS develops a negative flower structure (Fig. 4.3a), lowering the Aguajito ignimbrite down by about 20 m towards the NE. In several sites along the Azufre canyon decametric damage zone fault striae indicate a predominant dextral strike-slip component of motion (pitch 10°S) and vividly-coloured alteration phases permeating the Aguajito ignimbrite testify significant hydrothermal circulation. Associated with the main fault are a series of Riedel shears (antithetic and synthetic), including faults mainly striking NNW-SSE and ENE-WSW, and secondarily NE-SW and NW-SE (plot *b* Fig. 4.3). Right and left-lateral strike-slip faults trend NE-SW to NW-SE, with fault striae generally indicating a normal dip-slip component (plot *c* Fig. 4.3), and reverse (plot *d* Fig. 4.3)and normal (plot *e* Fig. 4.3) faults follow trends typical of the active stress field. Along the Carrizo canyon the AFS develops a less than 2 km wide rhomboidal-shaped pull-apart basin (Fig. 4.3), delimited by the AFS to the N and by a parallel structure marked by cataclastic bands to the S, whose geometry is a further confirmation of its right-lateral transtensive kinematics. At least four N-S trending faults internally dissect this basin. In the south-eastern parts of the Carrizo canyon, 20° to 55° inclined reverse faults strike ENE-WSW and ESE-WNW (plot *f* Fig. 4.3) and strike-slip and normal faults trend NW-SE to NE-SW (plot *h* Fig. 4.3), similarly as in the Azufre canyon. Reverse structures often develop drag-folds in the hanging wall

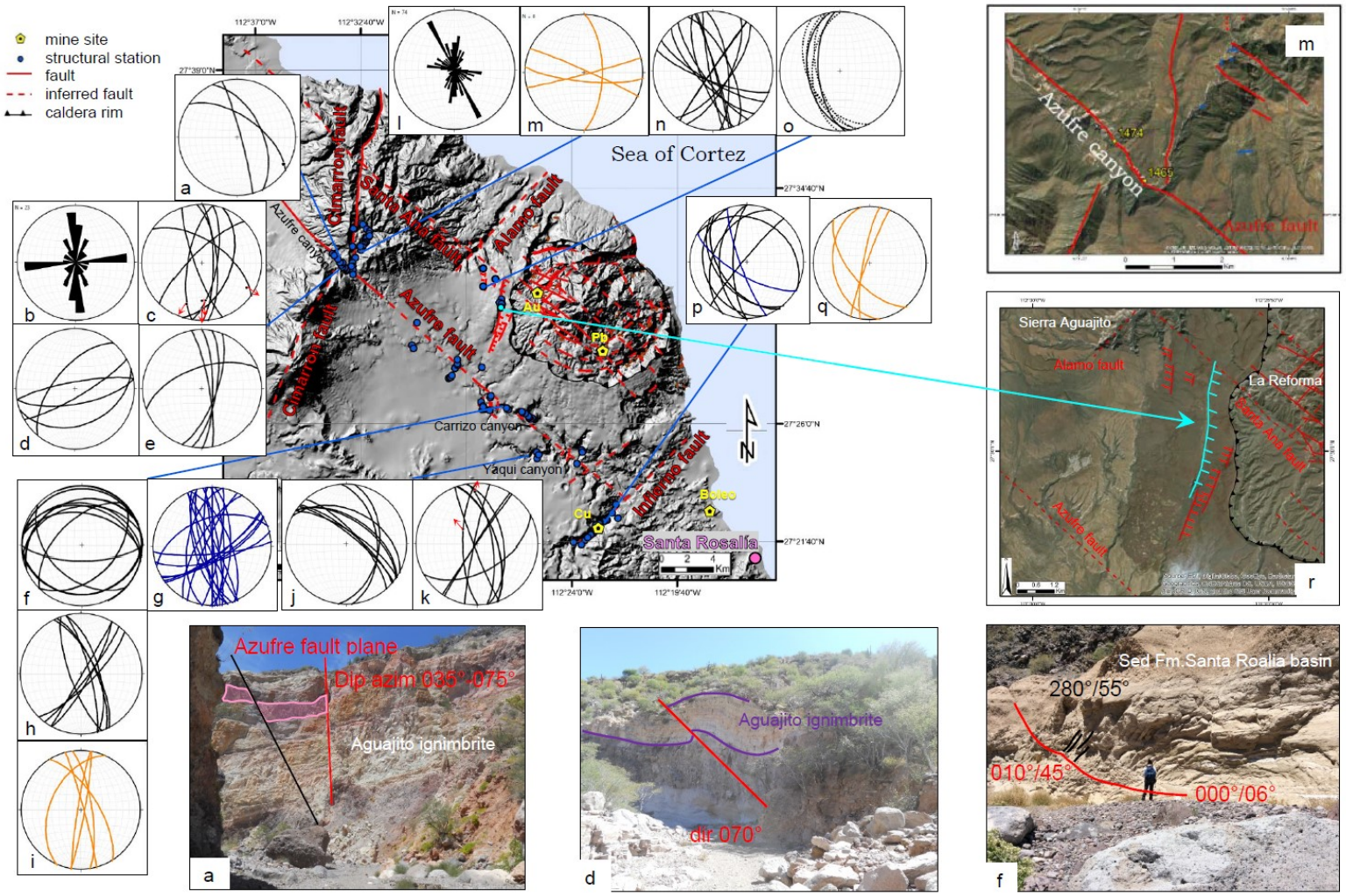

Figure 4.3 Structures outside the caldera depression (letters in pictures refer to corresponding plots). In all stereonets: faults in black, fractures in blue and veins in orange continuous lines. Stereonets illustrate: a) AFS main fault plane; b) unknown kinematics faults; c) strike-slip faults; d) reverse faults; e) normal faults; f) reverse faults; g) fractures; h) strike-slip and normal faults; i) veins; j) unknown kinematics faults; k) strike-slip and normal faults; l) unknown kinematics faults; m) veins; n) cataclasites; o) Mesa El Yaqui lavas (dashed) and scarp (continuous) attitudes; p) unknown kinematics faults and fractures; q) veins.

block or flat-and-ramp geometries and occasionally exhibit a secondary strike-slip component of motion (Fig. 4.3f) compatible with the AFS generalized right-lateral-normal kinematics, with throws generally of the same order of reverse faults along the Azufre canyon (1-2 m throw along dip, Fig. 4.3d). The general structural trends found in the Azufre and Carrizo canyons are also followed by normal and strike-slip (plot *k* Fig. 4.3) and minor faults (plot *j* Fig. 4.3) offsetting the Comondù Group deposits by few centimetres up to 3 m along the Yaqui canyon (Fig. 4.3). Contrarily to the Azufre canyon, in both the Yaqui and Carrizo canyons the AFS-related structures develop inside basement and pre-caldera units, only in few cases cutting through the overlying syn-caldera units (Los Balcones ignimbrite in the Carrizo canyon). Worth of note is the exposure of few slices of the *Laramide arc* crystalline Cretaceous plutonic rocks inside the AFS damage zone (Fig. 4.2A) just few hundred meters SE of the Yaqui canyon. They represent the highest outcrop of Cretaceous plutonic rocks in the study area not involved in resurgence processes. The shallow depth of Cretaceous crystalline basement inside the study area, and generally across the Baja California peninsula, results from slicing, segmentation and exhumation processes linked to the Gulf of California opening extensional and transtensional deformation phases (Ferrari et al. 2013; Ferrari et al., 2018).

4.6.1.2 The Cimarron south fault system

Due to the strict interplay and based on similarities observed in the field (E-W trending veins and fractures, plot *m* Fig. 4.3) between the CFS and the AFS in terms of structural patterns, we chose to include in our analysis the southern termination of the N-S trending CFS, the closest portion to the AFS (Fig. 4.3). All structures were measured in the N-S trending canyon crossing the Sierra Aguajito complex (Fig. 4.3) and within highly cataclased lavas lying below a substantially undeformed Aguajito ignimbrite. This suggests the lack of any important activity of this CFS segment in the last 1 Ma, as after all indicated by cross-cutting relationships with the AFS. Moreover, as NW-SE to NE-SW trending cataclastic bands (plot *n* Fig. 4.3) develop normal offset in lavas along the canyon walls, we argue that the CFS most likely is an oblique fault system with a predominant normal dip-slip component. In the light of this, we also suggest that the N-S trending CFS northern segment could represent a sidewall (or internal) structure of the pull-apart basin formed between the AFS and the Santa Ana faults system (SAFS), a parallel prominent feature running just few kilometres to the N (Fig. 4.3). This scenario is supported by Umhoefer et al. (1992), Garduño-Monroy et al. (1993) and Wong and Munguía (2006), who identified a N-S extensional zone (E-W direction of extension) responsible for the alignment of the Tres Vírgenes-Sierra Aguajito complexes, and resulting from dextral strike-slip movements along the AFS (*El Azufre fault*, Wong and Munguía, 2006) and a parallel major lineament running S of Tres Vírgenes (*La Virgen fault*, Wong and Munguía, 2006).

Nevertheless, the elevated morphologies built by following Sierra Aguajito volcanic complex (Garduño-Monroy et al., 1993) make hard to envisage a pull-apart basin.

4.6.1.3 The Infierno fault and copper mine site

Together with the NE-SW trending Alamo fault (AF) that runs between La Reforma and Sierra Aguajito complexes (Fig. 4.3), the parallel IF was firstly identified by Conly et al. (2005) as a sidewall fault of the Santa Rosalía transtensive basin. Structures included in the present study were measured along the IF decametric damage zone in the south-easternmost part of the Infierno canyon, SE from the inferred prolongation of the AFS (Figs. 4.2A and 4.3). Most of data relate to minor structures cross-cutting the Comondù Group, Santa Lucia formation and Sedimentary Formation of the Santa Rosalía basin pre-caldera phase units. Faults and fractures mostly strike NW-SE, with minor N-S and NE-SW trending sets (plot *p* Fig. 4.3). Of similar attitudes are veins (plot *q* Fig. 4.3). These geometries resemble those found in the Carrizo canyon along the AFS. Along the Infierno canyon is a copper mine site (Fig. 4.3), whose exploitation is to some degree still active today. Most of copper mineralization observed outside the mine restricted area consists of bright green-to-light blue copper sulphides associated to silica veins filling irregularly oriented fractures inside Santa Lucia formation intrusive bodies.

4.6.1.4 Western external caldera slope fault scarps

Along La Reforma western external caldera slope a set of up to 4 km long N-S to NNE-SSW trending fault scarps offsetting the Mesa El Yaqui formation lavas (Figs. 4.2A and 4.3) represents the only site where slip rate was qualitatively estimated (Fig. 4.3r). In the westernmost part of the slope, close to the SAFS, rather short and steeply inclined (45°-60°) scarps trend N-S and dip towards the west (plot *o* Fig. 4.3). Dipping towards the west are also few other NNE-SSW trending scarps further SE, close to the caldera rim (Fig. 4.3). On the opposite, two longer (up to 4 km) scarps located in the middle dip towards the east and trend NNE-SSW (010° dip azimuth, Fig 4.3r). The Mesa El Yaqui formation lava flows (dashed lines in plot *o*, Fig. 4.3) entirely cover and therefore post-date the westernmost scarps (black lines in plot *o*, Fig. 4.3), while on the contrary, these lavas pre-date the development of the longest NNE-SSW trending scarp (light blue dot in Fig. 4.3 and Fig 4.3r). In this site (Fig. 4.3r) they are in fact vertically offset by about 80 m into a graben-type structure formed eastward from the scarp (Fig. 4.3r). Although not directly observed in the field, the kinematics of this fault is most likely normal if considering its geometry and attitude with respect to the stress regime acting over the last few million years. Based on the Mesa El Yaqui formation age of emplacement (Table 4.2, García-Sánchez et al., 2019) and the vertical displacement observed in the field, an approximate normal slip

rate has been calculated, between 0.049 and 0.111 mm/yr. In the absence of any volcanic product younger than the Mesa El Yaqui formation in proximity of this structure, the calculated slip rates must be regarded as a conservative estimate.

4.6.2 Structures inside and cross-cutting the caldera depression

4.6.2.1 The Santa Ana fault system

The NW-SE trending prominent Santa Ana fault system (SAFS) is the only structure cross-cutting from side to side the caldera depression and dissecting both Sierra Aguajito and La Reforma complexes. It runs parallel and northward to the AFS, from the Santa Ana bay up to the Infierno canyon (Figs. 4.1A and 4.4A). Nevertheless, overall SAFS strike-slip and dip-slip offsets could not be properly quantified in the field. Despite most of the SAFS-related structures were measured inside the caldera depression, the SAFS best exposure was encountered outside La Reforma caldera complex, within the Sedimentary Formation of the Santa Rosalía basin sediments in the Santa Ana bay region (plots *b* to *d* Fig. 4.4A). As this site lacks a well-defined damage zone with striae, slickensides and other kinematic indicators, the SAFS transtensive kinematics was mostly deduced based on attitude, orientation and spatial extent analogies with the AFS. The right-lateral-normal kinematics inferred for the SAFS is also supported by the normal-dextral slipping sense of blocks along the NW-SE (305°-340°) trending steeply inclined and NE dipping Santa Ana fault plane (plot *b* Fig. 4.4A) in the Santa Ana bay region, and by few centimetres wide local rhomboidal patterns formed by fractures or gypsum veins (plot *c* and *d* Fig. 4.4A) in the same location. These gypsum and secondarily silica veins cross-cut Quaternary marine sediments or lavas pre-dating the Aguajto ignimbrite and their patterns at times resemble the ones found along the AFS.

Inside La Reforma caldera (plots *e* to *q* Fig. 4.4A), the SAFS hosts two mine sites, a lead mine on the SE and gold mine in the NW (Figs. 4.3 and 4.4A), the first set into Cerro La Reforma formation domes and the second into the Sedimentary Formation of the Santa Rosalía basin sediments. The overall orientation of silica veins and fractures proceeding from the gold mine to the largest intra-caldera exposure of Cretaceous basement is (Fig. 4.2A) is illustrated in plots *e*, *f*, *h*, *i, j* and *m*. Predominantly ENE-WSW oriented reverse faults (plot *g* Fig. 4.4A) cross-cut Quaternary marine sediments close to the largest intra-caldera exposure of Cretaceous basement (Fig. 4.2A), that appears pervasively cross-cut by several sets of fractures (plot *k* Fig. 4.4A). The contact between Cretaceous crystalline rocks and La Reforma volcanic younger units is indeed marked by the SAFS. Close and within the lead mine, in the SSE sector of the caldera depression, veins (plot *p* Fig. 4.4A) and fractures (plot *q* Fig.

4.4A) developed inside the Cerro La Reforma formation lava domes (image p in Fig. 4.4A) follow the SAFS trends or N-S oriented mapped structures.

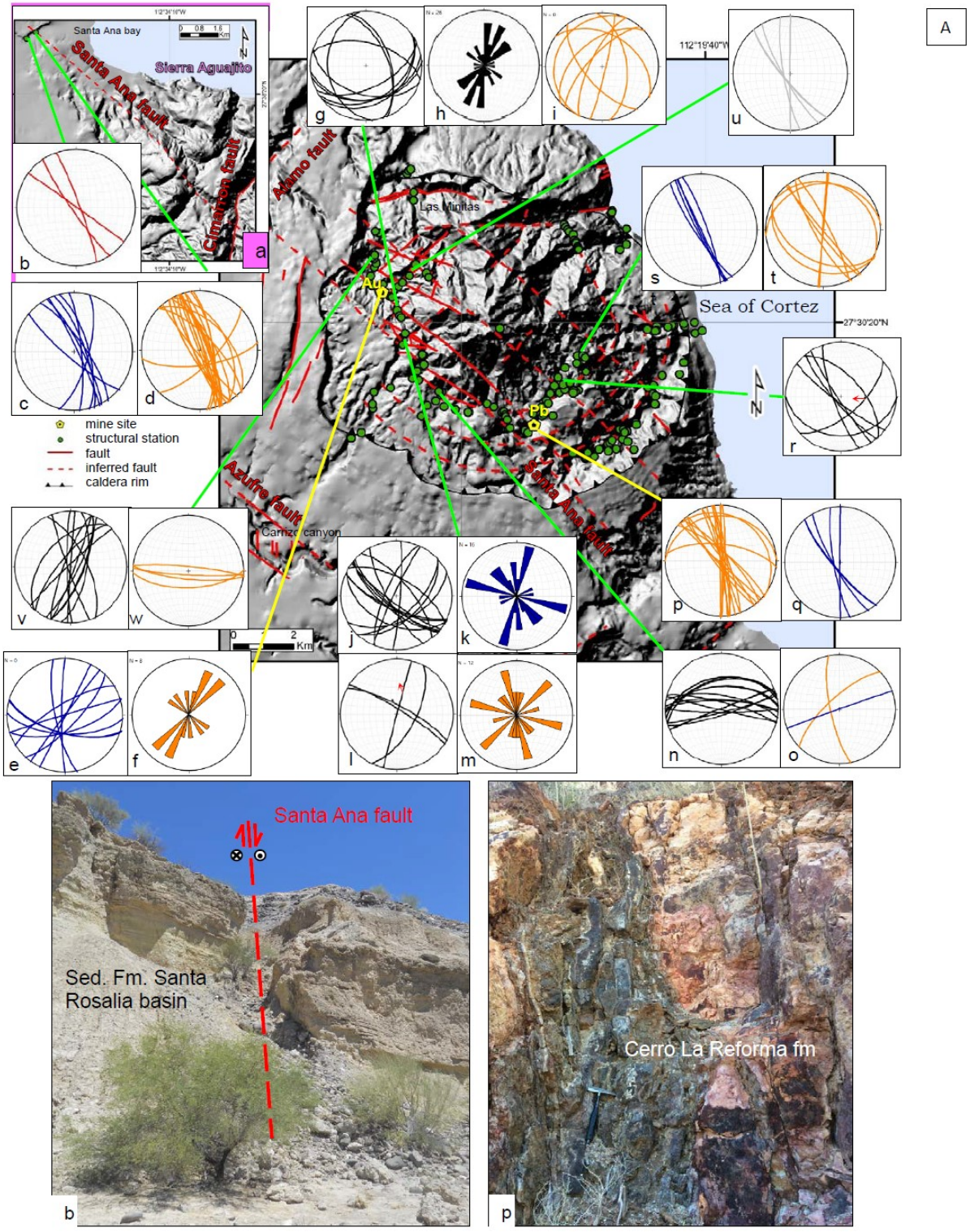

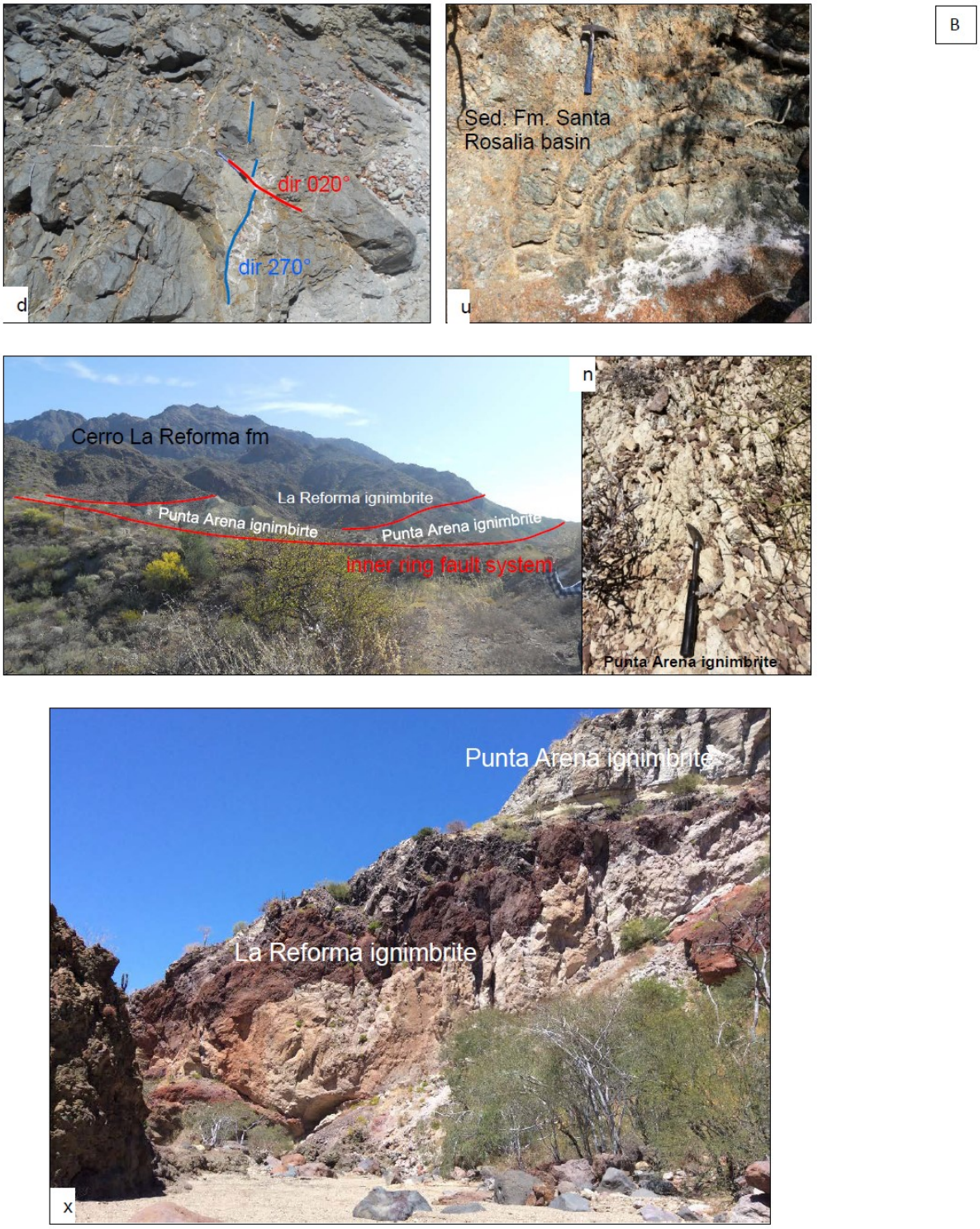

Figure 4.4 Intra-caldera structures: the Santa Ana fault system, ring faults and structures in the western sector (letters in pictures refer to corresponding plots). In all stereonets: faults in black, fractures in blue and veins in orange continuous lines. The Santa Ana main fault plane (b) is marked in red, while fold axial planes (u) in grey. Stereonets illustrate: a) location of the Santa Ana bay; c) fractures; d) veins; e) fractures; f) veins; g) reverse faults; h) unknown kinematics faults; i) veins; j) unknown kinematics faults and cataclasites; k) fractures; l) normal faults; m) veins; n) shear planes and cataclasites; o) fractures and veins; p) veins; q) fractures; r) faults and cataclasites; s) fractures; t) veins; v) unknown kinematics faults and cataclasites; w) veins.

4.6.2.2 Ring faults and structures in the western sector

Just few hundred meters S from the SAFS damage zone, approximately half-way between the gold and lead mines, is the innermost of the three inferred ring fault systems (Fig. 4.2A), mapped following a wide cataclastic horizon cross-cutting the Punta Arena ignimbrite and linking all observed lag breccia deposits (Fig. 4.5a). Close to the SAFS this ring fault system dips towards the ENE (035°), suggesting a local inward dipping geometry. In proximity of the westernmost site of lag breccia occurrence, resurgence-related reverse structures are abundant (plots *n* and *o* in Fig. 4.4A and image n of Fig. 4.4B). One of the most significant is the NW-SE oriented fault stacking the La Reforma ignimbrite on top of the younger Punta Arena ignimbrite (image n of Fig. 4.4B) and running in between the SAFS and the inner ring fault system. In the footwall of this structure, reverse throws are accommodated by E-W to ENE-WSW trending steep to vertical N-dipping small reverse shear planes cross-cutting the Punta Arena ignimbrite (plot *n* Fig. 4.4A and image n in Fig. 4.4B) and indicating a post-caldera resurgence pulse. Fractures and veins in this site (plot *o* in Fig. 4.4A) trend N-S to NE-SW. Proceeding NE from the lead mine site, along the inferred prolongation of the inner ring fault system (Figs. 4.4a and 4.5a), The Cueva Del Diablo formation lava flows and domes are cross-cut by predominantly NW-SE oriented faults and cataclastic bands (plot *r* Fig. 4.4A), and minorly by NE-SW and E-W oriented sets. In the same direction, the Punta Arena ignimbrite significantly increase its thickness, from about 50 m in the western sector to more than 200 m in the NE and SE sectors (geological cross section AA' in Fig. 4.2B), where it fills a palaeo-caldera depression. This, together with the remarkably different elevation of caldera floor on different sides (geological cross section BB' in Fig. 4.2B), led to suggest a trap-door geometry of the collapse, with a hinge located in the more elevated western sector (550 m, geological cross section BB' in Fig. 4.2B). Furthermore, along the inner ring fault system the Punta Arena ignimbrite overlying the Cerro La Reforma formation is uniformly and predominantly dipping up to 25° towards the SE (Fig. 4.5d), and permeated by greenish alteration facies (Fig. 4.5a and 4.5c), indicating post-emplacement tilting and hydrothermal circulation processes. Towards the NE termination of the mapped inner ring fault system, all fractures inside the Cerro La Reforma formation lava flows and overlying Punta Arena ignimbrite trend NW-SE (plot *s* Fig. 4.4A), while veins are oriented NW-SE, N-S and E-W to WNW-ESE (plot *t* Fig. 4.4A), probably in response to the structural control exerted by the several NW-SE oriented faults paralleling the SAFS to the N.

The western intra-caldera sector is by far the most complicated under the structural point of view, as here resurgence processes focus and interact with pervasive deformation linked to the SAFS. In detail, two sites N of the gold mine revealed interesting resurgence-related structures. The first site is a NE-SW trending fault running through the Sedimentary Formation of the Santa Rosalía basin sediments

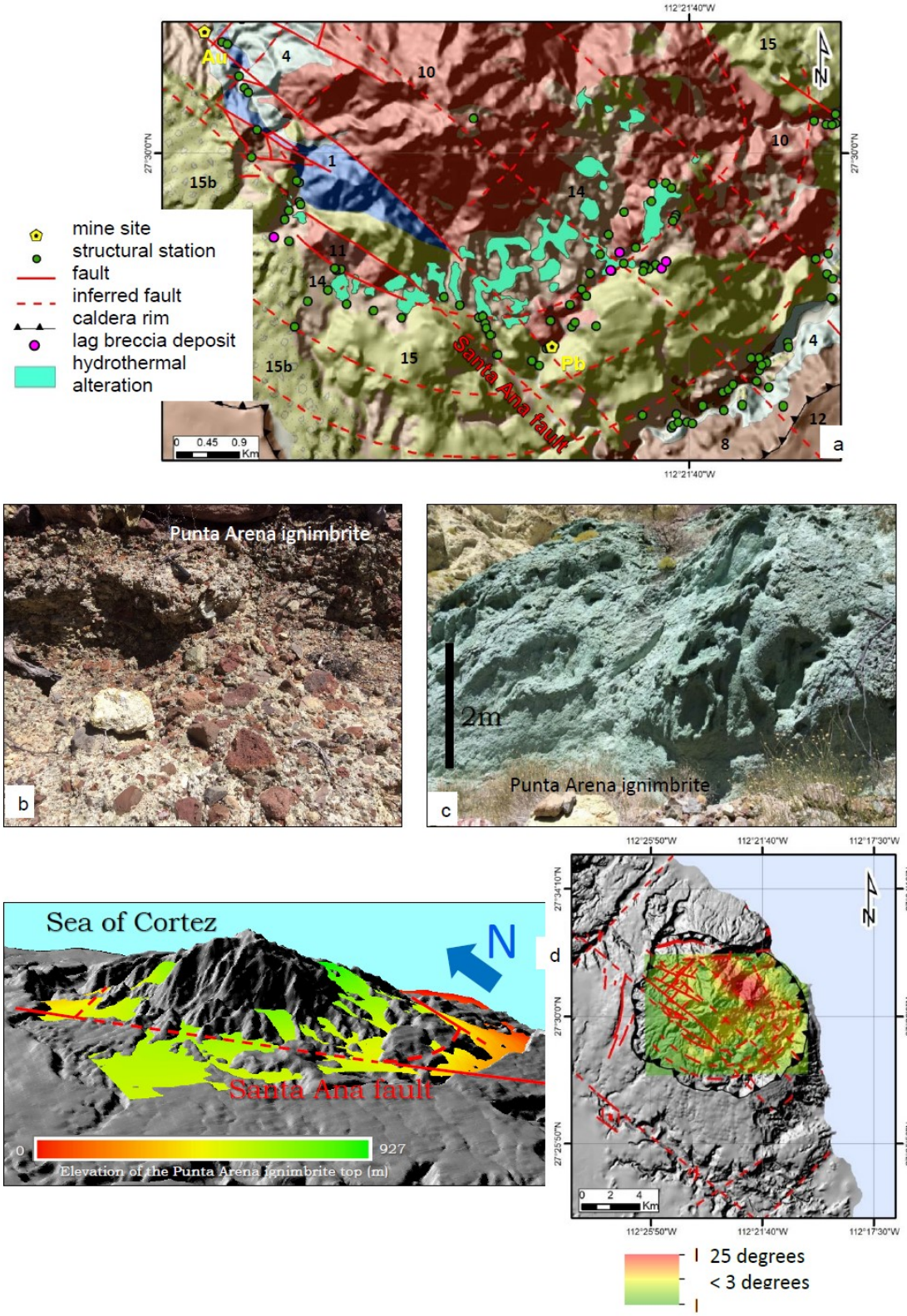

Figure 4.5 Location of lag breccia deposits (b) and hydrothermal alteration (c) along the inner ring fault systems (a). View of the SE-tilting of the top of the Punta Arena ignimbrite with main structures delimiting the central resurgent block and slope of the interpolated surface (d). Geology legend in Table 4.1.

from the gold mine up to few kilometres towards the NE (Fig. 4.4A). Along this structure, approximately in the middle and on the eastern side, Quaternary marly sediments are perturbed by a series of folds (plot *u* Fig. 4.4A and image u of Fig. 4.4B), whose axial surfaces trend ENE-WSW to E-W and dip towards the N-NW. No reverse faults are associated to these folds, contrarily to structures displayed in Fig. 4.3d, hence suggesting formation mechanisms other than thrusting, that we propose being resurgence processes. The resurgence-related nature of these folds is supported by the evidence that folds developed inside an uplifted and eroded sequence (geological cross section AA' in Fig. 4.2B) and along the most upraised block of the NE-SW oriented fault. This site is not far from where resurgence-related structures were recognised in proximity of Cretaceous plutonic rocks. We suggest the Sedimentary Formation of the Santa Rosalía basin was pinched-in, folded and straightened-up during the approximately 700 to 840 m uplift of the central resurgent block, calculated based on the Punta Arena ignimbrite elevation inside and outside the resurgence area (points 1, 2 and 3 geological cross section AA', Fig. 4.2B). Furthermore, we argue that the NE-SW trending structure along which folds developed could delimit the resurgent block towards the NW. Further information on structures crossing pre-caldera submarine lavas in this first site are illustrated in plots *v* and *w* in Fig. 4.4A. The second site displaying resurgence-related structures lies close to the caldera rim in Las Minitas region (Fig. 4.4A). Here a syn-caldera resurgence pulse is indicated by a strongly folded and straightened La Reforma ignimbrite topped by a relatively flat and undisturbed Punta Arena ignimbrite (image x of Fig. 4.4B).

4.6.2.3 Structures in the eastern sector

Most of structures measured in the outer parts of the caldera depression lie in the eastern sector and relate to the outermost inferred ring fault system (Fig. 4.6). This ring fault system is never well exposed and was traced based on the semi-circular alignment of the post-caldera Cueva Del Diablo formation domes and intrusions (Fig. 4.2A). Several structures cross-cut pre- and post-caldera units along the semi-circular canyon that parallels the south-eastern rim scarp and is dissected by the SAFS and related structures. In few cases, NW-SE trending fracture sets post-date CDDF intrusions, as in the south-western side of the canyon (plot *b* in Fig. 4.6). In other cases structures seems to guide intrusion patterns. Overall, the general trends of faults, cataclastic bands and fractures is NNW-SSE to NNE-SSW in pre-caldera submarine lavas and in Sedimentary Formation of the Santa Rosalía interlayered deposits close to the SAFS (plot *a* Fig. 4.6 and Fig. 4.2A), while NW-SE and NE-SW further NE along the canyon, inside pre-caldera submarine lavas (plots *c* and d in Fig. 4.6). This could indicate a prevalence of caldera collapse structures towards the NE, otherwise masked by the SAFS influence, in accordance with the fact that these structures only cross-cut pre-caldera rocks. Another site crossing

the outer ring fault system is the ENE-WSW trending canyon that reaches the sea less than 1.5 km S of Punta Prieta (Fig. 4.2A).

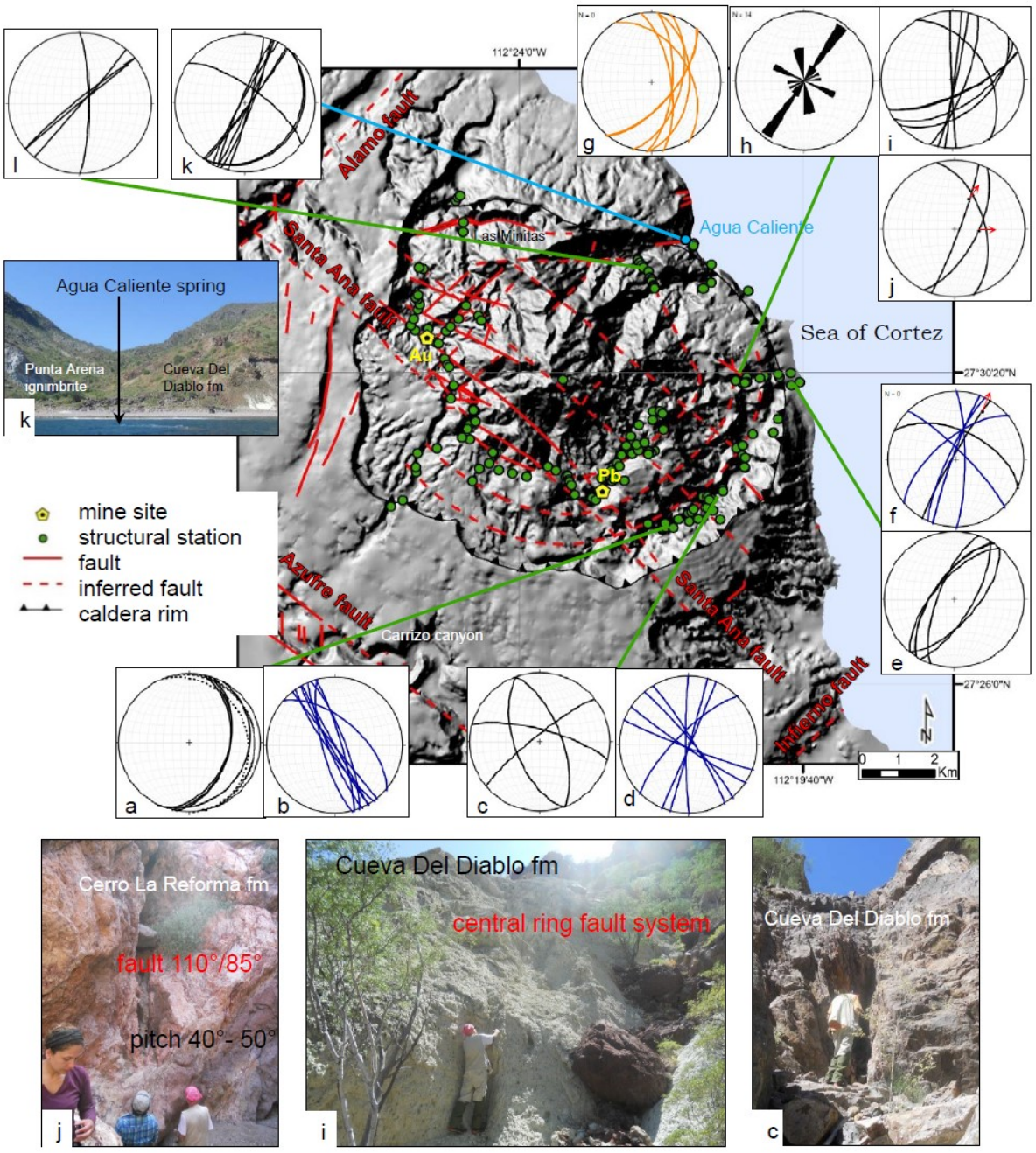

Figure 4.6 Intra-caldera structures: outer structures in the eastern sector (letters in pictures refer to corresponding plots). In all stereonets: faults in black, fractures in blue and veins in orange continuous lines. Stereonets illustrate: a) unknown kinematics faults (continuous) and cataclasites (dashed); b) fractures; c) unknown kinematics faults; d) fractures; e) unknown kinematics faults; f) normal faults and fractures; g) veins; h) cataclasites; i) unknown kinematics faults; j) strike-slip faults; k) cataclasites and normal faults; l) unknown kinematics faults.

Here, close to the caldera rim, NE-SW trending faults (plot *e* in Fig. 4.6) dissect the Punta Arena ignimbrite topped by post-caldera lava flows and domes. In the same site, normal faults and fractures predominantly trend NE-SW, with minor N-S and NW-SE oriented sets (plot f in Fig. 4.6). Further westward inside the canyon, a third ring fault structure was mapped between the inner and the outer ring faults systems, based on a decametric cataclastic damage zone dissecting both the Punta Arena ignimbrite and Cerro La Reforma lava flows. The general N-S to NNE-SSW trend of this central ring fault systems is indicated by the prevalent orientation of faults (plot *i* in Fig. 4.6) and cataclasites (plot *h* in Fig. 4.6), despite minor NW-SE and ENE-WSW trending sets are also present. NNE-SSW to NNW-SSE trending transtensive faults (plot *j* in Fig. 4.6), are also present inside the central ring fault system damage zone (Fig. 4.6j), together with silica veins (plot *g* in Fig. 4.6) occasionally exhibiting pervasive hydrothermal alteration (Fig. 4.6i).

In the northern-most part of the eastern sector, just offshore the caldera rim, is the Agua Caliente hot (50°C) water spring (Fig. 4.6k), set along the prolongation of an ENE-WSW to NE-SW oriented structure that reaches the sea close to the Cueva del Diablo cove (Fig. 4.2A), as indicated by cataclastic bands and normal faults cross-cutting the Punta Arena ignimbrite close to the shoreline (plot *k* in Fig. 4.6). To the W, the Agua Caliente structure intersects a NW-SE trending valley, set along a structure where a series of post-caldera aligned intrusions (Fig. 4.2A) are dissected by faults mainly trending NE-SW and minorly N-S (plot *l* in Fig. 4.6). Here, the SE-tilting of the top of the Punta Arena ignimbrite and the NE-dipping scarp suggest that this NW-SE oriented structure marks the north-eastern limit of the resurgent block.

4.6.3 Misoriented fracture and vein sets along regional structures

A series of fractures and veins displaying rather misoriented trends with respect to the stress field acting over the last few million years have been measured along the most prominent regional faults mapped in this study. These include: a) ENE-WSW trending fractures and veins in the Carrizo canyon (plots *g* and *i* Fig. 4.3 respectively) along the AFS; b) E-W trending veins and fractures (plot *m* Fig. 4.3) along the CFS southern segment, occasionally offset by N-S trending structures; c) ENE-WSW, WNW-ESE to E-W trending veins, also occasionally offset by N-S trending veins (Fig. 4.4d), along the SAFS in the Santa Ana bay region; d) ENE-WSW oriented fractures (plot *e* Fig. 4.4A) along the AFS, south from the golf mine; e) ENE-WSW to WNW-ESE trending fractures cross-cutting the Cretaceous plutonic rocks (plot *l* Fig. 4.4A) along the SAFS. Apart from e), whose trends could also represent pre-Oligocene deformation phases recorded in the Cretaceous basement (beyond the scope of this study), the persistent occurrence of these misoriented sets of fractures and veins along the regional lineaments reinforces the idea of a common tectonic style for these structures. Since these were

measured along regional structures that cross-cut the succession up to the Aguajito ignimbrite (AFS), it is not reasonable to suggest they are older structures developed under a different stress regime, as this would imply an implausible 90° clockwise stress rotation over the last 1 million year (Aguajito ignimbrite 1.17 Ma, Schmitt et al., 2006). Furthermore, caution should be used when interpreting cross-cutting relationships between these misoriented sets and N-S trending structures, as the first are far than frequent across the study area and certainly of minor importance both in terms of magnitude and throws with respect to the N-S, NNE-SSW and NNW-SSE structural trends. Instead, local stress perturbation or high-pressure conditions occurring during the emplacement of hydrothermal fluids along regional faults appear more plausible mechanisms. As analysis of focal mechanisms (Wong and Munguía, 2006) along the AFS in Azufre canyon does not show any evidence of seismicity-induced local stress perturbations, the chance of having pressurized fluids emplaced along regional structures appears more likely.

4.6.4 Dykes and intrusions

4.6.4.1 Dykes outside the caldera depression

Among intrusive bodies mapped outside the caldera depression (Fig. 4.7A), dykes in the southern termination of the CFS northern segment, close to the AFS (Fig. 4.7A-a), follow the NNE-SSW trend defining the alignment of the Tres Vírgenes eruptive centres (plot *b* in Fig. 4.7A), with minor sets paralleling the AFS or trending E-W. All these dykes intruded debris flow sequences postdating the Aguajito ignimbrite emplacement. Being dykes geological bodies whose emplacement is governed by tension forces, the minor E-W trending set of dykes mapped along the CFS could have emplaced in response to processes similar to those responsible for the misorientation of fractures and veins along major regional faults, illustrated in the above paragraph. Along the AFS and under its tectonic control are NNE-SSW and NNW-SSE oriented post-caldera dykes intruding the Sedimentary Formation of the Santa Rosalía basin and the Los Balcones ignimbrite across the Carrizo canyon, not far from the mapped pull-apart basin (plot *f* Fig. 4.7A). Pre-caldera submarine dykes intruded along the eastern coast cross-cut pre-caldera ignimbrites (Fig. 4.7A-h) and are probably linked to the volcanic edifice pre-dating La Reforma caldera formation, whose characteristics and areal extent are not well known. The ENE-WSW and NW-SE trending intrusions could represent dykes emplaced radially to the locally N-S to NNE-SSW oriented pre-caldera stratovolcano remaining flank (Fig. 4.2A), while the N-S to NNE-SSW sets probably followed regional trends (plot *h* in Fig. 4.7A). Belonging to the Santa Lucia formation are the NW-SE to NE-SW trending highly fractured dykes (Fig. 4.7B-i) intruding the Comondù Group along the Infierno canyon (plot *i* in Fig. 4.7A).

4.6.4.2 Dykes in the eastern and western intra-caldera sectors

The eastern intra-caldera sector is by far the region where intrusive bodies are most abundant (plots *k* to *o* in Fig. 4.7A-j). It is indeed the alignment of post-caldera bodies intruding the Punta Arena ignimbrite and pre-caldera submarine deposits to mark the outer ring fault system (Fig. 4.7A-j). In this site, NW-SE oriented dykes could either be radial to the caldera rim scarp or following the SAFS and parallel faults (plot *n* Fig. 4.7A), while minor cone-sheets trend NE-SW (image n of Fig. 4.7B). Further N, in proximity of the inner ring fault system, post-caldera dykes intruding the Punta Arena ignimbrite exhibit similar trends (plot *m* in Fig. 4.7A and image m of Fig. 4.7B). Across the E-W oriented canyon cross-cutting all three ring fault systems, the Cueva Del Diablo formation intrusions include N-S to NNE-SSW oriented cone-sheets and ring-dykes and ENE-WSW trending radial dykes (plot *o* in Fig. 4.7A and image o of Fig. 4.7B). Around the Cueva del Diablo cove (Fig. 4.2A), in the NE sector, NW-SE oriented post-caldera cone-sheets intrude the pre-caldera submarine deposits alongshore (plot *l* in Fig. 4.7A). Further inland, radial NE-SW to N-S trending Cueva Del Diablo formation dykes predominate. As previously introduced, post-caldera bodies intruding the Punta Arena ignimbrite emplace along the NW-SE oriented structure intersecting the Agua Caliente canyon and defining the north-eastern boundary of the resurgent block (plot *k* in Fig. 4.7A).

In the northern part of the western intra-caldera sector, predominantly NNE-SSW trending post-caldera cone-sheet dykes cross-cut pre-caldera submarine lava flows and the Punta Arena ignimbrite (plot *d* in Fig. 4.7A). NE-SW to E-W oriented Cueva Del Diablo formation dykes intruding the uplifted and eroded Quaternary marine sediments and Cretaceous plutonic rocks close to the gold mine (plot *e* in Fig. 4.7A) probably follow the variably oriented identified fault patterns. Lastly, in proximity of the inner ring fault system, NNW-SSE oriented post-caldera dykes display a ring-dyke geometry (plot *g* in Fig. 4.7A).

A

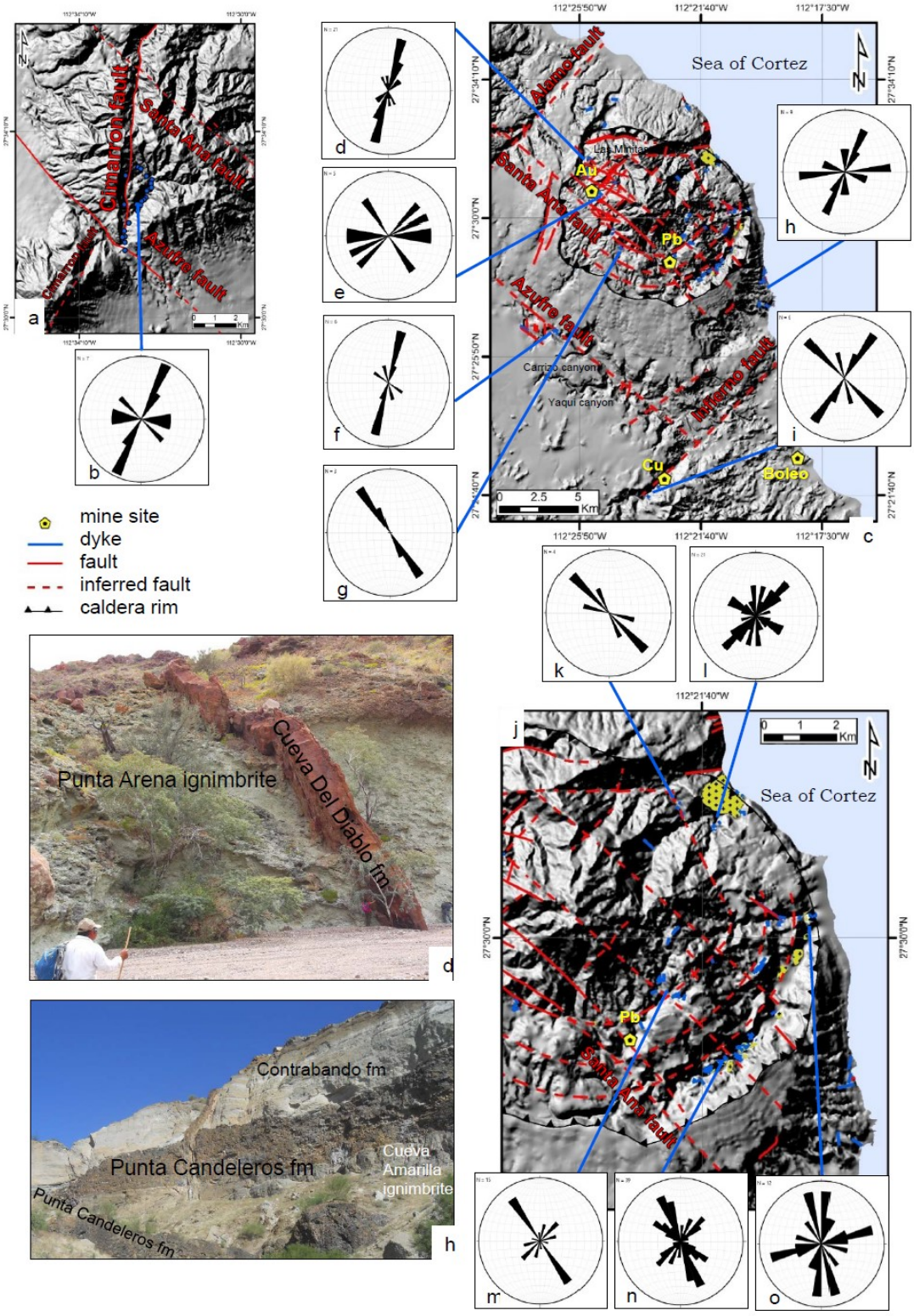
Cimarron fault
Santa Ana fault
Azufre fault
Cimarron fault
a
b
mine site
dyke
fault
inferred fault
caldera rim
d
e
f
g
Sea of Cortez
Alamo fault
Santa Ana fault
Au
Pb
Azufre fault
Carrizo canyon
Yaqui canyon
Inferno fault
Cu
Boleo
Las Minitas
h
i
c
k
l
Punta Arena ignimbrite
Cueva Del Diablo fm
d
Contrabando fm
Punta Candeleros fm
Cueva Amarilla ignimbrite
Punta Candeleros fm
h
j
Sea of Cortez
Pb
Santa Ana fault
m
n
o

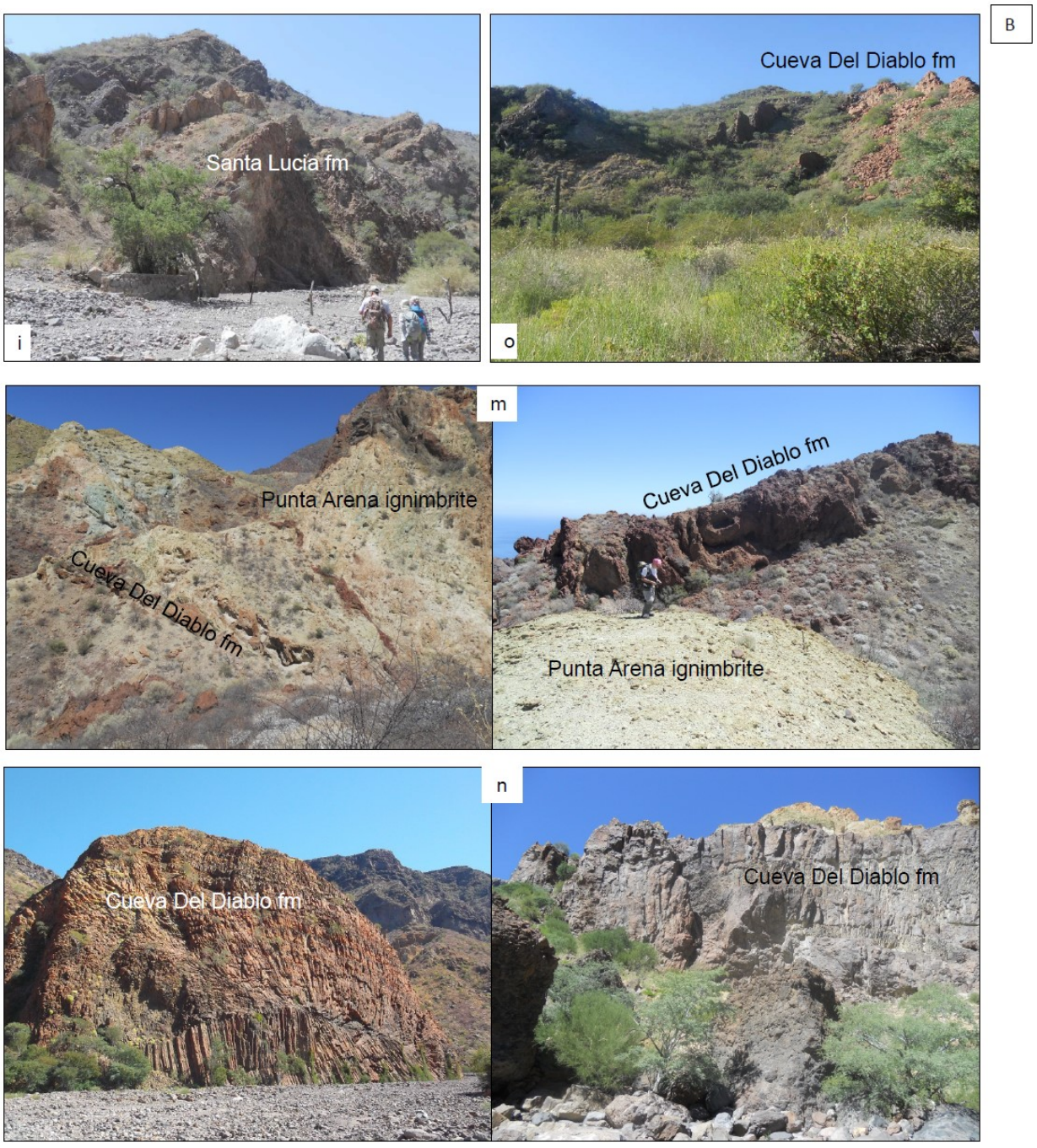

Figure 4.7 Dykes and intrusions (letters in pictures refer to corresponding plots). Dykes in the stereonets are: b) dykes of unknown age along the Cimarron fault system (a); Cueva Del Diablo fm dykes (d, e, f, g, j, k, l, m, n, o) intruded outside and inside the caldera depression (c and j); Punta Candeleros fm dykes (h) and Santa Lucia fm dykes (i).

4.7 Discussions

4.7.1 Regional structures and magmatism

Under the structural point of view, the study area is a jigsaw of blocks bounded by a network of strictly interfering and often hardly discernible regional and volcano-tectonic lineaments, leading Schmidt (1975) to state that La Reforma complex does not look like a caldera but as a system of tectonic blocks. This composite scenario derives from recent stress reorganization and consequent reactivation in a transtensive regime of major features inherited from the Gulf of California Miocene orthogonal extension phase, where volcanic structures of La Reforma-Sierra Aguajito-Tres Vírgenes Pliocene-to-Holocene magmatism established. The most prominent features mapped inside the study area are the regional AFS and SAFS, both NW-SE oriented dextral normal structures that entirely dissect the study area. The AFS runs outside La Reforma caldera depression, and lacks perturbations caused by the superimposition of volcanic structures that instead characterize the SAFS. It locally develops transtensive features, like pull-apart basins and negative flower structures, and offsets the CFS and the volcanic sequence up to the Aguajito ignimbrite (1.17 Ma, Schmitt et al., 2006, Fig. 4.3a). It is the closest structure to the Las Tres Vírgenes geothermal field and it is site of important hydrothermal circulation. The SAFS runs parallel to the AFS just few kilometres to the N, entirely cross-cuts Sierra Aguajito and La Reforma caldera depression and interferes with reverse structures related to caldera resurgence. It is site of important intra-caldera mineralization (gold and lead mines) and like the AFS it is a gulf-inherited structure that contributed to the slicing and exhumation of the Cretaceous *Laramide arc* pltonic rocks, now exposed along both the AFS and SAFS, inside and outside the caldera depression (Fig. 4.2A). Studies performed by Axen et al. (2000) and Mark et al. (2012) argued that Cretaceous basement was already exhumed by Eocene, at least in the eastern Baja California peninsula. Further uplift occurred during an Oligocene-Miocene extensional pulse (Duque-Trujillo et al., 2015; Balestrieri et al., 2017), as indicated by 25-17 Ma exhumation ages found near Loreto (Fig. 4.1A). Cretaceous plutonic rocks are currently around 1 km deep (TVD) in geothermal wells or 200 m below ground level throughout the Las Tres Vírgenes geothermal field (López H.A. et al., 1995). The N-S to NNE-SSW trending CFS is another regional feature marking the alignment of the Tres Vírgenes and Sierra Aguajito eruptive centres and running few kilometres west of La Reforma caldera depression. Further identified regional structures of minor extent are the NE-SW oriented AF and IF bordering the Santa Rosalía transtensive basin (Conly et al., 2005), the fault scarps located on the caldera western external slope, as well as a dense network of predominantly N-S, NE-SW and NW-SE minor faults of mostly oblique kinematics, in accordance with the present-day active stress

regime established since the Gulf of California became a transtensional plate boundary (Angelier et al., 1981; Zanchi, 1994). Throughout the study area, the strong imprint of transtensive regional tectonics is shown by the highly recursive and regular (fractal) repetition at different scales (meso- and macro-) of the "pull-apart" geometry. Starting from the macro-scale, the Santa Rosalía transtensional fault-termination basin (Dorsey and Umhoefer, 2012) is bounded by major NW-SE and NE-SW trending gulf-inherited regional features. Some of these bounding faults (AFS and SAFS) in turn define pull-apart basins, like the one delimited by the AFS and the SAFS inside the Sierra Aguajito volcanic complex, or the smaller one mapped along the AFS in proximity of the Carrizo canyon (Figs 4.2A and 4.3). Again, at the outcrop scale several few-meters wide pull-apart structures form along major gulf-inherited fault systems (SAFS). Despite mapped regional structures (Antayhua-Vera et al., 2015; Wong and Munguía, 2006) are potentially active under the current stress regime, strike-slip and dip-slip offsets could rarely be quantified in the field, also due to Pleistocene volcanic products covering most of fault surface exposures throughout the study area. In other words, barely known is timing of latest slip, as these regional structures do not systematically cut any volcanic rock throughout the study area. A pre-caldera collapse last slip along the SAFS and associated features could explain why these structures do not clearly displace La Reforma caldera rims and post-caldera domes (Fig. 4.2A). Apart from the AFS offsetting the succession up to the Aguajito ignimbrite, most of recognised regional structures possibly did not move in the last 1 million year, or did move but without generating appreciable offsets (i.e. NW-SE oriented fractures cross-cutting post-caldera intrusions close to the SAFS in the eastern intra-caldera sector). Nevertheless, a different issue is the potential reactivation of these structures, as areas of crustal weakness, during resurgence processes. Exceptions to this overall scenario include the NNE-SSW oriented fault scarp offsetting the Mesa El Yaqui formation lavas on the caldera western external slope inside the pull-apart bounded by the AFS and the SAFS, displaying a qualitative slip rate up to 1 order of magnitude higher than those estimated by Mayer and Vincent (1999) along the N-S trending Loreto fault northern segment (0.0116 mm/yr, approximately 200 km SE of Santa Rosalía), considered as capable of representing seismic hazard to the Loreto town.

Regional fault systems played a crucial role in controlling recent to present-day magmatism, as best shown by the CFS, along which magmatic and seismic activity progressively moved from N (Sierra Aguajito) to S (El Viejo-El Azufre-La Virgen, López H. A. et al., 1989; López H. A. et al., 1995; Garduño-Monroy et al., 1993; López A.C. et al., 1993; Wong and Munguía 2006; Gutiérrez-Negrín, 2015). If the location of Sierra Aguajito and Tres Vírgenes centres is somehow easier to justify, not so straightforward is the position of the older La Reforma caldera complex. We argue that magma trapping and rise to form La Reforma caldera complex was permitted by the intersection of the gulf-inherited SAFS and the AFS with the N-S faulting trend that developed following the onset of

transtensive deformation and that is herein considered as responsible of internally dissecting pull-apart structures, similarly to what already proposed by López H. A. et al. (1995). In fact, Lonsdale (1989), Fabriol et al. (1999) and Negrete-Aranda et al. (2010) recognized a series of 310° oriented volcanic edifices (i.e. the Santa Rosalía volcanic ridge) following fracture-zone extensions offshore the San Borja volcanic field (more than 200 km NW of Santa Rosalía). Moreover, according to Fabriol et al. (1999) regional mechanisms responsible for the development of the Santa Rosalía volcanic ridge also control volcanic activity in La Reforma-Sierra Aguajito-Tres Vírgenes complexes since Pliocene time.

4.7.2 Interplay between regional and volcanic structures within La Reforma caldera complex

One of the most obvious evidence of regional faults interfering with caldera structures is the trap-door geometry of La Reforma caldera collapse. The hinge of the trap-door lies in the western sector and is probably rooted in the regional SAFS, which guided the trap-door collapse (cross-section BB' in Fig. 4.2B). Furthermore, the SAFS and perpendicular NE-SW oriented regional structures in the western sector (Fig. 4.4A) are also the sites with most resurgence-related structures (reverse faults and folds), as well as where the largest Cretaceous basement slice is exposed. Hence these regional structures must have also played a significant role during resurgence, that consisted in several pulses, some of which occurred during the caldera phase (image x of Fig. 4.4B) while others during the post-caldera phase (image n of Fig. 4.4B). As already introduced, the NE-SW trending structure cross-cutting folded pre-caldera rocks in the western sector and the NW-SE trending structure intersecting the Agua Caliente fault in the north-eastern sector are likely to represent respectively the NW and NE boundary of the central resurgent block. An ENE-WSW oriented inferred structure (Fig. 4.2A), possibly representing the continuation of the Agua Caliente fault system, could connect these two structures, enclosing the resurgent block towards the N. The south-western limit of the resurgent block is marked by the SAFS, as indicated by the exposure of Cretaceous plutonic rocks cross-cut by resurgence-related structures, and by the reverse stacking of La Reforma ignimbrite on top of the Punta Arena ignimbrite along a NW-SE oriented structure located just S of the SAFS (image n of Fig. 4.4B). Lastly, on the SE the resurgent block is delimited by one of the three ring fault systems, that were inferred based on lag breccia deposits and on post-caldera domes and intrusions alignment. Consequently, the central resurgent block is bounded by volcanic structures only in the SE, elsewhere by regional structures (Fig. 4.8). This is the reason why it shows such an asymmetrical shape (Fig. 4.2A), as also found in the Ischia resurgent caldera and in the Pantelleria caldera complex (Acocella and Funiciello, 1999; Parker and White, 2008). At Ischia, the intersection of several regional and volcano-tectonic fault systems, both contributing to uplift, is responsible for the irregularly octagonal shape of the

Monte Epomeo resurgent block (Rittmann and Gottini, 1980; Vezzoli 1988; Orsi et al., 1991; Acocella and Funiciello, 1999; de Vita et al., 2006; de Vita et al., 2010; Della Seta et al., 2012), while Pantelleria was defined by Parker and White (2008) as a structurally resurgent dome.

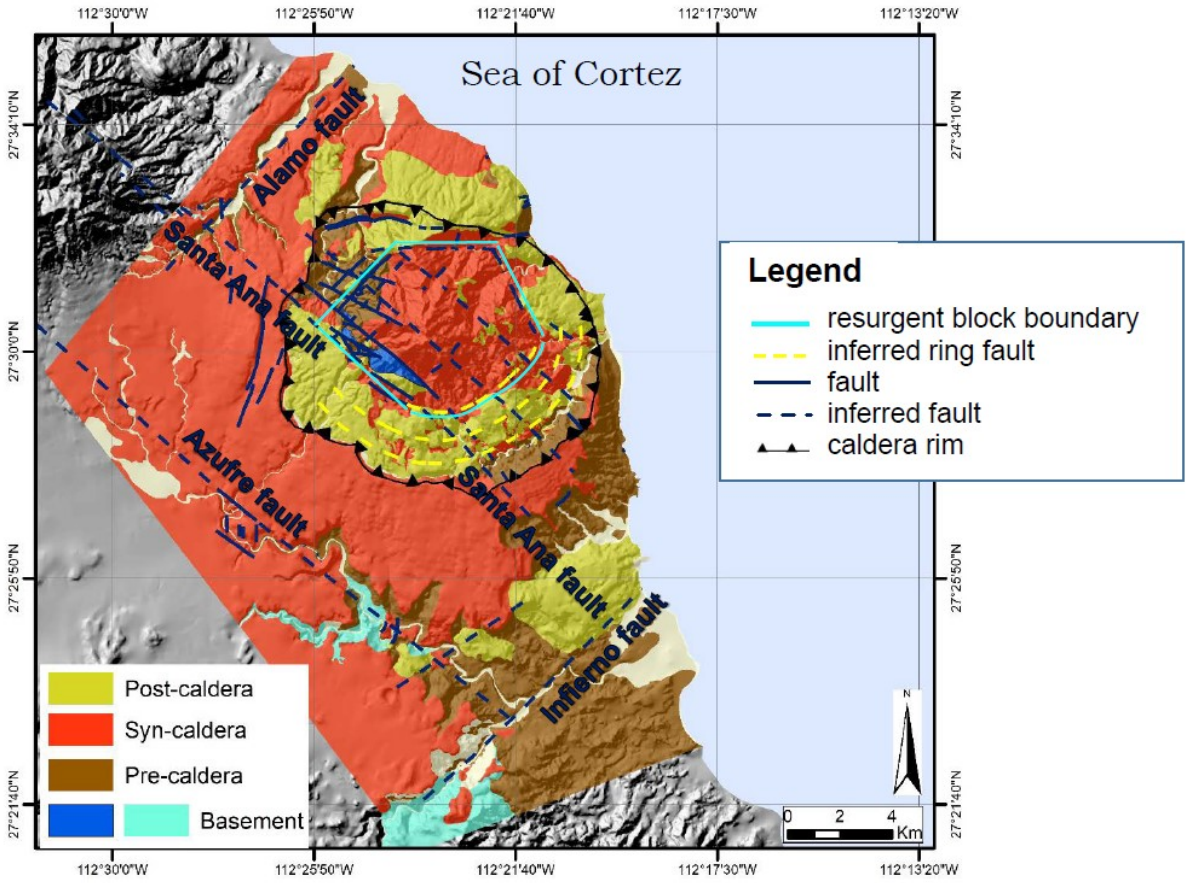

Figure 4.8 Structural model of La Reforma caldera complex.

4.7.3 Caldera resurgence

If by one side resurgence in La Reforma caldera took advantage of regional and collapse-inherited volcanic structures, on the other side new reverse shear planes also developed (image n of Fig. 4.4B) inside the Punta Arena ignimbrite, through mechanisms comparable to those identified by Norini et al. (2015) in the Los Humeros nested caldera complex (Puebla, Mexico). Resurgence is definitely responsible for the wider exposure, the higher altitude (600 m a.s.l.) and the intra-caldera location (Wilson and Rocha, 1955; García-Sánchez et al., 2019) of Cretaceous basement in comparison to other sites (E of the Yaqui canyon, Fig. 4.2A) across the study area, as well as for the present-day morphology of La Reforma caldera complex (Hausback et al., 2000), resulting from up to 840 m vertical uplift. The importance of resurgence inside La Reforma caldera complex is even more

straightforward if considering that computed uplift (cross section AA' Fig. 4.2B) represents a conservative estimate, due to the lack of information regarding erosion of Punta Arena ignimbrite in the last 1 Ma. However, still an open issue is the at least two times higher uplift of Cretaceous basement with respect to the rest of the resurgent block (geological cross-section BB' in Fig. 4.2A), either due to the fact that the central resurgent block comprises two independently uplifting released blocks, or to the tectonic control exerted by the close SAFS. Resurgence also causes the up to 25° SE and NE-tilting of the Punta Arena ignmbrite overlying the Cerro La Reforma formation in proximity of structure systems bounding the resurgent block (Fig. 4.5d). Such an uniform dip characterizing calderas resurgent blocks was also recognised in the Italian Ischia and Pantelleria calderas (Civetta et al., 1988; Acocella and Funiciello, 1999). This geometry develops, according to Acocella et al. (2001) analogue experiments on resurgent calderas, when the aspect ratio (thickness of the crust above the magma chamber compared to its width) is close to 1. Additionally, both Acocella et al. (2001) uniformly-dipping layers resurgence model and Orsi et al. (1991) explain the localization of volcanic activity in the less uplifted side of the resurgent block (peripheral volcanic activity) in the Ischia and Pantelleria calderas as linked to the presence of an extensional stress regime (normal faults). Conversely, the most uplifted sector lacks any volcanic activity as characterized by a compressive regime (high-angle reverse faults). Acocella et al. (2001) and Orsi et al. (1991) models seem to well resume what identified by García-Sánchez et al. (2019) in La Reforma caldera complex, where volcanic activity is significant along the resurgent block boundaries (Fig. 4.2A) and almost none inside the central resurgent block.

Resurgence throughout La Reforma caldera is also well documented by the post-caldera Cueva Del Diablo formation intrusive bodies patterns and geometries. Outward dipping ring-dykes are of minor occurrence, while prevalent radial and cone-sheet geometries (as defined by Tibaldi et al., 2011, Fig. 4.7A) respectively imply a circumferential or radial $\sigma 3$. Anderson (1937), Phillips (1974) and Troll et al. (2002) argued that the combination of radial and cone-sheet geometries represents a general proxy for magma chamber pressure increase, often expressed by bulging, uplift and resurgence inside the volcano edifice. Furthermore, Acocella et al. (2001) identify cone-sheets emplacement as a consequence of the uplift on reverse faults bordering the resurgent block. In spite of that, not much can be said about the link between intrusive bodies mapped across La Reforma caldera and associated magma chamber pressure regimes, because so not much is known about the depth and characteristics of magma reservoirs feeding La Reforma, Sierra Aguajito and Tres Vírgenes complexes. A 7-9 km deep magmatic chamber feeding the Tres Vírgenes volcanic centre was hypothesized by Wong and Munguía (2006), Macías and Jimenez (2012), Macías and Jimenez (2013) and Antayhua-Vera et al. (2015) by interpreting the maximum depth of seismic activity (7.4 km) as the brittle-to-ductile

rheological transition zone. Even if deeper than what expected based on Acocella et al. (2001) analogue models (5-6 km depth), a magma stagnation depth of about 7-9 km below the summit was confirmed by modelling of pre-eruptive temperatures and pressures from La Virgen rhyolitic tephra pumice (Avellán et al., 2018). This agrees with Kennedy et al. (2018), who stated that magma volumes characteristics of calderas, either being a single progressively-enlarging reservoir or small and initially-independent amalgamated magma pockets, usually reside at depths of up to 17 km but become shallower as the caldera system evolves. Besides from resurgence, the study of intra-caldera dyke patterns revealed how difficult sometimes is to understand the nature of the control (either regional or volcanic) exerted on these features merely based on their spatial orientation. The best example is provided by the NW-SE oriented post-caldera dykes along the semi-circular canyon marking the passage of the inferred ring fault systems in the eastern intra-caldera sector. These dykes could have emplaced taking advantage of the pre-existing SAFS damage zone or purely in response to volcanic processes that produced radial dykes. A possibility to explain the general difficulty in discerning regional from volcanic control on magmatic bodies emplacement could be the local variation in the minimum horizontal stress ($\sigma 3$) spatial trends, as found by Tibaldi et al. (2011) in the Cuillin complex (Isle of Skye, Scotland). Here, the coexistence of $\sigma 3$ opposed trends (circumferential and radial) linked to the simultaneous presence of cone-sheets and radial dykes often implies alternated periods where local stresses prevail over regional stresses acting in the background and vice versa.

4.7.4 Implications on geothermal potential

Regional structures certainly bear significant geothermal potential throughout the study area. Historically exploited mine sites lie along the SAFS (gold and lead mines) and the IF (copper mine, Fig. 4.3). Warm spots, where most of the currently producing geothermal wells lie, were identified by López H. A. et al. (1995) and Wong and Munguía (2006) S of the AFS (Fig. 4.1A), that is pervasively altered by hydrothermal circulation along the Azufre canyon. E-W trending veins and fractures also suggest the emplacement of pressurized hydrothermal fluids along the AFS, SAFS and CFS. The potential of gulf-inherited structures in driving hydrothermal fluids up to surface (Portugal et al., 2000) is not so hard to figure, given the lithospheric scale of these structures that easily connect Las Tres Vírgenes field geothermal reservoir (Cretaceous plutonic rocks) with the overlying volcanic and sedimentary units. In addition to gulf-inherited regional structures, geothermal potential linked to volcanic structures should not be neglected. Good examples in this sense are the wide and pervasive alteration facies developed inside the Punta Arena ignimbrite along the inner (Fig. 4.5a and c) and middle (Fig. 4.6i) ring fault systems. Overall, geothermal potential across the study area cannot be restricted to NW-SE oriented gulf-inherited largest structures. On the contrary, hydrothermal

circulation seems to focus where several fault systems intersect or in accommodation zones inside pull-apart basins. Permeability enhancement through fault intersection works both for regional crossing systems (i.e. the AFS and CFS in proximity of the Azufre canyon) and when regional and volcanic structures interact (i.e. the SAFS intersecting the inner and middle ring fault systems). This is not surprising, as accommodation zones are sites of common occurrence of geothermal fields and hydrothermal alteration in many important geothermal regions around the world (i.e. Taupo volcanic zone in New Zealand, Rowland and Sibson, 2004).

For what regards hydrothermal fluids heat source, according to Lopez H.A. et al (1995) heat is provided by the 7-9 km deep Tres Vírgenes magmatic reservoirs inferred by Macías and Jimenez (2012), Macías and Jimenez (2013) and Avellán et al. (2018). This can be easily envisaged for warm hydrothermal fluids circulating along the NW segment of the AFS (Azufre canyon), close to the Tres Vírgenes volcanic complex. On the other hand, not much can be stated regarding heating of fluids far from the magma chamber (i.e. the SE part of the AFS and the IF), as no robust study on crustal heat transfer, either linked to the magmatic chamber or to crustal-thinning associated to active oblique-rifting tectonic processes, has been performed so far in the region. Also, all geothermal wells lie NW of the Tres Vírgenes volcanic complex, and temperature gradients for surrounding areas are unknown. In our opinion, given that heat transfer currently focuses close to the Tres Vírgenes volcanic complex (warm spots) and that La Reforma caldera complex represents a fossil geothermal system, volcanic (magma chamber) rather than generalized tectonic (crustal thinning) processes are likely to produce the heat source.

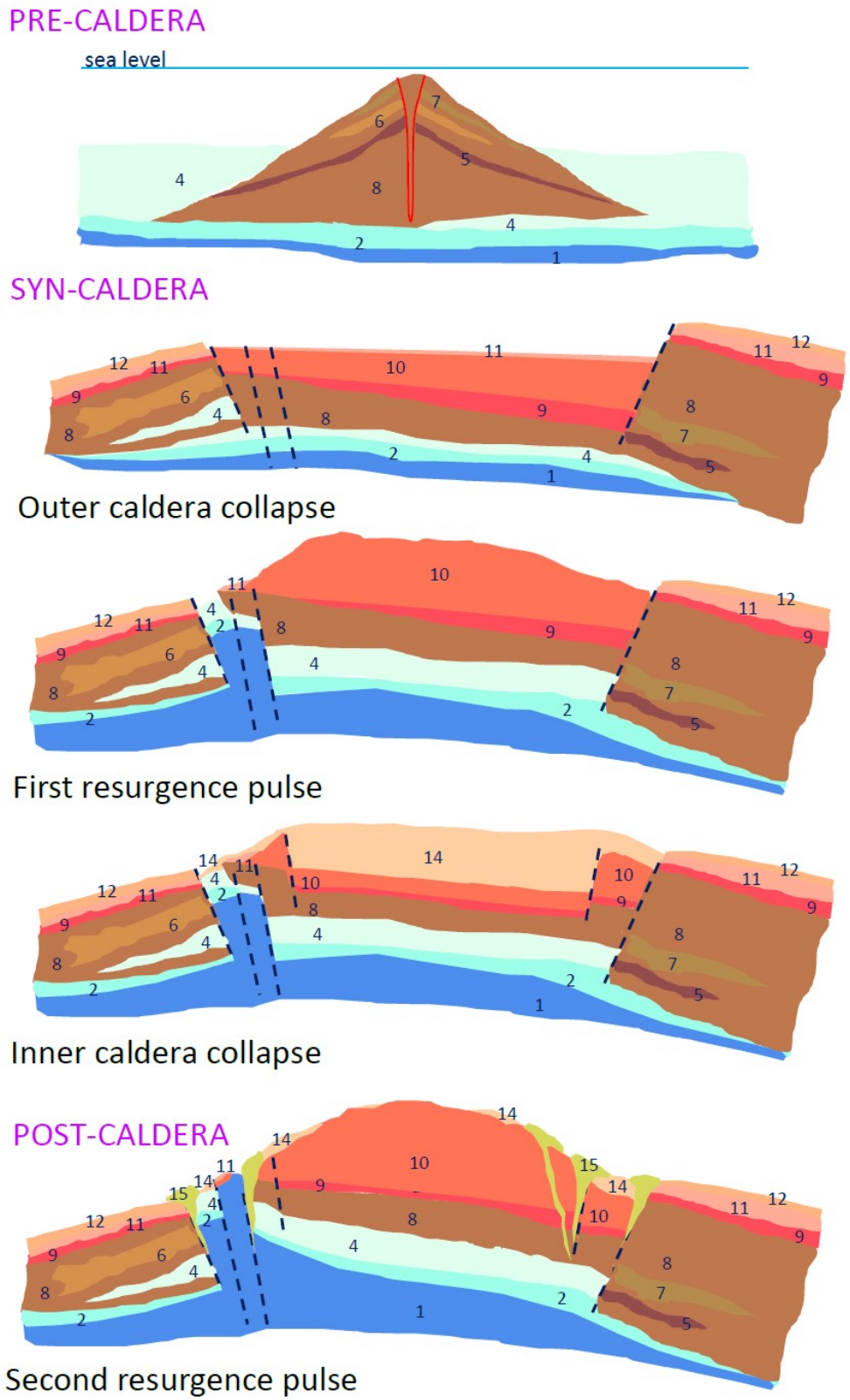

Figure 4.9 La Reforma caldera complex main evolution phases.

4.8 Concluding remarks

Following recent geological survey of La Reforma caldera complex (García-Sánchez et al., 2019), this work presents results of a structural study performed within and around La Reforma caldera complex (Fig. 4.8), whose implications include the role of regional structures in controlling caldera processes and evolution (Fig. 4.9) and geothermal potential. Main conclusions can be summarized as follows:

a) Together with the younger Sierra Aguajito and Tres Vírgenes volcanic centres, the Pleistocene La Reforma caldera complex lies within a pull-apart basin close to the Santa Rosalía town, in the Mulegé municipality of northern Baja California Sur. The basin is bordered by NW-SE and NE-SW regional structures, partly inherited from the Gulf of California orthogonal extension phase (early to middle Miocene) and reactivated since the onset of a transtensional plate boundary (Pliocene) characterized by an E-W directed horizontal minimum extensional stress.

b) Main regional fault systems include the NW-SE transtensive AFS and SAFS, the N-S to NNE-SSW CFS, the NE-SW IF and AF, and several NW-SE, NE-SW and N-S oriented faults scarps. Along the latter a 0.049-0.111 mm/yr slip rate was estimated. Apart from the latter, most structures did not generate appreciable offsets over the last 1 Ma, although favourably oriented under the currently active stress field. Gulf-inherited regional structures contributed to the slicing and exhumation of the *Laramide arc* Cretaceous plutonic rocks, nowadays exposed inside La Reforma caldera depression as a result of resurgence processes. They also favoured magma trapping and rise throughout Santa Rosalía area.

c) Inside La Reforma caldera complex, the strict interplay between regional and volcanic features (three inferred ring fault systems and resurgence-related reverse faults and folds) is testified by the trap-door geometry of the caldera collapse and by the role of regional faults in guiding resurgence processes and isolating an asymmetric resurgent block.

d) Syn- and post-caldera resurgence processes in La Reforma caldera complex are well described by Acocella et al. (2001) uniformly-dipping layers resurgence model, that justifies the uniform SE-tilting of the Punta Arena ignimbrite along the eastern intra-caldera sectors and the presence of peripheral volcanic activity. Prevalent radial and cone-sheet geometries of dykes seem to support magma chamber pressure increase, even though the location of the feeding system for La Reforma, Sierra Aguajito and Tres Vírgenes volcanic centres is poorly constrained.

e) Volcanic and regional structures can individually display pervasive hydrothermal circulation, especially regional structures due to their lithospheric-scale extension, even though geothermal potential across the study area cannot be restricted to NW-SE gulf-inherited structures. Hydrothermal circulation focuses where fault systems, either regional or volcanic, intersect.

4.9 Acknowledgements

This study benefited from CeMIE Geo project P15 of SENER-CONACyT to J.L.M. and UNAM (Universidad National Autónoma de México, Instituto de Geofísica, Morelia, Michoacán, México) to support 2015-2017 field trips to Santa Rosalía-Tres Vírgenes, and from *Italgas S.p.a.* funds issued by CNR-IDPA (Milan) to sponsor C. Pellicioli in her PhD research activity. We are thankful to UNAM also for managing logistic aspects of field trips, including employing local guides from UMA and Ecoturismo Borrego Cimarrón, Bonfil, B.C.S., who took care of people working in the field. Among UMA members, we are especially grateful to Francisco, for having led us to any site that could (and could not) be reached in the fastest way possible and for always patiently waiting for us to finish all of our measurements. Special thanks go to Laura García-Sánchez, Susana Osorio-Ocampo, Reyna-Marcela Lira-Beltran, Antonio Pola-Villaseñor, Pedro Martin Pacheco and Vincenzo Parisi for their support during fieldwork activity, post-field technical discussions and for hospitality in Morelia. Thanks also to Pedro Corona-Chávez and Michele Zucali for their interest and support in the present study and to Luca Ferrari and Rob Govers for the manuscript revision.

4.10 References cited

Acocella, V., 2007, Understanding caldera structure and development: An overview of analogue models compared to natural calderas: Earth-Science Reviews, 85(3-4), 125-160.

Acocella, V., and Funiciello, R., 1999, The interaction between regional and local tectonics during resurgent doming: the case of the island of Ischia, Italy: Journal of Volcanology and Geothermal Research, 88(1-2), 109-123.

Acocella, V., Cifelli, F., and Funiciello, R., 2001, The control of overburden thickness on resurgent domes: insights from analogue models: Journal of Volcanology and Geothermal Research, 111(1-4), 137-153.

Anderson, E. M., 1937, IX.—The dynamics of the formation of cone-sheets, ring-dykes, and caldron – subsidences, *in* Proceedings of the Royal Society of Edinburgh, 56, 128-157.

Angelier, J., Colletta, B., Chorowicz, J., Ortlieb, L., and Rangin, C., 1981, Fault tectonics of the Baja California Peninsula and the opening of the Sea of Cortez, Mexico: Journal of Structural Geology, 3(4), 347-357.

Antayhua-Vera, Y., Lermo-Samaniego, J., Quintanar-Robles, L., and Campos-Enríquez, O., 2015, Seismic activity and stress tensor inversion at Las Tres Vírgenes Volcanic and Geothermal Field (México): Journal of Volcanology and Geothermal Research, 305, 19-29.

Aragón-Arreola, M., Morandi, M., Martín-Barajas, A., Delgado-Argote, L., and González- Fernández, A., 2005, Structure of the rift basins in the central Gulf of California: Kinematic implications for oblique rifting. Tectonophysics, 409(1-4), 19-38.

Atwater, T., 1970, Implications of plate tectonics for the Cenozoic tectonic evolution of western North America: Geological Society of America Bulletin, 81(12), 3513-3536.

Atwater, T. M., and Severinghaus, J. P., 1989, Tectonic maps of the northeast Pacific. In: Winterer, E.L., Hussong, D.M., Decker, R.W. (Eds), The Geology of North America, v.N: The Northeastern Pacific Ocean and Hawaii. Geol. Soc. Amer, Boulder, CO, pp 15-20.

Atwater, T., and Stock, J., 1998, Pacific-North America plate tectonics of the Neogene southwestern United States: an update: International Geology Review, 40(5), 375-402.

Avellán, D. R., Macías, J. L., Arce, J. L., Jiménez-Haro, A., Saucedo-Girón, R., Garduño-Monroy, V. H., Sosa-Ceballos, G., Bernal, J. P., López-Loera, H., Cisneros, G., Layer, P. W., García-Sánchez, L., Reyes-Agustín, G., Rocha, V., S. and Rangel, E., 2018, Eruptive chronology and tectonic context of the late Pleistocene Tres Vírgenes volcanic complex, Baja California Sur (México): Journal of Volcanology and Geothermal Research, 360, 100-125.

Axen, Gary J., Grove M., Stockli D., Lovera O.M., Rothstein D.A., Fletcher J.M., Farley K., and Abbott P.L., 2000, Thermal evolution of Monte Blanco dome: Low-angle normal faulting during Gulf of California rifting and late Eocene denudation of the eastern Peninsular Ranges: Tectonics 19, no. 2 (2000): 197-212.

Balestrieri, M. L., Ferrari, L., Bonini, M., Duque-Trujillo, J., Cerca, M., Moratti, G., and Corti, G., 2017, Onshore and offshore apatite fission-track dating from the southern Gulf of California: Insights into the time-space evolution of the rifting: Tectonophysics, 719, 148-161.

Barragán, R. M., Iglesias, E., Arellano, V.M. and Ramírez, M., 2010, Fluid-mineral equilibrium at Las Tres Vírgenes B. C S. (México) geothermal reservoir: GRC Transactions, Vol. 34, 2010.

Bryan, S. E., Orozco-Esquivel, T., Ferrari, L., and Lopez-Martinez, M., 2014, Pulling apart the mid to late Cenozoic magmatic record of the Gulf of California: Is there a Comondú arc?: Geological Society, London, Special Publications, 385(1), 389-407.

Civetta, L., Cornette, Y., Gillot, P. Y., and Orsi, G., 1988, The eruptive history of Pantelleria (Sicily Channel) in the last 50 ka: Bulletin of Volcanology, 50(1), 47-57.

Cole, J. W., Milner, D. M., and Spinks, K. D., 2005, Calderas and caldera structures: a Review: Earth-Science Reviews, 69(1-2), 1-26.

Conly, A. G., Brenan, J. M., Bellon, H., and Scott, S. D., 2005, Arc to rift transitional volcanism in the Santa Rosalia region, Baja California Sur, Mexico: Journal of Volcanology and Geothermal Research, 142(3), 303-341.

de Vita, S., Sansivero, F., Orsi, G., and Marotta, E., 2006, Cyclical slope instability and volcanism related to volcano-tectonism in resurgent calderas: the Ischia island (Italy) case study: Engineering Geology, 86(2-3), 148-165.

de Vita, S., Sansivero, F., Orsi, G., Marotta, E., and Piochi, M., 2010, Volcanological and structural evolution of the Ischia resurgent caldera (Italy) over the past 10 ky. Stratigraphy and geology in volcanic areas, GSA Book series, Special paper, 464, 193-239.

Della Seta, M., Marotta, E., Orsi, G., de Vita, S., Sansivero, F., and Fredi, P., 2012, Slope instability induced by volcano-tectonics as an additional source of hazard in active volcanic areas: the case of Ischia island (Italy): Bulletin of Volcanology, 74(1), 79-106.

Demant, A., and Ortlieb, L., 1981, Plio-pleistocene volcano-tectonic evolution of La Reforma caldera, Baja California, Mexico: Tectonophysics, 71(1-4), 194.

Dorsey, R. J., nd Umhoefer, P. J., 2012, Influence of Sediment Input and Plate-Motion Obliquity on Basin Development Along an Active Oblique-Divergent Plate Boundary: Gulf of California and Salton Trough: Tectonics of Sedimentary Basins: Recent Advances, 209-225.

Duque-Trujillo, J., Ferrari, L., Orozco-Esquivel, T., López-Martínez, M., Lonsdale, P., Bryan, S. E., Kluesner, J., Pinero-Lajas, D., and Solari, L., 2015, Timing of rifting in the southern Gulf of California and its conjugate margins: Insights from the plutonic record: Bulletin, 127(5-6), 702-736.

Fabriol, H., Delgado-Argote, L. A., Dañobeitia, J. J., Córdoba, D., González, A., Garcıa-Abdeslem, J., Bartolomé, R., Martín-Atienza B., and Frias-Camacho, V., 1999, Backscattering and geophysical features of volcanic ridges offshore Santa Rosalia, Baja California Sur, Gulf of California, Mexico: Journal of volcanology and geothermal research, 93(1-2), 75-92.

Fenby, S.S., and Gastil, R.G., 1991, A seismo-tectonic map of the Gulf of California and surrounding areas: Dauphin, J.P., Simoneit, B.R. (Eds.), The Gulf and Peninsular Provinces of the Californias: AAPG Mem., vol. 47, pp. 79–83.

Ferrari, L., López-Martínez, M., Orozco-Esquivel, T., Bryan, S. E., Duque-Trujillo, J., Lonsdale, P., and Solari, L., 2013, Late Oligocene to Middle Miocene rifting and synextensional magmatism in the southwestern Sierra Madre Occidental, Mexico: The beginning of the Gulf of California rift: Geosphere, 9(5), 1161-1200.

Ferrari, L., Orozco-Esquivel, T., Bryan, S. E., Lopez-Martinez, M., and Silva-Fragoso, A., 2018, Cenozoic magmatism and extension in western Mexico: Linking the Sierra Madre Occidental silicic large igneous province and the Comondú Group with the Gulf of California rift: Earth-Science Reviews, 183, 115-152.

Fletcher, J. M., Grove, M., Kimbrough, D., Lovera, O., and Gehrels, G. E., 2007, Ridge-trench interactions and the Neogene tectonic evolution of the Magdalena shelf and southern Gulf of California: Insights from detrital zircon U-Pb ages from the Magdalena fan and adjacent areas.: Geological Society of America Bulletin, 119(11-12), 1313-1336.

Fuis, G. S., and Kohler, W. M., 1984, Crustal structure and tectonics of the Imperial Valley region, California: Rigsby, C.A. (Ed.), The Imperial Basin Tectonics, Sedimentation and Thermal Aspects. Pacific Section S.E.P.M., pp. 1 – 13.

García-Sánchez, L., Macías, J.L., Sulpizio, R., Osorio-Ocampo, L.S., Pellicioli, C., Pola, A., Avellán, D.R., Cisneros, G., García, F., Ocampo-Díaz, Y.Z.E, Lira-Beltran, R.M., Saucedo, R., Sánchez-Nuñez, J.M., Arce, J.L., Corona-Chávez, P., Reyes-Augustin, G., Cardona, M., Layer, P.W., Benowitz, J., Solari, L., and Groppelli, G., 2019, Geology of La Reforma caldera complex, Baja California, Mexico: *Journal of Maps*, 15:2, 487-498, DOI: 10.1080/17445647.2019.1612287, scale 1:50,000, 1 sheet, 12 p. text.

Garduño-Monroy, V. H., Vargas-Ledezma, H., and Campos-Enriquez, J. O., 1993, Preliminary geologic studies of Sierra El Aguajito (Baja California, Mexico): a resurgent-type caldera: Journal of Volcanology and Geothermal Research, 59(1-2), 47-58.

Gutiérrez-Negrín, L. C., 2015), Mexican geothermal plays, *in* Proceedings of the world geothermal congress 2015, Melbourne, Australia, 19–25 April.

Hausback, B. P., 1984, Cenozoic volcanic and tectonic evolution of Baja California Sur, Mexico: Frizzel, V. A., Jr. (ed.) Geology of the Baja California Peninsula. Pacific Section, SEPM Special Publications,Tulsa, 39, 219–236.

Hausback, B. P., Stock, J. M., Dmochowski, J. E., Farrar, C. D., Fowler, S. J., Sutter, K., Verke P., and Winant, C., 2000, To be or not be a caldera—La Reforma caldera, Baja California Sur, Mexico: Program with Abstracts-Geological Society of America, 32, A502.

Holt, J. W., Holt, E. W., and Stock, J. M., 2000, An age constraint on Gulf of California rifting from the Santa Rosalía basin, Baja California Sur, Mexico: Geological Society of America Bulletin, 112(4), 540-549.

Hook, S. J., Dmochowski, J. E., Howard, K. A., Rowan, L. C., Karlstrom, K. E., and Stock, J. M., 2005, Mapping variations in weight percent silica measured from multispectral thermal infrared imagery—Examples from the Hiller Mountains, Nevada, USA and Tres Virgenes-La Reforma, Baja California Sur, Mexico: Remote Sensing of Environment, 95(3), 273-289.

Kennedy, B. M., Holohan, E. P., Stix, J., Gravley, D. M., Davidson, J., and Cole, J. W., 2018, Magma plumbing beneath collapse caldera volcanic systems: Earth-Science Reviews, 177, 404-424.

Kimbrough, D. L., Smith, D. P., Mahoney, J. B., Moore, T. E., Grove, M., Gastil, R. G., Ortega- Rivera, A., and Fanning, C. M., 2001, Forearc-basin sedimentary response to rapid Late Cretaceous batholith emplacement in the Peninsular Ranges of southern and Baja California: Geology, 29(6), 491-494.

Kimbrough, D. L., Abbott, P. L., Balch, D. C., Bartling, S. H., Grove, M., Mahoney, J. B., and Donohue, R. F., 2014, Upper Jurassic Peñasquitos Formation—Forearc basin western wall rock of the Peninsular Ranges batholith: Geological Society of America Memoirs, 211, 625-643.

Lira, H., Ramirez, G., Herrera, F. J. J., and Vargas, H., 1983, Estudio geológico a semidetalle de la zona geotérmica de las Tres Vírgenes, BCS: Rep. Interno 30/83, GPG-*CFE*.

Lira, H. H., González, M. L., and Arellano, F. G., 1997, Actualización del modelo conceptual del campo geotérmico de Tres Vírgenes, Baja California Sur: Rep. Interno RE-12/97, GPG-CFE.

Lonsdale, P., 1989, Geology and tectonic history of the Gulf of California: The eastern Pacific Ocean and Hawaii: Boulder, Colorado, Geological Society of America, Geology of North America, v. N, 499-521.

Lonsdale, P., 1991, Structural patterns of the Pacific floor offshore of peninsular California: Dauphin, J.P.,Simoneit, B.R. (Eds), The gulf and peninsular province of the Californias, 47 Am. Assoc. Petr. Geol. Mem., 87-125.

López, A. C., and Casarrubias, U. Z. Z., y Leal, R., 1993, Estudio geológico regional de la zona geotérmica de Las Tres Vírgenes: Rep. Interno OGL-BC-002/93, GPG-CFE.

López, H. A., 1998, Síntesis geológica de la zona geotérmica de las Tres Vírgenes, BCS, México: Geoterm. Rev. Mex. Geoenerg, 14(1), 3-14.

López, H. A., Robin, C., and Vincent, O., 1989, Estudio geoquímico, mineralógico y edades radiométricas de la zona de Las Tres Vírgenes BCS Implicaciones geotérmicas: Rep. Interno 5/89, GPG-CFE.

López, H. A., García, G. H. and Arellano, F. G., 1995, Geothermal exploration at Las Tres Vírgenes, BCS, Mexico: In Proc. of the 1995 World Geoth. Congress (pp. 707-712).

Macías, J.L., and Jiménez, S., 2012, Actualización vulcanológica del complejo de Las Tres Vírgenes, BCS: Memorias del XX Congreso Anual de la Asociación Geotérmica Mexicana, Morelia, Mich., México, 26-28 September 2012 (2012).

Macías, J.L., and Jiménez, S., 2013, Estudio de Estratigrafía y Geología del Complejo Volcánico Tres Vírgenes. B.C.S: Geotermia 26 (1), 14–23.

Mark, C., Gupta, S., Carter, A., Mark, D., Gautheron, C., and Martin-Barajas, A., 2012, Temporal constraints on the landscape response to rifting in the Loreto region of Baja California Sur, Mexico: Geological Society of America Abstracts with Programs (Vol. 44, No. 3, p. 6).

Martín-Barajas, A., González-Escobar, M., Fletcher, J. M., Pacheco, M., Oskin, M., and Dorsey, R., 2013,Thick deltaic sedimentation and detachment faulting delay the onset of continental rupture in the northern Gulf of California: Analysis of seismic reflection profiles: Tectonics, 32(5), 1294-1311.

Mayer, L., and Vincent, K. R., 1999, Active tectonics of the Loreto area, Baja California Sur, Mexico: Geomorphology, 27(3-4), 243-255.

McLean, H., 1988, Reconnaissance geologic map of the Loreto and part of the San Javier quadrangles, Baja California Sur, Mexico: U.S. Geological Survey Miscellaneous Field Studies Map, Report No. MF-2000, 10 p., 1 mapa, escala 1:50,000.

Nava-Sánchez, E. H., Gorsline, D. S., and Molina-Cruz, A., 2001, The Baja California peninsula borderland: structural and sedimentological characteristics: Sedimentary Geology, 144(1-2), 63-82.

Negrete-Aranda, R., Cañón-Tapia, E., Brandle, J. L., Ortega-Rivera, M. A., Lee, J. K., Spelz, R. M., and Hinojosa-Corona, A., 2010, Regional orientation of tectonic stress and the stress expressed by post-subduction high-magnesium volcanism in northern Baja California, Mexico: Tectonics and volcanism of San Borja volcanic field: Journal of Volcanology and Geothermal Research, 192(1-2), 97-115.

Ness, G. E., Lyle, M. W., and Couch, R. W., 1991, Marine magnetic anomalies and oceanic crustal isochrones of the Gulf and Peninsular Province of the Californias: The Gulf and Peninsular Province of the Californias, American Association of Petroleum Geologists, Memoir, 47, 47-69.

Norini, G., Groppelli, G., Lagmay, A. M. F., and Capra, L., 2006, Recent left-oblique slip faulting in the central eastern Trans-Mexican Volcanic Belt: Seismic hazard and geodynamic implications: Tectonics, 25(4).

Norini, G., Groppelli, G., Sulpizio, R., Carrasco-Núñez, G., Dávila-Harris, P., Pellicioli, C., Zucca, F., and De Franco, R., 2015, Structural analysis and thermal remote sensing of the Los Humeros Volcanic Complex: Implications for volcano structure and geothermal exploration: Journal of Volcanology and Geothermal Research, 301, 221-237.

Orsi, G., Gallo, G., and Zanchi, A., 1991, Simple-shearing block resurgence in caldera depressions. A model from Pantelleria and Ischia: Journal of Volcanology and Geothermal Research, 47(1-2), 1-11.

Ortlieb, L. and Colletta, B., 1984, Síntesis cronoestratigráfica sobre el Neogeno y el Cuaternario marino de la cuenca de Santa Rosalía, Baja California Sur: Neotectonics and sea level variations in the Gulf of California Area, a symposium (Hermosillo, Son., April 21th-23rd). Malpica-Cruz, V., Celiz-Gutiérrez, S., Guerrero-García, J. And Ortlieb, L. (Eds). Univ. Nat. Autón. México, Inst. Geología, México, D.F.

Ortlieb, L., Ruegg, J. C., Angelier, J., Colletta, B., Kasser, M., and Lesage, P., 1989, Geodetic and tectonic analyses along an active plate boundary: The central Gulf of California: Tectonics, 8(3), 429-441.

Parker, D. F. and White, J. C., 2008, Large-scale silicic alkalic magmatism associated with the Buckhorn Caldera, Trans-Pecos Texas, USA: comparison with Pantelleria, Italy: Bulletin of Volcanology, 70(3), 403-415.

Persaud, P., Stock, J. M., Steckler, M. S., Martín-Barajas, A., Diebold, J. B., González-Fernández, A., and Mountain, G. S. 2003, Active deformation and shallow structure of the Wagner, Consag, and Delfín Basins, northern Gulf of California, Mexico: Journal of Geophysical Research: Solid Earth, 108(B7).

Phillips, W. J., 1974, The dynamic emplacement of cone sheets: Tectonophysics, 24(1-2), 69-84.

Portugal, E., Birkle, P., Tello, E., and Tello, M., 2000, Hydrochemical–isotopic and hydrogeological conceptual model of the Las Tres Vırgenes geothermal field, Baja California Sur, México: Journal of Volcanology and Geothermal Research, 101(3-4), 223-244.

Rittmann, A., and Gottini, V., 1980, L'Isola d'Ischia – Geologia: Boll. Serv. Geol. It., 101, 131-274.

Rowland, J. V., and Sibson, R. H., 2004, Structural controls on hydrothermal flow in a segmented rift system, Taupo Volcanic Zone, New Zealand: Geofluids, 4(4), 259-283.

Sawlan, M. G., 1991, Magmatic evolution of the Gulf of California rift: Dauphin, J.P. Simoneit, B.R.(eds)The Gulf and Peninsular province of the Californias, American Association of Petroleum Geologists, Memoirs, 47, 301-369.

Sawlan, M. G., and Smith, J. G., 1984, Petrologic characteristics, age and tectonic setting of Neogene volcanic rocks in northern Baja California Sur, Mexico: Frizzell, V. A., Jr. (ed.) Geology of the Baja California Peninsula. SEPM Special Publications, Tulsa, 39, 237–251.

Schmidt, E. K., 1975, Plate tectonics, volcanic petrology, and ore formation in the Santa Rosalía area, Baja California, Mexico: [M. Sc. Thesis], Univeristy of Arizona, 196 pp.

Schmitt, A. K., Stockli, D. F., and Hausback, B. P., 2006, Eruption and magma crystallization ages of Las Tres Vírgenes (Baja California) constrained by combined 230 Th/238 U and (U–Th)/He dating of zircon: Journal of Volcanology and Geothermal Research, 158(3), 281-295.

Stock, J. M., and Hodges, K. V., 1989, Pre-Pliocene extension around the Gulf of California and the transfer of Baja California to the Pacific plate: Tectonics, 8(1), 99-115.

Tibaldi, A., Pasquarè, A. F., and Rust, D., 2011, New insights into the cone sheet structure of the Cuillin Complex, Isle of Skye, Scotland: Journal of the Geological Society, 168(3), 689-704.

Troll, V. R., Walter, T. R., and Schmincke, H. U., 2002, Cyclic caldera collapse: Piston or piecemeal subsidence? Field and experimental evidence: Geology, 30(2), 135-138.

Umhoefer, P. J., 2011, Why did the southern Gulf of California rupture so rapidly?—Oblique divergence across hot, weak lithosphere along a tectonically active margin: GSA Today, 21(11), 4-10.

Umhoefer, P. J., Teyssier, C., Carrilo-Chávez, A., and Álvarez-Arellano, A., 1992, A preliminary structural geology study of the El Azufre Canyon area, north of the Tres Vírgenes volcano, northern Baja California Sur: *in* Proceedings of the First International Meeting on Geology of Baja California Peninsula (pp. 45-54). Peninsular Geol. Soc., Univ. Autón. of Baja California Sur, La Paz, BCS, Mexico.

Umhoefer, P. J., Dorsey, R. J., Willsey, S., Mayer, L., and Renne, P., 2001, Stratigraphy and geochronology of the Comondu Group near Loreto, Baja California Sur, Mexico: Sedimentary Geology, 144(1-2), 125-147.

Umhoefer, P. J., Mayer, L., and Dorsey, R. J., 2002, Evolution of the margin of the Gulf of California near Loreto, Baja California peninsula, Mexico: Geological Society of America Bulletin, 114(7), 849-868.

Verma, S. P., Pandarinath, K., Santoyo, E., González-Partida, E., Torres-Alvarado, I. S., and Tello- Hinojosa, E., 2006, Fluid chemistry and temperatures prior to exploitation at the Las Tres Vírgenes geothermal field, Mexico: Geothermics, 35(2), 156-180.

Vezzoli, L., 1988, Island of Ischia: CNR Quaderni de “La ricerca scientifica”, 114(10), 122 pp. Wilson, I. F., and Rocha, V. S., 1955, Geology and mineral deposits of the Boleo copper district, Baja California, Mexico (p. 134): US Government Printing Office.

Wong, V., and Munguía, L., 2006, Seismicity, focal mechanisms, and stress distribution in the Tres Vírgenes volcanic and geothermal region, Baja California Sur, Mexico: Geofísica internacional, 45(1), 23-37.

Zanchi, A., 1994, The opening of the Gulf of California near Loreto, Baja California, Mexico: from basin and range extension to transtensional tectonics: Journal of Structural Geology, 16(12), 1619-1639.

Chapter 5

Paper III

Kinematics and deformation patterns from micro-structural and image analysis on fault-rock samples in volcanic regions: the example of the Tres Vírgenes active geothermal region, Baja California (Mexico)

C. Pellicioli [a, b], *M. Zucali* [a, c] *and G. Groppelli* [b].

[a] Dipartimento di Scienze della Terra "Ardito Desio", Università degli Studi di Milano, Milano, Italia;
[b] C.N.R. - Istituto di Geologia Ambientale e Geoingegneria– sezione di Milano, Milano, Italia;
[c] Department of Earth and Atmospheric Sciences, University of Houston, Texas-USA.

SUBMITTED TO THE JOURNAL OF STRUCTURAL GEOLOGY IN AUGUST 2019,
REF: MANUSCRIPT NUMBER SG_2019_262.

Sample collection in the field: ***C. Pellicioli.***

Lithological, micro-structural and image analyses, statistical analysis and distributions (including fractal statistics): ***C. Pellicioli*** (under the supervision of *M. Zucali).*

PhD tutoring: *G. Groppelli.*

Manuscript writing: ***C. Pellicioli***.

Manuscript Details

Manuscript number	SG_2019_262
Title	Kinematics and deformation patterns from micro-structural and image analysis on fault-rock samples in volcanic regions: the example of the Tres Vírgenes active geothermal region, Baja California (Mexico)
Article type	Original article

Abstract

Investigation of kinematics and deformation patterns at the micro-scale provides detailed information that helps confirming or rejecting first-stage interpretations done at the field scale and provides a deeper insight on geodynamic processes deforming the upper crust. This is very challenging in volcanic regions, where structural mapping and interpretation could be severely complicated by volcanic products covering, interplay with volcano-tectonic structures and scarce occurrence of good quality kinematic data (slickensides and striae). This study investigates micro-fractures and veins at the thin section scale in eleven samples collected along the major regional structures dissecting the Tres Vírgenes active geothermal region (Baja California, Mexico) and linked to the Gulf of California opening. Micro-structural and image analysis techniques, fractal statistics and frequency analysis of micro-structures length distributions highlighted the following: a) a close link between Gulf-related faulting processes and fluid circulation; b) the emplacement of pressurized fluids along fault planes self-sealed by calcite deposition; c) a generalized deformation trend and statistical self-similarity of structures related to this sector of the Gulf of California. These results consolidate previous structural models and field-scale observations regarding the Tres Vírgenes area based on limited structural data and encourage performing quantitative characterization of fault-related micro-structural patterns in volcanic regions.

Keywords	micro-structures; Riedel shears; syn- and post-faulting fluid circulation; pressurized fluids; fractal
Corresponding Author	Claudia Pellicioli
Order of Authors	Claudia Pellicioli, Michele Zucali, Gianluca Groppelli
Suggested reviewers	Fabio Luca Bonali, valerio acocella, Victor Hugo Garduño-Monroy

Submission Files Included in this PDF

File Name [File Type]

Cover Letter_JSG.docx [Cover Letter]

Highlights_JSG.docx [Highlights]

Manuscript_JSG.docx [Manuscript File]

Figures_color_JSG.pdf [Figure]

Figures_b&w_JSG.pdf [Supplementary Material]

To view all the submission files, including those not included in the PDF, click on the manuscript title on your EVISE Homepage, then click 'Download zip file'.

5.1 Abstract

Investigation of kinematics and deformation patterns at the micro-scale provides detailed information that helps confirming or rejecting first-stage interpretations done at the field scale and provides a deeper insight on geodynamic processes deforming the upper crust. This is very challenging in volcanic regions, where structural mapping and interpretation could be severely complicated by volcanic products covering, interplay with volcano-tectonic structures and scarce occurrence of good quality kinematic data (slickensides and striae). This study investigates micro-fractures and veins at the thin section scale in eleven samples collected along the major regional structures dissecting the Tres Vírgenes active geothermal region (Baja California, Mexico) and linked to the Gulf of California opening. Micro-structural and image analysis techniques, fractal statistics and frequency analysis of micro-structures length distributions highlighted the following: a) a close link between Gulf-related faulting processes and fluid circulation; b) the emplacement of pressurized fluids along fault planes self-sealed by calcite deposition; c) a generalized deformation trend and statistical self-similarity of structures related to this sector of the Gulf of California. These results consolidate previous structural models and field-scale observations regarding the Tres Vírgenes area based on limited structural data and encourage performing quantitative characterization of fault-related micro-structural patterns in volcanic regions.

Keywords: *micro-structures, Riedel shears, syn- and post-faulting fluid circulation, pressurized fluids, fractal*.

5.2 Introduction

Mapping and interpreting structures in volcanic regions can be challenging. Volcanic regions are sometimes arduous to access and volcanic products tend to cover and hide pre-existing morphologies and discontinuities. In addition, the interaction of volcanic-driven processes with regional tectonics and stress distribution commonly complicates geometries of volcanic edifices, caldera collapses and resurgence processes (Cole et al., 2005; Acocella, 2007), making hard to identify the regional (i.e. tectonics) versus local (i.e. volcanic) origin of structures. Moreover, these structures might be quite often favourably oriented to both expected trends. On a smaller scale, detailed kinematic study of mapped structures is often complex, due to the generally bad preservation conditions of striae,

slickensides and other kinematic indicators mostly because of lithological issues (e.g. Norini et al., 2006). To overcome these problems, mesostructural analysis may be coupled with microstructural investigation to discern among different deformation mechanisms that have generated the observed structures and to reconstruct the timing of structures marked by specific products of volcanic or tectonic activities, such as fluid circulations and related mineralization at relative high temperatures vs. pure brittle deformation under shear regimes. The coupling and linking of meso- and micro-structural investigations is made throughout the use, at all scales, of well-known Riedel model (Riedel, 1929; Tchalenko and Ambraseys, 1970), which has been shown to be successful in understanding the mega- to meso-scale structures evolution in volcanic environments (Taylor et al., 1994; Sibson, 1996; Van Wyk de Vries et al., 1998, Lagmay et al., 2005; Norini et al., 2006; Holohan et al., 2008; Cembrano et al., 2009; Nkono et al., 2009; Lavallée et al., 2014).

The Tres Vírgenes volcanic and geothermal active region is a good example of the above-mentioned problematics. In fact it is located in the rather complex and tectonically active geodynamic setting of the Gulf of California. Here, recent studies (CeMIE Geo P15 of SENER-CONACyT research project) performed by Garcia-Sanchez et al. (2019) on the oldest of the three Quaternary volcanic complexes in the region, La Reforma caldera complex (1.29 Ma, Garcia-Sanchez et al., 2019), allowed to build a general structural model of the area and to highlight the control exerted by regional structures on the evolutionary stages of the caldera complex. Nevertheless, the scarcity of well-preserved fault-related structures at the field scale hampered any investigation regarding large-scale deformation patterns, chronology between faulting and fluid circulation and fractal character of the mapped structures.

By investigating kinematics this work consolidates the structural model proposed for the Tres Vírgenes area, which is described as an overall transtensive system (Conly et al., 2005; Wong and Munguía, 2006; Antayhua et al., 2015). It also reconstructs with the Riedel-type deformation patterns and highlights the general syn- or post-faulting character of fluid circulation events along analysed regional faults, in accordance with Sibson (1981) fault-valve model and field data, to suggest likely episodes of local fluid pressure rise along fault planes. Additionally, this study quantifies the fractal character of regional faults inside the Tres Vírgenes area and linked to the Gulf of California geodynamic setting. Micro-structural analysis by means of optical microscope and quantitative image analysis is performed on eleven fault-rock samples collected in the shallowest and exposed part of the fault zone. The used methodologies include description of fault-related micro-structures, definition of the chronology between faulting and fluid circulation episodes, statistical analysis of fault-related deformation scale through length distribution and computation of fractal dimension (McGrath and Davidson, 1995; Gundmundsson et al., 2001; Harris et al., 2003; Kim et al., 2003, 2004; Odling et al., 2004; Johansen et al., 2005; Agosta and Aydin, 2006). This work encourages quantitative characterization of fault-

related micro-structural patterns in volcanic regions, widely known as difficult settings for applying routine structural analysis approaches and techniques.

5.3 Geodynamic and geological setting

The Tres Vírgenes active geothermal region (10 MW installed running capacity, Gutiérrez-Negrín, 2015), lies in the Santa Rosalía basin, about 30 km NW from the Santa Rosalía town, on the eastern side of the Gulf of California, in the Baja California peninsula (Mexíco, Fig. 5.1). The whole region is affected by a complex and active tectonic setting, resulting from oblique divergence following Tertiary subduction ceasing between the Farallon and North America plates (Ferrari et al., 2018). The orthogonal and oblique rifting phases linked to the modern Gulf of California development (Stock and Hodges, 1989; Fletcher et al., 2007) led to the formation of a series of offshore and onshore basins delimited by active faults, like the Santa Rosalía basin, a NW-SE trending half-graben basin bounded by NE dipping structures (Aragón-Arreola et al., 2005). Following stress reorganization in the region since 3.5 Ma (Atwater, 1970; Angelier et al., 1981; Ortlieb et al., 1989; Zanchi, 1994; Umhoefer et al., 2002; Aragón-Arreola et al., 2005) the predominant style of active faulting inside the Santa Rosalía basin became right-lateral oblique-slip. Ongoing active faulting and erosion processes are also confirmed by the offshore slope morphology of the basin (Nava-Sanchez et al., 2001). Volcanic activity within the Santa Rosalía basin initiated in Quaternary, forming the only-known silicic polygenetic centres in the whole Gulf of California (Schmidt, 1975; Sawlan and Smith, 1984; Conly et al., 2005; Gutiérrez-Negrín, 2015): La Reforma (1.29 Ma, García-Sánchez et al., 2019), Sierra Aguajito (1.17 Ma, Schmitt et al., 2006) and Pleistocene to Holocene Tres Vírgenes (López et al., 1993; Avellán et al., 2018, Fig. 5.1). Since the early stages of geothermal exploration, appraisal and development of the currently producing Las Tres Vírgenes geothermal field (Fig. 5.1), several studies have been focusing on geological processes responsible for developing the warm spots feeding the plant and causing extensive hydrothermal circulation through the region (Wong and Munguía, 2006; Macías and Jiménez, 2012, 2013; Antayhua-Vera et al., 2015) and on the heat source of the system (Lopez et al., 1989, 1995; Lopez et al., 1993; Portugal et al., 2000; Verma et al., 2006). More recently, Pellicioli et al., (submitted, a) have tried to compensate the scarcity of published structural data for the region, by focusing on La Reforma caldera complex fossil geothermal system, with the aim of unravelling the interplay between structures (regional and volcanic) and geothermal processes. This study frames within a recent phase of renewed interest in the region (CeMIE Geo P15 of SENER-CONACyT research project awarded to Universidad Nacional Autónoma de México), that led to

improve the knowledge on geological, geochemical and evolutionary aspects of La Reforma caldera complex (García-Sánchez et al., 2019, Fig. 5.2c) and Sierra Aguajito (still ongoing, Osorio-Ocampo et al., 2016, Fig. 5.2b), with the aim of reinforcing the characterization of key aspects involved in the exploitation of the Las Tres Vírgenes geothermal plant, of high relevance for the Baja California peninsula population (Gutiérrez-Negrín, 2015).

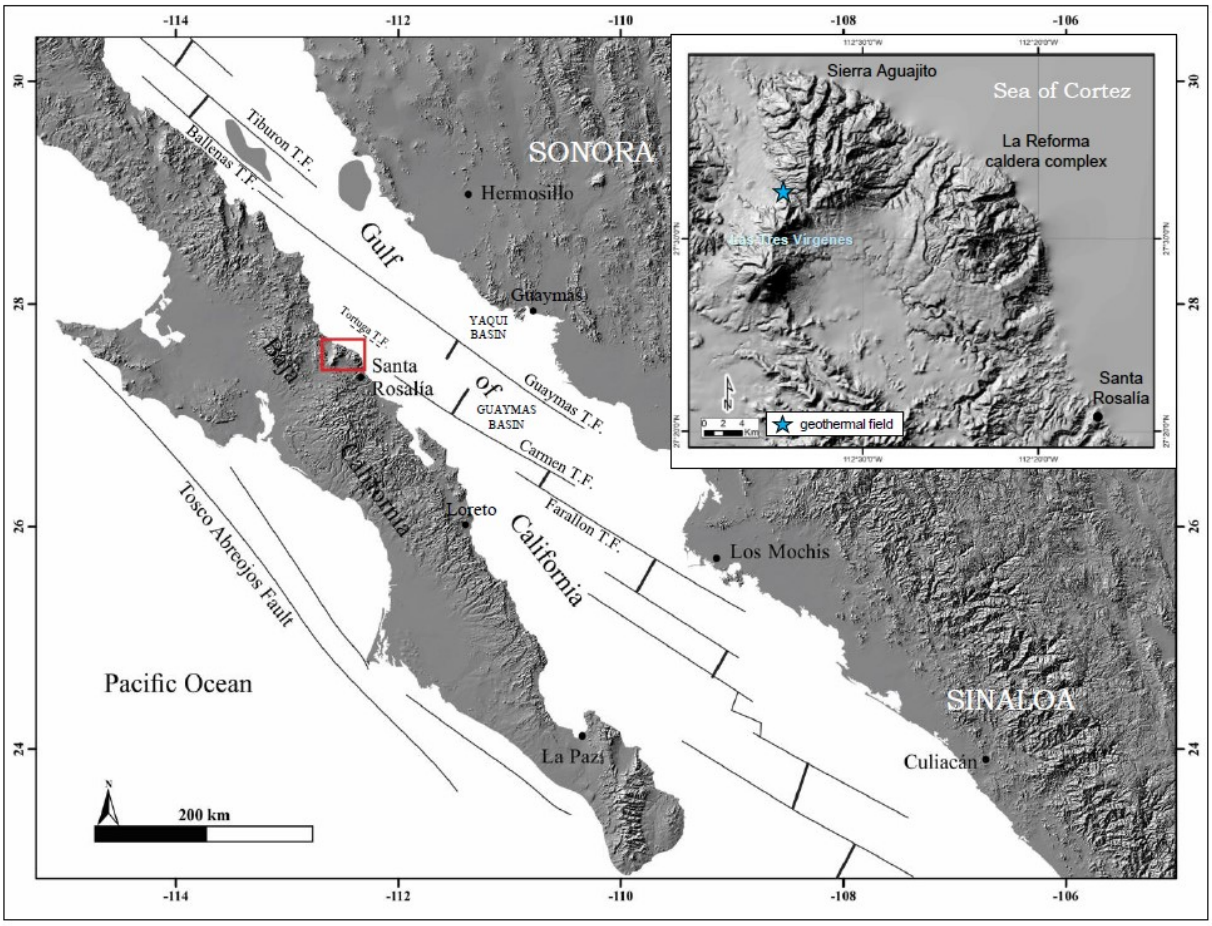

Figure 5.1 Location of the Tres Vírgenes region and geothermal field, Baja California, Mexico (modified after García-Sánchez et al., 2019 and Pellicioli et al., submitted, a).

5.4 Samples collection and methodologies of analysis

A total of eleven fault-rock samples (Table 5.1) were collected across the Tres Vírgenes area on structures crossing La Reforma and Sierra Aguajito complexes. Figure 5.2 and Table 5.1 illustrate the location, lithology and orientation of collected specimens. The major regional fault systems recently mapped by Pellicioli et al. (submitted, a) were chosen for this study: the Azufre, Santa Ana and

Infierno fault systems (Fig. 5.2). In detail, samples BC-C8 and BC-C17 to BC-C24 belong to the NW-SE trending Azufre transtensive fault system, samples BC-C7 and BC-C16 to the parallel Santa Ana fault system and sample BC-C14 to the NE-SW oriented Infierno fault. The uneven number of collected samples per fault is due to the intrinsic difficulty in finding well-exposed and preserved fault surfaces in the study area, and in active volcanic areas in general. When not covered by Quaternary volcanics belonging to La Reforma caldera and Sierra Aguajito complexes, the Azufre and Infierno fault systems run alongside set canyons outside La Reforma caldera depression (Fig. 5.2). Samples were collected within their decametric-wide damage zone, mostly along subsidiary structures that bound the gouge-cataclastic fault core (Chester and Logan, 1987; Smith et al., 1990; Andersson et al., 1991; Scholz and Anders, 1994; Goddard and Evans, 1995) and display few centimetres to meters displacement and locally poorly developed damage zones (Class A and B fault zones, Gray et al., 2005). BC-C24 was instead directly collected along the Azufre main fault plane, whose damage zone narrows to one or few discrete structures in the site of collection (Fig. 5.2B). On the contrary, the Santa Ana fault system entirely dissects La Reforma caldera depression (Fig. 5.2) and the Sierra Aguajito volcanic complex, interfering with related volcano-tectonic structures. Samples from the Santa Ana fault system (BC-C7 and BC-C16) were collected in La Reforma southern intra-caldera sector, where the Santa Ana fault system damage zone interferes with deformation linked to caldera collapse (ring-faults) and resurgence structures. Sample BC-C7 in particular could not be oriented, due to the pervasively brittle character of the sampling site (e.g. cataclastic rock). All other samples collected along the above-mentioned structures were directly oriented in the field, by marking the direction of shear with a felt-tip pen and collecting the sample perpendicularly to the shear direction, where the best chance of observing kinematic indicators and structures commonly is.

All collected samples were reduced to thin sections and then impregnated with blue dimethyl for planned future porosity and permeability characterization. An arrow on each thin section marks the projection of the shear direction. Following lithological analysis aimed to identify the main mineral assemblages occurring within the fault zone, the thin sections were carefully investigated for micro-structural elements like micro-fractures and veins and fault-related sigmoids. This was performed with the Axioskop Pol Routine Microscope (transmitted and reflected light) by Carl Zeiss Microscopy ® at the Earth Sciences Department “Ardito Desio” of the University of Milan. Particular attention was paid to the identification of the chronology between faulting-related deformation and fluid circulation, including hydro-fracturing processes. The generalized lack of relevant fracture and vein sets in the protolith away from fault zones allowed to exclude the inherited and non-fault-related character of the

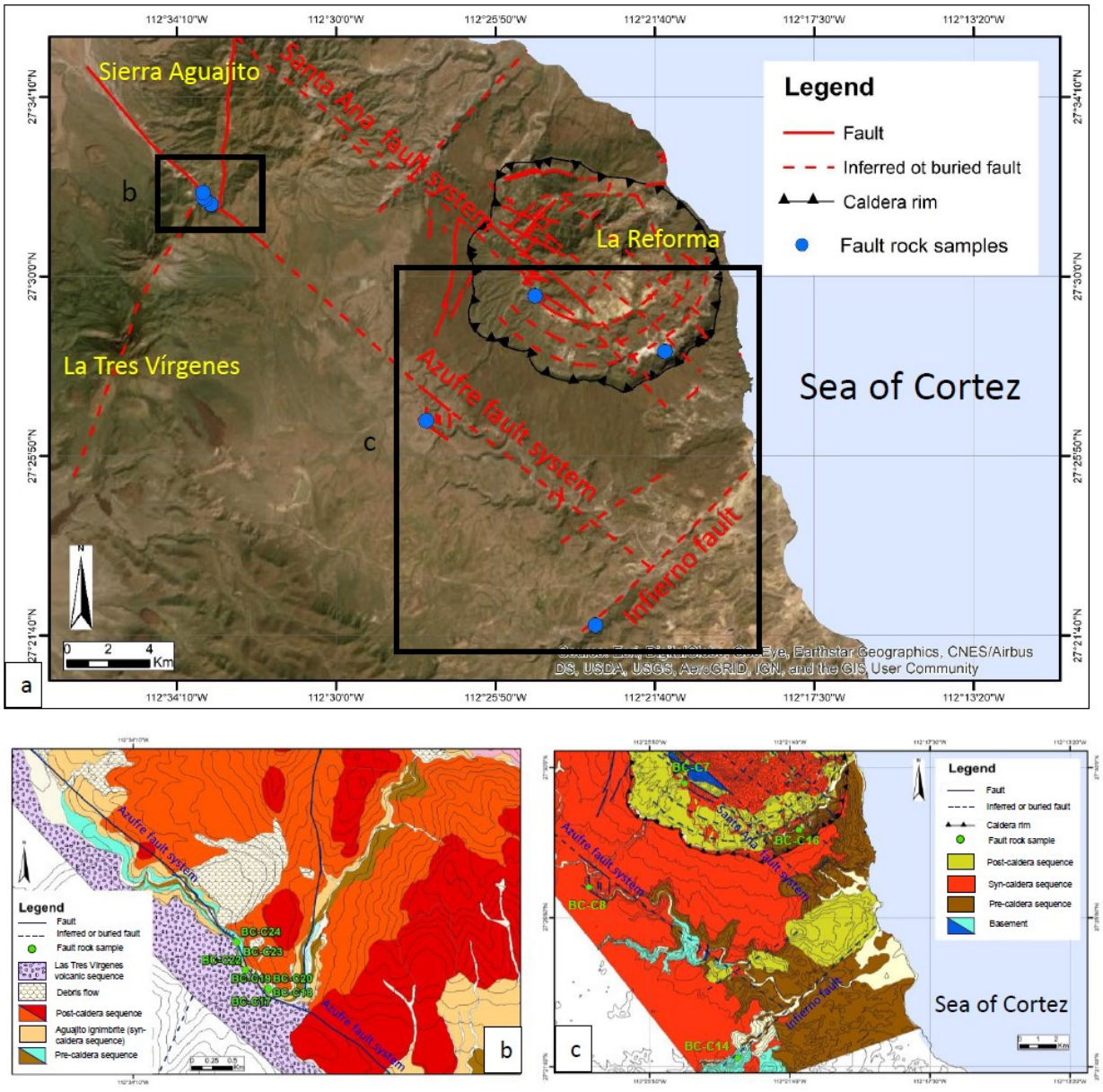

Figure 5.2 Location of samples collected across the Tres Vírgenes region (modified after Osorio-Ocampo et al., 2016, García-Sánchez et al., 2019 and Pellicioli et al., submitted, a).

analysed micro-structures. Elements captured by photos taken with the Axioskop microscope photographic equipment were manually re-traced and the resulting sketch uploaded and processed with the Fiji (Fiji Is Just ImageJ) © software, an open-source image processing package able to model the number of elements, total area covered by elements, elements average size, perimeter and angle with respect to a default axis. Direct measurement of the elements length was performed with the Fiji (Fiji Is Just ImageJ) © software in Fiji units, and then converted into millimetres for each sample based on the scale of the optical-microscope derived photo processed by Fiji software. The statistical

distribution of micro-fractures and veins lengths and angles formed with the fault projected shear direction was plotted, and the micro-fractures fractal dimension (D) was determined by simple fractal statistics (Mandelbrot, 1983). For the analysed datasets the fractal dimension was approximated to the *a* coefficient of the linear regression line ($y=ax+b$) fitting the ratio between the sample maximum micro-fracture length and the cumulative length interval (1/s) versus the frequency of micro-fractures falling within a certain length interval (N(s)) in a logarithmic scale plot. The ratio between the elements smallest measured length and the minimum length of the investigated structure was also estimated in order to gain information on the extent reached by deformation at the micro-scale. Image analysis could not be performed on samples BC-C7 and BC-C8, respectively due to its non-oriented character with respect to the shear zone (BC-C7) and to the lack of micro-structures (BC-C8).

Table 5.1 Location and characteristics of analysed fault rock samples

Location	Sample	Coordinates	Sample characteristics	Texture and Mineralogy
Santa Ana fault system	**BC-C7 IGNIMBRITE (LA REFORMA SYN-CALDERA SUCCESSION*)**	112°24'47.588"W 27°29'33.192"N	**Not oriented sample** collected in the south-western intra-caldera sector within a complicated site where resurgence-induced tectonically reverted ring faults juxtapose with regional gulf-inherited transtensive structures.	Eutaxitic texture with fine grained and vitreous ground mass (fluidal glass, shards); Phenocrysts of quartz, highly fractured plagioclase, K-feldspar, amphibole and rare pyroxene. Presence of lithics and pumices. Greenish alteration minerals pervade the sample and recrystallize inside pumice voids.
	BC-C16 LAVA (LA REFORMA POST-CALDERA SUCCESSION*)	112°21'23.773"W 27°28'15.673"N	**NW-SE trending (045°/70°) normal fault** located inside the outer ring fault damage zone in the south-eastern intra-caldera sector.	Trachytic texture given by aligned K-feldspar phenocrysts in the groundmass. Glass inside the groundmass. Phenocrysts include: K-feldspar, plagioclase, hornblende amphibole and oxides.
Azufre fault system	**BC-C8 IGNIMBRITE (LA REORMA SYN-CALDERA SUCCESSION*)**	112°27'38.085"W 27°26'39.097"N	**NW-SE trending cataclastic band** belonging to the NW-SE trending regional Azufre fault system, running south of La Reforma caldera complex.	Very poorly cohesive rock with unrealistically high porosity (blue-dimethyl coloured areas) due to issues during thin section preparation. Micro-crystalline and vitreous groundmass with loose plagioclase, orthopyroxene, quartz, green amphibole, K-feldspar fractured phenocrysts. Lithics affected by pervasive saussuritization. Recrystallization of fiammes (pumices).
	BC-C17 IGNIMBRITE (SIERRA AGUAJITO SYN-CALDERA SUCCESSION*)	112°33'15.934"W 27°31'39.999"N	**ENE-WSW trending (160/40) minor reverse fault** belonging to the NW-SE trending regional Azufre fault and running across the Azufre canyon, south from Sierra Aguajito volcanic complex.	Micro-crystalline groundmass with bands of fluidal glass embedding loose phenocrysts of highly fractured plagioclase plagioclase, K-feldspar, quartz, amphibole and orthopyroxene. Presence of plagioclase and K-feldspar re-crystallized lithics and pumices (often displaying fiamme texture). Lithics also affected by saussuritization and argillification. Rare amygdula.

	BC-C18 IGNIMBRITE (SIERRA AGUAJITO SYN-CALDERA SUCCESSION*)	112°33'16.026"W 27°31'40.064"N	**NNW-SSE trending (080/80) fault of unknown kinematics** belonging to the NW-SE trending regional Azufre fault and running across the Azufre canyon, south from Sierra Aguajito volcanic complex.	Undistinguishable and vitreous groundmass in which only few quartz, plagioclase and K-feldspar phenocrysts could be identified. Pumices and lithics could not be recognized. Presence of oxides and strong clay alteration that sometimes fully replaces phenocrysts (or lithics).
	BC-C19 IGNIMBRITE (SIERRA AGUAJITO SYN-CALDERA SUCCESSION*)	112°33'16.075"W 27°31'40.553"N	**NW-SE trending (240/65) fault of unknown kinematics** belonging to the NW-SE trending regional Azufre fault and running across the Azufre canyon, south from Sierra Aguajito volcanic complex.	Undistinguishable and vitreous groundmass in which only few quartz, plagioclase and K-feldspar phenocrysts could be identified. Lithics fully re-crystallized by calcite. strong clay alteration that sometimes fully replaces phenocrysts or lithics.
	BC-C20 IGNIMBRITE (SIERRA AGUAJITO SYN-CALDERA SUCCESSION*)	112°33'16.007"W 27°31'40.571"N	**NNW-SSE trending (080/80) reverse fault** belonging to the NW-SE trending regional Azufre fault and running across the Azufre canyon, south from Sierra Aguajito volcanic complex.	Vitreous groundmass (often with shards, fluidal glass and eutaxitic flow structures) containing lithics (including trachytic lavas with spinifex pyroxene) and loose phenocrysts of plagioclase, quartz, K-feldspar, clino- and ortho-pyroxene and amphibole. Presence of recrystallized fiammes. Diffuse argillitic alteration.
	BC-C22 IGMIMBRITE (SIERRA AGUAJITO SYN-CALDERA SUCCESSION*)	112°33'24.864"W 27°31'47.133"N	**NNE-SSW trending (110/70) normal fault** belonging to the NW-SE trending regional Azufre fault and running across the Azufre canyon, south from Sierra Aguajito volcanic complex.	Vitreous (often with shards, fluidal glass and eutaxitic flow structures) groundmass containing highly fractures quartz, plagioclase, K-feldspar and clino-pyroxene phenocrysts. Phenocrysts are often cross-cut by veins. Presence of pumices, often recrystallized. Diffuse argillitic alteration. Sample collected in the hanging wall block.
	BC-C23 IGNIMBRITE (SIERRA AUAJITO SYN-CALDERA SUCCESSION*)	112°33'27.842"W 27°31'50.046"N	**ENE-WSW trending (150/80) reverse fault** belonging to the NW-SE trending regional Azufre fault and running across the Azufre canyon, south from Sierra Aguajito volcanic complex.	Fine-grained to micro-crystalline groundmass with vitreous portions (eutaxitic textures and shards), containing K-feldspar, quartz, plagioclase and clino-pyroxene loose phenocrystals. Presence of oxides and abundant lithics (lava). Diffuse argillitic alteration.
	BC-C24 IGNIMBRITE (SIERRA AGUAJITO PRE-CALDERA SUCCESSION*)	112°33'28.869"W 27°31'57.057"N	**Azufre fault plane: NW-SE striking (035/60) with slickensides (120/15) indicating dextral-normal kinematics**. Sample collected directly on the Azufre canyon walls.	Very fine-grained groundmass displaying calcite microsparite and containing: mosaics of replacive calcite crystals (originally lithics and pumices), clay-altered lithics, quartz, plagioclase and hornblende amphibole sparse loose phenocrysts, oxides.
Infierno fault	**BC-C14 LAVAS (LA REFORMA PRE-CALDERA SUCCESSION*)**	112°23'12.894"W 27°21'54.19"N	**NW-SE trending (235/50) fault of unknown kinematics** within the Infierno fault damage zone along the Infierno canyon.	Fault breccia where fibrous calcite crystals cement pyroclastic flow and lava fragments and rare loose quartz crystals. Lava clasts display trachytic texture with glass, loose phenocrysts of K-feldspar, plagioclase, quartz, abundant and highly altered amphibole, clino- and ortho-pyroxene. Pyroclastic flow fragments display very fine-grained groundmass with sparse loose crystals of plagioclase, quartz and K-feldspar. Clay-altered lithics are also present.

(*) for La Reforma and Sierra Aguajito pre-, syn- and post-caldera succession please refer to García-Sánchez et al. (2019), Schmitt et al (2006) and Osorio-Ocampo et al. (2016).

5.5 Results

In addition to a brief description of mineralogical composition (Table 5.1) this section illustrates the outcomes of micro-structural and image analyses. Results are organized in sub-paragraphs accordingly to the structure of belonging and presented for each sample separately. Rose diagrams in Figures 5.3 to 5.5 summarize unweighted (red diagrams) and length-weighted (green diagrams) angles formed by the elements with the fault projected shear direction, based on Nixon et al. (2011). Length data in millimetres is plotted against the cumulative number of measured elements and summarized in histograms in Figure 5.6 to display the length range of identified elements, while information regarding their frequency distribution is contained in Table 5.2. Fractal dimension determined on micro-fractures is graphically illustrated in plots of Figure 5.7 for each sample and summarized in Table 5.3. Table 5.3 also contains indication of the ratio between the micro-fractures and faults minimum lengths.

5.5.1 Micro-structural analysis

5.5.1.1 The Santa Ana fault system

BC-C7

The non-oriented BC-C7 sample was collected inside a locally hydrothermally altered syn-caldera ignimbrite belonging to La Reforma caldera complex (Table 5.1, García-Sánchez et al., 2019). Detected micro-fractures include a set parallel to the primary magmatic flow foliation and to the stretching direction of pumices and another set cross-cutting flow structures and phenocrysts, although lacking clear dislocation. The younger set commonly arranges in rhomboidal or pull-apart structures (Appendix Fig. 5.9a), suggesting the presence of a transtensive component of motion, reasonably linked to the close transtensive NW-SE trending Santa Ana fault system (Fig. 5.2).

BC-C16

Sample BC-C16 relates to a 315°N trending local normal fault cross-cutting a post-caldera lava flow close to La Reforma caldera rim (Table 5.1, García-Sánchez et al., 2019). The prevalent normal dip-slip kinematics was inferred in the field based on slickensides and few centimeters displacements. At the thin section scale, sample BC-C16 displays sets of micro-fractures filled by brownish mineral assemblages, sometimes forming alteration bands along the micro-fractures edges. The lack of unfilled

micro-fractures across sample BC-C16 suggests a post-faulting fluid circulation episode. Identified micro-fractures often follow the primary magmatic flow foliation and trachytic texture, while at times deviate and cross-cut it, suggesting the concomitant presence of ductile (magmatism) and brittle (faulting) deformation (Appendix Fig. 5.9b). This is not surprising being BC-C16 collected inside La Reforma caldera ring-fault system damage zone (Fig. 5.2). The dislocation of magmatic foliation and phenocrysts is however too small to be quantified, even if weak clues of the presence of a strike-slip component of motion are provided by few en-echelon and pull-apart arrangement of micro-fractures (Appendix Fig. 5.9c).

5.5.1.2 The Azufre fault system

BC-C8

Sample BC-C8 was collected along the cataclastic horizons disjointing La Reforma syn-caldera ignimbrites in proximity a local pull-apart basin formed by the NW-SE trending Azufre fault system and a minor parallel structure running to the S (Fig. 5.2). The already mentioned lack of representative micro-structures, together with cohesion issues arisen during thin section preparation and linked to pervasive argillitic alteration prevented performing image analysis on this sample (Appendix Fig. 5.9d). All other samples belonging to the Azufre fault system were collected along the Azufre canyon, NW of the Sierra Aguajito younger volcanic complex (1.17 Ma, Schmitt et al., 2006).

BC-C17

Sample BC-C17 comes from the easternmost part of the canyon (Fig. 5.2) and represents a 070°N trending local reverse fault affecting the succession up to the Sierra Aguajito most recent caldera-forming ignimbrite eruption (1.17 Ma, Schmitt et al., 2006; García-Sánchez et al., 2019). Few distinct open micro-fractures and scarce veins cross-cut magmatic flow structures and phenocrysts. A strike-slip component of motion is suggested by the presence of en-echelon, rhomboidal and step-over geometries, even if offsets are too small to be quantified (Appendix Fig. 5.9e).

BC-C18 and BC-C19

Samples BC-C18 and BC-C19 represent NNW-SSE trending (respectively striking 350° and 330°, Table 5.1) faults of unknown kinematics (no slickensides) again crossing the whole canyon succession and displaying quite similar texture and mineralogy. Due to cohesion issues, BC-C18 and BC-C19 thin sections thickness is higher than normal, rendering hard to define the Aguajito ignimbrite mineralogical assemblage Table 5.1). Both samples are characterized by a dense network of open (blue-dimethyl filled) micro-fractures at times following and other times cross-cutting phenocrysts

borders but without developing clear dislocation. Mixed plagioclase, quartz and calcite veins were identified in sample BC-C18 (Appendix Fig. 5.9f), while sample BC-C19 totally lacks veins or other indicators of fluid circulation along the fault plane (Appendix Fig. 5.9g).

BC-C20

Sample BC-C20 was collected on the NNW prolongation of the BC-C18 fault. It is the only sample were offsets of eutaxitic magmatic textures and phenocrysts borders by open micro-fractures could be detected at the optical microscope (Appendix Figs. 5.9h and i). Contrarily to BC-C18 sample, this portion of the fault lacks signs of extensive fluid circulation (veins).

BC-C22

The BC-C22 NNE-SSW oriented normal fault zone cross-cutting the Aguajito ignimbrite is very poor in micro-fractures and lacks veins. The rare micro-fractures are small, difficult to follow and sometimes lining phenocrysts while other times cross-cutting them with no evident signs of dislocation (Appendix Fig. 5.9j).

BC-C23

Moving towards the NW, the BC-C23 NE-SW trending reverse fault cross-cutting the succession up to the Aguajito ignimbrite displays a large number of micro-fractures and veins, as well as differential alteration bands at high angle with respect to the shear direction (Appendix Fig. 5.9k). The differential degree of alteration seems to be controlled by lithology, as the reddish and more deeply altered portions are those where glass and pumices are more abundant, while quartz, plagioclase and K-feldspar phenocrysts borders are left intact. Open micro-fractures cross-cutting eutaxitic flow textures sometimes run along these alteration bands borders, suggesting they nucleated along weakness zones marked by local lithological heterogeneities within the rock. However, these micro-fractures terminations are uncertain and do not seem to extend beyond the thin section external borders. The brownish filling of some of BC-C23 micro-fractures suggests they carried fluids responsible for the lithologically-controlled differential alteration (Appendix Fig. 5.9l). This scenario thus supports post-faulting circulation episodes. Preliminary SEM and electron microprobe analyses on some of these fluid-carrying veins revealed a mixture of silicates, including plagioclase and quartz. Furthermore, these veins are smaller in amplitude than micro-fractures and quite often develop sigmoidal patterns suggesting the presence of a strike-slip shear component, also supported by few chlorite veins forming tension gashes.

BC-C24

Sample BC-C24 was collected inside the Sierra Aguajito pre-caldera succession as progressively older units crop out moving along the Azufre canyon. As already introduced, BC-C24 best represents the Azufre fault system, here dipping towards the NE, striking NW-SE (Table 5.1) and exhibiting a dextral-normal kinematics, as indicated by slickensides and striae along the canyon walls. BC-C24 is also the only sampled structure belonging to the Azufre fault system damage zone displaying significant amount of calcite sealing micro-fractures. Calcite is present under the form of: groundmass microsparite; prismatic to equant drusy calcite growing perpendicular to fracture walls (crystal size from 100 to 500 microns) and forming veins; few mm long and 50-100 microns thick mixed plagioclase-quartz-calcite veins; replacive calcite on volcanic clasts (possibly replacing lithics and pumices, Appendix Fig. 5.9m) forming an equant mosaic of calcite crystals 100 to 200 microns in size. Mixed plagioclase-quartz-calcite veins sometimes dextrally offset replacive calcite on volcanic clasts (Appendix Fig. 5.9n), although they line these calcite crystals equant mosaics in most cases. A later development of mixed plagioclase-quartz-calcite veins in respect to drusy calcite veins is indicated by their crosscutting relationships. In addition to calcite veins, several open micro-fractures were also recognised in sample BC-C24.

5.5.1.3 The Infierno fault system

BC-C14

Sample BC-C14 was collected on a NW-SE trending local fault plane of unknown kinematics cross-cutting the Santa Lucia andesites, providing the basement for La Reforma caldera complex (19.25 Ma, García-Sánchez et al., 2019), along the Infierno canyon damage zone, SW of the Azufre fault system inferred prolongation (Fig. 5.2, García-Sánchez et al., 2019). Similarly to and in greater measure than sample BC-C24, calcite mineralization pervades the fault plane cementing isolated and highly fractured pyroclastic and lava fragments and giving to BC-C14 sample the aspect of a proper fault breccia. Three calcite cement phases were recognised in sample BC-C14: an irregular 50-100 microns thick calcite rim of equant microsparite (10-50 microns in size) lining angular volcanic clasts (Appendix Fig. 5.9o); 1-2 mm long and 1 mm wide fans of fibrous cement with ondulose extinction growing on top of the 50-100 microns thick calcite rim and perpendicular to the volcanic clast outer surface (Appendix Fig. 5.9o); calcite-filled veins cross-cutting the previous cement phases but too small and sparse to perform any proper image analysis. Calcite also occurs inside volcanic clasts as replacive calcite. Most of BC-C14 sample open and calcite-filled micro-fractures are confined within volcanic clasts embedded in fibrous calcite cement.

5.5.2 Image analysis

5.5.2.1 Angles with shear direction and fluid circulation along fault planes

5.5.2.1.1 The Santa Ana fault system

BC-C16

The most common angles formed by micro-fractures filled by post-faulting fluid circulation and the fault projected shear direction in sample BC-C16 are, in order of abundance, 10° to 35°, around 60° and minor than 10° and 45°-50° (Figs. 5.3a to c). These have been interpreted respectively as R or P, R' and T Riedel shears (Fig. 5.10 Appendix, Cloos, 1928; Riedel, 1929; Hills, 1963). R and P Riedels and subordinately cross-cut both flow structures and phenocrysts, even though at times running parallel to magmatic flow.

5.5.2.1.2 The Azufre fault system

BC-C17

The biggest fracture characterizing sample BC-C17 is a R' Riedel shear forming an angle of about 85° with the shear direction and displaying a stepped or en-echelon geometry, where each segment shows a rhomboidal-type geometry (Fig. 5.3e). Segments connecting the steps develop at 50°-60° from the shear direction. Two smaller micro-fractures forming angles of 5° with the shear direction locally turn to form wider (30°-35°) angles, developing local step-overs and cross-cutting phenocrysts (Fig. 5.3d). Rose diagrams in Figures 5.3f to i display a predominance of R' Riedels oriented micro-fractures, followed by T and R or P. Similar trends apply to veins, even though no faulting-fluid circulation chronology could be established.

BC-C18 and BC-C19

Image analysis on sample BC-C18 confirmed the presence, in order of abundance, of T, R and P and R' Riedels micro-fractures and veins. Quite often micro-fractures forming angles of 45° with the shear direction (T Riedels) tend to vary their orientation, suggesting either a contemporaneity or an alternation over a short time interval of faulting and hydrofracturing processes (Figs. 5.3j to o). On the contrary, in sample BC-C19 T, Riedels are less abundant and R' Riedels predominate, followed by R and P low angle Riedels, as testified by few but prominent fractures dissecting the thin section from side to side and forming an average angle of 75° to 85° with the shear direction (Figs. 5.4a to c).

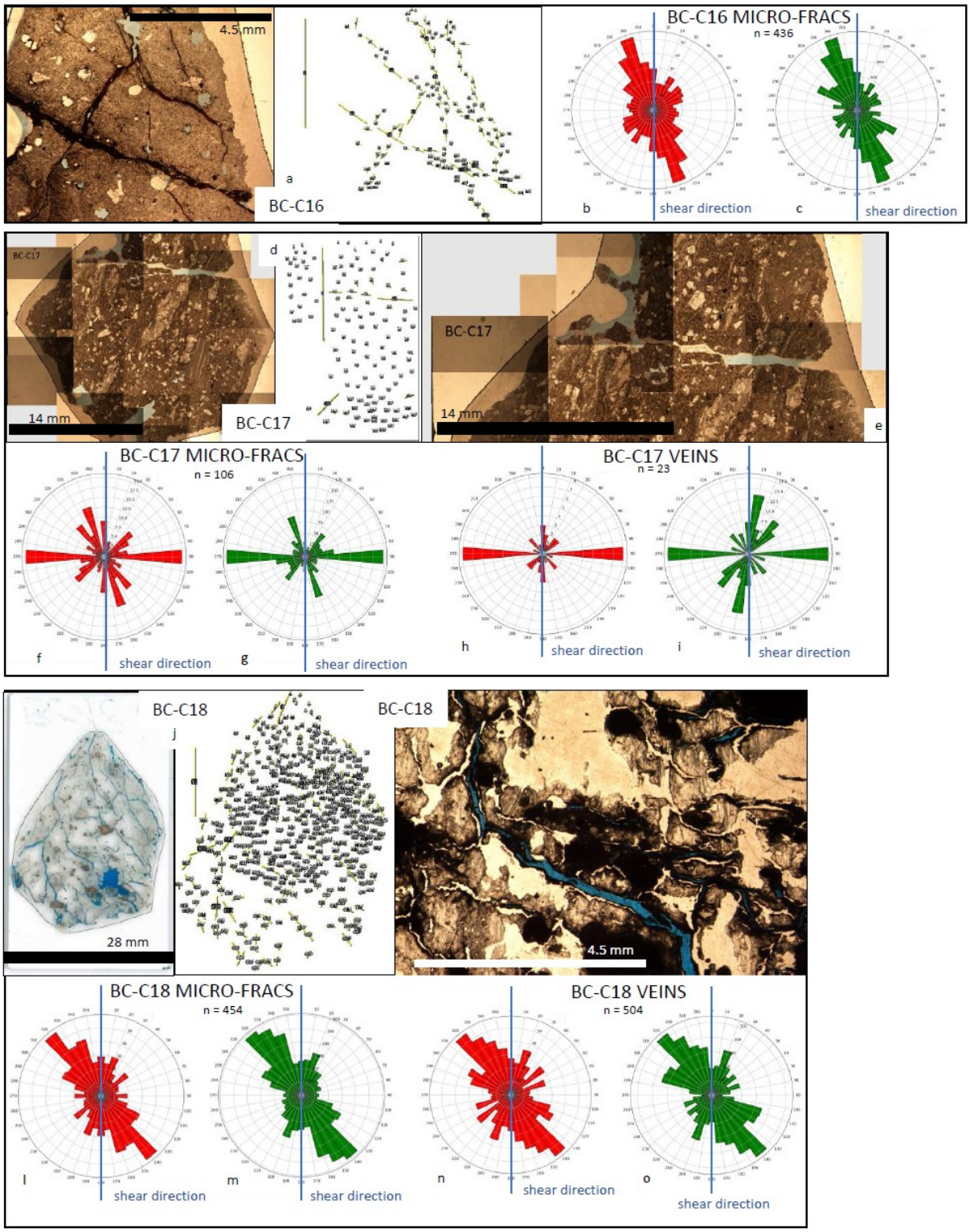

Figure 5.3 Results of image analysis on samples BC-C16, BC-C17 and BC-C18. Rose diagrams indicate the angles formed by micro-fractures and veins with the fault projected shear direction (red rose diagrams are unweighted, while green rose diagrams are length-weighted).

BC-C20

The most prominent micro-fracture characterizing BC-C20 sample displays an overall orientation at 45°-50° with respect to the shear direction and cross-cuts eutaxitic magmatic structures. Locally, this fracture changes orientation to form angles of 30° and 10°-15° with the shear direction (Figs. 5.4d and 5.4f). It is indeed along this lower angle segments, representing R or P Riedels, that most of the rhomboidal features (30°) and dextral or left-laterally offset phenocrysts (10°-15°) develop (Appendix Fig. 5.9i). This suggests hydrofracturing processes occurred synchronously to faulting processes that produced shear along this fracture (sigmoid structures and offset phenocrysts).

BC-C22

Scarce micro-fractures in sample BC-C22 mainly represent R' and R and P Riedels, and subordinately of T Riedels (Figs. 5.4g and i). No signs of extensive fluid circulation along the fault plane were recognised.

BC-C23

The largest of the micro-fractures marking differential alteration bands in sample BC-C23 forms an angle of 60°-80° with the shear direction, without showing any shear indicator. Micro-fractures and veins focus along R or P, R' and T Riedel shears directions (Figs. 5.4j to n) and predominantly form high angles (60°-85°) with the shear direction, suggesting a post-faulting nature of fluid circulation.

BC-C24

Both open micro-fractures and drusy calcite veins in sample BC-C24 form high angles (above 60°-70°) with the shear direction (R' Riedels). Micro-fractures patterns also include subordinate T Riedels. Despite typical of calcite tension veins, the drusy texture and the crystals growth perpendicular to fracture walls were also found by Benedicto et al. (2008) in calcite-sealed fault related structures. Mixed plagioclase-quartz-calcite veins also follow R' Riedels trends, but they also subordinately grow along R and P and T Riedels directions (Figs. 5.5a to g). The combination of micro-structural and image analyses led to the identification of the following deformation phases in sample BC-C24: a faulting episode developing Riedel shears (1), filled by a first fluid circulating event precipitating drusy calcite veins (2) subsequently cross-cut by micro-fractures developed during another faulting episode (3) at times filled by a second fluid circulation event forming mixed plagioclase quartz-calcite veins (4). Given that mixed plagioclase-quartz-calcite veins sometimes produce dextral offsets within replacive calcite mosaics, it is possible that phases 3 and 4 were contemporaneous.

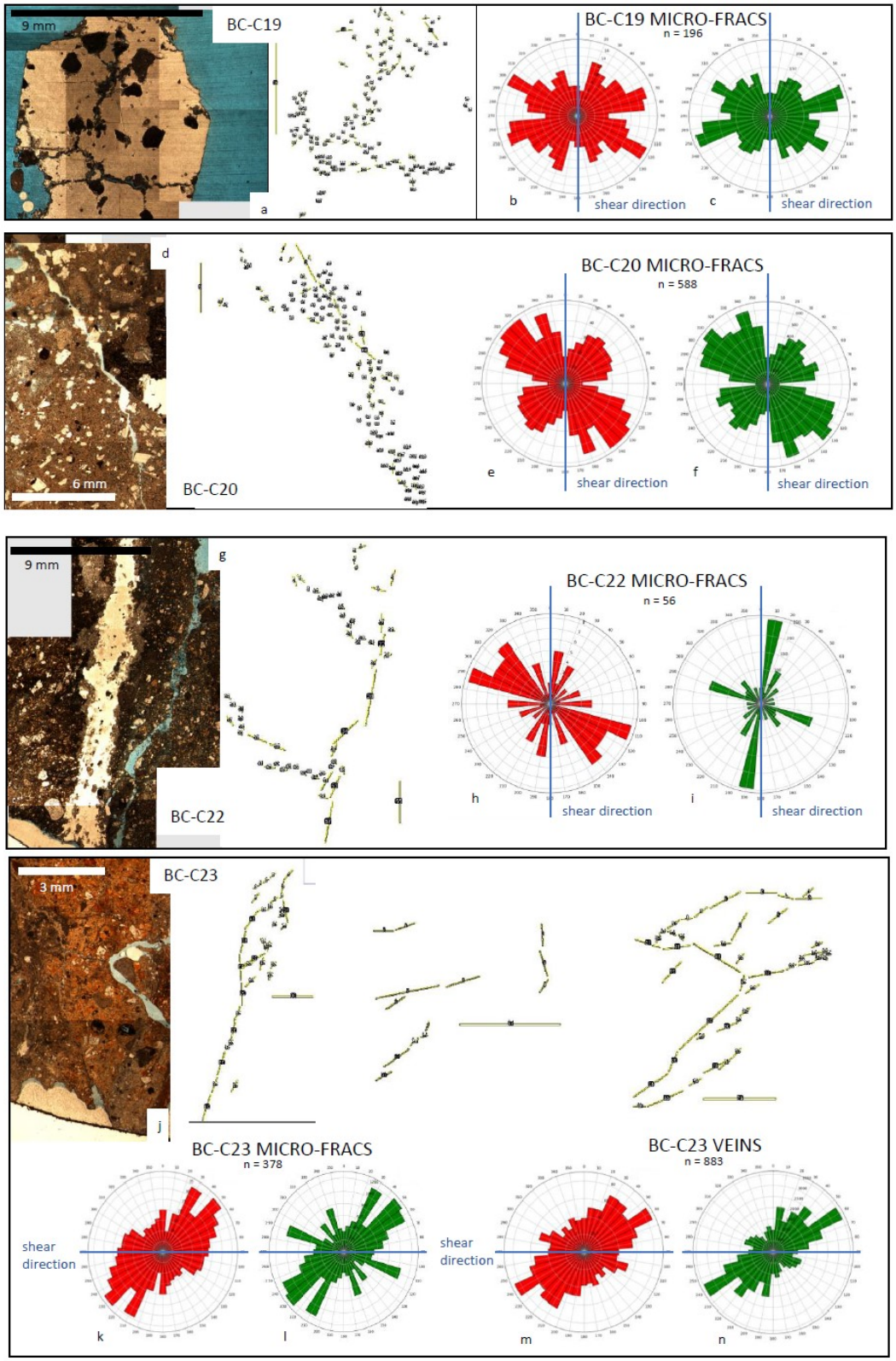

Figure 5.4 Results of image analysis on samples BC-C19, BC-C20, BC-C22 and BC-C23. Rose diagrams indicate the angles formed by micro-fractures and veins with the fault projected shear direction (red rose diagrams are unweighted, while green rose diagrams are length-weighted).

Overall, BC-C24 is thus characterized by repeated episodes of faulting followed by, or contemporaneous to, fluid circulation events. No relative chronology could be established in regards to groundmass microsparite.

5.5.2.1.3 The Infierno fault system

BC-C14

Angles formed by micro-fractures with the shear direction in sample BC-C14 are quite dispersed, but predominantly low (up to 30° and 40-45°) and representing R, P and T Riedels. The same applies to veins, with peaks in the distribution at very low angles (around 10°) and main frequency between 20° and 50° (Figs. 5.5h to m). These micro-fractures at times line lithics inside the embedded volcanic material while in other cases directly cut through them, with no evident signs of dislocation. Of particular interest is the en-echelon pattern of calcite crystals grown along a partially-filled micro-fracture crossing a volcanic fragment at an angle of 15°-35° with respect to the shear direction (Fig. 5.5i). This geometry indicates fluid circulation synchronous to a faulting episode bearing a strike-slip component of shear (en-echelon). The fact that most micro-fractures are confined within the volcanic clasts could indicate these developed during earlier deformation phases affecting the Santa Lucia volcanic basement before its involvement in the fault zone. This seems to be supported by the extensive circulation of calcite-rich fluids along these fractures and by the quite old age of the sampled fault-rock (Santa Lucia formation, 19.25 Ma, García-Sánchez et al., 2019). Also, the high dispersion of the angles formed with the shear direction supports this scenario. An alternative explanation could be that these not necessarily older micro-fracture sets could not propagate inside calcite cement fibrous crystals, due to the plastic deforming behaviour displayed by calcite when undergoing shear stresses, like in a fault-zone environment (Turner et al., 1954; Fredrich and Evans, 1989; Schubnel et al., 2006). This second hypothesis could explain why some of these fractures are open, even though washout of soft and/or clay fracture fillings could have occurred during thin section preparation and polishing operations on such a heterogeneous sample.

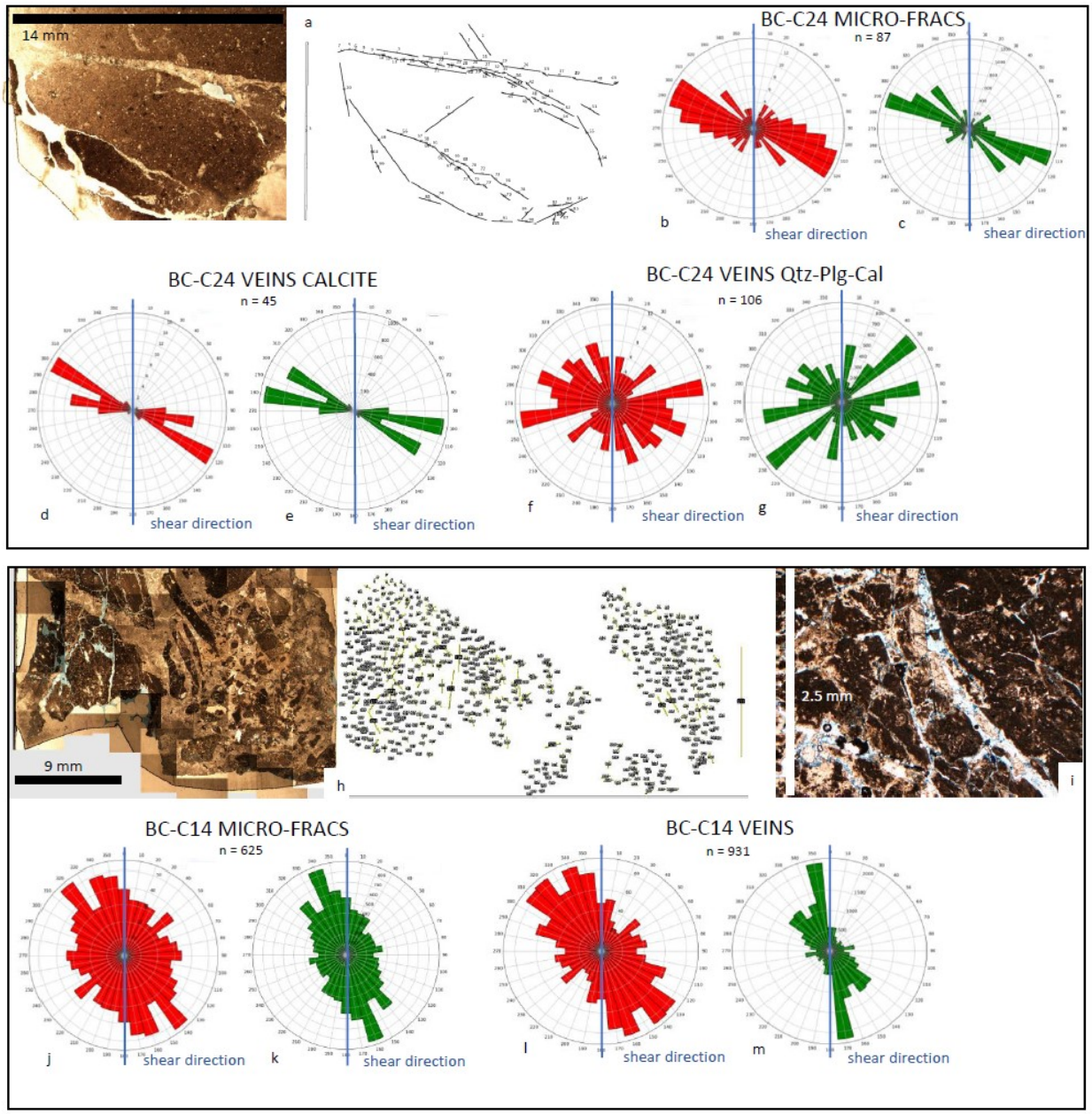

Figure 5.5 Results of image analysis on samples BC-C24 and BC-C14. Rose diagrams indicate the angles formed by micro-fractures and veins with the fault projected shear direction (red rose diagrams are unweighted, while green rose diagrams are length-weighted).

5.5.2.2 Length distribution and micro-fractures fractal dimension

Micro-fractures and veins measured lengths (mm) were plotted against the cumulative number of elements, and frequency histograms were derived for different length intervals (Fig. 5.6, Tables 5.2 and 5.3). The lognormal trend of the analysed samples length distributions implies that there is a large

number of short fractures and a very scarce number of long fractures. This is the opposite of what found in field-based works deploying scan lines (Cello et al., 2000; De Joussineau and Aydin, 2007),

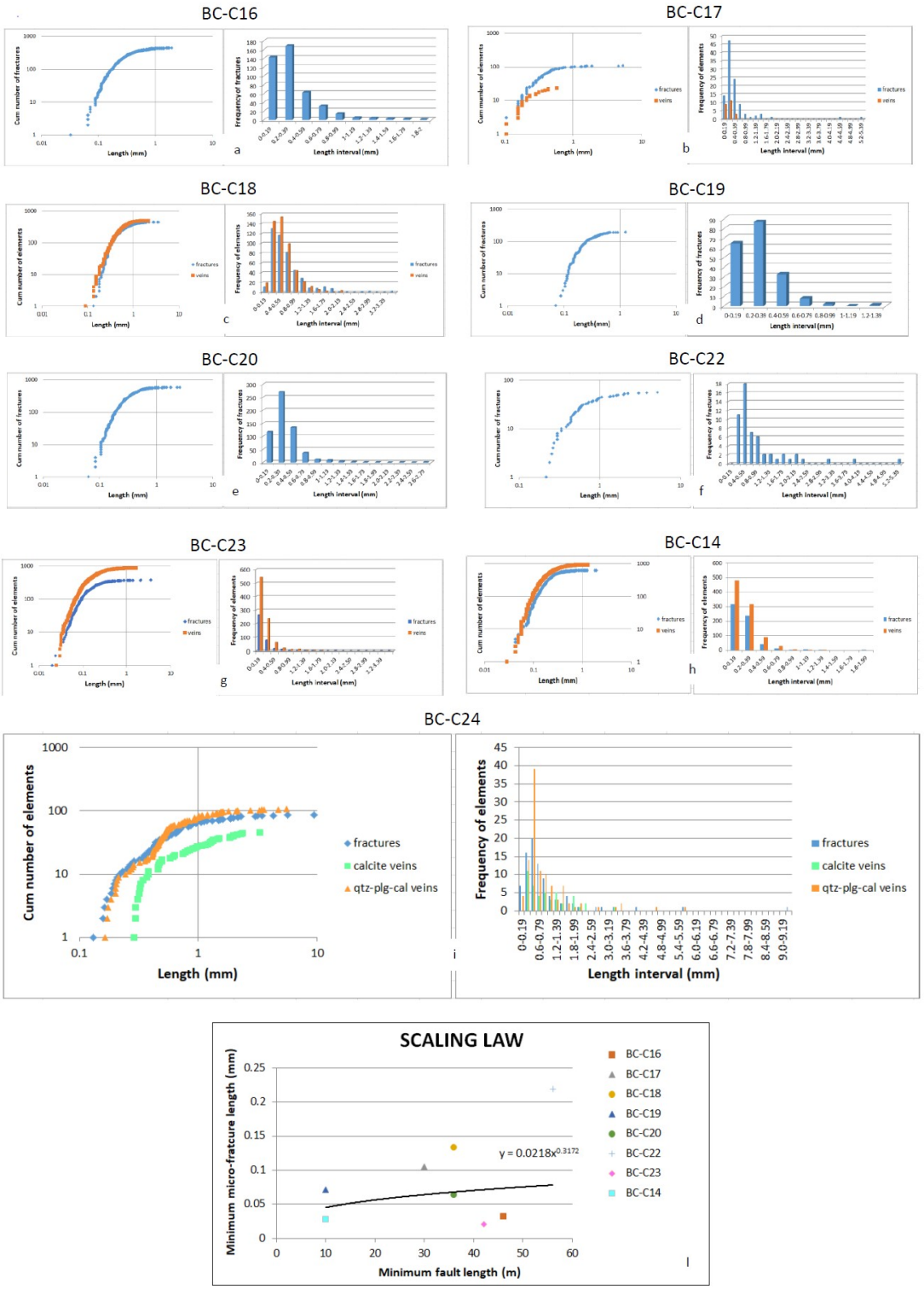

Figure 5.6 Micro-fractures and veins length distribution of analysed samples (a to i) and extrapolated scaling law (l) fitting the ratio between fault and micro-fractures minimum lengths for the Santa Ana, Azufre and Infierno fault systems.

where long structures are larger in number than short structures. This is probably due to the different

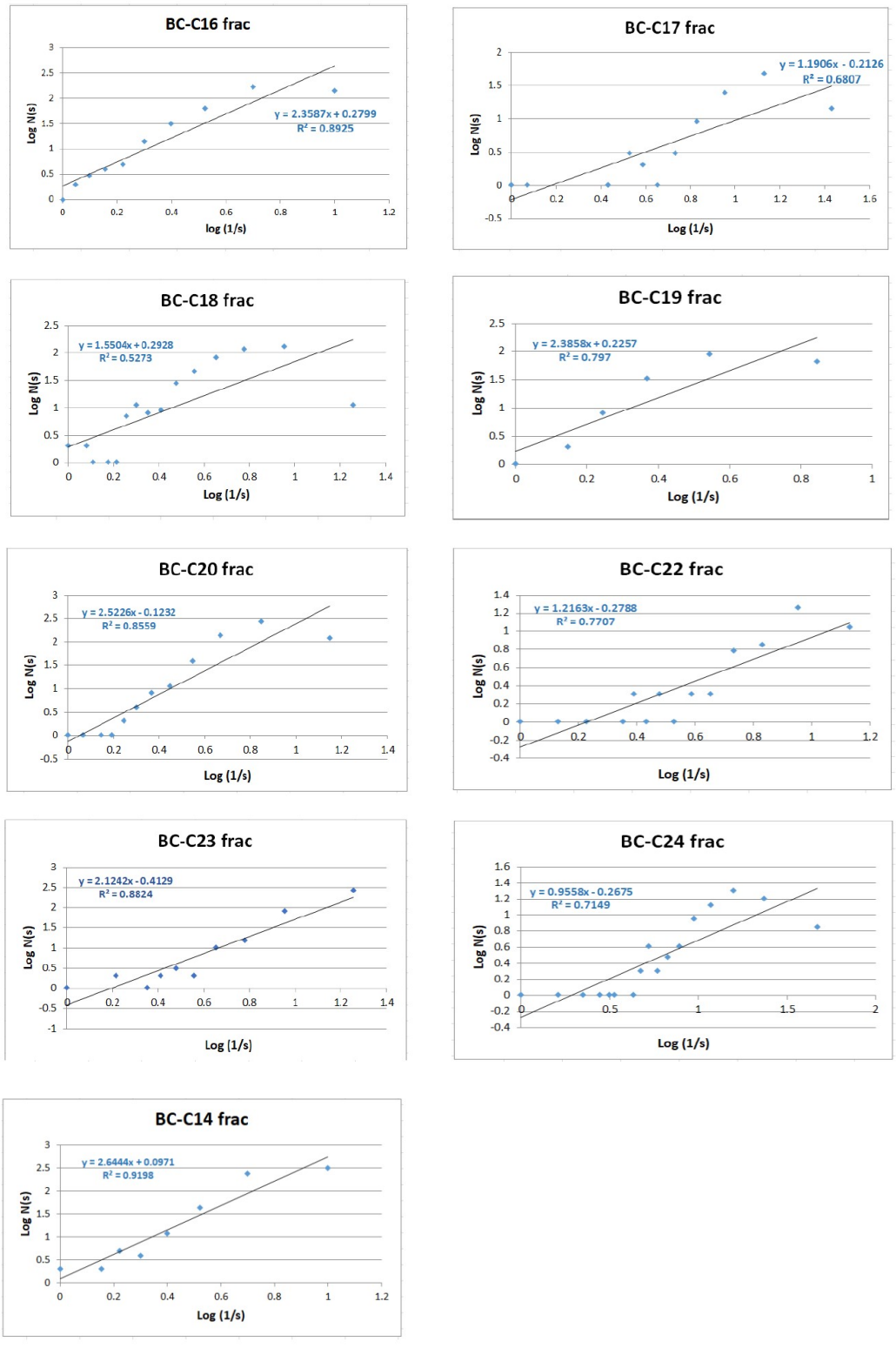

Figure 5.7 Micro-fractures fractal dimension (a coefficient in the y=ax+b equation) for the analysed samples.

scale and background context where these structures were analysed: mm to hundreds of meters long structures mapped along field-scale traced scan lines (Cello et al., 2000; De Joussineau and Aydin, 2007) and 10^{-2} to less than 10 mm long micro-structures measured inside standard thin sections (this study). Furthermore, a typical sampling bias linked to scan lines is the underestimation of small scale fracture lengths (Einstein and Baecher, 1983; Barton and Zoback, 1992; Pickering et al., 1995). Most of veins and micro-fractures do not exceed 1 mm length. This is the case of samples BC-C16, BC-C17, BC-C19, BC-C20, BC-C23 and BC-C14 (Figs. 5.6a, 5.6b, 5.6d, 5.6e, 5.5g and 5.6h). The three samples displaying the greater number of elements longer than 1 mm are BC-C24 (Fig. 5.6i), BC-C22 (Fig. 5.6f) and marginally BC-C18 (Fig. 5.6c and Table 5.3). This higher abundance in fractures longer than 1 mm is accompanied in samples BC-C24 and BC-C22 by a higher value of the elements maximum length (always below 10 mm, Figs. 5.6f and 5.6h). This seems also to be related to the length of the fault plane (buried and inferred segments excluded) along which samples were collected (Table 5.3). Another interesting point is that micro-fractures and veins length distributions for each sample are quite similar, and this well agrees with the fact that fluid circulation in all the analysed samples is either synchronous or consecutive to faulting. In order to evaluate the dimensional gap between the smallest detected micro-structure (micro-fracture or vein) and its fault zone of belonging, their ratio was calculated (Table 5.3). Fault segments minimum lengths were chosen to calculate this ratio, accounting for the fact that the overall extension of regional faults in the study area is not always known, due to partial to complete covering by Quaternary volcanic activity products. Results indicate that along up to 800 m long fault segments 6 to 7 orders magnitude smaller (Table 5.3) micro-fractures and veins can develop. In addition, a scaling law (power law) was identified as the best fit to the micro-fractures computed ratios (plot in Fig. 5.6l). Veins-to-faults minimum length ratio was not computed, due to the not statistically significant number of samples displaying veins. The identified scaling law (plot in Fig. 5.6l) fits all samples, with the exception of BC-C22 and BC-C24 (BC-C24 is not plotted for scale reasons). One possible reason to explain BC-C22 and BC-C24 misfit is the lower number of micro-fractures compared to other samples. The micro-fractures fractal dimension (D, Table 5.3), indicated by the *a* coefficient of the regression line in plots of Figure 5.7, varies between 0.96 and 2.64 in the analysed fault zones. To a careful look, two distinct intervals of fractal dimension can be envisaged: a first from 0.96 to 1.55 and a second from 2.12 to 2.64 (Fig. 5.7). The first interval is accompanied by quite low R^2 values of the regression line, always below 0.8 (0.52-0.77), while the second is characterized by stronger R^2 values (0.8-0.92), testifying a better correlation between the frequency of micro-fractures falling within a certain length interval and their length compared to the micro-fractures maximum length for the sample. Furthermore, all samples except BC-C18 within the 0.96-1.55 D interval display a quite low micro-fracture count, below or around 100 (Figs. 5.3 to 5.5).

Table 5.2 Characteristics of fault-related micro-fractures and veins length distributions.

Sample	Micro-structure length range (mm)	Distribution type	R^2 coefficient
BC-C16	0.03-1.9 (F)	lognormal	0.953 (F)
BC-C17	0.1-5.3 (F); 0.1-0.6 (V)	lognormal	0.854 (F); 0.958 (V)
BC-C18	0.1-3.6 (F); 0.09-2.2 (V)	lognormal	0.956 (F); 0.951 (V)
BC-C19	0.07-1.3 (F)	lognormal	0.967 (F)
BC-C20	0.06-2.6 (F)	lognormal	0.939 (F)
BC-C22	0.2-5.2 (F)	lognormal	0.925 (F)
BC-C23	0.02-3.5 (F); 0.02-1.7(V)	lognormal	0.907 (F); 0.958 (V)
BC-C24	0.1-9.4 (F); 0.3-3.3 (CV); 0.2-5.6 (OV)	lognormal	0.923 (F); 0.989 (CV); 0.918 (OV)
BC-C14	0.03-1.9 (F); 0.03-1.3 (V)	lognormal	0.907 (F); 0.966 (V)

(*) F: micro-fractures; V: veins; CV drusy calcite veins; OV: other veins.

Table 5.3 Fault segments and fault-related micro-structural elements length characteristics and fractal dimension of fault-related micro-fractures computed from image analysis.

FAULT SEGMENT (field scale)				MICRO-FRACTURES AND VEINS (thin section scale)			
Sample	**Strike**	**Kinematics**	**Minimum length (m) [a]**	**% Elements shorter than 1 mm**	**Element minimum length (mm)**	**Length ratio [b]**	**Fractal dimension (D)**
BC-C16	NW-SE	normal	46	96.6 (F)	0.03	10^{-7} (F)	2.36
BC-C17	ENE-WSW	reverse	30	91.5 (F); 100 (V)	0.1 (F and V)	10^{-6} (F and V)	1.19
BC-C18	NNW-SSE	unknown	36	84.6 (F); 91.3 (V)	0.1 (F); 0.09 (V)	10^{-6} (F and V)	1.55
BC-C19	NW-SE	unknown	10	99.5 (F)	0.07 (F)	10^{-6} (F)	2.39
BC-C20	NNW-SSE	unknown	36	96.9 (F)	0.06 (F)	10^{-6} (F)	2.52
BC-C22	NNE-SSW	normal	56	75 (F)	0.2 (F)	10^{-6} (F)	1.22
BC-C23	ENE-WSW	reverse	42	97.6 (F); 98.4 (V)	0.02 (F and V)	10^{-7} (F and V)	2.12
BC-C24	NW-SE	dextral-normal	810	74.7 (F); 60 (CV); 73.6 (OV)	0.1 (F); 0.3 (CV); 0.2 (OV)	10^{-7} (F); 10^{-7} (CV and OV)	0.96
BC-C14	NW-SE	unknown	<10	98.6 (F); 99.6 (V)	0.03 (F and V)	10^{-6} (F and V)	2.64

[a]: length of the fault plane mapped in the field (buried and inferred segments not included).
[b]: ratio between the micro-structural elements minimum length and the length of the outcropping fault plane.
F: micro-fractures; V: veins; CV: drusy calcite veins; OV: other veins.

5.6 Discussions

Micro-structural and image analyses on fault-rock samples from the Azufre, Santa Ana and Infierno fault systems allowed to confirm the predominant strike-slip oblique character of structures running

across the Tres Vírgenes active geothermal region (Fig. 5.8). Despite somehow indicated by previous works (Conly et al., 2005; Wong and Munguía, 2006; Antayhua et al., 2015), this outcome is of great value as none of the former studies sought for a confirmation of their field-based structural models at the micro-scale. Micro-scale analyses also revealed the predominant role of the Santa Ana fault system. Actually, the pervasive control exerted by this gulf-inherited large scale structure during volcanic processes is highlighted by the fact that local kinematics and deformation patterns observed for the intra-caldera collected sample BC-C16 do not distinguish from the ones found along the Azufre and Infierno fault systems, both running outside La Reforma caldera depression. This implies that despite the interaction with Quaternary volcanic-structures related to caldera collapse and resurgence, most of deformation throughout the Tres Vírgenes area is driven by active regional tectonics linked to the Gulf of California, similarly to what described for the Cerro Prieto volcanic complex (30 km SE of Mexicali, Baja California Norte, García-Sánchez et al., 2017), the only other example of Quaternary magmatism linked to geothermal exploitation inside the Baja California peninsula. As a consequence, kinematics and deformation patterns resulting from this study directly relate to the Gulf of California active tectonic processes.

In the Tres Vírgenes region, fluid circulation focuses at the crossing points between several sets of structures (Pellicioli et al., submitted, a), and along the investigated Gulf-related structures is either of syn- or post-faulting occurrence, as indicated by those samples which allowed defining a relative chronology. In some cases, the distinction between these two cases is not so straightforward (BC-C18), while in others more than one post-faulting fluid circulation or hydrofracturing episode has been recognized (BC-C24). The close link between faulting and fluid circulation is also demonstrated by the fact that T-type Riedel extensional veins are not so abundant in analysed samples (Figs. 5.3 to 5.5), and most veins emplace at low or high angle with the fault shear direction (R or P and R' Riedels), indicating that fluids must have circulated along already developed shear micro-fractures, whose chronological order of appearance cannot however be identified due to the tectonically active nature of the studied region (Tchalenko and Ambraseys, 1970). The overlap between micro-fractures and veins length distributions (Fig. 5.6) provides further evidence of the interconnection between faulting and fluid circulation processes. When analysing channel flow of aqueous fluids accompanying shallow crustal faulting, Sibson (1981) proposed two alternative models. In the first, the transitory post-seismic flow results from the collapse of the pre-failure dilatant fractures (extension veins arrays usually adjacent to normal faults) and the fault system can be regarded as a 'pump'. Alternatively, rising fluid pressure induces slip along the fault by reducing the effective shear stress, creating a temporary fracture permeability that allows partial draining of the reservoir (fault/fracture system acting as a 'valve' on the fluid reservoir). As the fluid pressure drops, self-sealing of the fracture systems occurs

by deposition of hydrothermal minerals and the whole cycle can be repeated (Sibson, 1981; Robert et al., 1995). Sibson (1981) 'valve' system model appears as the most suitable to explain processes observed along the analysed faults belonging to this sector of the Gulf of California. The 'valve' system model supports a cyclic nature of fluid pressure rise and fault reactivation (Ramsay, 1980; Sibson, 1981, 1987), as displayed by BC-C24 that is the most representative sample of gulf-inherited regional structures. Additionally, this model is in accordance with the secondary presence of purely extensional T Riedel shears characterizing nearly all analysed fault-rock samples, as pressurized fluids can lead to local stress perturbation and deposition of veins along directions that differ from the classical 45° tension angle, even though the origin of the fluid overpressure is still unclear (Sibson, 1996; Melchiorre et al., 1999; Gudmundsson et al., 2002; Gudmundsson et al., 2011). The 'valve' system model also much better explains the occurrence of en-echelon arrangements of minerals along micro-fractures (BC-C14) and syn-faulting fluid circulation processes in general than the 'pump' system model involving extension vein arrays collapse. Besides, evidences of pressurized fluids emplaced along the Azufre and Santa Ana fault systems have also been found in the field based on the occurrence of misoriented veins and fracture sets in respect to the currently active stress field. Regarding fracture systems self-sealing mechanisms proposed by Sibson (1981), these are mainly supported by calcite precipitation along the Azufre and Infierno faults, while no calcite was found in samples collected along the Santa Ana fault system (BC-C7 and BC-C16). This does not necessarily imply a different behaviour for the Santa Ana fault system or that this Gulf-related structure lacks important fluid circulation, as fluid flow properties are highly variable along the fault plane, as highlighted by Caine et al. (1996), Lin et al. (2007), Paul et al. (2009). Actually, proof of extensive fluid circulation along the Santa Ana fault system is indeed demonstrated by the presence of two historically exploited mine sites (lead and gold) set along this structure (Wilson and Rocha, 1955; Garcia-Sanchez et al., 2019). The high variability of fault-related fluid flow properties is also responsible for the occurrence of calcite along the Azufre fault system only where the damage zone narrows down and becomes closer to the fault core (BC-C24). A future sampling campaign might partly solve this issue and provide a more robust dataset, even though the above-mentioned issues regarding the study area and volcanic regions in general could anyway prevent obtaining a complete and statistically significant dataset. In addition to variable fluid flow properties along fault zones, lithology could also intrinsically control fault zones permeability and therefore hydrothermal fluid circulation (Caine et al., 1996; Lin et al., 2007; Paul et al., 2009). In our case the more porous caldera-forming Aguajito ignimbrite (BC-C17, BC-C18, BC-C19, BC-C20, BC-C22 and BC-C23) and the Comondù Group sediments (Hausback, 1984; Sawlan and Smith, 1984; Sawlan, 1991; López et al., 1995; Umhoefer et al., 2001; Conly et al., 2005; Bryan et al., 2014), inside which the Santa Lucia

formation (García-Sánchez et al., 2019) is interlayered (BC-C14), could provide an easier path for fluid flow (2D porosity illustrated in Appendix Fig. 5.12) than a pile of La Reforma syn-caldera ignimbrites (BC-C7 and BC-C8 sites) or post-caldera intrusions (BC-C16).

Regarding the length of regional fault-related micro-structures developed in this sector of the Gulf of California, nearly all analysed measured elements are shorter than 1 mm, rarely reach 5 mm maximum length and in all cases never exceed 10 mm. Moreover, micro-fractures and veins do not exhibit well-defined length sets based either on their azimuth/angle formed with the shear direction (Figs. 5.3 and 5.4 in Appendix), or on the presence/lack of shear (De Joussineau and Aydin, 2007). The observed azimuth-length invariance is not new in natural fracture systems, as found by Barton and Larsen (1985) who studied the scaling and fractal characteristics of fracture networks at different scales. The identified scaling law fitting the ratio between the micro-fractures and faults minimum lengths (Fig. 5.6l) supports the idea of a generalized deformation trend throughout the Tres Vírgenes area, as it fits data collected along separate structures often displaying different kinematics and orientation over an area of approximately 900 km^2. As previously mentioned, this generalized deformation trend is linked to the Gulf of California active tectonics, or at least to the studied Gulf sector, where the self-similarity of the fault-growth process could imply a universal faulting mechanism governed by either constant fracture toughness or constant yield stress (Hatton et al., 1994). Despite the generalized good fit of most samples, BC-C22 and BC-C24 represent exceptions, as they don't fall on the scaling law regression line (Fig. 5.6l). Given the limited dataset (11 samples) we suggest further data collection and the eventual use of scan lines and boxes (Cello et al., 2000; De Joussineau and Aydin, 2007; Zucchi et al., 2017) across the Tres Vírgenes area. These techniques, despite very hard to apply due to widespread covering by Quaternary volcanic products, could improve a lot the confidence in the identified scaling law or eventually highlight the presence of multiple scaling laws (Hatton et al., 1994), able to justify samples BC-C22 and BC-C24 misfit. Additionally, further work on fault-related structures in other regions across the eastern side of the Baja California peninsula (i.e. the Loreto region, Fig. 5.1) could refine the Gulf of California deformation trend resulting from this study. When it comes to quantifying the identified generalized deformation trend of Gulf-related structures across the Tres Vírgenes region, the computed fractal dimension (D) for the analysed samples displays two separate clusters (0.96-1.55 and 2.12-2.64), bearing different correlation coefficients R^2 for the linear regression line from which D is mathematically derived (Fig. 5.7). The widths of the identified fractal dimension intervals are comparable to those reported in literature for natural fracture systems (Hirata, 1989; Cello et al., 2000). The obtained good correlation between the frequency of fault-related micro-fractures falling within a certain length interval and their length compared to the sample micro-fractures maximum length (Fig. 5.7) testifies the repetition of the same deformation pattern at different

scales along regional faults across the Tres Vírgenes region, in agreement with field evidences of a highly recursive and regular replication of the pull-apart geometry at different scales (Fig. 5.8). Apart from BC-C18, all samples belonging to the lower-R^2 D interval (0.96-1.55) display a small number of measured fractures. If this, by one side, could raise doubts on the statistical reliability of these datasets, on the other hand seems to be intrinsically linked to the length of the shortest measured micro-fractures. In fact, all samples with a fractal dimension between 0.96 and 1.55 display a micro-fractures minimum length that is 1 of order of magnitude higher (10^{-1}) than the minimum length displayed by micro-fractures falling into the 2.12-2.64 D interval (10^{-2}, Table 5.3). In other words, samples displaying longer absolute lengths fall in the lower fractal dimension interval (0.96-1.55). Being most of the analysed samples related to the Azufre fault system (BC-C17, BC-C18, BC-C19, BC-C20, BC-C22, BC-C23 and BC-C24), this could imply two slightly distinct faulting mechanisms during micro-fracture generation, in accordance with the over 1 order of magnitude (10^{-6}–10^{-7}) variation of the computed ratio between minimum length values of micro-structural elements and fault segments for the Azufre fault zone (Table 5.3), as well as the already mentioned possibility of having multiple scaling laws (Hatton et al., 1994) fitting our dataset. Notwithstanding the local variability of the computed scaling law and fractal dimension parameters, results of this study demonstrate a statistical self-similarity (fractal geometry) of regional structures across this sector of the Gulf of California.

Finally, we would like to emphasize that this study quantitative results could be of high relevance as input parameters for any fluid flow modelling simulation. It is actually since the 1980s that many studies focused on obtaining statistically based predictions beyond the scale of observation (Cowie et al., 1996) based on quantitative analyses of fault and fracture systems (Barton et al., 1995; Turcotte, 1997), aimed to identify their fractal nature and related characteristics in a variety of geological settings (Mandelbrot, 1983; Walsh and Watterson, 1993). When it comes to active geothermal regions like the Tres Vírgenes and Cerro Prieto areas, where magma chambers provide the heating source to hydrothermal fluids circulating along gulf-related structures (Lopez et al., 1995; García-Sánchez et al., 2017), information regarding the maximum/minimum elements length, length frequency distribution and fractal dimension could really improve the reliability of dynamic reservoir simulations and could

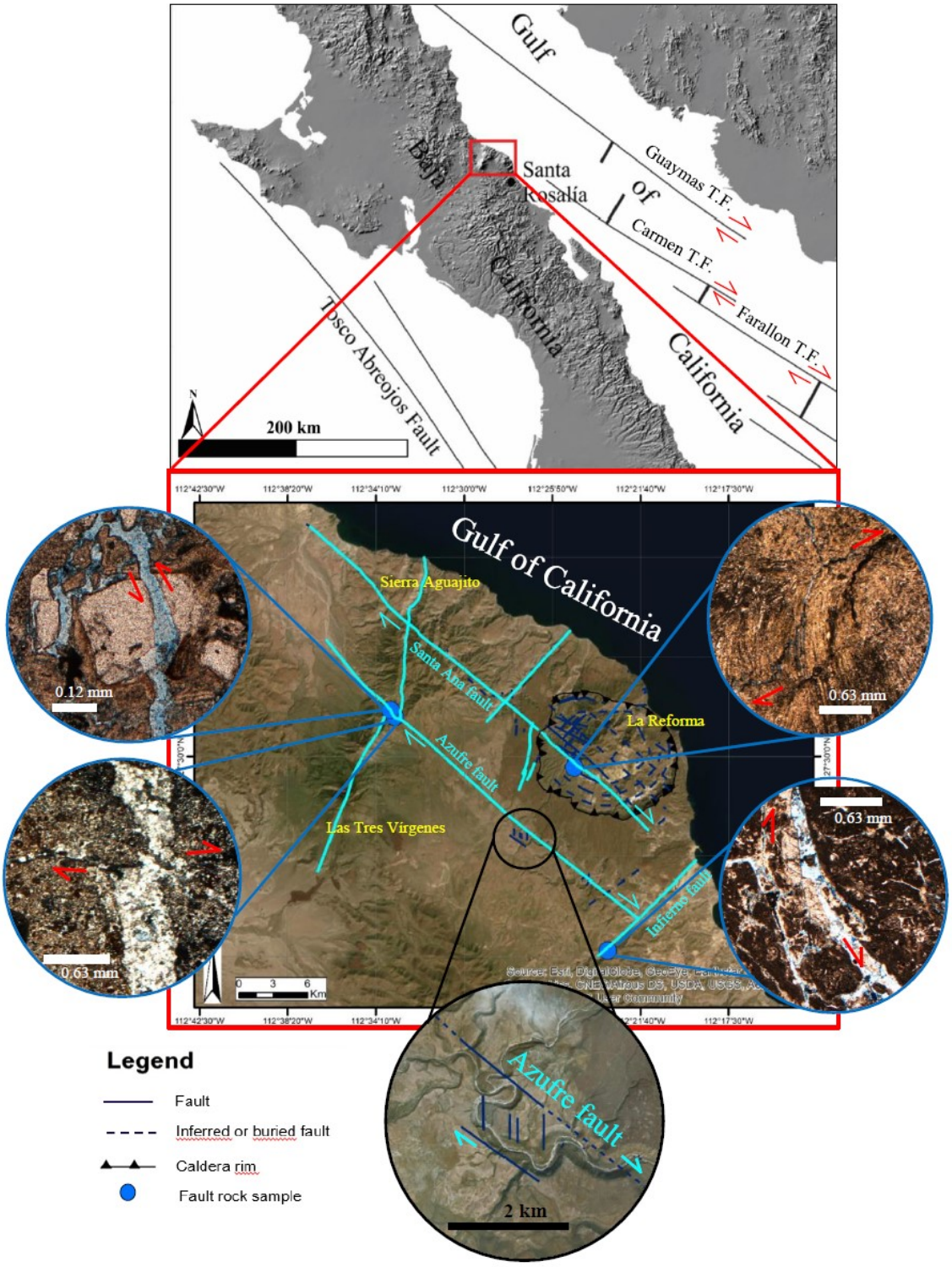

Figure 5.8 Self-similarity (fractal nature) of dextral strike-slip oblique structures related to the Gulf of California across the Tres Vírgenes area, illustrated at the meso-, macro- (field-scale) and micro-scale. Faults belonging to the Santa Rosalía half-graben transtensive basin are highlighted in light blue (modified after Pellicioli et al., submitted, a).

also represent a predictive tool for deformation patterns throughout the Gulf of California. Besides from the industry, quantitative fluid flow modelling along faults can also have important social and hazard implications, mainly linked to seismic-source modelling within the currently deforming crustal volume (Tchalenko and Ambraseys, 1970; Cello et al., 2000). This is of particular relevance along the seismically active eastern side of the Baja California peninsula (Tres Vírgenes, Santa Rosalía and Loreto regions, Mayer and Vincent, 1999; Wong and Munguía, 2006) and in volcanic regions in general, commonly set within tectonically and seismically active geodynamic settings. For all above mentioned reasons, we thus strongly encourage performing quantitative characterization of fault-related micro-structural patterns in volcanic regions, where structural issues are often underdeveloped due to the widely known difficult application of routine structural analysis approaches and techniques.

5.7 Concluding remarks

By investigating fault-related micro-structures across the Tres Vírgenes volcanic region (Baja California, Mexico) this study provides relevant information regarding deformation patterns, fluid circulation and fractal character of regional structures linked to the Gulf of California that, despite the interaction with Quaternary volcanic structures, mainly drive deformation across the Tres Vírgenes region, similarly to other volcanic districts located along the Gulf (i.e. the Cerro Prieto district, Baja California Norte). The volcanic nature of the setting chosen for this study is also relevant, as the application of routine structural analysis methodologies and techniques in volcanic regions is usually challenging. Additionally, the advanced exploitation stage reached by geothermal resources in the Tres Vírgenes area implies that many of the quantitative structural parameters derived from this work could be of high relevance for the industry, mostly in terms of fluid flow modelling along Gulf-related regional faults. This study thus encourages future and further quantitative characterization of fault-related micro-structures across the Gulf of California and globally. In summary, the present study allowed the followings:

a) Consolidation of the idea of regionally-controlled volcanic activity and confirmation of the predominant strike-slip oblique character of regional structures running across the Tres Vírgenes active geothermal region, along with better quantification of the role of fluid pressure rise in faulting-related mechanisms and of the fractal character of structures linked to this sector of the Gulf of California (García-Sánchez et al., 2019).

b) Identification of the close link between faulting and fluid circulation processes (syn- or post-faulting fluid circulation events), of Riedel deformation patterns and of micro-fractures and veins length distributions, in accordance with Sibson (1981) fault 'valve' systems model that suggests emplacement of pressurised fluids along fault planes and fracture systems self-sealing by hydrothermal minerals deposition, in line with field evidences along the Azufre, Santa Ana and Infierno Gulf-related regional structures.

c) Recognition and quantification of the generalized deformation trend and statistical self-similarity (fractal nature) affecting regional structures across the Gulf of California, by means of computation of minimum/maximum micro-structural elements lengths and length distributions, extrapolation of a scaling law fitting the ratio between micro-fractures and faults minimum lengths and determination of fractal dimension, even though local misfit within the set of analysed samples leaves space for further refining of the identified parameters (i.e. presence of locally distinct faulting mechanisms and/or multiple scaling laws).

5.8 Acknowledgements

This study benefited from CeMIE Geo project P15 of SENER-CONACyT to J.L.M. and UNAM (Universidad National Autónoma de México, Instituto de Geofísica, Morelia, Michoacán, México) to support 2015-2017 field trips to Santa Rosalía-Tres Vírgenes, and from *Italgas S.p.a.* funds issued by CNR-IDPA (Milan) to sponsor C. Pellicioli in her PhD research activity. We are thankful to UNAM also for managing logistic aspects of field trips, including employing local guides from UMA and Ecoturismo Borrego Cimarrón, Bonfil, B.C.S., who took care of people working in the field. Among UMA members, we are especially grateful to Francisco, for having led us to any site that could (and could not) be reached in the fastest way possible and for always patiently waiting for us to finish all of our measurements. Special thanks go to Josè Luis Macias, Laura García-Sánchez, Susana Osorio-Ocampo, Reyna-Marcela Lira-Beltran, Antonio Pola-Villaseñor, Pedro Martin Pacheco and Vincenzo Parisi for their support during fieldwork activity, post-field technical discussions and for hospitality in Morelia. Thanks to Curzio Malinverno for thin sections preparation and to Agostino Rizzo and Andrea Risplendente for preliminary SEM and electron microprobe analyses and to Giovanna Della Porta for her support in mineralogical and petrographic analysis of fault-related calcite phases.

5.9 References

Acocella, V., 2007. Understanding caldera structure and development: An overview of analogue models compared to natural calderas: Earth-Science Reviews, 85, 125-160.

Agosta, F., Aydin, A., 2006. Architecture and deformation mechanism of a basin-bounding normal fault in Mesozoic platform carbonates, central Italy. Journal of Structural Geology, 28, 1445-1467.

Andersson, J. E., Ekman, L., Nordqvist, R., Winberg, A., 1991. Hydraulic testing and modelling of a low-angle fracture zone at Finnsjön, Sweden. Journal of Hydrology, 126, 45-77.

Angelier, J., Colletta, B., Chorowicz, J., Ortlieb, L., Rangin, C., 1981. Fault tectonics of the Baja California Peninsula and the opening of the Sea of Cortez, Mexico. Journal of Structural Geology, 3, 347-357.

Antayhua-Vera, Y., Lermo-Samaniego, J., Quintanar-Robles, L., Campos-Enríquez, O., 2015. Seismic activity and stress tensor inversion at Las Tres Vírgenes Volcanic and Geothermal Field (México). Journal of Volcanology and Geothermal Research, 305, 19-29.

Aragón-Arreola, M., Morandi, M., Martín-Barajas, A., Delgado-Argote, L., González-Fernández, A., 2005. Structure of the rift basins in the central Gulf of California: Kinematic implications for oblique rifting. Tectonophysics, 409, 19-38.

Atwater, T., 1970. Implications of plate tectonics for the Cenozoic tectonic evolution of western North America. Geological Society of America Bulletin, 81, 3513-3536.

Avellán, D. R., Macías, J. L., Arce, J. L., Jiménez-Haro, A., Saucedo-Girón, R., Garduño-Monroy, V. H., Sosa-Ceballos, G., Bernal, J. P., López-Loera, H., Cisneros, G., Layer, P. W., García-Sánchez, L., Reyes-Agustín, G., Rocha, V., S. Rangel, E., 2018. Eruptive chronology and tectonic context of the late Pleistocene Tres Vírgenes volcanic complex, Baja California Sur (México). Journal of Volcanology and Geothermal Research, 360, 100-125.

Barton, C.C., Larsen, E., 1985. Fractal geometry of two-dimensional fracture networks at Yucca Mountain, southwestern Nevada. Conference Proceedings at the International Symposium of Fundamental of Rock Joints, Björkliden, Lapland, Sweden, 1985.

Barton, C. C., Paul, R., Pointe, L., 1995. Fractals in the earth sciences, pp. 141-178. New York: Plenum Press.

Barton, C. A., Zoback, M. D., 1992. Self-similar distribution and properties of macroscopic fractures at depth in crystalline rock in the Cajon Pass Scientific Drill Hole. Journal of Geophysical Research: Solid Earth, 97, 5181-5200.

Benedicto, A., Plagnes, V., Vergély, P., Flotté, N., Schultz, R. A., 2008. Fault and fluid interaction in a rifted margin: integrated study of calcite-sealed fault-related structures (southern Corinth margin). Geological Society, London, Special Publications, 29, 257-275.

Bryan, S. E., Orozco-Esquivel, T., Ferrari, L., Lopez-Martinez, M., 2014. Pulling apart the mid to late Cenozoic magmatic record of the Gulf of California: Is there a Comondú arc?. Geological Society, London, Special Publications, 385, 389-407.

Caine, J. S., Evans, J. P., Forster, C. B., 1996. Fault zone architecture and permeability structure. Geology, 24, 1025-1028.

Cello, G., Gambini, R., Mazzoli, S., Read, A., Tondi, E., Zucconi, V., 2000. Fault zone characteristics and scaling properties of the Val d'Agri Fault System (Southern Apennines, Italy). Journal of Geodynamics, 29, 293-307.

Cembrano, J., Lara, L., 2009. The link between volcanism and tectonics in the southern volcanic zone of the Chilean Andes: a review. Tectonophysics, 471, 96-113.

Chester, F. M., Logan, J. M., 1987. Composite planar fabric of gouge from the Punchbowl fault, California. Journal of Structural Geology, 9, 621-IN6.

Cloos, H., 1928. Experimente zur inneren Tektonik. Cetralblatt fur Mineralogie, 5, 609-621.

Cole, J. W., Milner, D. M., Spinks, K. D., 2005, Calderas and caldera structures: a Review: Earth-Science Reviews, 69, 1- 26.

Conly, A. G., Brenan, J. M., Bellon, H., Scott, S. D., 2005. Arc to rift transitional volcanism in the Santa Rosalia region, Baja California Sur, Mexico. Journal of Volcanology and Geothermal Research, 142, 303-341.

Cowie, P.A., Knipe, R.J., Main, I.G., 1996. Scaling laws for fault and fracture populations: analyses and applications. Journal of Structural Geology (Special Issue) 18, 135-383.

De Joussineau, G., Aydin, A., 2007. The evolution of the damage zone with fault growth in sandstone and its multiscale characteristics. Journal of Geophysical Research: Solid Earth, 112.

Einstein, H. H., Baecher, G. B., 1983. Probabilistic and statistical methods in engineering geology. Rock mechanics and rock engineering, 16, 39-72.

Evans, J. P., 1990. Textures, deformation mechanisms, and the role of fluids in the cataclastic deformation of granitic rocks. Geological Society, London, Special Publications, 54, 29-39.

Ferrari, L., Orozco-Esquivel, T., Bryan, S. E., Lopez-Martinez, M., Silva-Fragoso, A., 2018. Cenozoic magmatism and extension in western Mexico: Linking the Sierra Madre Occidental silicic large igneous province and the Comondú Group with the Gulf of California rift. Earth-Science Reviews, 183, 115-152.

Fletcher, J. M., Grove, M., Kimbrough, D., Lovera, O., Gehrels, G. E., 2007. Ridge-trench interactions and the Neogene tectonic evolution of the Magdalena shelf and southern Gulf of California: Insights from detrital zircon U-Pb ages from the Magdalena fan and adjacent areas. Geological Society of America Bulletin, 119, 1313-1336.

Fredrich, J. T., Evans, B.,Wong, T. F., 1989. Micromechanics of the brittle to plastic transition in Carrara marble. Journal of Geophysical Research: Solid Earth, 94, 4129-4145.

García-Sánchez, L., Macías, J. L., Sosa-Ceballos, G., Arce, J. L., Garduño-Monroy, V. H., Saucedo, R., Avellán, D.R., Rangel, E., Layer, P.W., López-Loera, H., Rocha, V. S., Cisneros, G., Reyes-Agustín, G., Jiménez, A., Benowitz, J.A., 2017. Genesis and evolution of the Cerro Prieto Volcanic Complex, Baja California, Mexico. Bulletin of Volcanology, 79, 44.

García-Sánchez, L., Macías, J.L., Sulpizio, R., Osorio-Ocampo, L.S., Pellicioli, C., Pola, A., Avellán, D., Cisneros, G., García, F., Ocampo-Díaz, Y.Z.E, Lira-Beltran, R.M., Saucedo, R., Sánchez-Nuñez, J.M., Arce, J.L., Corona-Chávez, P., Reyes-Augustin, G., Cardona, M., Layer, P.W., Benowitz, J., Solari, L., Groppelli, G., 2019. Geology of La Reforma caldera complex, Baja California, Mexico. Journal of Maps, 15, 487-498.

Goddard, J. V., Evans, J. P., 1995. Chemical changes and fluid-rock interaction in faults of crystalline thrust sheets, northwestern Wyoming, USA. Journal of Structural Geology, 17, 533-547.

Gray, M. B., Stamatakos, J. A., Ferrill, D. A., Evans, M. A., 2005. Fault-zone deformation in welded tuffs at Yucca Mountain, Nevada, USA. Journal of Structural Geology, 27, 1873-1891.

Gudmundsson, A., 2011. Rock fractures in geological processes. Cambridge University Press, printed in the United Kingdom at the University press, Cambridge.

Gudmundsson, A., Berg, S. S., Lyslo, K. B., Skurtveit, E., 2001. Fracture networks and fluid transport in active fault zones. Journal of Structural Geology, 23, 343-353.

Gudmundsson, A., Fjeldskaar, I., Brenner, S. L., 2002. Propagation pathways and fluid transport of hydrofractures in jointed and layered rocks in geothermal fields. Journal of Volcanology and Geothermal Research, 116, 257-278.

Gutiérrez-Negrín, L. C., 2015. Mexican geothermal plays. In Proceedings of the world geothermal congress 2015, Melbourne, Australia, 19–25 April.

Harris, S. D., McAllister, E., Knipe, R. J., Odling, N. E., 2003. Predicting the three-dimensional population characteristics of fault zones: a study using stochastic models. Journal of Structural Geology, 25, 1281-1299.

Hatton, C.G., Main, I.G., Meredith, P.G., 1994. Non-universal scaling of fracture length and opening displacement. Nature, 367, 160.

Hausback, B. P., 1984. Cenozoic volcanic and tectonic evolution of Baja California Sur, Mexico. Society for Sedimentary Geology.

Hills, E. S., 1963. Elements of structural geology: London, Metheron and Co.

Hirata, T., 1989. Fractal dimension of fault systems in Japan: fractal structure in rock fracture geometry at various scales. In Fractals in geophysics, 157-170. Birkhäuser, Basel.

Holohan, E. P., de Vries, B. V. W., Troll, V. R., 2008. Analogue models of caldera collapse in strike-slip tectonic regimes. Bulletin of Volcanology, 70, 773-796.

Johansen, T. E. S., Fossen, H., Kluge, R., 2005. The impact of syn-faulting porosity reduction on damage zone architecture in porous sandstone: an outcrop example from the Moab Fault, Utah. Journal of Structural Geology, 27, 1469-1485.

Kim, Y. S., Peacock, D. C. P., Sanderson, D. J., 2003. Mesoscale strike-slip faults and damage zones at Marsalforn, Gozo Island, Malta. Journal of Structural Geology, 25, 793-812.

Kim, Y. S., Peacock, D. C., Sanderson, D. J., 2004. Fault damage zones. Journal of structural geology, 26, 503-517.

Lagmay, A. M. F., Tengonciang, A. M. P., Uy, H. S., 2005. Structural setting of the Bicol Basin and kinematic analysis of fractures on Mayon Volcano, Philippines. Journal of Volcanology and Geothermal Research, 144, 23-36.

Lavallée, Y., Hirose, T., Kendrick, J. E., De Angelis, S., Petrakova, L., Hornby, A. J., Dingwell, D. B., 2014. A frictional law for volcanic ash gouge. Earth and Planetary Science Letters, 400, 177-183.

Lin, A., Maruyama, T., Kobayashi, K., 2007. Tectonic implications of damage zone-related fault-fracture networks revealed in drill core through the Nojima fault, Japan. Tectonophysics, 443, 161-173.

López, A. C., Casarrubias, U. Z. Z., Leal, R., 1993. Estudio geológico regional de la zona geotérmica de Las Tres Vírgenes. Rep. Interno OGL-BC-002/93, GPG-CFE.

López, H. A., Robin, C., Vincent, O., 1989. Estudio geoquímico, mineralógico y edades radiométricas de la zona de Las Tres Vírgenes BCS Implicaciones geotérmicas. Rep. Interno 5/89, GPG-CFE.

López, H. A., García, G. H., Arellano, F. G., 1995. Geothermal exploration at Las Tres Vírgenes, BCS, Mexico. In Proceedings of the 1995 World Geothermal Congress, pp. 707-712.

Macías, J.L., Jiménez, S., 2012. Actualización vulcanológica del complejo de Las Tres Vírgenes, BCS. Memorias del XX Congreso Anual de la Asociación Geotérmica Mexicana, Morelia, Mich., México, 26-28 September 2012.

Macías, J.L., Jiménez, S., 2013. Estudio de Estratigrafía y Geología del Complejo Volcánico Tres Vírgenes. B.C.S. Geotermia 26, 14–23.

Mandelbrot, B. B., 1983. The fractal geometry of nature, Vol. 173, p. 51. New York: WH freeman.

Mayer, L., Vincent, K. R., 1999. Active tectonics of the Loreto area, Baja California Sur, Mexico. Geomorphology, 27, 243-255.

Melchiorre, E. B., Criss, R. E., Davisson, M. L., 1999 Relationship between seismicity and subsurface fluids, central Coast Ranges, California. Journal of Geophysical Research: Solid Earth, 104, 921-939.

McGrath, A. G., Davison, I., 1995. Damage zone geometry around fault tips. Journal of Structural Geology, 17, 1011-1024.

Nava-Sánchez, E. H., Gorsline, D. S., Molina-Cruz, A., 2001. The Baja California peninsula borderland: structural and sedimentological characteristics. Sedimentary Geology, 144, 63-82.

Nixon, C. W., Sanderson, D. J., Bull, J. M., 2011. Deformation within a strike-slip fault network at Westward Ho!, Devon UK: Domino vs conjugate faulting. Journal of Structural Geology, 33, 833-843.

Nkono, C., Féménias, O., Demaiffe, D. (2009). Geodynamic framework of large volcanic fields highlighted by SRTM DEMs: Method evaluation and perspectives exampled on three areas from the Cameroon Volcanic Line. Journal of volcanology and geothermal research, 187, 13-25.

Norini, G., Groppelli, G., Lagmay, A. M. F., Capra, L., 2006, Recent left-oblique slip faulting in the central eastern Trans- Mexican Volcanic Belt: Seismic hazard and geodynamic implications: Journal of Volcanology and Geothermal Research, 310, 221-237.

Odling, N. E., Harris, S. D., Knipe, R. J., 2004. Permeability scaling properties of fault damage zones in siliclastic rocks. Journal of Structural Geology, 26, 1727-1747.

Ortlieb, L., Ruegg, J. C., Angelier, J., Colletta, B., Kasser, M., Lesage, P., 1989. Geodetic and tectonic analyses along an active plate boundary: The central Gulf of California. Tectonics, 8, 429-441.

Osorio-Ocampo, S., Macías, J.L., García-Sánchez, Sosa-Ceballos, G., Pola, A., García-Tenorio, F., 2016. Calc-alkaline magmatism of El Aguajito Caldera, Baja California Sur, México. [Poster]. Conf. Cities on Volcanoes 9, September 2016, Puerto Varas, Chile.

Paul, P. K., Zoback, M. D., Hennings, P. H., 2009. Fluid flow in a fractured reservoir using a geomechanically constrained fault-zone-damage model for reservoir simulation. SPE Reservoir Evaluation & Engineering, 12, 562-575.

Pellicioli, C., Groppelli, G., Macías, J.L. and Sulpizio, R. (submitted, a). Interplay between regional and volcanic structures across the Pleistocene La Reforma caldera complex, Baja California Sur, Mexico: implication on caldera processes and geothermal potential. GSA Bullettin.

Pickering, G., Bull, J. M., Sanderson, D. J., 1995. Sampling power-law distributions. Tectonophysics, 248, 1-20.

Portugal, E., Birkle, P., Tello, E., Tello, M., 2000. Hydrochemical–isotopic and hydrogeological conceptual model of the Las Tres Vırgenes geothermal field, Baja California Sur, México. Journal of Volcanology and Geothermal Research, 101, 223-244.

Ramsay, J. G., 1980. The crack–seal mechanism of rock deformation. Nature, 284, 135.

Riedel, W., 1929. Zur Mechanik geologischer Brucherscheinungen ein Beitrag zum Problem der Fiederspatten. Zentbl. Miner. Geol. Palaont. Abt., 354-368.

Robert, F., Boullier, A. M., Firdaous, K., 1995. Gold-quartz veins in metamorphic terranes and their bearing on the role of fluids in faulting. Journal of Geophysical Research: Solid Earth, 100, 12861-12879.

Sawlan, M. G., 1991. Magmatic Evolution of the Gulf of California Rift: Chapter 17: Part III. Regional Geophysics and Geology.

Sawlan, M. G., Smith, J. G., 1984. Petrologic characteristics, age and tectonic setting of Neogene volcanic rocks in northern Baja California Sur, Mexico.

Schmidt, E. K., 1975. Plate tectonics, volcanic petrology, and ore formation in the Santa Rosalía area, Baja California, Mexico.

Schmitt, A. K., Stockli, D. F., Hausback, B. P., 2006. Eruption and magma crystallization ages of Las Tres Vírgenes (Baja California) constrained by combined 230Th/238U and (U–Th)/He dating of zircon. Journal of Volcanology and Geothermal Research, 158, 281-295.

Scholz, C. H., Anders, M., 1994. The permeability of faults. The mechanical involvement of fluids in faulting: US Geological Survey Open File Report, 94, 247-253.

Schubnel, A., Walker, E., Thompson, B. D., Fortin, J., Guéguen, Y., Young, R. P., 2006. Transient creep, aseismic damage and slow failure in Carrara marble deformed across the brittle-ductile transition. Geophysical Research Letters, 33.

Sibson, R. H., 1981. Fluid flow accompanying faulting: field evidence and models. Earthquake prediction: an international review, 4, 593-603.

Sibson, R. H., 1987. Earthquake rupturing as a mineralizing agent in hydrothermal systems. Geology, 15, 701-704.

Sibson, R. H., 1996. Structural permeability of fluid-driven fault-fracture meshes. Journal of Structural Geology, 18, 1031-1042.

Smith, L., Forster, C. B., Evans, J. P., 1990. Interaction between fault zones, fluid flow and heat transfer at the basin scale.

Stock, J. M., Hodges, K. V., 1989. Pre-Pliocene extension around the Gulf of California and the transfer of Baja California to the Pacific plate. Tectonics, 8, 99-115.

Taylor, B., Crook, K., Sinton, J., 1994. Extensional transform zones and oblique spreading centers. Journal of Geophysical Research: Solid Earth, 99, 19707-19718.

Tchalenko, J.S., Ambraseys, N.N., 1970. Structural analysis of the Dasht-e Bayaz (Iran) earthquake fractures. Geological Society of America Bulletin, 81, 41-60.

Teufel, L. W., Rhett, D. W., Farrell, H. E., Lorenz, J. C., 1993. Control of fractured reservoir permeability by spatial and temporal variations in stress magnitude and orientation. In SPE Annual Technical Conference and Exhibition. Society of Petroleum Engineers.

Turcotte, D. L., 1997. Fractals and chaos in geology and geophysics. Cambridge university press.

Turner, F. J., Griggs, D. T., Heard, H., 1954. Experimental deformation of calcite crystals. Geological Society of America Bulletin, 65, 883-934.

Umhoefer, P. J., Dorsey, R. J., Willsey, S., Mayer, L., Renne, P., 2001. Stratigraphy and geochronology of the Comondu Group near Loreto, Baja California Sur, Mexico. Sedimentary Geology, 144, 125-147.

Umhoefer, P. J., Mayer, L., Dorsey, R. J., 2002. Evolution of the margin of the Gulf of California near Loreto, Baja California peninsula, Mexico. Geological Society of America Bulletin, 114, 849-868.

Van Wyk de Vries, B., Merle, O., 1998. Extension induced by volcanic loading in regional strike-slip zones. Geology, 26, 983-986.

Verma, S. P., Pandarinath, K., Santoyo, E., González-Partida, E., Torres-Alvarado, I. S., Tello-Hinojosa, E., 2006. Fluid chemistry and temperatures prior to exploitation at the Las Tres Vírgenes geothermal field, Mexico. Geothermics, 35, 156-180.

Walsh, J. J., Watterson, J., 1993. Fractal analysis of fracture patterns using the standard box-counting technique: valid and invalid methodologies. Journal of structural Geology, 15, 1509-1512.

Wilson, I. F., Rocha, V. S., 1955. Geology and mineral deposits of the Boleo copper district, Baja California, Mexico. Geological Survey Special Paper, 273. Washington, DC: U.S. Government Publishing Office, 140 pp.

Wong, V., Munguía, L., 2006. Seismicity, focal mechanisms, and stress distribution in the Tres Vírgenes volcanic and geothermal region, Baja California Sur, Mexico. Geofísica internacional, 45, 23-37.

Zanchi, A., 1994. The opening of the Gulf of California near Loreto, Baja California, Mexico: from basin and range extension to transtensional tectonics. Journal of Structural Geology, 16, 1619-1639.

Zucchi, M., Brogi, A., Liotta, D., Rimondi, V., Ruggieri, G., Montegrossi, G., Caggianelli, A., Dini, A., 2017. Permeability and hydraulic conductivity of faulted micaschist in the eastern Elba Island exhumed geothermal system (Tyrrhenian sea, Italy): insights from Cala Stagnone. Geothermics, 70, 125-145.

5.10 Appendix

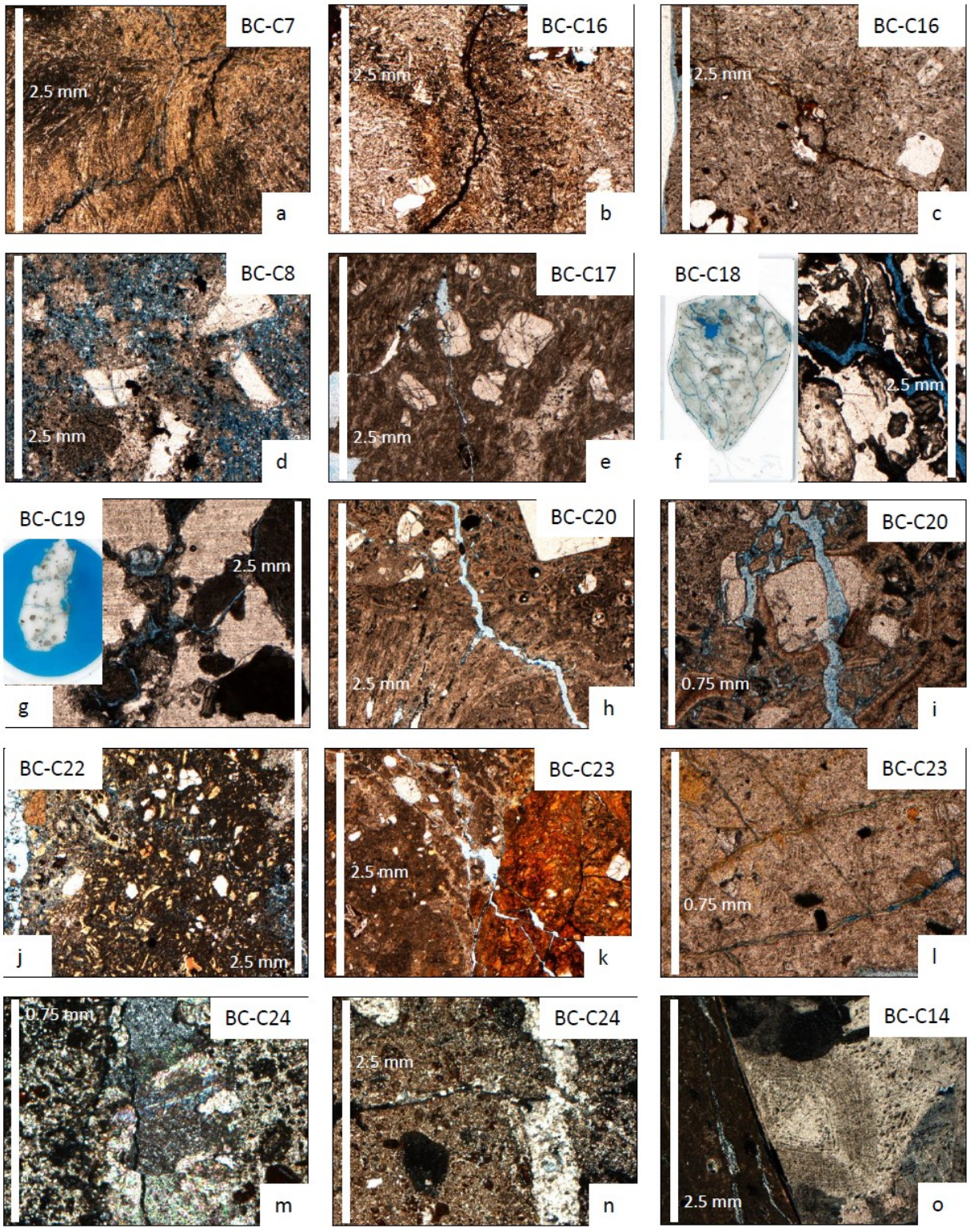

Figure 5.9 Detailed views at the thin section scale of analysed samples: transtensive rhomboidal feature (a); brittle-ductile deformation parallelism (b); transtensive pull-apart feature (c); pervasive argillitic alteration and lack of cohesion (d);

micro-fractures cutting though phenocrysts (e); dense network of open micro-fractures (f and g); micro-fracture dislocating phenocrysts (h and i); scarce micro-fractures (j); micro-fractures and lithologically-controlled alteration bands (k); evidence of fluid circulation along micro-fractures (l); drusy veins calcite, mixed quartz-plagioclase-calcite veins and groundmass microsparite (m); replacive calcite offset by mixed quartz-plagioclase-calcite veins (n); mm-sized fans of fibrous cement calcite and calcite cement rim lining volcanic clasts (o).

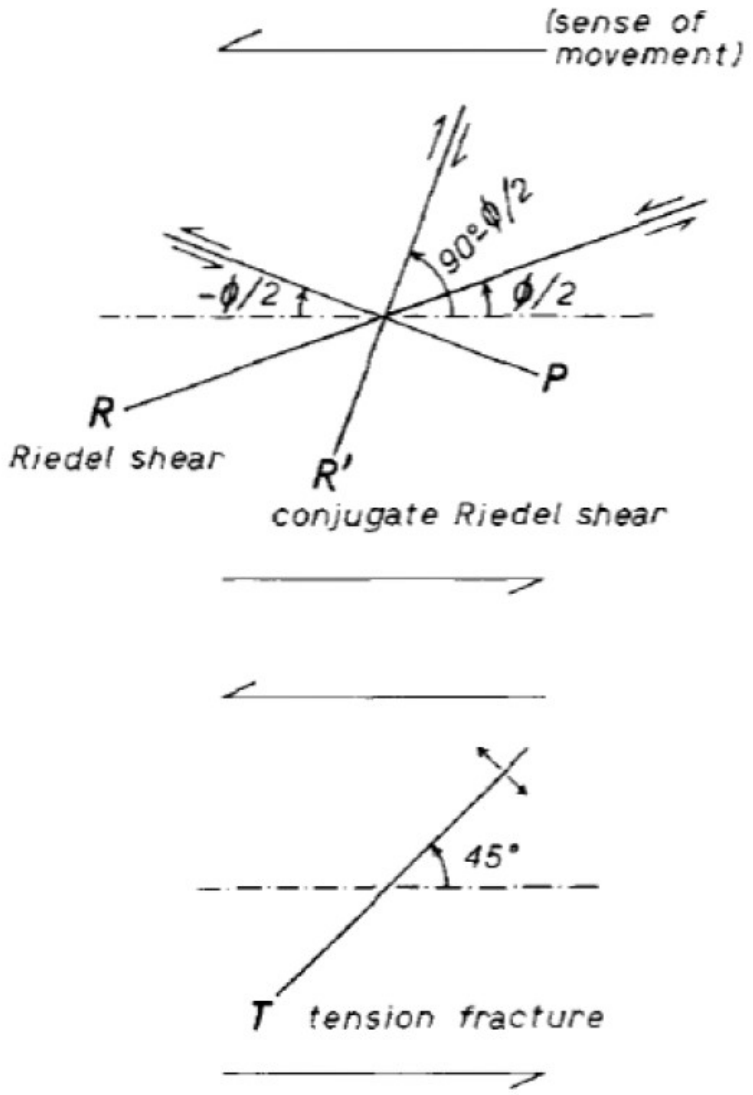

Figure 5.10 Riedel shears for a left-lateral fault, modified after Tchalenko and Ambraseys (1970).

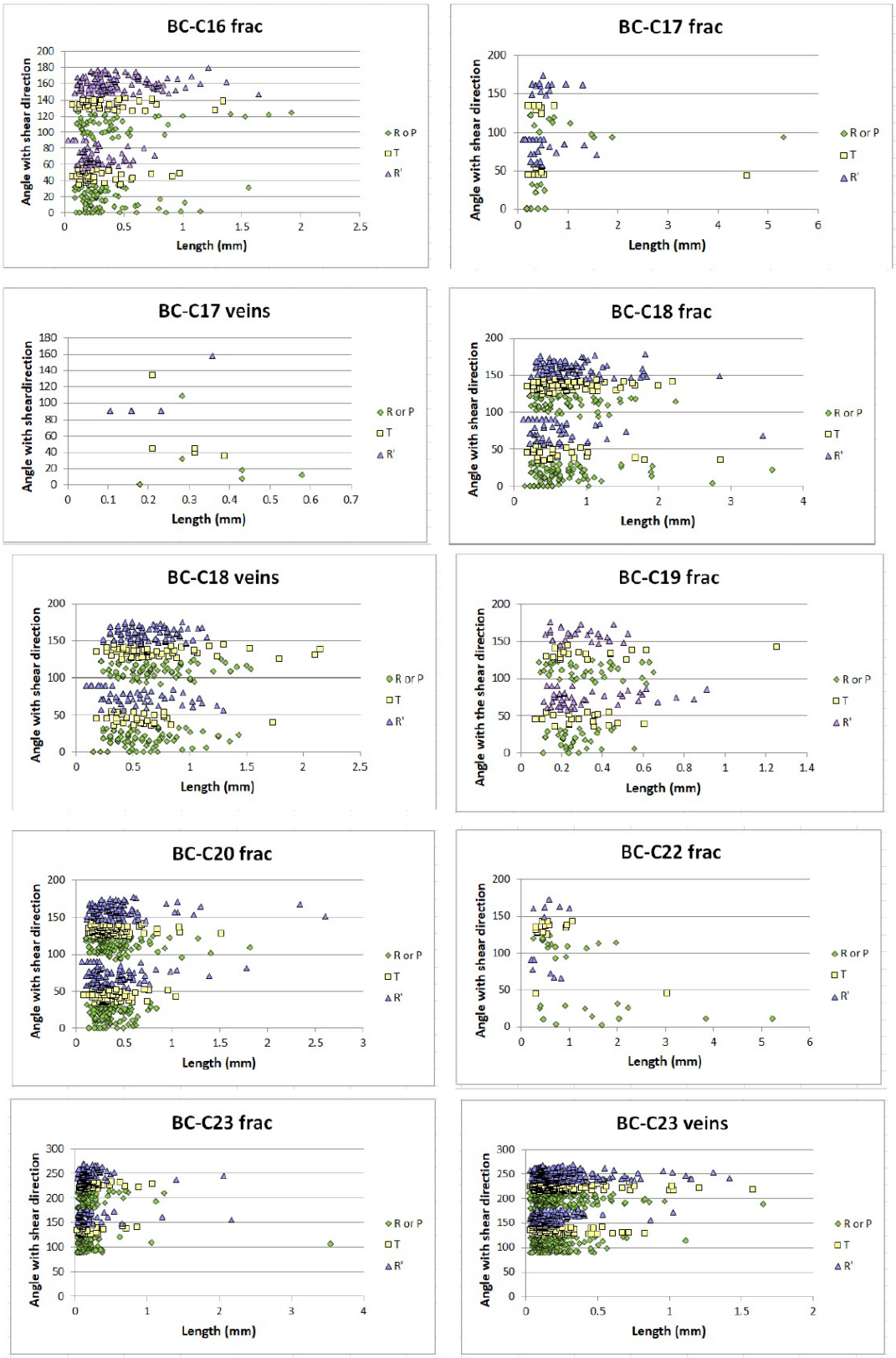

Figure 5.11 Azimuth-length invariance for BC-C16, BC-C17. BC-C18. BC-C19, BC-C20, BC-C22 and BC-C23 micro-fractures and veins length distributions.

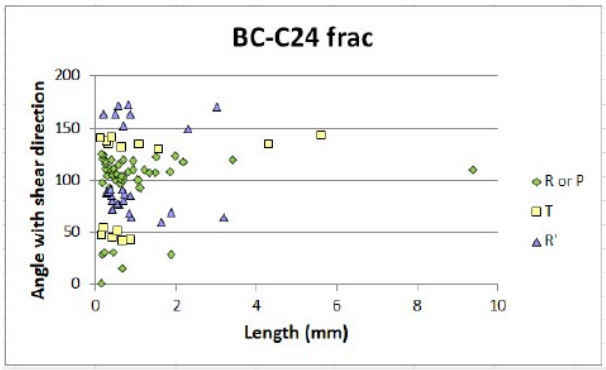

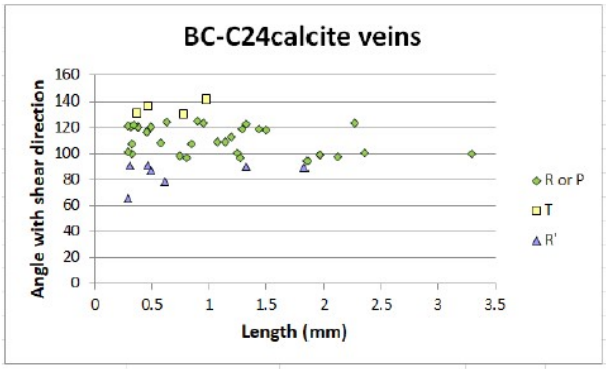

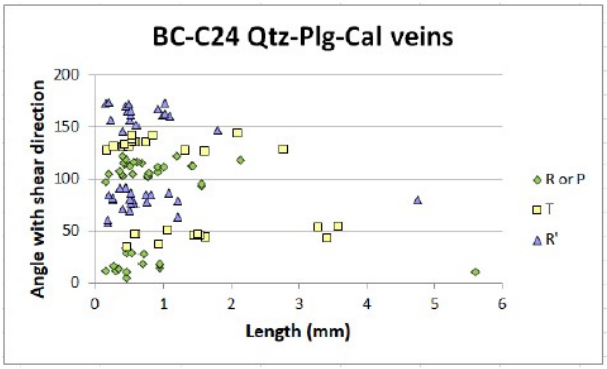

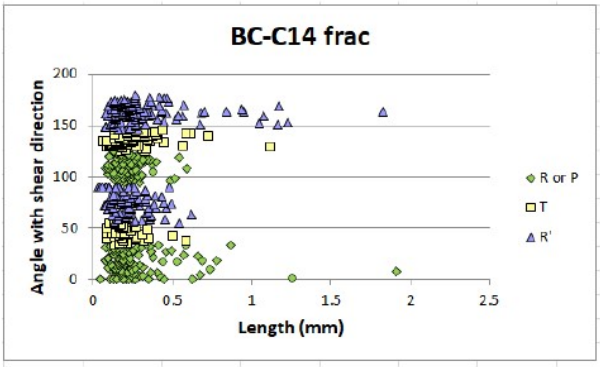

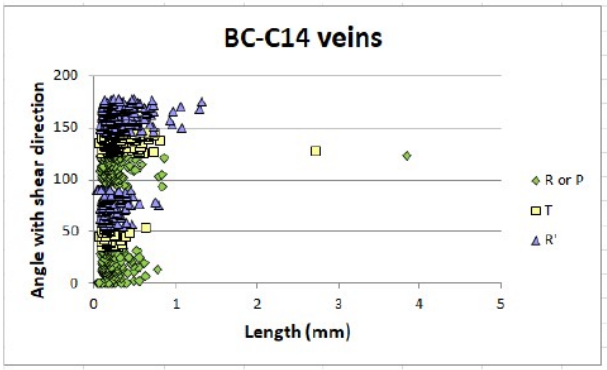

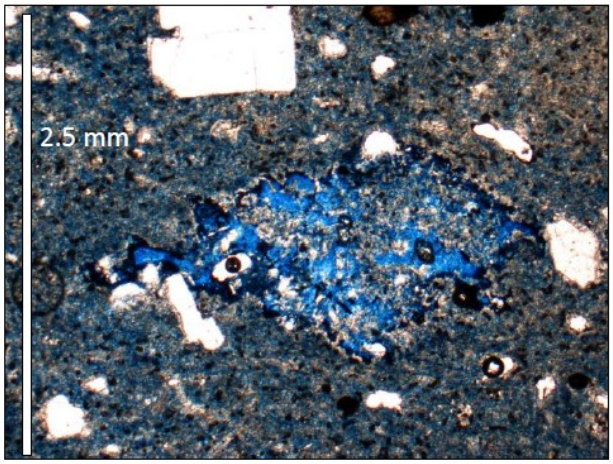

Figure 5.12 Azimuth-length invariance for BC-C24 and BC-C14 micro-fractures and veins length distributions and overall high porosity (blu-dimethyl filled void space) of the Aguajito ignimbrite.

Chapter 6

Paper IV

Insights on fluid origin from multi-scale petrographic and geochemical investigation of fault-related calcites in volcanic-geothermal regions (Tres Vírgenes area, Baja California, Mexico)

C. Pellicioli [a, b], *G. Della Porta* [a], *A. Langone* [c], *M. Zucali* [a, d] *and G. Groppelli* [b].

[a] Dipartimento di Scienze della Terra "Ardito Desio", Università degli Studi di Milano, Milano, Italia;
[b] C.N.R. - Istituto di Geologia Ambientale e Geoingegneria– sezione di Milano, Milano, Italia;
[c] C.N.R. – Istituto di Geoscienze e Georisorse – sezione di Pavia, Pavia, Italia;
[d] Department of Earth and Atmospheric Sciences, University of Houston, Texas-USA.

SUBMITTED TO THE JOURNAL OF VOLCANOLOGY AND GEOTHERMAL RESEARCH IN SEPTEMBER 2019,
REF: MANUSCRIPT NUMBER VOLGEO_2019_341.

Sample collection in the field: ***C. Pellicioli.***

Laboratory analyses: ***C. Pellicioli*** under the supervision of *G. Della Porta* (petrographic and catodoluminescence analyses, carbon and oxygen stable isotopes), of *A. Langone* (laser ablation inductively coupled plasma mass spectrometry, LA-ICP-MS) and of *M. Zucali* (electron microprobe).

Data processing and results interpretation: ***C. Pellicioli*** under the supervision of *G. Della Porta.*

PhD tutoring: *G. Groppelli.*

Manuscript writing: ***C. Pellicioli*** and *G. Della Porta.*

Manuscript Details

Manuscript number	VOLGEO_2019_341
Title	Insights on fluid origin from multi-scale petrographic and geochemical investigation of fault-related calcites in volcanic-geothermal regions (Tres Vírgenes area, Baja California, Mexico)
Article type	Research Paper

Abstract

Faults play a fundamental role in sustaining fluid circulation across volcanic-geothermal regions, often underestimated or simplified in commonly performed studies (i.e. characterization of thermal springs and fluid simulation models). The investigation of fault-related calcite and alteration phases (Tres Vírgenes active geothermal region, Baja California, Mexico) through multi-scale and multi-disciplinary approaches provided new insights on temperature, origin and characteristics of fault-sustained fluid circulation events. Deployed techniques on few selected samples include X-ray diffraction, petrographic, cathodoluminescence and stable isotopes (oxygen and carbon) analyses, and electron microprobe and laser ablation inductively coupled plasma mass spectrometry (LA-ICP-MS) trace element analyses, including Rare Earth Elements (REE). Their sequential application and integration allowed distinguishing several calcite phases based on their chemical, petrographic and luminescence characteristics and identifying the multi-event nature of fluid circulation along faults. Results of this work excluded a marine origin of fault-sustained fluid circulation and of calcite precipitating fluids, highlighting a meteoric to mixed meteoric-hydrothermal provenance, depending on the proximity to the Tres Vírgenes feeding system and in agreement with previous conceptual hydrological models proposed for the study area. Two different fluids circulating along distinct regional structures were identified based on calcite stable isotopes and oxygen-derived palaeotemperatures and electron microprobe analysis: a hotter (up to 100°C) and reducing fluid of mixed hydrothermal-meteoric origin possibly rising from deep metamorphic sequences representing the geothermal reservoir (Azufre fault system) and a cooler (up to 34°C) predominantly meteoric fluid depositing calcite in oxygenated conditions and interacting with organic carbon-rich palaeosoils (Infierno fault). Despite maximum surface to near-surface temperatures reached along regional faults are of 100°C based on calcite stable isotopes and field evidences (clinoptilolite occurrence), shale-normalized (sn) and chondrite-normalized (cn) REE concentrations of calcites provided (Ce/Ce*)sn, (Ce/Ce*)cn, (Eu/Eu*)sn and (Eu/Eu*)cn anomalies suggestive of possibly higher (200-250°C) temperatures for fluids precipitating luminescent calcite.

Keywords	fault-related calcite, geochemistry, petrography, palaeotemperature, geothermal system
Corresponding Author	Claudia Pellicioli
Order of Authors	Claudia Pellicioli, Giovanna Della Porta, Antonio Langone, Michele Zucali, Gianluca Groppelli
Suggested reviewers	valerio acocella, Luca Ferrari, Victor Hugo Garduño-Monroy, Guido Giordano

Submission Files Included in this PDF

File Name [File Type]

Cover Letter_JVGR.docx [Cover Letter]

Manuscript_JVGR.docx [Manuscript File]

Figures_JVGR.pdf [Figure]

To view all the submission files, including those not included in the PDF, click on the manuscript title on your EVISE Homepage, then click 'Download zip file'.

Research Data Related to this Submission

There are no linked research data sets for this submission. The following reason is given:
Data will be made available on request

6.1 Abstract

Faults play a fundamental role in sustaining fluid circulation across volcanic-geothermal regions, often underestimated or simplified in commonly performed studies (i.e. characterization of thermal springs and fluid simulation models). The investigation of fault-related calcite and alteration phases (Tres Vírgenes active geothermal region, Baja California, Mexico) through multi-scale and multi-disciplinary approaches provided new insights on temperature, origin and characteristics of fault-sustained fluid circulation events. Deployed techniques on few selected samples include X-ray diffraction, petrographic, cathodoluminescence and stable isotopes (oxygen and carbon) analyses, and electron microprobe and laser ablation inductively coupled plasma mass spectrometry (LA-ICP-MS) trace element analyses, including Rare Earth Elements (REE). Their sequential application and integration allowed distinguishing several calcite phases based on their chemical, petrographic and luminescence characteristics and identifying the multi-event nature of fluid circulation along faults. Results of this work excluded a marine origin of fault-sustained fluid circulation and of calcite precipitating fluids, highlighting a meteoric to mixed meteoric-hydrothermal provenance, depending on the proximity to the Tres Vírgenes feeding system and in agreement with previous conceptual hydrological models proposed for the study area. Two different fluids circulating along distinct regional structures were identified based on calcite stable isotopes and oxygen-derived palaeotemperatures and electron microprobe analysis: a hotter (up to 100°C) and reducing fluid of mixed hydrothermal-meteoric origin possibly rising from deep metamorphic sequences representing the geothermal reservoir (Azufre fault system) and a cooler (up to 34°C) predominantly meteoric fluid depositing calcite in oxygenated conditions and interacting with organic carbon-rich palaeosoils (Infierno fault). Despite maximum surface to near-surface temperatures reached along regional faults are of 100°C based on calcite stable isotopes and field evidences (clinoptilolite occurrence), shale-normalized (sn) and chondrite-normalized (cn) REE concentrations of calcites provided (Ce/Ce*)sn, (Ce/Ce*)cn, (Eu/Eu*)sn and (Eu/Eu*)cn anomalies suggestive of possibly higher (200-250°C) temperatures for fluids precipitating luminescent calcite.

Keywords: *fault-related calcite, geochemistry, petrography, palaeotemperature, geothermal system*.

6.2 Introduction

Successful exploration and exploitation of geothermal resources in volcanic areas cannot be achieved without a proper understanding of fluid migration processes through the upper crust (Costa, 2006; Bignall et al., 2010). Given the extremely low permeability of volcanic successions, faults and other discontinuities usually provide the main pathways for hydrothermal fluids, even if fluid properties are highly variable along fault planes (Caine et al., 1996). Understanding the provenance of fluids recharging the geothermal reservoir is also fundamental to assess lifetime of geothermal energy production (Portugal et al., 2000). Chemical and isotopic characterization of thermal surface manifestations and reservoir fluids (Truesdell, 1980; Henley et al., 1984; Bau and Dulski, 1999; Portugal et al., 2000; Möller et al., 2004; Verma et al., 2006) and numerical simulation models for fluid circulation (Zhang and Sanderson, 1996; Kloditz and Clauser, 1998), crucial for defining resources exploitation strategies (O'Sullivan et al., 2001; Barbier, 2002), represent the most commonly deployed techniques to assess fluid temperature, origin and migration patterns. However, these approaches are seldom integrated and disregard the fundamental role played by faults, as not all investigated thermal surface manifestations occur along faults and faults included in numerical simulation models are not always proved to be fluid-conductive (Bignall et al., 2010). Despite the assessment of fluid characteristics in volcanic-geothermal regions directly from fault-related mineralization and alteration phases could represent a more relevant approach, this has only been marginally taken into account so far (Liotta et al., 2010).

This study aims to test various multi-scale petrographic and geochemical techniques on a selected limited number of fault-related samples (three alteration facies and two calcite samples) in a volcanic-geothermal environment. The setting chosen for this study is the currently producing Tres Vírgenes geothermal area (10MW_e operating net capacity, Gutierrez-Negrin et al., 2010), located in Baja California Sur (Mexico). Due to the increasing energy demand of electricity linked to the growth of tourism across the Baja California peninsula in the last few decades (Arango-Galván et al., 2015), this region represents a key-area for investigating characteristics of fault-sustained circulating fluids. Actually, notwithstanding the series of studies that accompanied the first exploration phases (Lopez et al., 1989, 1995; Lopez et al., 1993; Wong and Munguía, 2006; Verma et al., 2006; Macías and Jiménez, 2012, 2013; Antayhua-Vera et al., 2015) culminated in the establishment of the Las Tres Vírgenes (LTV) geothermal field by the *CFE* (*Comision Federal de Electricidad)* in 1988 and several projects recently sponsored by the Mexican authorities (among which the CeMIE Geo project P15 of SENER-CONACyT which this study has benefited from), adequate hydrochemical investigations still

lack in the region (Birkle et al., 2016). In addition, the marine (Gulf of California) or meteoric (Holocene or Pleistocene fossil meteoric water) nature of fluid recharge, and consequently the hydrodynamic characteristics of the geothermal reservoir, are still a matter of debate (Portugal et al., 2002; Verma et al., 2006).

Despite the limited number of analysed samples, this work presents an innovative approach and provides novel results concerning fluid temperature, origin and migration. The utilized techniques allowed the identification of mineral phases and related isotopic signature (X-ray diffraction and carbonate stable oxygen and carbon isotopes), the discrimination of several calcite phases often displaying distinct chemical composition and luminescent behaviour (electron microprobe and cathodoluminescence) and the identification of the link between distinct calcite phases and different fault-sustained fluid circulation episodes (microprobe and LA-ICP-MS trace element concentrations).

The results of this investigation provide interesting insights on fluid migration processes and set the bases for future application to other regional or volcano-tectonic lineaments across the Tres Vírgenes area. Moreover, this study encourages the application of the presented methodologies to any other volcanic area of proven or prospective geothermal potential.

6.3 Geodynamic and geological setting

The Tres Vírgenes geothermal region is located about 33 km NW of the Santa Rosalía town, on the western coast of the Gulf of California, in the Baja California Peninsula, Mexico (Figs. 6.1A and B). It lies within the NW-SE trending Santa Rosalía half graben basin, developed from oblique divergence following Cenozoic subduction ceasing between the Farallon and North America plates (Ferrari et al., 2018). The Santa Rosalía basin is bordered by NE dipping and NW-SE trending active faults (Nava-Sanchez et al., 2001; Aragón-Arreola et al., 2005) and has been displaying a normal right-lateral oblique faulting style since 3.5 Ma, when stress reorganization occurred in the region (Angelier et al., 1981; Zanchi, 1994; Aragón-Arreola et al., 2005). The onset of Quaternary siliciclastic volcanism in the Santa Rosalía basin is marked by La Reforma caldera complex (1.29 Ma, Garcia-Sánchez et al., 2019), followed by the Sierra Aguajito (1.17 Ma, Schmitt et al., 2006) and Tres Vírgenes (Holocene, Avellán et al., 2018) volcanic complexes. Recent studies linked to the CeMIE Geo P15 SENER-CONACyT project defined the detailed stratigraphy of La Reforma caldera and Sierra Aguajito volcanic complexes and improved mapping and characterization of Cretaceous to Pleistocene crystalline and sedimentary formations providing the basement to the Quaternary volcanism throughout the Tres Vírgenes region (Garcia-Sánchez et al., 2019). Widely exposed Quaternary

volcanic products consist of several rhyolitic ignimbrites intercalated with basaltic andesitic to andesitic and dacitic lava flows, grouped into syn- and post-caldera phases products by Garcia-Sánchez et al. (2019) for La Reforma caldera complex. These volcanic units lie above several local PDCs, lava flows (pillow lavas) and hyaloclastites representing La Reforma and Sierra Aguajito early submarine activity. Below and locally interfingered with these submarine deposits the regional basement for the Tres Vírgenes area includes (from oldest to youngest): a) crystalline Cretaceous plutonic rocks (*Batolithes Peninsulares,* Gastil, 1975; Schmidt, 1975; McLean, 1988) intruded into the Early Cretaceous supra-crustal volcanic and sedimentary sequence and largely exposed inside La Reforma caldera depression due to resurgence and secondarily along regional Gulf-inherited faults across the Tres Vírgenes region, due to regional exhumation and uplift processes (Pellicioli et al., submitted, a); b) the Comondù Group (12-30 Ma, Umhoefer et al., 2001), composed of red sandstones, siltstones and conglomerates interlayered with the Santa Lucia formation (19.25 Ma, Garduno-Monroy et al., 1993; Garcia-Sánchez et al., 2019), deposited in an arc-forearc setting linked to the Farallon-Guadalupe and North America plates subduction and possibly extending through the Gulf early rifting phases (Umhoefer et al., 2001; Ferrari et al., 2013, 2018; Garcia-Sánchez et al., 2019); c) the Sedimentary Formation of the Santa Rosalia basin (Pliocene-middle Pleistocene, Garcia-Sánchez et al., 2019) mainly composed of siltstones, fossiliferous sandstones and conglomerates representing marine sedimentation coeval to scattered volcanic activity occurring inside the Santa Rosalía basin. Structural studies performed across the region both at the macro- and micro-scale (Pellicioli et al., submitted, a and b) highlighted the control of regional structures on Quaternary volcanic processes (including caldera-collapse and resurgence) and hydrothermal alteration and identified the strict link between faulting and fluid circulation processes, indicated by the syn- and post-faulting character of fault-related calcite mineralization (Pellicioli et al., submitted, b). Besides, hydrochemical and isotopic studies on thermal springs, domestic and geothermal wells across the Tres Vírgenes area performed by Portugal et al. (2000) and Hinojosa et al. (2005) revealed pH values between 1.39 and 8.55, temperatures between 98°C and 18°C and $\delta^{18}O$ between 0.0 and -10.6 ‰ (V-SMOW), with lower pH and higher temperature and $\delta^{18}O$ values close to the currently producing LTV geothermal field.

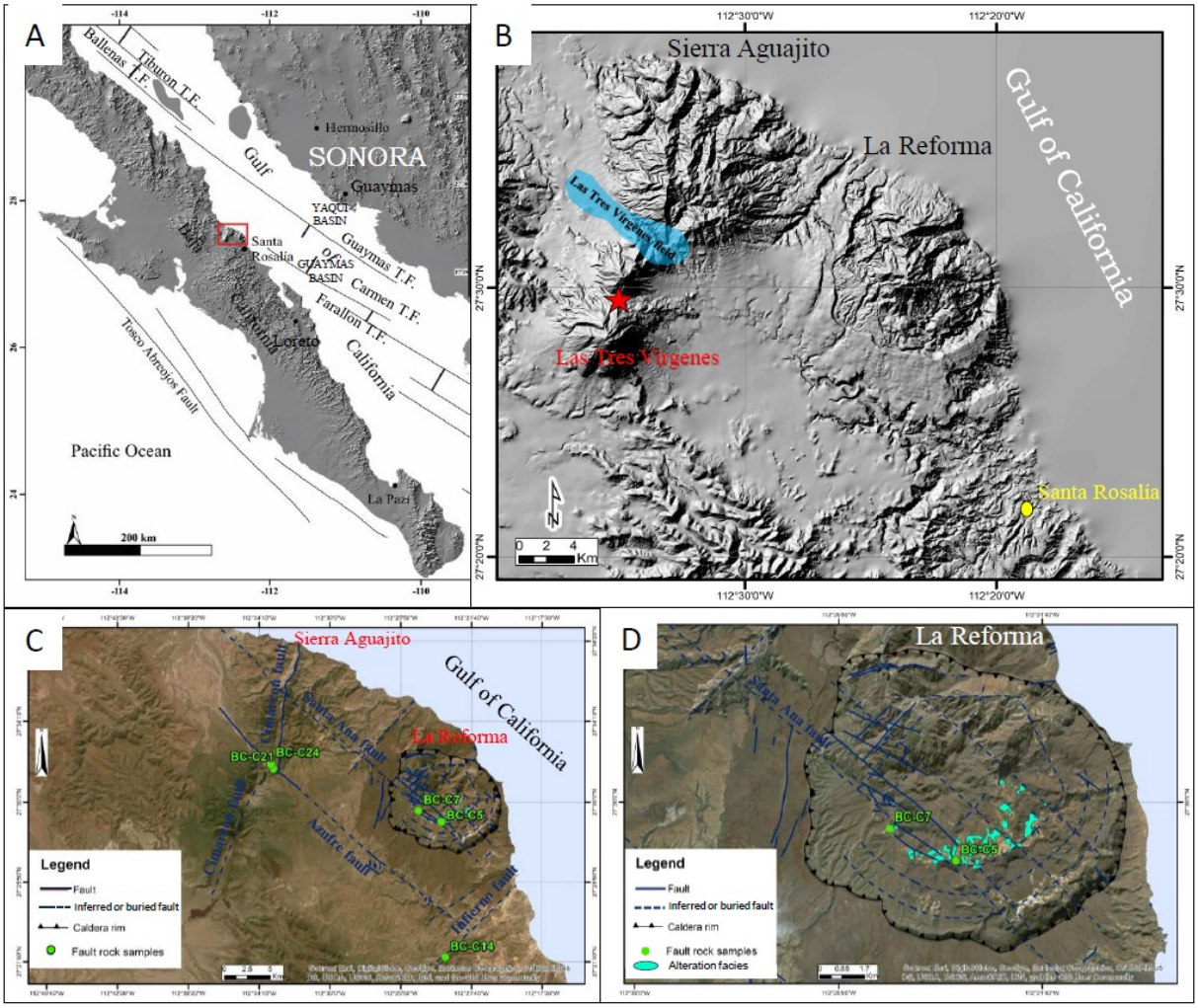

Figure 6.1 Location of the Tres Vírgenes area and geothermal field (A) and of collected samples (B), modified after Pellicioli et al. (submitted, a).

6.4 Material and methods

A total of five fault-related samples (three alteration facies and two calcite samples) were analysed with multi-scale petrographic and geochemical techniques. Information regarding the location, lithology and type of performed analyses on each sample is summarized in Figure 6.1B and Table 6.1. Samples BC-C5, BC-C7 and BC-C21 underwent X-ray diffraction analysis in order to identify mineral phases linked to the pervasive alteration mapped in the field (Pellicioli et al., submitted, a) along the interference zone between the NW-SE trending regional Santa Ana fault and La Reforma caldera complex ring faults (BC-C5 and BC-C7, Fig. 6.1D), as well as along the regional NW-SE trending Azufre fault system, not far from the intersection point with the N-S to NNE-SSW oriented Cimarron

fault system (BC-C21). Samples BC-C24 and BC-C14 were the only among the fault-rock samples analysed by Pellicioli et al. (submitted, b) to bear calcite phases and thus to undergo cathodoluminescence, electron microprobe and LA-ICP-MS major and trace elements analyses and stable O and C isotopes in this study. Samples BC-C24 and BC-C14 were collected along the NNW-SSE trending Azufre and the NNE-SSW oriented Infierno regional fault systems (Fig. 6.1C). In detail, sample BC-C24 was collected where the Azufre fault plane cross-cuts a local PDC of Pliocene age directly lying on top of marine fossiliferous conglomerates (Sedimentary Formation of the Santa Rosalia basin, Garcia-Sánchez et al., 2019) interlayered with hyaloclastites and submarine lava flows representing the basement of Sierra Aguajito volcanism (1.17 Ma, Schmitt et al., 2006). Sample BC-C14 was collected along the Infierno fault damage zone, within an intrusive body belonging to the Miocene Santa Lucia formation (19.25 Ma, Garduno-Monroy et al., 1993; Garcia-Sánchez et al., 2019), here locally emplaced within the Sedimentary Formation of the Santa Rosalia basin.

Table 6.1 List of samples and type of performed analyses.

Sample	Area	Lithology	Coordinates	Age (Ma)	Performed Analyses
BC-C5	La Reforma	altered ignimbrite (Punta Arena ignimbrite)	112°23'26.094"W 27°28'58.396"N	0.96 ± 0.21 [a]	XRD (X-ray diffractometry)
BC-C7	La Reforma	altered ignimbrite (Punta Arena ignimbrite)	112°24'47.588"W 27°29'33.192"N	0.96 ± 0.21 [a]	XRD (X-ray diffractometry)
BC-C14	La Reforma	Intrusive body (Santa Lucia formation)	112°23'12.894"W 27°21'54.19"N	19.25 ± 0.08 [a]	Cathodoluminescence, C and O stable isotopes, electron micro-probe, LA-ICP-MS
BC-C21	Sierra Aguajito	Altered ignimbrite (Aguajito ignimbrite)	112°33'19.514"W 27°31'44.525"N	1.17 ± 0.07 [b]	XRD (X-ray diffractometry)
BC-C24	Sierra Aguajito	Local PDC deposit (pre-Aguajito ignimbrite)	112°33'28.869"W 27°31'57.057"N	>1.17 ± 0.07 [b]	Cathodoluminescence, C and O stable isotopes, electron micro-probe, LA-ICP-MS

[a] Garcia-Sánchez et al. (2019); [b] Schmitt et al. (2006).

6.4.1 X-ray diffraction

X-ray diffraction is a non-destructive analysis technique that provides detailed information on solids structures, in terms of chemical bonds between the atoms. It is a powerful tool to identify minerals in rocks and soils and it is routinely applied to several contexts including geological/mineralogical, pedological, chemical, forensic investigations (Hanawalt et al., 1938; Périnet, 1964; Eberl, 2003; Harris et al., 2008). One of the most important application of this technique consists in the identification of clay minerals, frequently too small to be recognised by classical optical crystallographic methods (Carrol, 1970; Brown, 1982). As a result, X-ray diffraction analysis is the most suitable technique to investigate alteration phases of unknown mineralogy, such as those displayed by samples BC-C5, BC-C7 and BC-C21. The analysis was performed on four manually-

grounded sample powders (one analysis on each samples for BC-C5 and BC-C7 and two analyses for BC-C21) with the high-resolution X-ray powder diffractometer Panalytical X' pert Pro at 40 kV and 40mA at the Department of Earth Sciences "Ardito Desio" of Milan University. The deployed instrument is equipped with an incident beam monochromator separating the ka1 and ka2, and only allowing measurement with the ka1. Allowed geometries include both the Bragg-Brentano (divergent) geometry and the parallel beam geometry, and the X'Celerator detector guarantees very quick data collection and an excellent signal-to-noise ratio. Data were collected from 5° to 80 or 90° 2θ, with steps every 0.02° having a counting time of 20 seconds.

6.4.2 Petrographic and cathodoluminescence analyses

Standard petrographic analyses of 4 thin sections with the polarized transmitted and reflected light Axioskop Pol Routine Microscope by Carl Zeiss Microscopy ® were accompanied by cathodoluminescence investigation. Cathodoluminescence by electron bombardment is a commonly studied phenomenon on polished thin sections or surfaces of carbonate and clastic sedimentary rocks (Richter et al., 2003). This analysis technique is routinely deployed on carbonate rocks to provide information on diagenetic features, such as calcite cement phases, replacement reactions, pore water chemistry and redox conditions during calcite precipitation (Machel, 1985; Budd et al., 2000), while in siliciclastic sedimentary rocks it is used to investigate grain provenance and diagenetic cement phases (Richter et al., 2003). This technique was applied to samples BC-C24 and BC-C14 to investigate calcite phases precipitated along fault planes and derive information on the redox conditions and origin of the calcite-precipitating fluids, given that luminescence of calcite is activated and quenched by the concentration of Mn^{2+} and Fe^{2+} within the calcite crystals, respectively (Machel, 1985; Barnaby and Rimstidt, 1989). This technique has previously been applied in volcanic-hydrothermal settings and along deformation zones by Benedicto et al. (2008), Barker et al. (2009) and Uysal et al. (2011). The analysis was performed at the Department of Earth Sciences "Ardito Desio" of Milan University with a luminoscope Cambridge Image Technology Limited (CITL), Cambridge, UK (model MK 5-2 operating system at 10-16 kV with a beam current between 200-400 μA, and vacuum gauge 50-70 millitor).

6.4.3 Electron microprobe

To determine the chemical composition of luminescent and non-luminescent calcite phases the supplementary higher precision electron microprobe analysis technique was deployed. The electron microprobe is commonly used to characterize silicate minerals and metal oxides (Sweatman et al., 1969; Paquette et al., 1990); it allows the identification of mineral compositional zoning and in the

case of calcite it is often combined with cathodoluminescence (Paquette et al., 1990; Pagel et al., 2000) to investigate the Fe and Mn content of luminescent/non luminescent calcite phases. The analyses on samples BC-C24 and BC-C14 were performed with the JEOL 8200 Super Probe of the Electron Microprobe Laboratory of the Department of Earth Sciences "Ardito Desio" at Milan University, allowing accelerating voltages of 200V to 30kV, a 10-12 to 10-5 A current range and magnifications from 40x up to 300,000x. The WDS and EDS X-ray systems display detectable element ranges of 4Be to 92U (WDS) and 11Na to 92U (EDS), a less/equal to 0.1 CuZ atomic number resolution (WDS) and a 144 eV or better FWHM energy resolution (EDS). A 5 μm wide electron beam was deployed for calcite phases. Previously identified luminescent and non-luminescent analysis points on thin sections were directly mapped, drawn and labelled during the electron microprobe analysis and images up to 2048 x 2048 pixels of resolution were generated. Based on measured major elements abundance the calcite nature of the chosen points was double-checked, unwanted results were excluded and double-checked outputs were converted to ppm.

6.4.4 Laser ablation inductively coupled plasma mass spectrometry (LA-ICP-MS)

Samples BC-C24 and BC-C14 were also analysed with the LA-ICP-MS technique, commonly deployed to determine minor and trace element (including rare earths elements REE) abundances on natural and synthetic solid materials (rock forming minerals, gem-stones, carbonate materials, glasses and ceramics). This technique is utilized on calcite phases to derive REE patterns and anomalies, useful to typify fluids of different origin, to investigate equilibrium/dis-equilibrium conditions of the fluid-rock system, as well as to determine REE fractionation and partition coefficients of complexing species (Bau, 1991; Bau and Möller, 1992; Bau, 1996; Bau and Dulski, 1999; Möller et al., 2004; Uysal et al., 2007 and 2011; Benedicto et al., 2008; Della Porta et al., 2015). Trace element mineral composition of samples BC-C24 and BC-C14 was determined by laser ablation inductively coupled plasma mass spectrometry (LA-ICP-MS) at the IGG-CNR (Istituto di Geoscienze e Georisorse of the National Research Council) of Pavia. The instrument couples an Eximer Laser 193nm ArF (GeoLas200 Microlas) with a Triple Quadrupole (8900 QQQ from Agilent). NIST-SRM610 was used as an external standard, whereas ^{44}Ca was adopted as internal standard. In each analytical run the USGS reference samples BCR2 and NIST612 (Norman et al. 1996; Pearce et al. 1997; Rocholl et al. 1997; Wilson, 1997) were analysed together with the unknowns for quality control. Precision and accuracy are better than 5% and 10%, respectively. Data reduction was performed using the *Glitter* software package (van Achterbergh et al., 2001). LA-ICP-MS analysis on samples BC-C24 and BC-C14 was performed on specifically prepared and polished 100 μm thick thin sections. Despite the lack of exact correspondence between points analysed with cathodoluminescence and electron microprobe

and points investigated with the LA-ICP-MS technique, the latter were carefully chosen in order to represent samples characteristics and variability observed with previously utilized analytical techniques. A 50 μm wide laser beam was deployed to analyse calcite phases and an average 55-56% CaO content was considered for both BC-C24 and BC-C14 samples based on electron microprobe analysis results.

6.4.5 Carbon and oxygen stable isotopes

Carbon and oxygen stable isotope measurements on calcite were performed to further investigate the temperature and origin of precipitating fluids in samples BC-C24 and BC-C14. Delta values of hydrogen (δD), oxygen ($\delta^{18}O$) and carbon ($\delta^{13}C$) are routinely measured in sedimentary geology (Arthur et al., 1983), as they can provide information on fluid origin (hydrogen and carbon, Hoefs, 1980; Sharp, 2007), calcite precipitation temperature (oxygen, McCrea 1950; Epstein et al., 1953; Craig, 1965; Tarutani et al., 1969; Hoefs, 1980; Kim and O'Neil, 1997; Sharp, 2007; Coplen 2007), as well as insights on diagenesis, palaeoclimatology and palaeoceanography (Hudson and Anderson 1989; Lajtha and Michener, 1994; Hiatt and Pufhal, 2014). Sedimentary geology is not the exclusive field of application of this analytical technique, also commonly deployed for similar purposes in geothermal-volcanic contexts (Barker et al., 2009; Uysal et al., 2009; Liotta et al., 2010) and on fault-related calcite phases (Travè et al., 1998; Boles and Grivetti, 2000; Pili et al., 2002; Benedicto et al., 2008; Liotta et al., 2010). $\delta^{18}O$ and $\delta^{13}C$ measurements were determined on BC-C24 and BC-C14 calcite phases (12 calcite powders analysed for sample BC-C24 and 10 for sample BC-C14) with an automated carbonate preparation device (Gasbench II) and a Thermo Fischer Scientific Delta V Advantage continuous flow isotopic ratio mass spectrometer (IRMS) at the Department of Earth Sciences "Ardito Desio" of Milan University. Carbonate powder samples, extracted with a micro-drill, were reacted with > 99% orthophosphoric acid at 70°C. The carbon and oxygen isotopic compositions are expressed in the conventional delta notation calibrated to the Vienna Pee-Dee Belemnite (V-PDB) scale by the international standards IAEA 603 and NBS-18. IRMS measurements were normalized using the two point linear normalization (Paul et al., 2007). Analytical reproducibility for these analyses was better than ± 0.1‰ for both $\delta^{18}O$ and $\delta^{13}C$ values. The BC-C24 and BC-C14 luminescent and non-luminescent calcite phases could not be properly separated during micro-drilling, due to their sub-millimetre scale. Results therefore represent the isotopic signature of a mixture of luminescent and non-luminescent calcite phases. Furthermore, of the three identified calcite cement phases in BC-C14, only one (millimetre size fans of fibrous cement) could be extracted with the micro-drill and thus analysed with the IRMS, whilst the remaining calcite cement phases were too small to be extracted.

6.5 Results and data interpretation

6.5.1 X-ray diffraction

Besides from quartz, mica, plagioclase and K-feldspar, which are all expected minerals in the trachydacitic to dacitic Punta Arena ignimbrite (Table 6.1), clinoptilolite and calcite were detected in

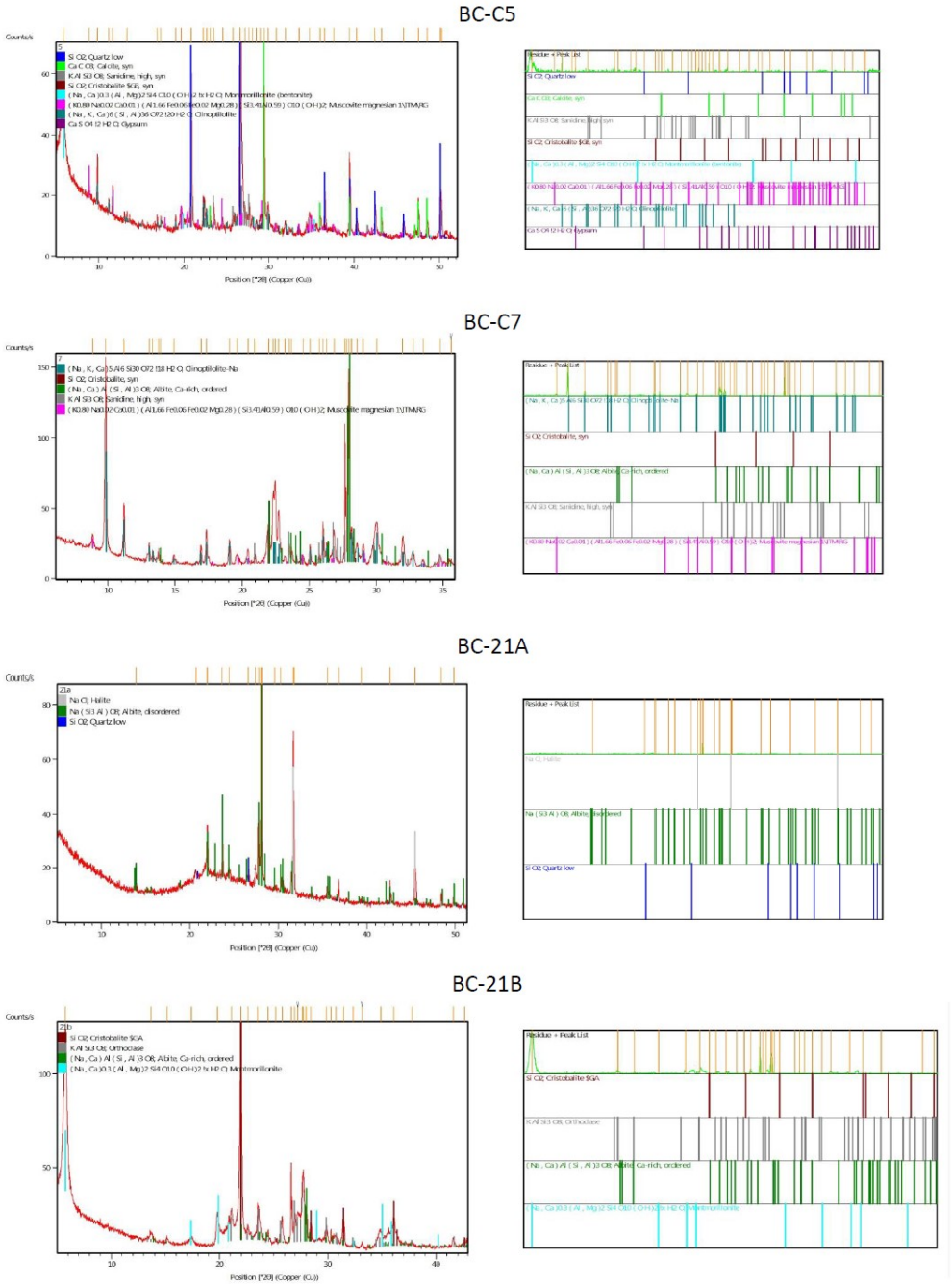

Figure 6.2 BC-C5, BC-C7 and BC-C21 samples composition from X-ray diffraction analysis. To notice the identification of the zeolite mineral clinoptilolite in samples BC-C5 and BC-C7.

samples BC-C5 and BC-C7 (Fig. 6.2). The calcite amount contained in samples BC-C5 and BC-C7 was too low to justify any further analysis. No clinoptilolite or calcite, or other zeolite minerals were instead found in sample BC-C21 that displays a rhyolite-typical mineral assemblage (albite-plagioclase, quartz, K-feldspar, volcanic glass) and smectite (montmorillonite, Fig. 6.2).

Interpretation

Clinoptilolite is a zeolite mineral stable in a variety of different geological settings, but generally indicative of low (up to 100°C) temperatures (Iijima, 1980; Ogihara, 2000). Calcite is commonly found in volcanic and hydrothermal contexts due to CO_2 abundance in magma, but it also generally characterizes deformation and shear zones in non-volcanic settings (calcite veins and slickensides; Pili et al., 2002) and is a common alteration mineral of silicic volcanic glass, biotite and plagioclase (Gifkins et al., 2005).

6.5.2 Petrographic and cathodoluminescence analyses

Calcite occurs under several phases inside BC-C24 and BC-C14 samples. Calcite phases in sample BC-C24 include (Figs. 6.3A-D, 6.4): non-luminescent prismatic to equant calcite with drusy fabric (e.g., crystal size increasing towards the centre of the pore) in veins growing perpendicular to fracture walls (crystal size from 100 to 500 μm) labelled in this study drusy vein calcite; non-luminescent groundmass calcite composed of microsparite crystals precipitated within matrix porosity; non-luminescent calcite filling millimetres long and 50-100 μm thick mixed plagioclase-quartz-calcite veins; replacive calcite on volcanic clasts consisting of an equant mosaic of calcite crystals, 100 to 200 μm in size, sometimes displaying a luminescence (Fig. 6.4). In BC-C14 calcite forms three cement phases (Figs. 6.3E-H, 6.5). The first cement calcite is an irregular 50-100 μm thick calcite rim of equant luminescent microsparite (10-50 μm in size) lining angular volcanic (pyroclastic and lava) rock fragments (or clasts) crossed by irregular and sometimes open micro-fractures (Pellicioli et al., submitted, b). The second calcite phase consists of non-luminescent fans of fibrous cement with undulose extinction up to 1 to 2 millimetres in length and 1 millimetre wide, growing on top of the 50-100 μm thick calcite rim and perpendicular to the volcanic clasts outer surface, as commonly occurring in fault and fault-breccia environments (cf. Benedicto et al., 2008). The third non-luminescent calcite phase fills veins cross-cutting the previous cement phases. Additionally, calcite in BC-C14 occurs inside volcanic clasts, and is often luminescent. Calcite within clasts probably originated by partial replacement of volcanic fragments or minerals by calcite crystals related to the same fluids that precipitated the luminescent cement rim.

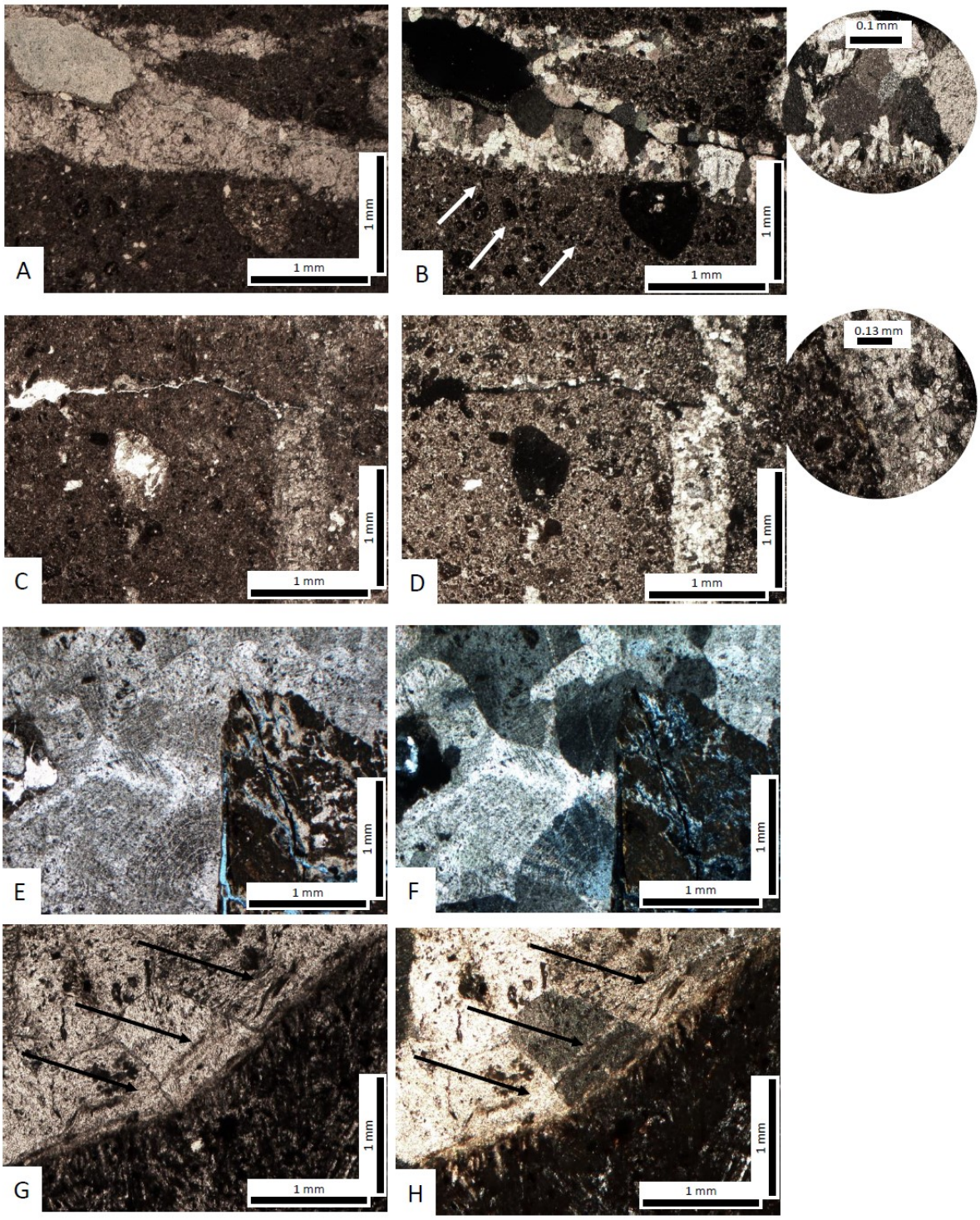

Figure 6.3 Calcite phases in samples BC-C24 (A to D) and BC-C14 (E to H). (A-B) Images in parallel (A) and crossed (B) polarizers of prismatic to equant drusy calcite crystals growing perpendicular to fracture walls (crystal size 100 to 500 µm) and groundmass microsparite calcite crystals precipitated within matrix porosity (white arrows). (C-D) Images in parallel (C) and crossed (D) polarizers of replacive calcite on volcanic clasts forming an equant mosaic of calcite crystals 100-200 µm in size. (E) Image in parallel polarizers of fans of fibrous calcite cement with undulose extinction, up to 1 to 2 mm in length and 1 mm wide growing perpendicular to the clast outer surface. (F) Image in crossed polarizers of panel E showing the undulose extinction of fibrous crystal fans followed by equant calcite cement crystals, 0.5 mm in size. (G-H) Images in

parallel (G) and crossed (H) polarizers of equant calcite rim lining volcanic clasts and calcite filling vein cross-cutting previous cement phases (black arrows).

Interpretation

Sample BC-C24 is characterized by multiple circulation events along the fault plane as evidenced by cathodoluminescence results (Fig. 6.4). A first circulation episode precipitated luminescent (Mn-rich and Fe-poor) replacive calcite within volcanic clasts from reducing fluids. This event was followed by circulation of a probably oxygenated fluid that precipitated non-luminescent replacive calcite within volcanic clasts on top of previously precipitated luminescent calcite, few millimetres long and 50-100 μm thick, mixed plagioclase-quartz-calcite veins, prismatic to equant drusy vein calcite and also groundmass microsparite crystals within the fault-rock matrix porosity. Cathodoluminescence analysis results indicate at least three along-fault circulation phases for sample BC-C14 (Fig. 6.5). Firstly, a Mn-rich and Fe-poor luminescent calcite phase forming rims around fractured volcanic clasts precipitated from reducing (e.g. late phreatic or shallow burial fluids) fluids that allowed the incorporation of Mn^{2+} in calcite cement crystals causing bright luminescence. These reducing fluids also probably entered some open micro-fractures within angular volcanic clasts and partially replaced volcanic minerals, as testified by the sometimes luminescent replacive calcite in clasts phases. This first circulation event was followed by two other circulation episodes that precipitated non-luminescent mm-sized fans of fibrous cement calcite, later on cross-cut by calcite filling veins. Non-luminescent calcite in clasts also probably precipitated coevally to fibrous cement calcite. The non-luminescent character of cement calcite phases belonging to the second and third circulating events could indicate either precipitation in oxygenated conditions or from Fe-rich fluids, with Fe quenching the luminescence activated by Mn (cf. Machel, 1985).

6.5.3 Electron microprobe

Results from a selected set of points analysed with the electron microprobe are illustrated in Tables 6.2 and 6.3 and Figures 6.4 and 6.5, while complete results for samples BC-C24 and BC-C14 are illustrated in Tables 6.10 and 6.11 of the Appendix section. In the absence of Fe, or with very low Fe concentrations (up to 10 ppm), calcite luminescence in BC-C24 is activated at concentrations of Mn > 96 ppm (dull luminescence in analysed spot 24-24 in Table 6.2) and Mn/Fe ratios > 4.9 in replacive calcite on volcanic clasts (bright spot luminescence in analysed spot 24-12 in Table 6.2), whereas in drusy vein calcite no luminescence is observed for Mn concentrations ranging from 37 to 177 ppm in absence of Fe (Table 6.2). Luminescence in BC-C24 replacive calcite is observed for rather high Mn concentrations (> 6000 ppm Fig. 6.4 and Table 6.2), while the non-luminescent character of some of the analysed spots is observed in the absence or with very low Mn content. The same applies to non-

luminescent drusy vein calcite. Replacive luminescent calcite displaying the highest Mn concentrations shows a bright zoning (e.g. analysed spots 2 and 5 in Fig. 6.4). Electron microprobe analysis results on BC-C14 are more variable (Table 6.3). Calcite luminescence is activated at concentrations of Mn > 184 ppm and Mn/Fe ratios > 0.19 in rim calcite and for Mn > 140 ppm and Mn/Fe ratios > 0.06 in calcite in clasts. Luminescence in BC-C14 rim calcite and calcite in clasts is observed for high Mn concentrations (up to 650-660 ppm, Table 6.3), whilst the non-luminescent character of these phases is due to the absence or very low Mn content, and in the case of rim calcite is probably due to erroneously sampled portions of non-luminescent fibrous cement calcite, also displaying rather low Mn contents. The only non-luminescent calcite phase displaying comparable (several hundred ppm, Table 6.3) Mn and Fe contents is calcite filling veins. Contrarily to sample BC-C24, luminescent rim calcite and calcite in clasts display a dark zoning (e.g. analysed spots 32 or 20 in Fig. 6.5). Mn concentrations of BC-C24 luminescent phases are one order of magnitude higher than in BC-C14 (Tables 6.2 and 6.3). Fe concentrations are instead one order of magnitude higher in BC-C14 than in BC-C24 (Tables 6.2 and 6.3).

Table 6.2 BC-24 selected analysis points Mn, Fe and Mn/Fe values from electron microprobe analyses. Calcite luminescence is activated at concentrations of Mn > 100 ppm and Mn/Fe ratios > 5 in replacive calcite on volcanic clasts, whereas in drusy vein calcite no luminescence is observed for Mn concentrations ranging from 37 to 177 ppm in absence of Fe.

Image	Analysis point	Mn (ppm)	Fe (ppm)	Mn/Fe	Si (ppm)	luminescent	calcite phase
24-12	1	111	0	-	262	**YES**	Replacive calcite on volc clasts
24-12	2	6641	0	-	169	**YES**	Replacive calcite on volc clasts
24-12	3	589	0	-	128	**YES**	Replacive calcite on volc clasts
24-12	4	906	0	-	15	**YES**	Replacive calcite on volc clasts
24-12	5	5888	0	-	26	**YES**	Replacive calcite on volc clasts
24-12	6	0	168	0	275	NO	Replacive calcite on volc clasts
24-12	7	0	0	0	100	NO	Replacive calcite on volc clasts
24-12	8	162	4	40.5	326	**YES**	Replacive calcite on volc clasts
24-12	9	928	798	1.16	105	NO	Replacive calcite on volc clasts
24-12	10	317	65	4.9	176	**YES**	Replacive calcite on volc clasts
24-12	11	0	0	0	790	NO	Replacive calcite on volc clasts
24-12	12	0	560	0	366	NO	Replacive calcite on volc clasts
24-12	13	0	181	0	627	NO	Replacive calcite on volc clasts
24-13	16	4905	0	-	0	**YES**	Replacive calcite on volc clasts
24-13	17	391	353	1.11	281	NO	Replacive calcite on volc clasts
24-13	18	8	240	0.03	355	NO	Replacive calcite on volc clasts
24-13	19	4251	0	-	0	**YES**	Replacive calcite on volc clasts
24-13	20	0	0	0	272	NO	Replacive calcite on volc clasts
24-13	21	4901	259	18.9	436	**YES**	Replacive calcite on volc clasts
24-13	22	0	0	0	0	NO	Replacive calcite on volc clasts
24-13	23	0	921	0	0	NO	Replacive calcite on volc clasts

24-13	24	37	158	0.23	228	NO	Replacive calcite on volc clasts
24-13	25	0	366	0	173	NO	Replacive calcite on volc clasts
24-13	26	155	393	0.39	338	NO	Replacive calcite on volc clasts
24-24	27	494	0	-	557	**YES**	Replacive calcite on volc clasts
24-24	28	81	181	0.45	0	NO	Replacive calcite on volc clasts
24-24	29	0	141	0	510	NO	Replacive calcite on volc clasts
24-24	30	162	10	16.2	929	**YES**	Replacive calcite on volc clasts
24-24	31	280	0	-	43	**YES**	Replacive calcite on volc clasts
24-24	32	0	0	0	0	NO	Replacive calcite on volc clasts
24-24	33	0	29	0	7	NO	Replacive calcite on volc clasts
24-24	34	0	9	0	236	NO	Replacive calcite on volc clasts
24-24	35	450	302	1.49	118	NO	Replacive calcite on volc clasts
24-24	36	96	0	-	0	**DULL**	Replacive calcite on volc clasts
24-24	37	125	0	-	288	**DULL**	Replacive calcite on volc clasts
24-18	42	37	0	-	0	NO	Drusy vein calcite
24-18	43	0	7	0	211	NO	Drusy vein calcite
24-18	44	0	0	0	210	NO	Drusy vein calcite
24-18	45	0	0	0	457	NO	Drusy vein calcite
24-18	46	177	0	-	90	NO	Drusy vein calcite
24-18	47	0	283	0	73	NO	Drusy vein calcite
24-18	48	37	0	-	129	NO	Drusy vein calcite
24-18	49	8	0	-	31	NO	Drusy vein calcite

Table 6.3 BC-C14 selected analysis points Mn, Fe and Mn/Fe values from electron microprobe analyses. Calcite luminescence is activated at concentrations of Mn > 184 ppm and Mn/Fe ratios > 0.19 in rim calcite, Mn > 140 ppm and Mn/Fe ratios > 0.06 in calcite in clasts. Most of rim calcite, calcite in clasts and calcite filling veins analysed points display silicate-contamination by volcanic material ([a]), causing the low Mn/Fe ratios of luminescent calcite phases. In fibrous cement no luminescence is observed for Mn concentrations ranging from 66 to 251 ppm and Fe between 111 and 539 ppm.

Image	Analysis point	Mn (ppm)	Fe (ppm)	Mn/Fe	Si (ppm)	luminescent	calcite phase
14-1	29	96	749	0.13	21400	NO	Rim calcite [a]
14-1	30	560	114	4.9	14516	**YES**	Rim calcite [a]
14-1	35	280	631	0.44	15119	**YES**	Rim calcite [a]
14-1	39	656	1305	0.5	24800	**YES**	Rim calcite [a]
14-16	19	0	2421	-	10296	NO	Rim calcite [a]
14-16	20	420	2189	0.19	38300	**YES**	Rim calcite [a]
14-16	21	74	1147	0.06	7938	NO	Rim calcite [a]
14-16	22	0	647	0	2841	NO	Rim calcite [a]
14-16	23	251	60	4.18	490	**YES**	Rim calcite
14-16	24	243	0	-	830	**YES**	Rim calcite
14-16	25	184	495	0.37	3741	**YES**	Rim calcite [a]
14-16	26	0	734	0	554	NO	Rim calcite
14-16	27	0	1480	0	5289	NO	Rim calcite [a]
14-1	31	376	599	0.63	13549	**DULL**	Calcite in clasts [a]
14-1	32	140	166	0.84	7082	**DULL**	Calcite in clasts
14-4	40	449	887	0.5	9543	**YES**	Calcite in clasts [a]
14-4	41	0	1444	0	27800	NO	Calcite in clasts [a]
14-4	42	663	310	2.14	11019	**YES**	Calcite in clasts [a]

14-4	43	597	353	1.69	10192	**YES**	Calcite in clasts [a]
14-4	44	0	70	0	1975	NO	Calcite in clasts [a]
14-4	45	221	3666	0.06	33200	**YES**	Calcite in clasts [a]
14-9	8	221	0	-	238	NO	Calcite in clasts
14-9	11	0	565	0	9643	NO	Calcite in clasts [a]
14-9	16	324	1638	0.2	96500	**YES**	Calcite in clasts [a]
14-1	33	280	266	1.05	423	NO	Calcite filling vein
14-1	36	398	3064	0.13	67500	**YES**	Calcite filling vein [a]
14-9	10	258	203	1.27	732	NO	Calcite filling vein
14-9	15	0	620	0	175	NO	Calcite filling vein
14-9	17	649	359	1.81	21051	**YES**	Calcite filling vein [a]
14-1	34	0	0	0	101	NO	mm-sized fans of fibrous cement
14-1	38	66	111	0.59	253	NO	mm-sized fans of fibrous cement
14-4	46	118	0	-	158	NO	mm-sized fans of fibrous cement
14-9	7	0	539	0	0	NO	mm-sized fans of fibrous cement
14-16	28	0	266	0	100	NO	mm-sized fans of fibrous cement
14-383-1	1	0	142	0	0	NO	mm-sized fans of fibrous cement
14-383-2	2	0	164	0	218	NO	mm-sized fans of fibrous cement
14-405-3	3	0	219	0	115	NO	mm-sized fans of fibrous cement
14-405-4	4	133	0	-	113	NO	mm-sized fans of fibrous cement
14-409-5	5	251	129	1.95	541	NO	mm-sized fans of fibrous cement
14-409-6	6	133	126	1.06	0	NO	mm-sized fans of fibrous cement

[a] : silicate-contaminated calcite, derived from accidental inclusion of volcanic silicate material during analyses.

Interpretation

Although published Mn concentration lower limits for the activation of luminescence in calcite are variable (Frank et al., 1982; Hemming et al., 1989; Mason and Mariano, 1990; Savard et al., 1995; Habermann et al., 1998; Budd et al., 2000) or even absent (Richter et al., 2003), usually Fe starts exerting a quenching effect on calcite luminescence at concentrations > 100 ppm and for Mn/Fe ratios < 1.8 (Budd et al., 2000). This is observed in BC-C24 replacive calcite on volcanic clasts that shows bright luminescence at Mn/Fe ratios > 4.9 and displays a good correlation between the observed luminescence and the Mn-Fe concentrations in calcite crystals (Table 6.2). The absent or very low Mn content of BC-C24 non-luminescent calcite phases indicates the oxygenated conditions (i.e. phreatic or vadose waters) and the meteoric nature of fluids precipitating non-luminescent replacive calcite and drusy vein calcite. A clean calcite typical composition characterises BC-C24 analysed points (CaO > 99%), even though Si content reaches 450 ppm in drusy vein calcite (Fig. 6.4 and Table 6.2), probably due to silicate-contamination during the analysis. Contrarily, BC-C14 calcite phases sometimes display luminescence for very low Mn/Fe ratios (down to 0.06, Table 6.3). When this happens, measured Mn concentrations are rather high (300-600 ppm), Fe is up to 3600 ppm (Table 6.3) and Si concentrations are up to 70,000 ppm (Table 6.3 and Fig. 6.5). As Si cannot be hosted by calcite crystal lattice in such

high contents, measured concentrations must refer to contaminated sampled spots. These contaminated sampled spots were labelled in this study silicate-contaminated calcites (e.g. CaO 83% and remaining 17% represented by Mg, Si and Al) and indicate accidental inclusion of silicates during electron microprobe analysis. This is facilitated by BC-C14 sample texture, where the sub-millimetre targeted calcite phases are surrounded (Fig. 6.3E-H) by siliciclastic (volcanic) rock fragments, and the output chemical signatures of analysed spots easily represent the sum of calcite and silicates signatures. The overlap between the silicate and calcite chemical signatures in BC-C14 analysed spots is sometimes so pervasive that several results (analysis points 9, 12 ,13, 18 and 47 missing in Table 6.2 in the Appendix section) were discarded as bearing a typical silicate signature, while caution was used in the interpretation of silicate-contaminated calcite phases (analysis point 16, 17, 20, 29, 36, 40, 41, 42 and 43 in Table 6.3). The silicate-contaminated nature of these calcite phases causes the anomalous Mn/Fe ratios displayed by some BC-C14 luminescent calcite phases. Being the silicate-contaminated calcite phases output chemical signature the sum of calcite and silicate (volcanic) signatures, the high contents of Mn causing luminescence are provided by calcite phases, while the high Fe contents by accidentally analysed silicate portions. In fact, if such high Mn and Fe contents were contemporaneously derived from calcite phases, luminescence could not be observed as quenched by Fe. In analogy with sample BC-C24, the absent or very low Mn content of BC-C14 non-luminescent calcite phases indicates oxygenated and meteoric fluids precipitating non-luminescent calcite in clasts and fibrous cement calcite phases. The one order of magnitude difference in Mn and Fe concentrations between samples BC-C24 and BC-C14 suggests difference in the chemical composition of fluids circulating along the Azufre and Infierno fault systems. Furthermore, the silicate-contamination of calcite phases in sample BC-C14 may explain the higher Fe content of BC-C14 fluids.

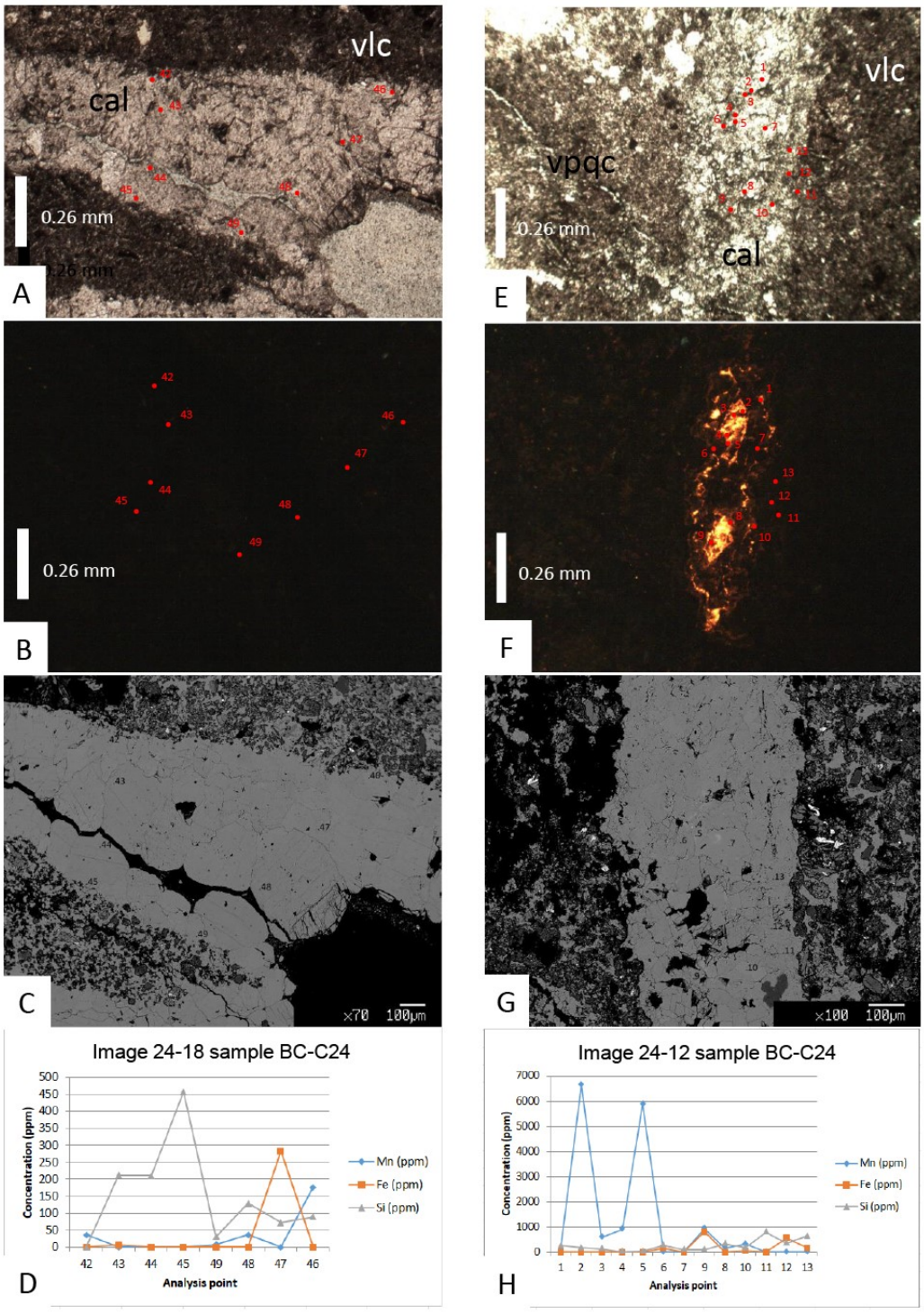

Figure 6.4 Results of cathodoluminescence and electron microprobe analyses on few selected points of sample BC-C24 collected along the NNW-SSE trending Azufre fault system. The calcite crystals, prismatic to drusy in fractures, are non-luminescent as well as the microsparite crystals within the groundmass matrix (A-D) whereas the equant calcite crystals replacing the volcanic clasts (E-H) can display bright luminescence. The lack of luminescence is confirmed by the scarce content of manganese in the vein calcite (D), whereas luminescent replacive calcite can contain manganese over 6000 ppm (H). Vlc = volcanic clast; cal = calcite; vpqc = plagioclase-quartz-calcite vein.

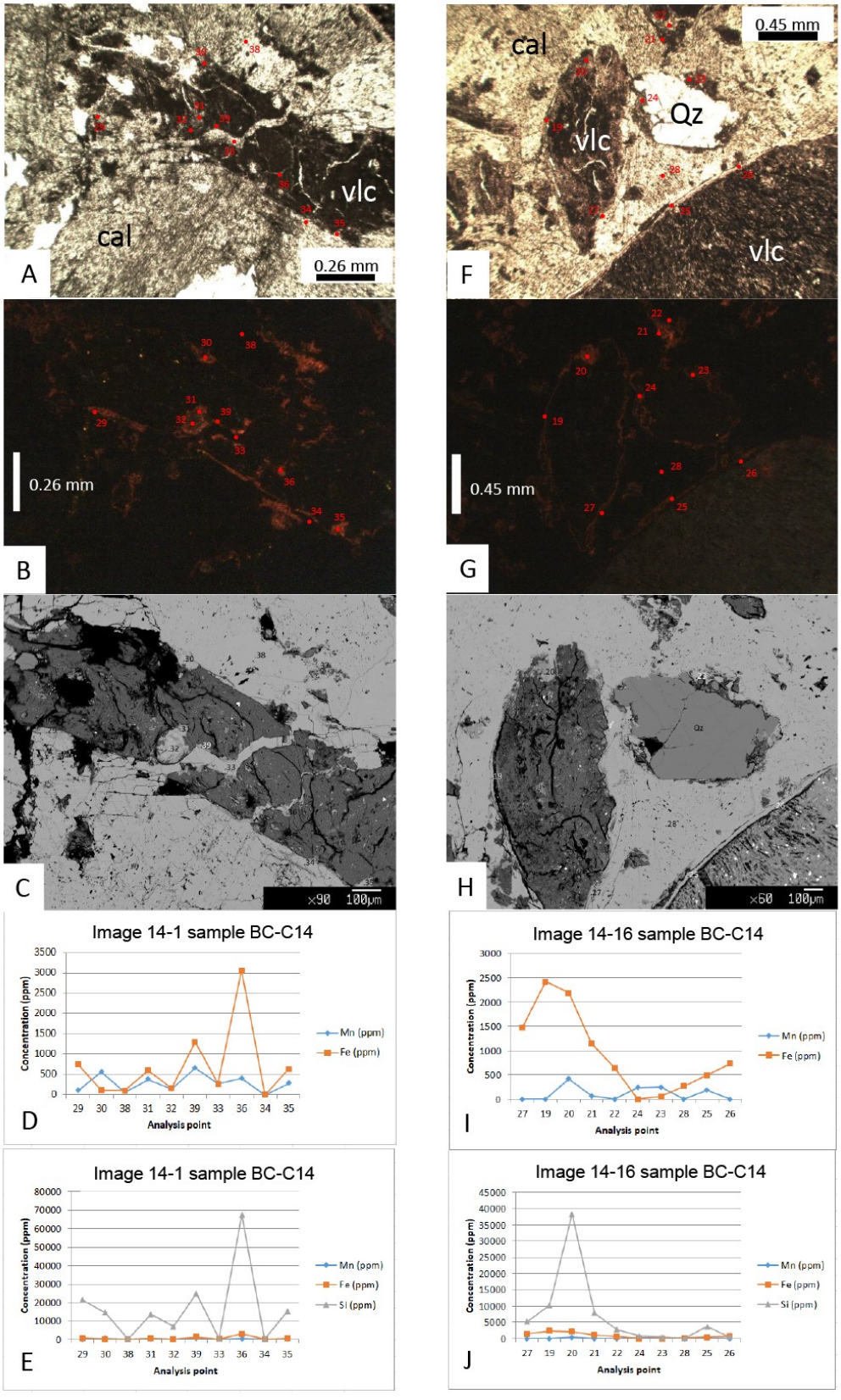

Figure 6.5 Results of cathodoluminescence and electron microprobe analyses on few selected points of sample BC-C14 collected along the NNE-SSW oriented Infierno fault. Rim calcite and calcite in clasts display luminescence, whereas

fibrous cement calcite is non-luminescent (A-H). Luminescence in rim calcite and calcite in clasts is associated with manganese contents up to 650-660 ppm (D and I), while non-luminescence in fibrous calcite cement is indicated by the absence of manganese (analysed spots 38 in images A-D; analysed spot 28 in images F-I). The silicate-contaminated nature of calcite phases analysed in sample BC-C14 is indicated by the high Fe (D and I) and Si contents (E and J). Diagrams E and J represent the same data contained in diagrams D and I respectively, but with a larger scale on the Y axis to include high Si values derived from contamination by volcanic silicate material. Vlc = volcanic clast; cal = calcite; Qz = quartz.

6.5.4 Laser ablation inductively coupled plasma mass spectrometry (LA-ICP-MS)

Elements abundance (ppm) from the LA-ICP-MS, together with total REE (∑REE), Y/Ho, Zr/Hf and Sm/Nd ratios are reported in Tables 6.4 and 6.5. Information regarding the luminescent or non-luminescent character of the analysed phases is also presented. BC-C24 average ∑REE (16.54 ppm) is one order of magnitude smaller than BC-C14 (107.96 ppm). Also, substantial difference characterizes distinct calcite phases within the samples, as BC-C24 drusy vein calcite displays an average ∑REE of 0.17 ppm versus 3.53 ppm of replacive calcite on volcanic clasts, and for BC-C14 mm-size fans of fibrous cement calcite ∑REE is 27.99 ppm versus 134.61 ppm of calcite in clasts. At least one order of magnitude smaller are BC-C24 Zr, U and Th concentrations (drusy vein calcite: Zr: 0.01 ppm, U: 0.02 ppm, Th: 0 ppm and replacive calcite on volcanic clasts: Zr: 0.06 ppm, U: 0.03 ppm, Th: 0.005 ppm) compared to BC-C14 (fibrous cement calcite: Zr: 0.34 ppm, U: 0.22 ppm, Th: 0.03 ppm and calcite in clasts: Zr: 146 pmm, U: 5.14 ppm, Th: 1.42 ppm). Cu and Zn concentrations are also greater in sample BC-C14. Average Y/Ho ratios are respectively 47.32 for sample BC-C24 and 35.23 for sample BC-C14. BC-C24 drusy vein calcite and replacive calcite on volcanic clasts exhibit Y/Ho ratios of 77.85 and 47.89, respectively. BC-C14 fibrous cement calcite displays Y/Ho ratios of 51.30 and calcite in clasts of 29.87. Average Zr/Hf ratios are 30.10 for BC-C24 and 33.46 for BC-C14. Average Zr/Hf values of 26.53 were found in BC-C24 replacive calcite on volcanic clasts, whilst no Zr/Hf ratio was calculated for BC-C24 drusy vein calcite as this phase does not contain Hf. Average Zr/Hf values of 26.82 and 34.79 were respectively found in BC-C14 fibrous cement calcite and calcite in clasts. BC-C24 average Sm/Nd ratios are 0.136 in drusy vein calcite and 0.170 in replacive calcite on volcanic clasts, 0.148 in BC-C14 fibrous cement calcite and 0.209 in BC-C14 calcite in clasts.

Table 6.4 Non-normalized elements abundance (ppm) from LA-ICP-MS analysis on sample BC-C24. Luminescent (L) and non-luminescent (NL) phases indicated in top row (CL) and type of analysed phase in brackets: (v) = drusy vein calcite; (r) = replacive calcite on volcanic clasts; (vpqc) = mixed plagioclase-quartz-calcite veins; (s) = silicate.

CL	L	NL	NL	NL	L	NL	L	L	L	L	NL	L	L	NL
Element	**C2-1 (r)**	**C2-2 (v)**	**C2-3 (v)**	**C1-1 (r)**	**C1-2 (r)**	**C1-3 (r)**	**C4-1 (r)**	**C4-2 (r)**	**C3-1 (r)**	**C3-2 (r)**	**C3-3 (r)**	**C5-1 (r)**	**C5-2 (r)**	**C5-3 (s)**
Li7	0.0277	0.0688	0.0848	0.0469	<0.0116	0.937	0.188	<0.0130	0.123	<0.0179	0.248	0.392	0.196	2.37
Be9	0.029	0.055	0	0.026	0	0.014	0.026	0	0	0.028	0	0	0	0
B11	10.47	12.28	9.55	10.41	10.4	10.82	11.25	10.47	9.6	10.48	10.83	14.46	11.91	9.78
Mg25	439.45	1132.95	2244.45	690.75	1203.54	2022.03	1471.61	922.31	1235.03	707.2	1428.36	1875	1692.82	2484.09
Al27	56.88	45.89	4.01	30.96	7.83	30.21	65.8	4.29	56.47	4.71	33.66	140.13	103.36	1446.76
Si29	532.38	489.21	391.57	502.53	415.71	1369.29	724.88	439.07	808.94	474.96	889.41	1129.03	961.18	7652.58
Ca43	429106.5	426466.4	407173.06	415466.53	431328.3	424420.5	411289.53	412717.91	407875.09	403704.06	402477.41	416328.8	407861.47	428540.2
Ca44	400232.5	400232.5	400232.5	400232.47	400232.5	400232.5	400232.47	400232.47	400232.47	400232.47	400232.47	400232.5	400232.53	400232.5
Sc45	0.0228	<0.0059	0.0084	0.0264	0.0847	0.1538	0.1086	0.0673	0.0629	<0.0074	0.0408	0.1547	0.1686	2.143
Ti47	2.199	13.24	6.95	1.42	0.398	3.14	0.925	0.34	1.454	0.054	0.867	0.679	0.283	80.55
V51	0.1606	0.0195	<0.0037	0.0531	0.0305	0.1118	0.048	<0.0036	0.0734	0.0065	0.118	0.0685	0.0412	0.403
Cr53	0.91	0.356	0.294	0.816	0.416	1.532	0.752	1.018	1.047	0.55	1.219	1.597	1.422	2.32
Mn55	184.88	0.255	0.0884	7.7	1257.82	5.33	53.31	454.38	82.67	15.16	13.8	51.79	203.21	4.35
Fe57	41.43	13.84	8.02	103.36	17.23	54.06	34.79	14.07	66.49	12.27	58.83	25.74	18.88	1648.6
Co59	0.1879	0.01197	0.0222	0.0226	0.133	0.0295	0.0824	0.0493	0.0566	0.0313	0.0316	0.1847	0.1712	0.465
Ni60	0.843	0.154	0.1244	0.413	0.226	0.2454	0.4	0.457	0.306	0.1653	0.2366	0.369	0.2331	1.477
Cu63	0.798	0.369	0.281	0.871	1.09	0.886	0.615	0.399	0.485	0.1188	0.748	0.474	0.902	3.68
Zn66	1.584	1.063	0.898	1.675	1.924	1.605	1.555	1.234	2.051	1.289	1.826	1.678	1.07	6.8
Rb85	0.0658	0.0334	<0.00136	0.0456	0.0051	0.1236	0.00719	0.0108	0.0175	0.00728	0.01304	0.0541	0.00535	1.181
Sr88	82.68	154.94	68.83	59.56	83.63	135.91	59.81	62.68	63.22	66.65	77.14	82.93	82.89	84.94
Y89	**0.479**	**0.449**	**0.0656**	**0.265**	**1.412**	**1.671**	**1.151**	**1.056**	**1.113**	**0.37**	**1.254**	**1.849**	**2.232**	**9.67**
Zr90	0.0796	0.01783	0.0028	0.063	0.01046	0.0292	0.0757	0.00934	0.0633	0.007	0.0934	0.1139	0.0745	2.02
Nb93	0.02475	0.01359	0.00076	0.00393	0.00071	0.00356	0.00627	0.00136	<0.00	<0.00	0.01531	0.00205	<0.00	0.0956
Mo95	0.0248	<0.00	0.00769	0.00461	0.1189	0.0195	0.0043	0.0385	0.018	0.0087	0.019	0.0083	0.0135	0.0086
In115	0.00074	0.00134	0.00197	<0.00042	0.00018	0.00054	0.00055	0.0008	<0.00035	<0.00033	<0.00061	0.00067	<0.00024	0.01078
Cs133	0.0024	<0.00095	<0.00083	0.00209	<0.00061	<0.00078	<0.00084	0.00171	0.00116	<0.00104	0.00356	<0.00074	0.00136	0.0812
Ba138	0.2741	0.0834	0.01671	0.398	0.642	3.81	0.2324	0.1045	0.2388	0.0666	1.339	1.064	0.2268	2.56

La139	**0.215**	**0.0532**	**0.00439**	**0.1799**	**0.833**	**1.413**	**0.752**	**0.89**	**0.587**	**0.1592**	**0.863**	**1.478**	**1.52**	**9.04**
Ce140	**0.1984**	**0.0909**	**0.00203**	**0.0715**	**0.847**	**0.563**	**0.2637**	**0.464**	**0.1498**	**0.0521**	**0.179**	**0.376**	**0.657**	**1.185**
Pr141	**0.0303**	**0.00774**	**0.0019**	**0.0254**	**0.1354**	**0.2599**	**0.1067**	**0.1111**	**0.0934**	**0.0322**	**0.1568**	**0.2438**	**0.2372**	**2.122**
Nd146	**0.1704**	**0.057**	**0.00579**	**0.1536**	**0.584**	**1.299**	**0.562**	**0.495**	**0.594**	**0.172**	**0.719**	**1.155**	**1.27**	**8.72**
Sm147	**0.0292**	**0.00233**	**0.00134**	**0.0193**	**0.0896**	**0.2117**	**0.1339**	**0.0653**	**0.1212**	**0.0207**	**0.1606**	**0.2235**	**0.2153**	**1.473**
Eu153	**0.01595**	**0.00294**	**0.00116**	**0.00706**	**0.0249**	**0.0495**	**0.0292**	**0.0218**	**0.01648**	**0.00829**	**0.0427**	**0.0509**	**0.052**	**0.432**
Gd157	**0.0315**	**0.01078**	**0.00212**	**0.0218**	**0.1327**	**0.292**	**0.1102**	**0.1019**	**0.0802**	**0.0327**	**0.1135**	**0.2237**	**0.2408**	**1.489**
Tb159	**0.00787**	**0.00211**	**0.00028**	**0.00554**	**0.01764**	**0.0261**	**0.01485**	**0.01843**	**0.01355**	**0.0052**	**0.0229**	**0.031**	**0.0291**	**0.198**
Dy163	**0.0551**	**0.0343**	**0.00701**	**0.0236**	**0.1411**	**0.2389**	**0.1127**	**0.0875**	**0.1114**	**0.0601**	**0.159**	**0.2141**	**0.276**	**1.788**
Ho165	**0.01112**	**0.00532**	**0.00092**	**0.00345**	**0.0286**	**0.0415**	**0.0247**	**0.0241**	**0.0233**	**0.00789**	**0.0292**	**0.0508**	**0.0516**	**0.331**
Er166	**0.0466**	**0.01556**	**0.00714**	**0.0182**	**0.099**	**0.121**	**0.085**	**0.0803**	**0.0777**	**0.0251**	**0.0901**	**0.1632**	**0.1775**	**1.135**
Tm169	**0.00308**	**0.00325**	**0.00057**	**0.00217**	**0.01513**	**0.01898**	**0.01192**	**0.00776**	**0.01433**	**0.00348**	**0.00911**	**0.0223**	**0.0229**	**0.1511**
Yb172	**0.0248**	**0.01188**	**0.00167**	**0.0187**	**0.1337**	**0.137**	**0.1114**	**0.0775**	**0.0944**	**0.0143**	**0.0924**	**0.1873**	**0.222**	**1.332**
Lu175	**0.00267**	**0.00064**	**0.00031**	**0.00147**	**0.00936**	**0.01305**	**0.0135**	**0.00953**	**0.01554**	**0.00216**	**0.01078**	**0.0221**	**0.0276**	**0.167**
Hf178	0	0	0	0.00247	0.00245	0	0.00602	0	0.00233	0	0	0	0.00118	0.0665
Ta181	<0.00	0.00061	<0.00	<0.00	0.00111	<0.00	<0.00	<0.00	<0.00	<0.00	<0.00	0.00041	0.00027	0.00276
Pb208	0.176	0.053	0.0454	0.1081	0.176	0.1053	0.0986	0.164	1.122	0.641	0.171	0.0798	0.0411	0.182
Th232	0.00239	0	0	0.0183	0.00085	0.00379	0.00084	0	0	0	0.00138	0.00188	0	0.0939
U238	0.00484	0.0419	0.00138	0.00646	0.00258	0.063	0.01229	0.00747	0.0371	0.00482	0.0385	0.059	0.0203	0.1125
∑ REE	0.842	0.298	0.037	0.552	3.091	4.685	2.332	2.454	1.992	0.595	2.648	4.442	4.999	29.563
Y/Ho	43.08	84.40	71.30	76.81	49.37	40.27	46.60	43.82	47.77	46.89	42.95	36.40	43.26	29.21
Zr/Hf	-	-	-	25.51	4.27	-	12.57	-	27.17	-	-	-	63.14	30.38
Sm/Nd	0.17	0.04	0.23	0.13	0.15	0.16	0.24	0.13	0.20	0.12	0.22	0.19	0.17	0.17

Table 6.4 (continued)

CL	L	L	NL	NL	NL	NL	NL	NL	NL
Element	**C6-1 (r)**	**C6-2 (r)**	**C6-3 (r)**	**C7-1 (r)**	**C7-2 (r)**	**C8-1 (vpqc)**	**C8-2 (vpqc)**	**C9-1 (vpqc)**	**C9-2 (vpqc)**
Li7	0.064	0.094	0.689	0.39	0.544	93.03	72.79	80.72	20.2
Be9	0.049	0	0	0.031	0	1.92	2.13	0	1.96
B11	11.47	12.45	13.63	11.64	10.57	64.29	44.96	78.52	27.08
Mg25	1794.11	593.65	1574.91	886.91	1616.06	41605.09	36472.67	59087.58	10985.86

Al27	107.35	18.17	107.58	47.96	157.69	70236.45	51059.99	28671.82	14016.49
Si29	735.59	528.2	2875.33	2101.43	1342.31	323477.06	212948.4	228100.31	58102.41
Ca43	399137.75	406839.16	398150.97	407346.47	419292.56	399166.5	388558	602491.75	424587.7
Ca44	400232.53	400232.53	400232.53	400232.53	400232.53	400232.53	400232.5	400232.53	400232.5
Sc45	0.1023	0.0223	0.1094	0.318	0.635	17.93	15.24	15.37	5.4
Ti47	3.96	0.867	2.113	0.584	7.85	5049.09	3913.37	13299.55	828.65
V51	0.1128	0.0161	0.1016	0.0648	0.1395	56.41	35.96	25.2	0
Cr53	0.7	1.122	0.77	0.677	0.975	44.06	27.19	192.8	20.23
Mn55	97.39	22.16	20.95	6.58	5.67	202.66	155.05	105.55	53.85
Fe57	30.3	17.56	32.92	16.85	110.86	45887.09	34408.49	11927.54	12661.4
Co59	0.0656	0.0516	0.0582	0.01453	0.0886	10.41	8.32	1.07	4.41
Ni60	0.244	0.1985	0.2152	0.1847	0.291	29.71	24.68	14.47	12.49
Cu63	1.508	1.339	1.196	<0.027	8.46	40.43	36.27	776.93	35.33
Zn66	1.933	2.79	26.85	1.528	4.69	26.22	23.88	582.09	32.32
Rb85	0.029	0.0767	0.0393	0.0326	0.0572	101.2	63.73	30.98	17
Sr88	86.24	55.86	68.08	81.33	89.11	217.49	144.94	433.72	154.62
Y89	**1.947**	**0.465**	**1.413**	**3.42**	**4.73**	**25.86**	**21.13**	**6**	**9.58**
Zr90	0.0898	0.01409	0.1417	0.0029	0.1444	221.44	81.34	19.58	15.45
Nb93	0.00144	0.0596	0.0394	0.009	0.00087	6.07	5.15	1.38	0.923
Mo95	0.0254	0.017	0.0104	0.00783	0.0058	0.458	0.196	2	0.127
In115	<0.00039	0.00095	0.00048	0.00136	<0.00037	0.0674	0.0592	1.38	0.0578
Cs133	0.00586	0.00518	0.00518	0.00737	0.00601	6.27	4.21	2.22	1.184
Ba138	0.405	0.1309	1.312	0.61	1.073	370.12	80.41	317.05	17.38
La139	**1.327**	**0.2299**	**1.142**	**2.39**	**3.69**	**24.18**	**19.85**	**2.64**	**10.93**
Ce140	**0.343**	**0.0928**	**0.1985**	**0.343**	**0.675**	**21.85**	**16.42**	**21.97**	**4.71**
Pr141	**0.2258**	**0.0384**	**0.2155**	**0.48**	**0.749**	**5.92**	**4.87**	**21.32**	**2.74**
Nd146	**1.1**	**0.253**	**0.994**	**2.238**	**3.18**	**28.39**	**23.74**	**9.14**	**13.79**
Sm147	**0.226**	**0.0213**	**0.1457**	**0.48**	**0.566**	**5.62**	**4.44**	**3.62**	**2.46**
Eu153	**0.0548**	**0.018**	**0.042**	**0.1154**	**0.1602**	**1.58**	**1.224**	**0.94**	**0.381**
Gd157	**0.2289**	**0.0534**	**0.2028**	**0.427**	**0.69**	**4.67**	**4.14**	**<0.00**	**1.084**
Tb159	**0.0289**	**0.0086**	**0.0244**	**0.0587**	**0.0736**	**0.627**	**0.589**	**<0.00**	**0.282**
Dy163	**0.245**	**0.0484**	**0.1889**	**0.472**	**0.702**	**4.79**	**4.53**	**<0.00**	**1.78**
Ho165	**0.049**	**0.0057**	**0.0305**	**0.0809**	**0.1209**	**0.828**	**0.753**	**<0.00**	**0.313**
Er166	**0.1573**	**0.0382**	**0.1279**	**0.305**	**0.4**	**2.72**	**2.44**	**<0.00**	**1.175**
Tm169	**0.0256**	**0.00655**	**0.01353**	**0.0307**	**0.052**	**0.362**	**0.316**	**<0.00**	**0.186**
Yb172	**0.1757**	**0.029**	**0.0825**	**0.295**	**0.497**	**2.79**	**2.4**	**1.33**	**2.34**

Lu175	**0.0283**	**0.00293**	**0.01388**	**0.0409**	**0.0493**	**0.332**	**0.262**	**0**	**0.243**
Hf178	0	0	0	0	0	5.11	2.11	0	0.594
Ta181	<0.00	<0.00022	<0.00	<0.00	<0.00	0.412	0.252	0.48	0.0584
Pb208	0.1374	0.185	0.1245	0.0686	0.86	8.48	5.6	24.84	4.14
Th232	0.00078	0.00125	0.00122	0.00194	0.05	4.77	6.01	1.13	0.729
U238	0.0285	0.00569	0.0632	0.0468	0.0474	2.89	2.08	3.83	0.747
∑ REE	4.215	0.846	3.422	7.757	11.605	104.659	85.974	60.96	42.414
Y/Ho	39.73	81.58	46.33	42.27	39.12	31.23	28.06	-	30.61
Zr/Hf	-	-	-	-	-	43.33	38.55	-	26.01
Sm/Nd	0.21	0.08	0.15	0.21	0.18	0.20	0.19	0.40	0.18

Table 6.5 Non-normalized elements abundance (ppm) from LA-ICP-MS analysis on sample BC-C14. Luminescent (L) and non-luminescent (NL) phases indicated in top row (CL) and type of analysed phase in brackets: (c) = calcite in clasts; (ce) = mm-sized fans of fibrous cement; (s) = silicate.

CL	NL	NL	NL	NL	NL	NL	NL	NL	NL	NL	L	NL	L	L	NL	NL
Element	**C1-1 (c)**	**C1-2 (c)**	**C2-1 (ce)**	**C2-2 (c)**	**C3-1 (c)**	**C3-2 (c)**	**C3-3 (c)**	**C5-1 (c)**	**C5-2 (c)**	**C8-1 (c)**	**C8-2 (c)**	**C8-3 (ce)**	**C4-1 (c)**	**C4-2 (c)**	**C4-3 (ce)**	**C7-1 (ce)**
Li7	18.45	25.37	0.124	11.51	17.61	139.98	0.107	2466.85	37.74	798.44	22.78	0.0412	6.16	13.74	0.0511	0.164
Be9	1.93	4.21	0.063	0.82	0.22	6.17	<0.00	150.85	0.97	12.25	1.15	<0.00	0.52	0.6	<0.00	0.085
B11	69.27	113.44	20.72	36.32	31.48	59.21	16.08	687.47	32.9	199.88	33.86	15.72	24.2	28.69	14.14	10.71
Mg25	79462.47	84817.87	2341.1	18949.22	91920.02	199889.7	2527.08	3284535	80079.9	925387.1	63821.75	2307.06	43724.11	87172.45	2722.56	3715.54
Al27	86536.52	166775.7	27.6	10252.19	20006.09	111996.9	26.12	1848949	34994.31	720496.6	23423.32	19.8	6462.35	13777.86	3.44	59.38
Si29	280486.9	638330	597.57	38420.61	105263	525557.3	558.74	7980512	164051.3	2926859	90067.7	441.33	27719.21	57926.8	412.66	648.05
Ca43	413545	412629.4	432161.9	416304.6	402888.5	372901.6	435432.06	463883.8	405488.5	443930.3	407198.8	401825.28	402729.9	410197	398740.88	400254.06
Ca44	400232.6	400232.5	404520.8	400232.5	400232.5	400232.5	400232.56	400232.5	400232.5	400232.5	400232.5	400232.53	400232.5	400232.6	400232.53	400232.53
Sc45	12.49	19.91	0.0445	4.22	2.475	46.15	0.2361	422.54	6.62	153.69	3.95	<0.0097	1.736	3.69	0.1466	0.0531
Ti47	3664.25	8919.92	1.804	513.01	160.07	647.55	1.348	11464.7	262.16	5347.65	356.8	0.428	62.36	92.81	0.066	0.822
V51	64.65	117.28	0.0899	109.47	60.69	486.18	0.1446	3492.79	74.98	823.23	34.44	0.1275	18.94	63.86	0.033	0.332
Cr53	13.17	19.55	0.365	69.54	14.48	37.88	0.53	1251.62	25.84	382.58	8.41	0.479	4.04	4.42	<0.091	0.338
Mn55	269.68	423.71	0.463	391.38	196.03	961.09	0.253	17548.26	368.83	3793.99	192.61	0.566	103.16	184.93	0.337	2.198
Fe57	43467.66	66776.17	67.38	28810.31	5811.41	84344.25	38.39	1000224	17480.39	324909.1	8627.68	23.16	1761.37	3386.22	19.45	32.72
Co59	16.73	23.87	0.0666	25.4	13.66	156.13	0.0751	3193.01	37.24	689.9	15.49	0.0464	3.45	18.67	0.0187	0.1638
Ni60	33.55	51.65	0.683	17.84	25.32	230.89	0.352	2215.34	39.69	1363.09	31.31	0.289	7.16	15.99	0.193	0.805
Cu63	337.95	367.44	1.213	128.35	337.37	2898.11	1.518	15655.61	303.61	12110.51	286.95	0.682	90.71	152.9	0.565	2.91
Zn66	5023.07	5872.56	53.58	1652.66	5160.8	10827.6	85.3	125017.5	3702.83	63254.1	4040.72	91.31	2510.54	2603.02	37.93	450.91

Rb85	44.83	146.32	0.0149	8.04	3.48	13.5	<0.00157	202.12	3.45	114.56	6.28	0.0121	1.385	1.797	<0.00176	0.359
Sr88	1122.8	1349	26.75	145.61	431.29	584.32	35.73	1553.96	213.09	1536.66	355.37	29.81	352.87	611.75	20.98	69.85
Y89	**23.26**	**37.68**	**2.147**	**15.22**	**9.84**	**345.25**	**8.5**	**113.75**	**10.96**	**45.3**	**5.83**	**1.272**	**4.44**	**11.85**	**11.3**	**1.553**
Zr90	174.33	515.38	0.0453	8.86	5.89	30.4	0.0288	1902.41	8.67	192.11	26.71	0.01282	2.87	4.54	0.0198	0.0458
Nb93	5.18	14.11	0.00317	0.225	0.1001	0.38	<0.00	10.19	0.117	2.92	0.328	0.00094	0.0447	0.0303	<0.00	<0.00025
Mo95	1.238	2.96	0.0049	0.693	0.189	1.766	0.0083	5.42	0.175	12.71	0.312	<0.0040	0.0816	0.206	<0.00210	0.0043
In115	0.0624	0.1049	<0.00060	0.0667	0.0845	2.4	0.00415	39.33	0.594	6.51	0.1133	0.00202	0.01625	0.051	0.00463	0.00104
Cs133	2.91	5.18	0.00435	1.58	0.866	3.36	0.00256	45.85	0.81	22.63	0.929	0.00219	0.234	0.375	0.00194	0.00159
Ba138	893.4	1832.65	0.441	59.67	77.23	216.23	0.65	1509.49	33.88	1119.01	107.39	0.689	46.16	93.34	0.27	1.153
La139	**25.62**	**44.94**	**1.651**	**18.43**	**2.36**	**28.39**	**13.6**	**22.95**	**9.98**	**27.32**	**8.14**	**0.399**	**6.56**	**2.4**	**12.09**	**1.941**
Ce140	**39.29**	**77.16**	**0.0662**	**31.49**	**29.71**	**477.88**	**2.091**	**546.38**	**25.52**	**56.15**	**4.86**	**0.0998**	**2.24**	**55.46**	**0.708**	**0.419**
Pr141	**6.6**	**12.38**	**0.1539**	**3.72**	**1.328**	**20.64**	**2.66**	**8.93**	**2.448**	**7.5**	**1.665**	**0.0356**	**1.109**	**1.843**	**2.159**	**0.268**
Nd146	**34.74**	**56.18**	**0.753**	**18.62**	**7.5**	**132.57**	**13.2**	**99.24**	**10.33**	**37.09**	**8.14**	**0.2081**	**5.47**	**10.68**	**10.76**	**1.412**
Sm147	**6.58**	**11.49**	**0.1187**	**3.33**	**2.078**	**44.91**	**1.993**	**17.91**	**2.095**	**14.15**	**1.618**	**0.0268**	**0.939**	**2.81**	**1.666**	**0.1818**
Eu153	**1.684**	**2.54**	**0.01372**	**0.548**	**0.223**	**6.61**	**0.2104**	**3.34**	**0.339**	**2.24**	**0.266**	**0.00713**	**0.1867**	**0.432**	**0.2021**	**0.0336**
Gd157	**5.7**	**9.37**	**0.1283**	**3.13**	**2.091**	**47.82**	**1.556**	**29.41**	**1.949**	**4.28**	**1.091**	**0.0413**	**0.806**	**2.46**	**1.397**	**0.2068**
Tb159	**0.715**	**1.286**	**0.01631**	**0.346**	**0.301**	**7.66**	**0.1978**	**3.04**	**0.259**	**1.248**	**0.1387**	**0.00391**	**0.1024**	**0.34**	**0.1742**	**0.0248**
Dy163	**4.69**	**8.08**	**0.1247**	**2.53**	**1.789**	**58.44**	**1.283**	**18.4**	**1.859**	**10.44**	**1.017**	**0.0736**	**0.698**	**2.24**	**1.096**	**0.1576**
Ho165	**0.82**	**1.255**	**0.0317**	**0.5**	**0.387**	**11.4**	**0.247**	**3.63**	**0.331**	**2.46**	**0.2028**	**0.01545**	**0.1256**	**0.377**	**0.239**	**0.0417**
Er166	**2.43**	**4.05**	**0.1071**	**1.666**	**1.01**	**34.5**	**0.71**	**10.4**	**1.7**	**8.82**	**0.648**	**0.0603**	**0.493**	**1.185**	**0.764**	**0.1041**
Tm169	**0.268**	**0.474**	**0.01242**	**0.1965**	**0.1682**	**4.5**	**0.0779**	**1.21**	**0.1416**	**0.827**	**0.0644**	**0.00894**	**0.0681**	**0.1316**	**0.0995**	**0.01205**
Yb172	**2.319**	**3.75**	**0.1049**	**1.928**	**1.149**	**33.91**	**0.835**	**10.85**	**1.224**	**6.3**	**0.708**	**0.1044**	**0.663**	**0.89**	**0.769**	**0.1331**
Lu175	**0.289**	**0.485**	**0.02004**	**0.292**	**0.1371**	**4.41**	**0.1117**	**1.88**	**0.1674**	**0.571**	**0.1147**	**0.01147**	**0.0813**	**0.1215**	**0.1271**	**0.015**
Hf178	4.45	13.65	0.0017	0.249	0.1307	0.843	0	57.27	0.277	6.09	0.665	0	0.0955	0.1137	0.00251	0
Ta181	0.285	0.698	0.00038	0.01283	0.0213	0.0145	0.00108	0.876	0.0039	0.421	0.0174	<0.00	0.00058	0.00095	<0.00	<0.00
Pb208	28.76	39.92	0.575	24.73	8.91	13.65	0.648	109.7	7.82	95.98	5.65	0.759	3.23	4.2	0.451	1.59
Th232	2.49	7.51	0	0.355	0.354	5.22	0.045	9.2	0.402	1.07	0.2112	0	0.0891	0.831	0.0507	0.00315
U238	6.39	7.77	0.098	0.973	2.73	8.45	0.1391	35.49	1.786	17.93	2.048	0.133	2.144	4.28	0.1056	0.0926
∑ REE	131.745	233.44	3.302	86.727	50.231	913.64	38.773	777.57	58.343	179.396	28.674	1.096	19.542	81.370	32.251	4.951
Y/Ho	28.37	30.02	67.73	30.44	25.43	30.29	34.42	31.34	33.11	18.41	28.75	82.33	35.35	31.43	47.28	37.24
Zr/Hf	39.18	37.76	26.65	35.58	45.07	36.06	-	33.22	31.30	31.55	40.17	-	30.05	39.93	7.89	-
Sm/Nd	0.19	0.20	0.16	0.18	0.28	0.34	0.15	0.18	0.20	0.38	0.20	0.13	0.17	0.26	0.15	0.13

Table 6.5 (continued)

CL	NL	NL	NL	L	L	L	L	L	L	L	NL	L	NL
Element	**C9-1 (ce)**	**C9-2 (ce)**	**C9-3 (c)**	**C10-1 (c)**	**C10-2 (c)**	**C12-1 (c)**	**C12-2 (c)**	**C11-1 (c)**	**C11-2 (c)**	**C11-3 (c)**	**C11-4 (ce)**	**C13-1 (c)**	**C14-1 (s)**
Li7	<0.028	12.91	0.062	22.26	41.35	15.97	15.52	29.91	21.78	13.82	0.0287	72.47	4634.41
Be9	<0.00	0.51	<0.00	1.73	1.66	0.26	0.26	0.89	0.64	0.45	<0.00	1.44	130.16
B11	13.36	24.91	14.95	43.25	45.57	32.07	34.12	50.11	41.61	33.64	18.12	82.16	2636.39
Mg25	1923.78	23933.69	2336.06	55173.69	88808.75	67020.39	68271.04	80927.71	57047.66	58633.59	2590.92	94517.38	4191585.5
Al27	28.33	12659.72	169.43	29298.22	44469.02	19010.29	20060.39	30820.73	28790.7	16154.36	4.18	66787.27	3027831
Si29	405.41	51796.18	898.23	109965.5	203467.9	88675.51	86792.19	129504.1	106328.5	84119.89	624.92	280446.8	0
Ca43	393945.03	393431.31	414197.7	404149.9	403982	399143.6	395105.9	403810.2	397493.4	400498.5	394593.84	402295.4	411683.44
Ca44	400232.53	400232.53	400232.5	400232.5	400232.5	400232.5	400232.5	400232.5	400232.5	400232.5	400232.53	400232.5	400232.53
Sc45	0.345	1.812	0.2548	5.71	5.69	3.55	2.266	3.21	3.14	2.282	0.1349	8.49	472.36
Ti47	0.404	111.56	7.14	482.44	483.78	199.95	262.9	290.68	338.6	184.52	<0.050	946.21	55732.66
V51	0.07	17.4	0.369	54.03	58.3	35.79	30.31	33.16	24.54	27.35	0.084	54.16	4380.62
Cr53	<0.102	4.6	0.731	32.1	24.39	5.53	4.62	8.43	6.56	4.55	0.634	23.32	2715.83
Mn55	2.226	99.51	1.426	316.44	640.63	209.45	147.94	204.79	167.2	242.38	0.274	332.1	11457.41
Fe57	24.7	4727.98	93.53	13368.64	12707.58	5015.35	5267.62	8580.49	8288.85	4134.25	11.56	24938.22	1229099.9
Co59	0.0417	9.62	0.1486	12.18	33.94	6.03	6.09	12.42	10.09	6.49	0.0148	69.1	3284.74
Ni60	0.382	17.73	0.467	21.96	40.29	19.19	16.14	47.65	26.39	16.64	0.191	117.15	2619.25
Cu63	14.17	179.34	14.74	163.24	332.75	181.78	174.83	303.17	236.13	143.37	0.443	667.84	12469.82
Zn66	76.69	2179.21	75.12	2581.95	4326.37	2860.49	2903.65	2739.49	2153.43	1773.34	40.65	6084.87	91242.5
Rb85	0.0088	2.2	0.0329	21.09	7.74	3.31	7.37	5.94	6.4	3.09	0.00797	13.07	839.7
Sr88	25.34	179.48	30.61	296.15	296.45	434.14	576.81	392.77	350.76	294.23	19.72	323.49	4216.13
Y89	**27.06**	**11.55**	**17.77**	**7.64**	**6.12**	**3.32**	**2.128**	**3.61**	**5.35**	**4.76**	**14.14**	**4.4**	**180.07**
Zr90	0.0427	2.81	0.202	22.29	80.87	7.66	12.75	8.8	15.23	6.9	0.0187	40.41	1815.1
Nb93	<0.00033	0.0442	0.00655	0.456	0.57	0.1157	0.342	0.237	0.342	0.1665	0.0005	0.792	60.47
Mo95	0.0077	0.0487	0.00753	0.346	0.331	0.14	0.217	0.1011	0.1679	0.0757	0.0029	0.948	17.84
In115	0.00077	0.1306	0.00566	0.1676	0.232	0.0473	0.0482	0.0602	0.04	0.031	0.00169	0.613	23.79
Cs133	<0.00180	0.357	<0.00121	5.42	1.605	0.683	0.761	0.971	0.85	0.575	<0.00116	1.641	138.53
Ba138	1.391	58.98	1.257	98.69	94.89	69.89	113.09	119.79	139.74	53.93	0.398	142.51	6867.69
La139	**24.86**	**18.66**	**19.76**	**9.62**	**8.25**	**3.25**	**1.44**	**4.08**	**7.34**	**5.93**	**11.02**	**4.18**	**151.96**
Ce140	**1.727**	**3.27**	**1.08**	**9.21**	**7.86**	**3.69**	**6.47**	**1.611**	**3.21**	**3.35**	**0.645**	**1.94**	**280.47**
Pr141	**4.68**	**3.15**	**3.85**	**1.735**	**1.658**	**0.707**	**0.398**	**0.804**	**1.349**	**1.089**	**1.791**	**1.206**	**25**
Nd146	**22.92**	**15.95**	**19.51**	**8.72**	**7.98**	**3.6**	**2.138**	**4.46**	**6.6**	**5.92**	**9.53**	**4.11**	**137.55**

Sm147	**3.85**	**2.3**	**3.26**	**1.6**	**1.326**	**0.896**	**0.496**	**0.656**	**1.025**	**0.902**	**1.507**	**0.856**	**27.35**
Eu153	**0.626**	**0.498**	**0.388**	**0.297**	**0.255**	**0.1458**	**0.1101**	**0.1125**	**0.298**	**0.185**	**0.2**	**0.214**	**8.44**
Gd157	**3.41**	**1.797**	**2.93**	**1.296**	**1.356**	**0.605**	**0.611**	**0.638**	**1.04**	**0.791**	**1.66**	**0.767**	**26.32**
Tb159	**0.423**	**0.298**	**0.311**	**0.2102**	**0.1376**	**0.0839**	**0.0583**	**0.101**	**0.1154**	**0.107**	**0.1786**	**0.1047**	**4.76**
Dy163	**3.11**	**2.03**	**2.48**	**1.319**	**1.201**	**0.498**	**0.364**	**0.588**	**0.836**	**0.769**	**1.382**	**0.915**	**39.06**
Ho165	**0.639**	**0.325**	**0.444**	**0.252**	**0.209**	**0.1106**	**0.0719**	**0.1492**	**0.172**	**0.1662**	**0.303**	**0.1645**	**7.06**
Er166	**2.43**	**1.239**	**1.681**	**0.861**	**0.704**	**0.31**	**0.201**	**0.39**	**0.569**	**0.529**	**1.028**	**0.407**	**23.4**
Tm169	**0.31**	**0.1755**	**0.223**	**0.1012**	**0.0969**	**0.0448**	**0.0372**	**0.0592**	**0.0855**	**0.0709**	**0.1409**	**0.0606**	**3**
Yb172	**2.77**	**1.535**	**1.891**	**0.972**	**0.852**	**0.519**	**0.336**	**0.426**	**0.681**	**0.616**	**1.234**	**0.622**	**32.24**
Lu175	**0.401**	**0.1953**	**0.288**	**0.1418**	**0.1159**	**0.0745**	**0.038**	**0.0521**	**0.0879**	**0.0741**	**0.1647**	**0.0875**	**3.06**
Hf178	0.00125	0.0728	0.01155	0.614	2.32	0.315	0.398	0.301	0.316	0.225	0	0.944	57.19
Ta181	<0.00	<0.00	0.00033	0.0304	0.0253	0.00951	0.017	0.0153	0.00615	0.00544	<0.00	0.0601	3.2
Pb208	1.204	5.6	1.308	10.04	11.37	10	11.18	2.19	2.36	5.29	0.484	6.2	186.91
Th232	0.0457	0.0791	0.0228	0.347	0.1557	0.1679	0.283	0.226	0.221	0.1373	0.0191	0.426	23.63
U238	0.0754	0.962	0.0813	1.984	2.21	2.32	2.88	2.11	1.869	2.06	0.0813	2.24	59.52
∑ REE	72.156	51.423	58.096	36.335	32.001	14.535	12.770	14.127	23.409	20.499	30.784	15.634	769.67
Y/Ho	42.24	35.54	40.02	30.32	29.28	30.02	29.60	24.20	31.11	28.64	46.67	26.74	25.51
Zr/Hf	34.16	38.60	17.49	36.30	34.86	24.32	32.04	29.24	48.20	30.67	-	42.81	31.74
Sm/Nd	0.17	0.14	0.17	0.18	0.17	0.25	0.23	0.15	0.16	0.15	0.16	0.21	0.20

Figure 6.6 and Tables 6.6 and 6.7 illustrate shale-normalized (suffix sn) and chondrite-normalized (suffix cn) BC-C24 and BC-C14 REY (REE + Y) trends and calculated light REE (LREE), middle REE (MREE) and heavy REE (HREE) enrichment/depletion trends and (Ce/Ce*)sn, (Ce/Ce*)cn, (La/La*)sn, (La/La*)cn, (Eu/Eu*)sn, (Eu/Eu*)cn, (Gd/Gd*)sn and (Gd/Gd*)cn anomalies. REY normalizations were performed to Post Archean Australian Shale (PAAS, McLennan, 2001; Möller, 2002; Piper and Bau, 2013; Figs. 6.6A, C and E) and C1-chondrite (Evensen et al., 1978; Bau and Dulski, 1999; Möller, 2002; Figs. 6.6B, D and F). As a result of different normalizations, C1-chondrite normalized REY trends appear strongly depleted in Tb (strong negative peak, (Pr/Tb)cn up to 40.75, Table 6.7 and Figs. 6.6B, D and F), while only weakly depleted when normalized to PAAS (Figs. 6.6A, C and E). Average enrichment/depletion patterns ((Nd/Yb)sn, (Nd/Yb)cn, (Dy/Yb)sn, (Dy/Yb)cn, (Pr/Yb)sn, (Pr/Yb)cn, (Pr/Tb)sn and (Pr/Tb)cn ratios) and (Ce/Ce*)sn, (Ce/Ce*)cn, (La/La*)sn, (La/La*)cn, (Eu/Eu*)sn, (Eu/Eu*)cn, (Gd/Gd*)sn and (Gd/Gd*)cn anomalies were derived (Table 6.7) using Lawrence et al. (2006) geometric calculation method, which was chosen as the more appropriate to describe the linear behaviour of near neighbours on a log-normal plot. BC-C24 replacive calcite and BC-C14 calcite phases display quite similar and subparallel trends, flat to slightly increasing or decreasing according to the normalization applied from La up to Eu, while flat from Eu to Lu (Figs. 6.6A and B) for both PAAS and C1-chondrite normalizations. BC-C24 drusy vein calcite trends are slightly different, increasing or decreasing according to normalization from La to Eu and fluctuating between Eu and Lu, with positive Dy and Tm peaks (Figs. 6.6A and B). PAAS normalized REY trends for BC-C24 and BC-C14 calcite phases result slightly LREE-depleted ((Nd/Yb)sn <1, Table 6.7), while C1-chondrite normalized REY trends show a LREE-enrichment ((Nd/Yb)cn strongly >1, Table 6.7). Average (Ce/Ce*)sn and (Ce/Ce*)cn anomalies are negative in BC-C24 replacive calcite ((Ce/Ce*)sn = 0.44; (Ce/Ce*)cn = 0.47) and BC-C14 fibrous cement calcite ((Ce/Ce*)sn = 0.15; (Ce/Ce*)cn = 0.16), while variable (both positive and negative) in BC-C14 calcite in clasts with average positive value ((Ce/Ce*)sn = 2.13); (Ce/Ce*)cn = 2.27) and positive in BC-C24 drusy vein calcite ((Ce/Ce*)sn = 1.30; (Ce/Ce*)cn = 1.38). Whilst both luminescent and non-luminescent BC-C24 replacive calcite phases display negative (Ce/Ce*)sn and (Ce/Ce*)cn anomalies, BC-C14 calcite in clasts positive (Ce/Ce*)sn and (Ce/Ce*)cn anomalies seem to predominate in non-luminescent phases. Despite the above mentioned discrepancies between shale- and chondrite-normalized trends, the positive polarity of the (Eu/Eu*)sn and (Eu/Eu*)cn anomalies is rather consistent in BC-C24 and BC-C14 samples, and slightly stronger in BC-C24 drusy vein calcite (Figs. 6.6A and B), even though BC-C14 fibrous cement calcite (Table 6.7) displays a weak negative (Eu/Eu*)sn anomaly and a weak positive (Eu/Eu*)cn anomaly. All analysed calcite phases except for BC-C14 calcite in clasts display a positive Y peak, stronger in BC-C24 drusy vein calcite (Figs. 6.6A and B) that also displays a rather

pronounced negative peak of Sm (Figs. 6.6A and B). Strong positive (La/La*)sn, (La/La*)cn, (Gd/Gd*)sn and (Gd/Gd*)cn anomalies characterize all BC-C24 and BC-C14 analysed phases.

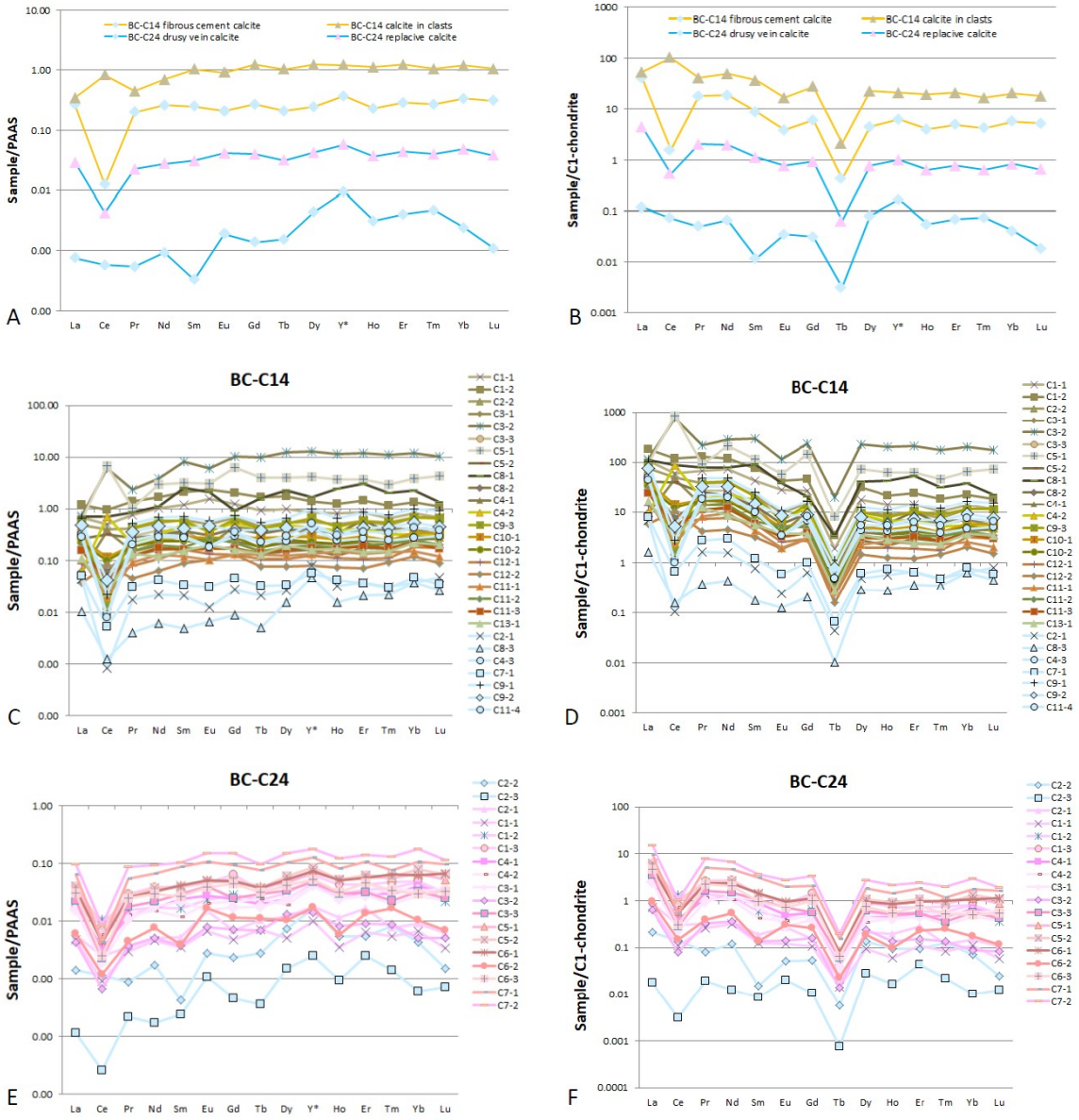

Figure 6.6 Average shale PAAS-normalized and average C1-chondrite normalized plots (A and B) and complete PAAS-normalized and C1-chondrite normalized plots (C-F) for samples BC-C24 and BC-C14 from LA-ICP-MS analysis.

Table 6.6 Average REE abundances of samples BC-C24 and BC-C14 normalized against shale (PAAS, McLennan, 2001; Möller, 2002; Piper and Bau, 2013) and C1-chondrite (Evensen et al., 1978; Bau and Dulski, 1999; Möller, 2002).

Type of normalization	Analysed calcite phase	La	Ce	Pr	Nd	Sm	Eu	Gd	Tb	Dy	Y	Ho	Er	Tm	Yb	Lu
PAAS	Average BC-C24 drusy vein calcite	0	0	0	0	0	0	0	0	0	0.01	0	0	0	0	0
	Average BC-C24 replacive calcite	0.03	0	0.02	0.03	0.03	0.04	0.04	0.03	0.04	0.06	0.04	0.04	0.04	0.05	0.04
CHON	Average BC-C24 drusy vein calcite	0.12	0.07	0.05	0.07	0.01	0.04	0.03	0	0.08	0.16	0.06	0.07	0.07	0.04	0.02
	Average BC-C24 replacive calcite	4.51	0.54	2.04	1.97	1.11	0.76	0.91	0.06	0.77	0.99	0.64	0.76	0.63	0.83	0.65
PAAS	Average BC-C14 fibrous cement	0.26	0.01	0.20	0.26	0.25	0.21	0.26	0.21	0.24	0.37	0.23	0.29	0.27	0.34	0.31
	Average BC-C14 calcite in clasts	0.34	0.83	0.45	0.70	1.04	0.91	1.22	1.04	1.23	1.21	1.13	1.22	1.05	1.21	1.06
CHON	Average BC-C14 fibrous cement	41.25	1.55	18.14	18.55	8.95	3.89	6.04	0.43	4.48	6.32	4.02	4.93	4.24	5.75	5.26
	Average BC-C14 calcite in clasts	53.45	103.51	41.32	49.93	37.39	16.93	27.90	2.14	22.57	20.97	19.72	21.02	16.56	20.61	18.04

Table 6.7 Calculated LREE, MREE and HREE enrichment/depletion trends and geometric Ce, La, Eu and Gd anomalies for samples BC-C24 and BC-C14 normalized against shale (PAAS, McLennan, 2001; Möller, 2002; Piper and Bau, 2013) and chondrite (C1-chondrite, Evensen et al., 1978; Bau and Dulski, 1999; Möller, 2002) element abundances based on Lawrence et al. (2006).

NORM TYPE	PAAS	CHON	PAAS	CHON	PAAS	CHON	PAAS	CHON	PAAS	CHON	PAAS	CHON	PAAS	CHON	PAAS	CHON
Analysed calcite phase	**(Nd/Yb) sn**	**(Nd/Yb) cn**	**(Dy/Yb) sn**	**(Dy/Yb) cn**	**(Pr/Yb) sn**	**(Pr/Yb) cn**	**(Pr/Tb) sn**	**(Pr/Tb) cn**	**(Ce/Ce*) sn**	**(Ce/Ce*) cn**	**(La/La*) sn**	**(La/La*) cn**	**(Eu/Eu*) sn**	**(Eu/Eu*) cn**	**(Gd/Gd*) sn**	**(Gd/Gd*) cn**
Average BC-C24 drusy vein calcite [a]	0.34	1.44	2.13	2.30	0.29	1.53	0.46	20.31	1.30	1.38	3.09	3.21	3.68	4.93	1.51	6.43
Average BC-C24 replacive calcite [a]	0.63	2.62	1.03	1.11	0.46	2.46	0.57	25.39	0.44	0.47	2.80	2.92	1.54	2.07	1.16	4.95
Average BC-C14 fibrous cement	0.71	2.99	0.69	0.75	0.54	2.89	0.92	40.75	0.15	0.16	3.21	3.34	0.91	1.22	1.33	5.68
Average BC-C14 calcite in clasts	0.79	3.31	0.91	0.98	0.59	3.18	0.78	34.44	2.13	2.27	1.81	1.88	1.00	1.33	1.21	5.14

[a] = uncontaminated analysis points showing the smallest Al content deriving from silicate-contamination by volcanic material.

Interpretation

∑REE concentrations and sample contamination

The one order of magnitude difference in average ∑REE concentrations between samples BC-C24 and BC-C14 is indicative of the silicate-contaminated nature of BC-C14 calcite phases, also spotted by the electron microprobe. Regarding average ∑REE abundance differences within the samples, ∑REE of BC-C24 drusy vein calcite is lower than ∑REE of BC-C24 replacement calcite and the ∑REE of BC-C14 fibrous cement calcite is lower than ∑REE of BC-C14 calcite in clasts. These differences reflect the lower ∑REE of veins with respect to host rocks, that is explained by Hopf et al. (1991), Pili et al. (2002) and Uysal et al. (2011) with the fact that calcite crystals depositing in veins inside deformation zones (faults) barely incorporate REE during their formation, leaving a REE-enriched fluid. Alternatively, the lower ∑REE of veins with respect to host rocks in both BC-C24 and BC-C14 samples may depend on the lack of contamination of calcite phases precipitating in fractures of pores by (volcanic) silicates, differently from replacive calcite phases that were sampled together with accidental volcanic silicates during both electron microprobe and LA-ICP-MS analyses. Similarly to electron microprobe analysis results, pure silicate phases of samples BC-C24 and BC-C14 were discarded, together with BC-C24 mixed plagioclase-quartz-calcite veins, whose measurement error is too high following the subtraction of the silicate-typical signature. On the contrary, even though of low quality due to their rather small thickness (less than 100 μm) and high Si content (Fig. 6.4D) due to silicate contamination by volcanic material lying below these veins, BC-C24 drusy vein calcite (analysis points C2-2 and C2-3, Table 6.4) analysis results were kept because of their rather distinguishable REE abundance and shale-normalized REY trends with respect to the other analysed calcite phases belonging to the host rock (Table 6.6 and Fig. 6.6), as previously noted on mono-mineral veins in Swedish dolerite dykes by Maskenskaya et al. (2013). A clear ∑REE vs Al linear trend (R^2=0.94, Fig. 6.7A) was recognised in sample BC-C24, suggesting contamination of calcite by silicate (volcanic) material. BC-C24 analysis points displaying the smallest Al concentration (shaded in green in Table 6.4) were thus isolated as the most representative of calcite and related fluid geochemical characteristics. Also sample BC-C14 displays a ∑REE vs Al trend, despite with a lower R^2 (R^2= 0.53, Fig. 6.7B). Commonly, Zr, U and Th concentrations in calcite can provide information regarding calcite contamination from terrigenous and organic sources (Delaney and Boyle, 1983; Schwarcz and Latham, 1989), while Cu, Pb and Zn are indicative of metal contamination (Kamber et al., 2005). Zr, U and Th in BC-C24 calcite phases and in BC-C14 fibrous cement calcite are in line with contamination-free values in carbonates (Della Porta et al., 2015), whereas higher Zr, U and Th concentrations of BC-C14 calcite in clasts are typical of siliciclastic volcanic material, due to their above-discussed silicate-contaminated nature. Cu and Zn concentration in BC-C24 resemble the

average concentrations of the upper crust (17 ppm Pb, 25 ppm Cu and 71 ppm Zn; McLennan, 2001), while in both BC-C14 calcite in clasts and fibrous cement calcite phases Cu and Zn concentrations are two to three orders of magnitude higher, thus excluding a siliciclastic-volcanic source for the extra metal. Zn-Pb plots for samples BC-C24 and BC-C14 (Figs. 6.7C to E) reinforce this idea, even though minor metal contamination by siliciclastic-volcanic material in BC-C24 (contaminated high-Al analysis points) cannot be excluded. It is interesting to note that Zn-Pb correlation coefficients (R^2) found in this study are higher than those used by Kamber et al. (2005) to infer metal contamination in Queensland alluvial sediments. Combined information on Zr, U, Th, Cu and Zn abundances in BC-C14 raises the issue of metal contamination from historically and present-day ongoing mining activity within and close to the Infierno canyon (copper mine and Boleo mine, Garcia-Sánchez et al., 2019; Pellicioli et al., submitted, a), where the sample was collected. In fact, a higher background of sulphides in the catchment causing BC-C14 high measured metal concentrations is less likely than an anthropic metal contamination in the area, as indicated by Ni and Cr high concentrations in BC-C14 (BC-C14 Ni:155 ppm, Cr: 74 ppm; BC-C24 Ni: 4 ppm, Cr: 13 ppm) that are in line with the highest values found by Kamber et al. (2005) close to Brisbane, where industrial pollution represents the source of the extra-metal.

Y/Ho, Zr/Hf and Sm/Nd ratios

Y/Ho ratios displayed by BC-C24 replacive calcite on volcanic clasts and by all phases of BC-C14 fall inside the overlapping field between seawater and hydrothermal fluids (Y/Ho = 15-55 in hydrothermal calcite veins intruding crystalline rocks, Zhang et al., 1994; Bau et al., 1995; Bau, 1996; Y/Ho = 22-64 in thermal waters and geothermal fluids ranges, Möller et al., 2004; Y/Ho = 49.8-64.6 or 25-66, in calcite veins along fault planes, Pili et al., 2002; Uysal et al., 2007), while Y/Ho ratios of BC-C24 drusy vein calcite fall close to the seawater range (Y/Ho = 44-74) determined by Zhang et al. (1994), Bau et al. (1995) and Bau, (1996). A non-marine origin of fluids circulating along the Azufre and Infierno faults is also independently supported by Zr/Hf values, falling outside the range of seawater (Zr/Hf = 85-130; Zhang et al., 1994; Bau et al., 1995; Bau, 1996) and closer to those of the upper continental crust (Zr/Hf = 36-39; David et al., 2000; Kamber et al., 2005, or Zr/Hf = 32-33 according to Taylor and McLennan, 1985) for all analysed calcite phases. Besides from Zr/Hf and Y/Ho ratios, further indications of a relevant (BC-C24) to minor (BC-C14) hydrothermal component come from average Sm/Nd ratios and Rb contents, in line with values found by Barker et al. (2009) in Australian hydrothermal calcite veins (Sm/Nd=0.11-0.16, Rb < 1 ppm). Seawater alike Y/Ho ratios of BC-C24 drusy vein calcite thus seem to represent an exception, maybe linked to the high Si content of these calcite phases contaminated by volcanic material.

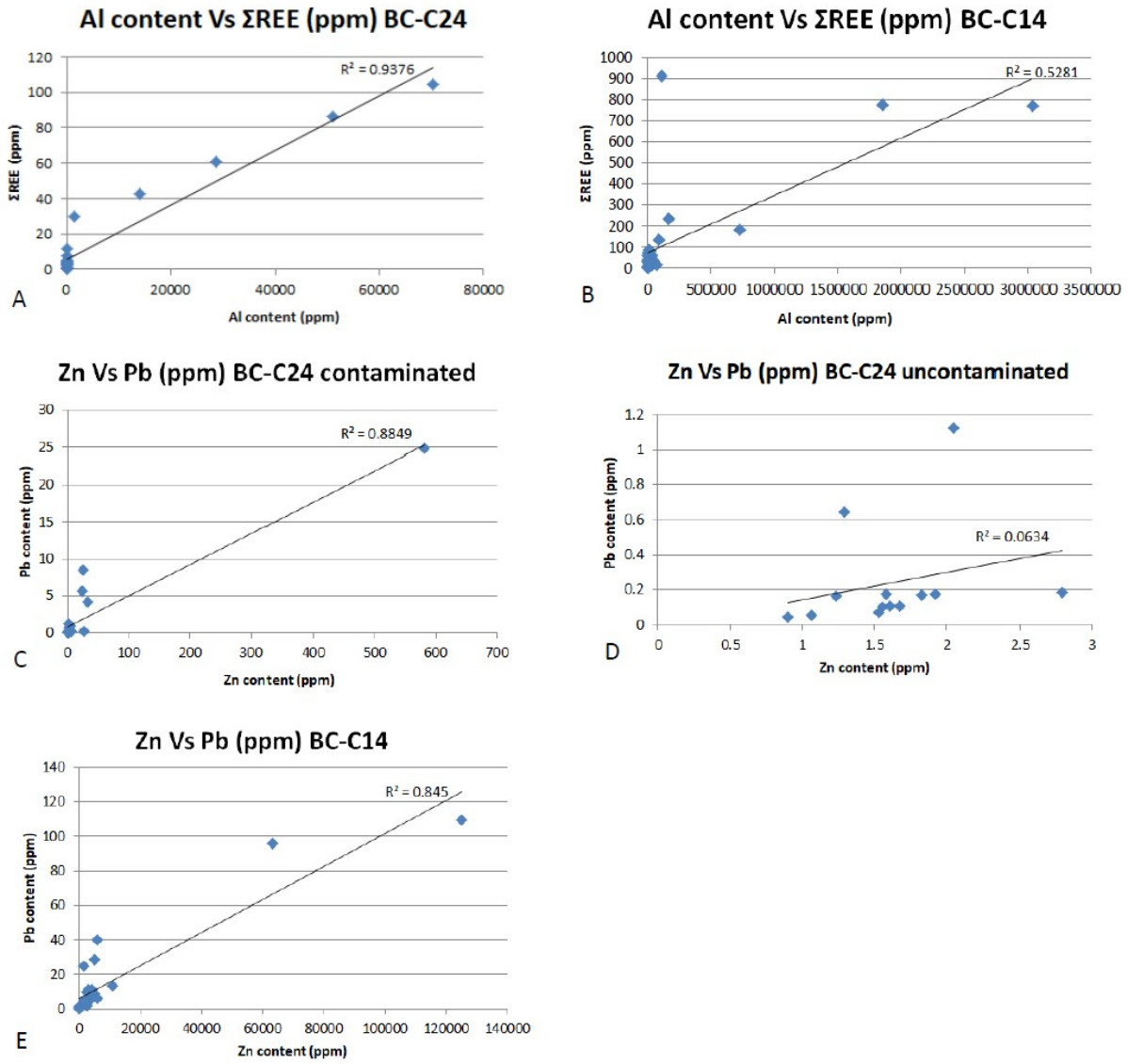

Figure 6.7 Al-∑REE plots (A and B) and Zn-Pb plots (C-E) for samples BC-C24 and BC-C14 from LA-ICP-MS analysis. To notice the good Al-∑REE correlation in both samples (A-B). Good correlations also characterize Zn-Pb concentrations displayed by BC-C24 analysed spots contaminated by silicate volcanic material (high Al content, C) and Zn-Pb concentrations of BC-C14 (E). A lack of correlation instead characterises Zn vs Pb contents of those analysed points of BC-C24 sample displaying the smallest silicate-contamination (D) by volcanic material.

Shale PAAS- and C1-chondrite normalized REY trends, enrichment/depletion patterns and anomalies

Despite two different normalizations were applied to LA-ICP-MS output data, the overall flatness of PAAS- and C1-normalized REY trends (Fig. 6.6), and the consistent polarity of the computed geometric anomalies (Table 6.7) demonstrate that observed peak and anomalies are not artefacts deriving from inappropriate normalization but are of real geochemical significance (Lawrence et al., 2006). The only exception regards the (Eu/Eu*)sn and (Eu/Eu*)cn anomalies computed for BC-C14

fibrous cement calcite that change polarity according to the different normalization performed. This could depend on the higher or lower magnitude of the Eu anomaly within the normalizing rocks, as previously noted by Lawrence et al. (2006) for stream water samples normalized to average shale composition, such as PAAS and MUQ. BC-C24 and BC-C14 REY trends are flat and contrast with typical marine LREE-depleted and increasing REY trends (Zhang and Nozaki, 1996; Bau and Dulski, 1999; Haley et al., 2004; Shields and Webb, 2004; Amzy et al., 2011; Della Porta et al., 2015), with the exception of BC-C24 drusy vein calcite that is LREE-depleted (Fig. 6.6). The only case in which BC-C24 and BC-C14 REY trends could resemble those of marine origin is that of marine calcite veins where progressive detrital contamination results in a gradual flattening of REE trends (Morad et al., 2010). Nevertheless, this geological setting does not apply to the analysed calcite phases. Similarly flat trends have been instead described for meteoric waters of various origins (Aquilina et al., 2002; Möller et al., 2004; Kamber et al., 2005; Lawrence et al., 2006). The more fluctuating trend exhibited by BC-C24 drusy vein calcite compared to flatter BC-C24 replacive calcite and BC-C14 calcite phases is in agreement with differences in normalized REY trends encountered by Hopf et al. (1991) and Uysal et al. (2011) between veins and host rocks. Despite (La/La*)sn, (La/La*)cn, (Gd/Gd*)sn, (Gd/Gd*)cn and Y strong positive anomalies and peaks, (Ce/Ce*)sn and (Ce/Ce*)cn variable anomalies and (Eu/Eu*)sn and (Eu/Eu*)cn overall positive anomalies like the ones characterizing BC-C24 and BC-C14 samples are in line with typical seawater and marine carbonate trends described by several authors (Elderfield, 1988; Bau et al., 1995; Bau, 1996; Zhang and Nozaki, 1996, 1998; Bau and Dulski, 1999; Alibo and Nozaki, 1999; Nozaki and Alibo, 2003; Shields and Webb, 2004; Lawrence et al., 2006; Della Porta et al., 2015), similar La/La*, Gd/Gd* and Eu/Eu* anomalies have also been found by Pili et al. (2002) in fault-zone calcite veins along the San Andreas Fault. BC-C24 and BC-C14 positive (Gd/Gd*)sn and (Gd/Gd*)cn anomalies are also in line with freshwater signatures found by Albo and Nozaki (1999) and Lawrence et al. (2006), while a positive Y anomaly can be acquired, rather than inherited from seawater, due to FeOOH precipitation along infiltrating water pathways like faults (Möeller et al., 2004). A Ce/Ce* negative anomaly is commonly considered as typical of seawater and carbonates precipitated in oxygenated marine environment (Fleet, 1984; Liu et al., 1988; Elderfield et al., 1990), although studies on non-marine calcite have demonstrated that Ce/Ce* negative anomalies can also characterize fault-related (San Andreas Fault, Pili et al., 2002) and hydrothermal calcite (Lake Tanganyika, Barrat et al., 2000) and that its polarity is equally indicative of oxygenated (negative) or reducing (positive) precipitation conditions, as in the case of marine settings (Bau and Dulski, 1999; Möller, 2000; Möller et al., 2003). BC-C24 replacive calcite on volcanic clasts should thus have formed in oxygenated conditions, while drusy vein calcite in reducing conditions. Analogously, BC-C14 fibrous cement calcite precipitated in oxygenated conditions, while calcite in clasts in variable

oxygenated and reducing conditions. However, given the high Si content of BC-C24 drusy vein calcite and the silicate-contaminated nature of BC-C14 calcite, Ce contamination cannot be excluded. The overall weak character of both the positive and the negative Eu peaks displayed by BC-C24 and BC-C14 calcite phases suggests calcite precipitation temperatures below 200-250°C, above which stronger positive Eu/Eu* anomalies (an possibly a Yb anomaly) commonly develop (Bau and Möller 1992; Yamagutchi et al., 2011).

6.5.5 Carbon and oxygen stable isotopes

The $\delta^{13}C$ and $\delta^{18}O$ values of calcites in samples BC-C24 and BC-C14 are reported in Table 6.8 and plotted in Figure 6.8. In BC-C24 sample, drusy vein calcite displays average $\delta^{13}C$ values of -4.4 ‰ and $\delta^{18}O$ average values of -11.7 ‰; replacive calcite on volcanic clasts shows average $\delta^{13}C$ of -4.3 ‰ and average $\delta^{18}O$ of -10.6 ‰. Groundmass microsparite is characterized by average $\delta^{13}C$ of -4.0 ‰ and $\delta^{18}O$ of -10.3 ‰. Millimetre-size fans of fibrous cement in sample BC-C14 display $\delta^{13}C$ average values of -12.8 ‰ and average $\delta^{18}O$ of -10.7 ‰. Table 6.9 reports computed palaeotemperatures and $\delta^{13}C$ values of dissolved CO_2 in the calcite precipitating fluids, together with published information regarding pH and $\delta^{18}O$ isotopic value of spring water in the Tres Vírgenes region (Portugal et al., 2000; Hinojosa et al., 2005).

Table 6.8 C and O stable isotope measurements on calcite samples analysed with IRMS.

Sample	Calcite phase	$\delta^{13}C$ (‰ V-PDB)	$\delta^{18}O$ (‰ V-PDB)
BC-C24A	Drusy vein calcite	-4.5	-11.3
BC-C24A	Drusy vein calcite	-4.5	-11.3
BC-C24B	Drusy vein calcite	-4.0	-11.9
BC-C24C	Drusy vein calcite	-4.3	-11.0
BC-C24D	Drusy vein calcite	-4.5	-11.8
BC-C24I	Calcite slickenside/Drusy vein calcite	-4.7	-12.4
BC-C24J	Drusy vein calcite	-4.4	-11.9
Average BC-C24 drusy vein calcite		**-4.4**	**-11.7**
Standard deviation BC-C24 drusy vein calcite		**0.2**	**0.5**
BC-C24E	Replacive calcite on volcanic clasts	-4.3	-10.7
BC-C24F	Replacive calcite on volcanic clasts	-4.4	-10.2
BC-C24G	Replacive calcite on volcanic clasts	-4.2	-10.8
Average BC-C24 replacive calcite on volcanic clasts		**-4.3**	**-10.6**
Standard deviation BC-C24 replacive calcite on volcanic clasts		**0.1**	**0.3**
$BC\text{-}C24H_1$	Groundmass microsparite	-4.0	-10.4
$BC\text{-}C24H_2$	Groundmass microsparite	-4.0	-10.2
Average BC-C24 groundmass microsparite		**-4.0**	**-10.3**
Standard deviation BC-C24 groundmass microsparite		**0.0**	**0.1**
BC-C14A	mm-sized fans of fibrous cement	-12.8	-11.0
BC-C14B	mm-sized fans of fibrous cement	-12.8	-10.7
BC-C14C	mm-sized fans of fibrous cement	-12.8	-10.9
BC-C14D	mm-sized fans of fibrous cement	-12.9	-10.7
BC-C14E	mm-sized fans of fibrous cement	-12.8	-10.7

BC-C14F	mm-sized fans of fibrous cement	-12.7	-10.5
BC-C14G	mm-sized fans of fibrous cement	-12.6	-10.3
BC-C14H$_1$	mm-sized fans of fibrous cement	-12.7	-10.7
BC-C14H$_2$	mm-sized fans of fibrous cement	-12.7	-10.8
BC-C14I	mm-sized fans of fibrous cement	-12.9	-10.8
Average BC-C14 mm-sized fans of fibrous cement		**-12.8**	**-10.7**
Standard deviation BC-C14 mm-sized fans of fibrous cement		**0.1**	**0.2**

Interpretation

Both BC-C24 and BC-C14 $\delta^{13}C$ and $\delta^{18}O$ calcite phases display rather negative values (Table 6.8 and Fig. 6.8), contrarily to calcite of typical marine provenance (average $\delta^{13}C$=0 ‰, Veizer and Hoefs, 1976; Freeman et al., 1990; Kump and Arthur, 1999; Swart, 2015). Generally low negative $\delta^{18}O$ values might be related either to high temperature of precipitation or to meteoric water, whereas negative $\delta^{13}C$ values might suggest the influence of ^{13}C depleted organic carbon from soils or buried organic matter within sediments (Tucker and Wright, 1990; Swart, 2015).

Palaeotemperatures shown in Table 6.9 were calculated using different published equations (Craig, 1965; O'Neil et al., 1969; Coplen et al., 1983; Kim and O'Neil, 1997; Mulitza et al., 2003; Sharp, 2007; Coplen, 2007) that use IRMS-measured $\delta^{18}O$ of calcite (‰ V-PDB) and $\delta^{18}O$ water values (‰ V-SMOW, Portugal et al., 2000; Hinojosa et al., 2005) as input parameters. Among published water $\delta^{18}O$ values (Portugal et al., 2000; Hinojosa et al., 2005) those measured closer to BC-C24 and BC-C14 sampling sites (named respectively Azufre, Agua Caliente and Yaqui and R. Virgenes) were chosen for the computation. Coplen et al. (1983) relationship was used to convert measured $\delta^{18}O$ calcite values from V-PDB to V-SMOW when needed. Based on different oxygen isotopic compositions of water and equations, resulting palaeotemperature ranges are 42.5-87.5°C for sample BC-C24 and 12.5-33.6°C for sample BC-C14 based on Craig (1965), while 41.0-99.6°C for BC-C24 and 12.3-33.6°C for BC-C14 based on O'Neil et al (1969), Kim and O'Neil (1997), Mulitza et al. (2003), Sharp (2007) and Coplen (2007) equations (Table 6.9). Worth of note is that the highest obtained palaeotemperatures (corresponding to the $\delta^{18}O$ lowest values measured) relate to BC-C24 drusy vein calcite (Tables 6.8 and 6.9). $\delta^{13}C$ values of the CO_2 indicative of the isotopic signature of the Dissolved Inorganic Carbon (DIC) of the fluids precipitating calcite vary between -11.5 and -4.5‰ for sample BC-C24 and -23.2 to -20.7‰ for sample BC-C14 (Table 6.9) based on Romanek et al. (1992) equation using the previously computed $\delta^{18}O$-derived palaeotemperatures (O'Neil et al., 1969; Kim and O'Neil, 1997; Mulitza et al., 2003; Sharp, 2007; Coplen, 2007, Table 6.9) as input parameter. Less variability characterizes $\delta^{13}C$ DIC values resulting from the application of the more generalized Panichi and Tongiorgi (1976) relationship (-15.3 to -16.1 ‰ for sample BC-C24 and -26.0 to -25.6 ‰ for sample BC-C14, Table 6.9). The use of Panichi and Tongiorgi (1976) and Romanek et al. (2002)

relationships was the only possible approach to derive $\delta^{13}C$ signature of the DIC in the calcite precipitating fluid, given that Tres Vírgenes geothermal waters lack adequate hydrochemical investigations (Birkle et al., 2016) and most of performed studies did not determine $\delta^{13}C$ isotopic signature of the DIC in spring waters (Portugal et al., 2000; Hinojosa et al., 2005; Verma et al., 2006; Conly et al., 2006).

The differences between $\delta^{18}O$-derived palaeotemperature ranges and $\delta^{13}C$ DIC values of fluids precipitating calcite in samples BC-C24 and BC-C14 suggest a different origin of fluids circulating along the Azufre and Infierno fault systems. In detail, along-fault circulation of a higher temperature (up to 100°C) fluid with a DIC isotopic composition indicative of a mixed origin from hydrothermal and meteoric sources is suggested for sample BC-C24, whilst a cooler (up to 34°C) likely meteoric fluid, whose $\delta^{13}C$ DIC isotopic signature has been modified by interaction with soil derived organic matter, represents BC-C14 last circulation event that deposited the non-luminescent mm-size fans of fibrous calcite cement.

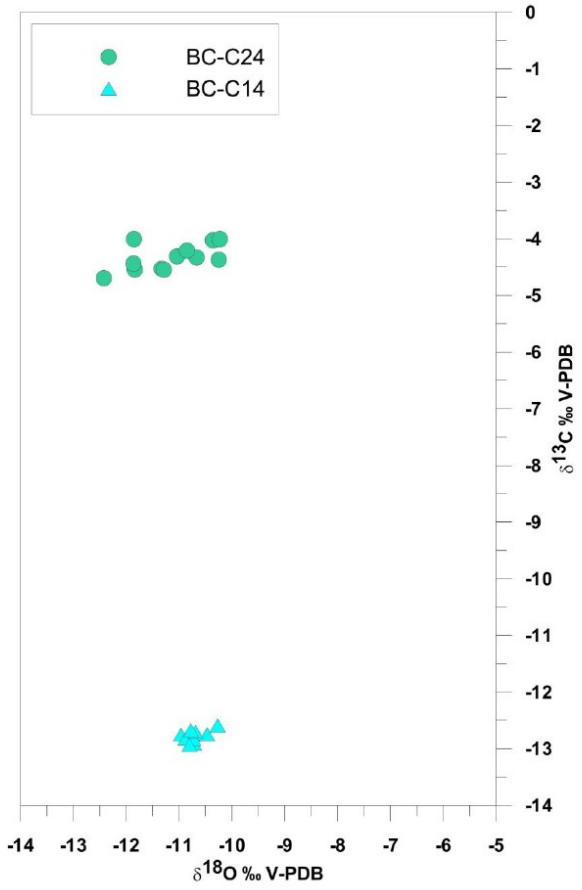

Figure 6.8 Stable oxygen and carbon isotope analyses (‰, V-PDB) for samples BC-C24 and BC-C14. Detailed measurements are reported in Table 6.8. The two analysed samples display similar $\delta^{18}O$ but different δ^{13C} values, with sample BC-C14 millimetre-size fans of fibrous calcite cement characterized by negative $\delta^{13}C$ averaging -12.8 ‰ whereas sample BC-C24 replacive calcite on clasts and calcite crystals in veins displaying values around -4.4 ‰.

Table 6.9 Palaeotemperature (°C) and $\delta^{13}C$ CO_2 indicative of the fluid DIC (Dissolved Inorganic Carbon) calculated using different published equations. $\delta^{18}O$ cal (V-PDB) and $\delta^{13}C$ cal (V-PDB) are IRMS measured values, spring $\delta^{18}O$ wat (V-SMOW) and pH are derived from published data (Portugal et al., 2000; Hinojosa et al., 2005).

Sample	Spring location	Spring pH	$\delta^{18}O$ wat (SMOW)	$\delta^{18}O$ cal (V-PDB)	T (°C) [c]	T (°C) [d]	T (°C) [e]	T (°C) [f]	T (°C) [g]	$\delta^{13}C$ cal (V-PDB)	$\delta^{13}C$ DIC [h] (V-PDB)	$\delta^{13}C$ DIC [c] (V-PDB)	$\delta^{13}C$ DIC [d] (V-PDB)	$\delta^{13}C$ DIC [e] (V-PDB)	$\delta^{13}C$ DIC [f] (V-PDB)	$\delta^{13}C$ DIC [g] (V-PDB)
BC-C24A	Azufre	1.41 [b]	0 [a]	-11.3	82.2	71.6	90.8	76.1	81.5	-4.5	-15.9	-6.6	-7.9	-5.6	-7.3	-6.7
	Azufre	1.39 [b]	-0.4 [b]		79.3	69.3	87.8	73.4	78.3			-7.0	-8.2	-5.9	-7.7	-7.1
	Agua Caliente	8.14 [b]	-4.4 [a]		52.1	47.2	60.1	48.6	50.7			-10.2	-10.8	-9.3	-10.6	-10.4
	Agua Caliente	8.50 [b]	-4.5 [b]		51.5	46.7	59.5	48.1	50.1			-10.3	-10.9	-9.3	-10.7	-10.5
BC-C24B	Azufre	1.41 [b]	0 [a]	-11.9	86.7	75.2	95.6	80.3	86.6	-4	-15.3	-5.6	-7.0	-4.5	-6.3	-5.6
	Azufre	1.39 [b]	-0.4 [b]		83.7	72.8	92.5	77.5	83.3			-5.9	-7.2	-4.9	-6.7	-6.0
	Agua Caliente	8.14 [b]	-4.4 [a]		55.9	50.4	64.1	52.2	54.6			-9.3	-9.9	-8.3	-9.7	-9.4
	Agua Caliente	8.50 [b]	-4.5 [b]		55.2	49.8	63.5	51.6	53.9			-9.4	-10.0	-8.4	-9.8	-9.5
BC-C24C	Azufre	1.41 [b]	0 [a]	-11	80.0	69.9	88.4	74.0	79.1	-4.3	-15.7	-6.7	-7.9	-5.7	-7.4	-6.8
	Azufre	1.39 [b]	-0.4 [b]		77.1	67.6	85.5	71.3	76.0			-7.0	-8.2	-6.0	-7.7	-7.2
	Agua Caliente	8.14 [b]	-4.4 [a]		50.2	45.6	58.1	46.9	48.9			-10.3	-10.8	-9.3	-10.7	-10.4
	Agua Caliente	8.50 [b]	-4.5 [b]		49.6	45.1	57.5	46.3	48.3			-10.3	-10.9	-9.4	-10.7	-10.5
BC-C24D	Azufre	1.41 [b]	0 [a]	-11.8	86.0	74.6	94.7	79.6	85.7	-4.5	-15.9	-6.2	-7.5	-5.1	-6.9	-6.2
	Azufre	1.39 [b]	-0.4 [b]		83.0	72.2	91.7	76.8	82.4			-6.5	-7.8	-5.5	-7.3	-6.6
	Agua Caliente	8.14 [b]	-4.4 [a]		55.2	49.8	63.4	51.6	53.9			-9.9	-10.5	-8.9	-10.3	-10.0
	Agua Caliente	8.50 [b]	-4.5 [b]		54.6	49.3	62.8	51.0	53.3			-9.9	-10.6	-8.9	-10.4	-10.1
BC-C24E	Azufre	1.41 [b]	0 [a]	-10.7	77.8	68.1	86.1	71.9	76.7	-4.3	-15.7	-6.9	-8.1	-5.9	-7.6	-7.1
	Azufre	1.39 [b]	-0.4 [b]		74.9	65.8	83.2	69.3	73.6			-7.3	-8.4	-6.3	-8.0	-7.4
	Agua Caliente	8.14 [b]	-4.4 [a]		48.4	44.1	56.2	45.1	47.0			-10.5	-11.0	-9.5	-10.9	-10.6
	Agua Caliente	8.50 [b]	-4.5 [b]		47.8	43.5	55.6	44.6	46.4			-10.5	-11.1	-9.6	-10.9	-10.7
BC-C24F	Azufre	1.41 [b]	0 [a]	-10.2	74.2	65.3	82.3	68.6	72.7	-4.4	-15.8	-7.5	-8.5	-6.5	-8.2	-7.7
	Azufre	1.39 [b]	-0.4 [b]		71.3	63.0	79.5	66.0	69.8			-7.8	-8.8	-6.8	-8.5	-8.0
	Agua Caliente	8.14 [b]	-4.4 [a]		45.4	41.5	53.0	42.3	44.0			-10.9	-11.4	-10.0	-11.3	-11.1
	Agua Caliente	8.50 [b]	-4.5 [b]		44.8	41.0	52.4	41.7	43.4			-11.0	-11.5	-10.1	-11.4	-11.2
BC-C24G	Azufre	1.41 [b]	0 [a]	-10.8	78.5	68.7	86.9	72.6	77.4	-4.2	-15.5	-6.8	-7.9	-5.8	-7.5	-6.9
	Azufre	1.39 [b]	-0.4 [b]		75.6	66.4	83.9	70.0	74.4			-7.1	-8.2	-6.1	-7.8	-7.3
	Agua Caliente	8.14 [b]	-4.4 [a]		49.0	44.6	56.9	45.7	47.6			-10.3	-10.8	-9.4	-10.7	-10.5
	Agua Caliente	8.50 [b]	-4.5 [b]		48.4	44.1	56.2	45.1	47.0			-10.4	-10.9	-9.4	-10.8	-10.5
$BC\text{-}C24H_1$	Azufre	1.41 [b]	0 [a]	-10.4	75.6	66.4	83.9	69.9	74.3	-4	-15.3	-6.9	-8.0	-5.9	-7.6	-7.1

	Azufre	1.39 [b]	-0.4 [b]		72.8	64.1	80.9	67.3	71.3			-7.3	-8.3	-6.3	-7.9	-7.4
	Agua Caliente	8.14 [b]	-4.4 [a]		46.6	42.5	54.3	43.4	45.2			-10.4	-10.9	-9.5	-10.8	-10.6
	Agua Caliente	8.50 [b]	-4.5 [b]		46.0	42.0	53.7	42.8	44.6			-10.5	-10.9	-9.5	-10.8	-10.6
$BC\text{-}C24H_2$	Azufre	1.41 [b]	0 [a]	-10.2	74.2	65.3	82.3	68.6	72.7	-4	-15.3	-7.1	-8.1	-6.1	-7.8	-7.3
	Azufre	1.39 [b]	-0.4 [b]		71.3	63.0	79.5	66.0	69.8			-7.4	-8.4	-6.4	-8.1	-7.6
	Agua Caliente	8.14 [b]	-4.4 [a]		45.4	41.5	53.0	42.3	44.0			-10.5	-11.0	-9.6	-10.9	-10.7
	Agua Caliente	8.50 [b]	-4.5 [b]		44.8	41.0	52.4	41.7	43.4			-10.6	-11.1	-9.7	-11.0	-10.8
BC-C24I	Azufre	1.41 [b]	0 [a]	-12.4	90.6	78.2	99.6	83.9	91.0	-4.7	-16.1	-5.8	-7.3	-4.7	-6.6	-5.8
	Azufre	1.39 [b]	-0.4 [b]		87.5	75.8	96.5	81.1	87.6			-6.2	-7.6	-5.1	-6.9	-6.2
	Agua Caliente	8.14 [b]	-4.4 [a]		59.1	53.0	67.5	55.3	57.9			-9.6	-10.3	-8.6	-10.0	-9.7
	Agua Caliente	8.50 [b]	-4.5 [b]		58.5	52.5	66.8	54.7	57.2			-9.7	-10.4	-8.7	-10.1	-9.8
BC-C24J	Azufre	1.41 [b]	0 [a]	-11.9	86.7	75.2	95.6	80.3	86.6	-4.4	-15.8	-6.0	-7.4	-4.9	-6.7	-6.0
	Azufre	1.39 [b]	-0.4 [b]		83.7	72.8	92.5	77.5	83.3			-6.3	-7.6	-5.3	-7.1	-6.4
	Agua Caliente	8.14 [b]	-4.4 [a]		55.9	50.4	64.1	52.2	54.6			-9.7	-10.3	-8.7	-10.1	-9.8
	Agua Caliente	8.50 [b]	-4.5 [b]		55.2	49.8	63.5	51.6	53.9			-9.8	-10.4	-8.8	-10.2	-9.9
BC-C14A	Yaqui	7.73 [b]	-8.7 [a]	-11	26.4	24.5	33.1	24.2	25.8	-12.8	-25.9	-21.6	-21.8	-20.8	-21.9	-21.7
	Yaqui	8.20 [b]	-8.6 [b]		26.9	25.0	33.6	24.7	26.3			-21.6	-21.8	-20.7	-21.8	-21.6
	R. Virgenes	7.76 [b]	-10.1 [a]		19.7	18.2	25.7	17.5	19.3			-22.4	-22.6	-21.7	-22.7	-22.5
	R. Virgenes	8.01 [b]	-10.5 [b]		17.9	16.5	23.7	15.6	17.5			-22.6	-22.8	-21.9	-22.9	-22.7
BC-C14B	Yaqui	7.73 [b]	-8.7 [a]	-10.7	24.9	23.2	31.4	22.7	24.3	-12.8	-25.9	-21.8	-22.0	-21.0	-22.1	-21.9
	Yaqui	8.20 [b]	-8.6 [b]		25.4	23.6	32.0	23.2	24.8			-21.7	-21.9	-20.9	-22.0	-21.8
	R. Virgenes	7.76 [b]	-10.1 [a]		18.4	16.9	24.1	16.0	17.9			-22.6	-22.8	-21.9	-22.9	-22.6
	R. Virgenes	8.01 [b]	-10.5 [b]		16.6	15.2	22.1	14.2	16.1			-22.8	-23.0	-22.1	-23.1	-22.8
BC-C14C	Yaqui	7.73 [b]	-8.7 [a]	-10.9	25.9	24.1	32.5	23.7	25.3	-12.8	-25.9	-21.7	-21.9	-20.9	-21.9	-21.7
	Yaqui	8.20 [b]	-8.6 [b]		26.4	24.5	33.1	24.2	25.8			-21.6	-21.8	-20.8	-21.9	-21.7
	R. Virgenes	7.76 [b]	-10.1 [a]		19.3	17.8	25.2	17.0	18.8			-22.5	-22.6	-21.8	-22.7	-22.5
	R. Virgenes	8.01 [b]	-10.5 [b]		17.5	16.0	23.2	15.1	17.0			-22.7	-22.9	-22.0	-23.0	-22.7
BC-C14D	Yaqui	7.73 [b]	-8.7 [a]	-10.7	24.9	23.2	31.4	22.7	24.3	-12.9	-26.0	-21.9	-22.1	-21.1	-22.2	-22.0
	Yaqui	8.20 [b]	-8.6 [b]		25.4	23.6	32.0	23.2	24.8			-21.8	-22.0	-21.0	-22.1	-21.9
	R. Virgenes	7.76 [b]	-10.1 [a]		18.4	16.9	24.1	16.0	17.9			-22.7	-22.9	-22.0	-23.0	-22.7
	R. Virgenes	8.01 [b]	-10.5 [b]		16.6	15.2	22.1	14.2	16.1			-22.9	-23.1	-22.2	-23.2	-22.9
BC-C14E	Yaqui	7.73 [b]	-8.7 [a]	-10.7	24.9	23.2	31.4	22.7	24.3	-12.8	-25.9	-21.8	-22.0	-21.0	-22.1	-21.9

	Yaqui	8.20 [b]	-8.6 [b]		25.4	23.6	32.0	23.2	24.8			-21.7	-21.9	-20.9	-22.0	-21.8
	R. Virgenes	7.76 [b]	-10.1 [a]		18.4	16.9	24.1	16.0	17.9			-22.6	-22.8	-21.9	-22.9	-22.6
	R. Virgenes	8.01 [b]	-10.5 [b]		16.6	15.2	22.1	14.2	16.1			-22.8	-23.0	-22.1	-23.1	-22.8
BC-C14F	Yaqui	7.73 [b]	-8.7 [a]	-10.5	23.9	22.3	30.3	21.7	23.3	-12.7	-25.7	-21.8	-22.0	-21.0	-22.1	-21.9
	Yaqui	8.20 [b]	-8.6 [b]		24.4	22.7	30.9	22.2	23.8			-21.7	-22.0	-21.0	-22.0	-21.8
	R. Virgenes	7.76 [b]	-10.1 [a]		17.5	16.0	23.1	15.1	17.0			-22.6	-22.8	-21.9	-22.9	-22.6
	R. Virgenes	8.01 [b]	-10.5 [b]		15.8	14.3	21.1	13.2	15.2			-22.8	-23.0	-22.1	-23.1	-22.9
BC-C14G	Yaqui	7.73 [b]	-8.7 [a]	-10.3	23.0	21.3	29.2	20.7	22.4	-12.6	-25.6	-21.8	-22.0	-21.1	-22.1	-21.9
	Yaqui	8.20 [b]	-8.6 [b]		23.5	21.8	29.8	21.2	22.8			-21.8	-22.0	-21.0	-22.0	-21.8
	R. Virgenes	7.76 [b]	-10.1 [a]		16.6	15.2	22.1	14.1	16.1			-22.6	-22.8	-21.9	-22.9	-22.6
	R. Virgenes	8.01 [b]	-10.5 [b]		14.9	13.5	20.1	12.3	14.4			-22.8	-23.0	-22.2	-23.1	-22.9
$BC\text{-}C14H_1$	Yaqui	7.73 [b]	-8.7 [a]	-10.7	24.9	23.2	31.4	22.7	24.3	-12.7	-25.7	-21.7	-21.9	-20.9	-22.0	-21.8
	Yaqui	8.20 [b]	-8.6 [b]		25.4	23.6	32.0	23.2	24.8			-21.6	-21.8	-20.8	-21.9	-21.7
	R. Virgenes	7.76 [b]	-10.1 [a]		18.4	16.9	24.1	16.0	17.9			-22.5	-22.7	-21.8	-22.8	-22.5
	R. Virgenes	8.01 [b]	-10.5 [b]		16.6	15.2	22.1	14.2	16.1			-22.7	-22.9	-22.0	-23.0	-22.7
$BC\text{-}C14H_2$	Yaqui	7.73 [b]	-8.7 [a]	-10.8	25.4	23.6	32.0	23.2	24.8	-12.7	-25.7	-21.6	-21.8	-20.8	-21.9	-21.7
	Yaqui	8.20 [b]	-8.6 [b]		25.9	24.1	32.5	23.7	25.3			-21.6	-21.8	-20.8	-21.8	-21.6
	R. Virgenes	7.76 [b]	-10.1 [a]		18.8	17.4	24.7	16.5	18.3			-22.4	-22.6	-21.7	-22.7	-22.5
	R. Virgenes	8.01 [b]	-10.5 [b]		17.1	15.6	22.6	14.7	16.6			-22.6	-22.8	-22.0	-22.9	-22.7
BC-C14I	Yaqui	7.73 [b]	-8.7 [a]	-10.8	25.4	23.6	32.0	23.2	24.8	-12.9	-26.0	-21.8	-22.0	-21.0	-22.1	-21.9
	Yaqui	8.20 [b]	-8.6 [b]		25.9	24.1	32.5	23.7	25.3			-21.8	-22.0	-21.0	-22.0	-21.8
	R. Virgenes	7.76 [b]	-10.1 [a]		18.8	17.4	24.7	16.5	18.3			-22.6	-22.8	-21.9	-22.9	-22.7
	R. Virgenes	8.01 [b]	-10.5 [b]		17.1	15.6	22.6	14.7	16.6			-22.8	-23.0	-22.2	-23.1	-22.9

The Azufre and Agua Caliente sampling sites (Portugal et al., 2000; Hinojosa et al., 2005) are those closer to BC-C24 sample location, while the Yaqui and R. Virgenes (Portugal et al., 2000; Hinojosa et al., 2005) are the closest to BC-C14 sample location.

[a] Hinojosa et al. (2005); [b] Portugal et al. (2000).

[c] Sharp (2007): $T\ (°C) = 15.75 - 4300 * (\delta^{18}O\ cal - \delta^{18}O\ wat) + 140000 * (\delta^{18}O\ cal - \delta^{18}O\ wat)^2$

[d] Mulitza et al. (2003): $t\ (°C) = 14.32 - 4280 * (\delta^{18}O\ cal - \delta^{18}O\ wat) + 70000 * (\delta^{18}O\ cal - \delta^{18}O\ wat)^2$

[e] Coplen (2007): $(\alpha\ -1) * 1000 = 17.4 * (1000 / T) - 28.6$; where $(\alpha\ -1) * 1000 = \varepsilon \approx 1000 * ln\ (\delta^{18}Ocal\ (SMOW) - \delta^{18}O\ wat\ (SMOW))$

[f] Kim and O'Neil (1997): $(\alpha\ -1) * 1000 = 18.03 * (1000 / T) - 32.42$; where $(\alpha\ -1) * 1000 = \varepsilon \approx 1000 * ln\ (\delta^{18}Ocal\ (SMOW) - \delta^{18}O\ wat\ (SMOW))$

[g] O'Neil et al. (1969): $(\alpha\ -1) * 1000 = [(2.78 * 10^6) / T^2] - 2.89$; where $(\alpha\ -1) * 1000 = \varepsilon \approx 1000 * ln\ (\delta^{18}Ocal\ (SMOW) - \delta^{18}O\ wat\ (SMOW))$

[h] Panichi and Tongiorgi (1976): $\delta^{13}C\ CO_2 = 1.2 * \delta^{13}C\ cal - 10.5$

$\delta^{13}C\ CO_2$ [c, d, e, f, g] calculated from Romanek et al. (2002): $\varepsilon\ (cal\text{-}CO_2) = 11.98\ (\pm\ 0.13) - 0.12\ (\pm\ 0.01) * T$; where $\varepsilon\ (cal\text{-}CO_2) = \delta^{13}C\ cal\ (V\text{-}PDB) - \delta^{13}C\ CO_2\ (V\text{-}PDB)$

6.6 Discussion

6.6.1 Origin of fluids circulating along regional faults

As highlighted by Travè et al. (1998), Boles and Grivetti (2000) and Pili et al. (2002), $\delta^{18}O$ and $\delta^{13}C$ isotope analysis on fault-related calcite is one of the tools allowing the discussion on the origin of the fluid from which those calcites formed. In addition to fault-related calcite $\delta^{13}C$ isotopic signatures (negative values), combined information regarding Y/Ho, Zr/Hf, Sm/Nd ratios, average ∑REE abundances and normalized REY trends excluded the marine origin of fluids circulating along the Azufre and Infierno fault systems. Even though some of the analysed calcite phases display Y/Ho ratios falling within the seawater interval (BC-C24 drusy vein calcite) or in the overlapping field between seawater and hydrothermal fluids, several examples of hydrothermal calcite veins intruding crystalline rocks display Y/Ho ratios falling within seawater typical ranges (Kamber et al., 2005; Uysal et al., 2007). This is probably due to the high variability of REE patterns and trace element ratios in hydrothermal fluids (Barrat et al., 2000), resulting from different geological and temperature boundary conditions. Average ∑REE abundance of BC-C24 calcite phases and of BC-C14 fibrous cement are similar to those found in hydrothermal aragonite veins in Tanganyika Lake (Barrat et al., 2000) and in hydrothermal calcite veins of the German Rhenish Massif (Bau, 1996). Shale- and chondrite-normalized REY trends displayed by analysed fault-related calcite both along the Azufre and Infierno fault systems resemble those reported for several non-marine geological settings comparable to those expected in the study area, here listed: a) fault-zone calcite veins (San Andreas Fault system; Pili et al., 2002); b) fluvial freshwater (Kamber et al., 2005; Lawrence et al., 2006); c) meteoric karst water (Möller et al., 2004); d) hydrothermal calcite-silica scales and calcite veins (Uysal et al., 2007; Barker et al., 2009) and geothermal fluids from wells or springs (T>100°C in Turkey, Barrat et al., 2000; Möller et al., 2004); d) volcanic-free continental shelf thermal waters (27-50°C, Aquilina et al., 2002); e) weakly to highly altered volcanic crust (rhyolites, andesites and basalts) containing secondary calcite and relic igneous textures (Hopf et al., 1991). This also applies to REY trends of drusy vein calcite along the Azufre fault system which, despite high variability, resemble those found in Turkish geothermal spring waters by Möller et al. (2004). The hydrothermal and/or meteoric origin of fluids circulating along fault planes in the Tres Vírgenes region is a relevant result when considering the debated origin of fluids recharging the Tres Vírgenes geothermal reservoir. The results from this study argue in favour of Portugal et al. (1998a, and 2000) and Hinojosa et al. (2005), who stated that, notwithstanding the proximity of the Tres Vírgenes area with the Gulf of California and the Pacific Ocean, no influences of marine seawater ingressions could be observed in the geothermal reservoir,

and against Verma et al. (2006), who accounted for significant volumes of seawater from the Gulf of California recharging the geothermal reservoir. If any marine influence is inferred (i.e., BC-C24 drusy vein calcite) this must be of local significance and surely does not result from the interaction with present marine water, as indicated by non-marine isotopic signatures of analysed calcite phases. A local marine influence could instead derive from fluid-rock interaction processes of fault-related fluids with Cenozoic carbonates already influenced by burial diagenesis, which represent the basement to Quaternary volcanism in the region (Garcia-Sánchez et al., 2019). Despite the common non-marine origin, fluids circulating along the Azufre and Infierno fault systems bear some different characteristics, as indicated by stable isotopes and major and trace elements analyses. Fluids circulating along the Azufre fault (BC-C24) are warmer (up to 100°C) and of mixed meteoric-hydrothermal ($\delta^{13}C$ DIC from -11‰ up to -4.5‰) origin, in line with higher Mn concentration of luminescent calcite phases suggesting precipitation in reducing conditions and a deeper provenance. Along the Infierno fault (BC-C14) fluids are Fe-richer, predominantly meteoric, of relatively cool temperature (up to 34°C) and enriched in ^{13}C depleted organic carbon ($\delta^{13}C$ DIC up to -23‰; Veizer and Hoefs, 1976; Freeman et al., 1990; Kump and Arthur, 1999). The most likely explanation involves degradation of the soil organic matter (Chiodini et al., 2008), that, in active seismic zones like the Tres Vírgenes region (Wong and Munguia, 2006), might be associated with biogenic gas flow along fault and fracture zones (Lewicki et al., 2003; Uysal et al., 2011). In the case of the Infierno fault, the interaction with organic matter could be favoured by the several palaeosoils identified by Garcia-Sánchez et al. (2019) throughout La Reforma caldera complex stratigraphic succession that instead lack within the succession crossed by the Azufre fault system (BC-C24). $\delta^{18}O$ and $\delta^{13}C$ values of calcite precipitated along the Azufre fault system (BC-C24) are in line with those encountered by Pili et al. (2002) in slickensides and veins along the San Andreas Fault system ($\delta^{18}O$ ranges around 20‰ V-SMOW and $\delta^{13}C$ around -3 to -4‰ V-PDB). This could suggest the rise of deep metamorphic fluids along fault zones, and in the specific case from the Cretaceous granitic crystalline basement (Garcia-Sánchez et al., 2019) that provides the reservoir for Las Tres Vírgenes geothermal fluids. This interpretation is also in agreement with Portugal et al. (2000) hydrogeological conceptual model of Las Tres Vírgenes area, where the isotopic signature of spring waters sampled close to BC-C24 (Azufre and Agua Caliente, Table 6.9) is interpreted as deriving from the heating of the shallow aquifer system and from oxidation of H_2S to SO_4 under surface conditions by the rise of H_2S vapour together with a dominant CO_2-phase. The lack of geothermal contributions in fluids circulating along the Infierno fault highlighted by the present study also confirms what stated by Portugal et al. (2000) concerning the predominance of shallow meteoric water and minor contributions of magmatic-geothermal water SE of La Reforma caldera (Yaqui and R.Virgenes sampling sites, Table 6.9), probably due to the higher

distance from the magmatic feeding system (Macias and Jimenez, 2012, 2013; Avellán et al., 2018) with respect to the Azufre canyon area (BC-C24).

6.6.2 Temperature of multiple fluid circulation events along regional faults

Palaeotemperatures calculated from $\delta^{18}O$ isotopic values of calcite precipitated along the Azufre and Infierno faults vary between 12°C (Infierno fault) and 99°C (Azufre fault system). Unfortunately, no direct confirmation via thermometric analysis on fluid inclusions could be performed. Nevertheless, analogue temperature ranges were deduced by Barker et al. (2009) based on similar $\delta^{18}O$ isotopic values for calcite veins emplaced in a low temperature (100-200°C) fault and fracture hosted hydrothermal system in Australia (eastern Lachlan Fold Belt). Temperatures up to 100°C are also in line with a pronounced meteoric water influx typical of open fluid-rock systems characterized by disequilibrium conditions commonly characterizing evolved fault systems (Benedicto et al., 2008) like the Azufre and Infierno structures. Surface or near-surface temperatures up to 100°C for mixed hydrothermal-meteoric fluids rising along faults are also in agreement with along-fault occurrence of clinoptilolite mineralization (BC-C5 and BC-C7 samples) mapped in the field, whose stability field is typically below 100°C (Iijima, 1980; Ogihara, 2000). In addition to evidences from stable isotopes, fault-related calcite precipitation at low temperature conditions (below 200°-250°C) is also supported by the weak character of the Eu peak in both samples BC-C24 and BC-C14. In addition, negative (Ce/Ce*)sn and (Ce/Ce*)cn anomalies indicative of oxygenated conditions (Elderfield and Scholkovitz, 1987; Elderfield et al., 1990), like the one exhibited by the majority of analysed points along the Infierno and Azufre fault systems, are very unlikely to form under conditions of high temperature (200°-250°C, Bau, 1991; Bau and Möller, 1992) and moreover, the contemporaneous development in the same setting of a negative Ce/Ce* anomaly and of a positive Eu/Eu* anomaly is impossible (Bau, 1991; Bau and Möller, 1992). Yet, the presence of positive (Eu/Eu*)sn and (Eu/Eu*)cn anomalies and the fact that $\delta^{18}O$-derived palaeotemperatures were derived for a mixture of luminescent and non-luminescent calcite phases in sample BC-C24 and only refer to non-luminescent fibrous calcite cement in sample BC-C14 (displaying a negative (Eu/Eu*)sn anomaly), do raise the issue of possibly higher precipitation temperatures for not-properly isolated luminescent calcite phases. Interesting insights on this issue come from redox conditions indicated by the Ce/Ce* anomaly and from the polarity of the Eu/Eu* anomaly. In detail, recognized circulation events precipitating calcite along the Azufre fault were two, including: reducing fluids precipitating luminescent replacive calcite on volcanic clasts (1) followed by mixed meteoric-hydrothermal fluids precipitating non-luminescent replacive calcite on volcanic clasts, mixed plagioclase-quartz-calcite veins, drusy vein calcite and ground mass microsparite (2). Ce contamination in high-Si contaminated drusy vein calcite

is definitely responsible for the simultaneous occurrence of (Ce/Ce*)sn, (Ce/Ce*)cn and (Eu/Eu*)sn and (Eu/Eu*)cn positive anomalies (C2-2, Tables 6.4 and 6.7) that disagree with the up to 100°C $\delta^{18}O$-derived palaeotemperatures. Contrarily, the occurrence of (Ce/Ce*)sn and (Ce/Ce*)cn negative and (Eu/Eu*)sn and (Eu/Eu*)cn positive anomalies (C2-3, Tables 6.4 and 6.7) could be indicative of redox conditions change during fluid migration (Bau and Möller, 1992). This is in agreement with multiple identified fluid circulation events along the Azufre fault system, linked to its cyclic nature interpreted according to Sibson (1981) 'valve' system model by Pellicioli et al. (submitted, a and b). Concomitant (Ce/Ce*)sn, (Ce/Ce*)cn and (Eu/Eu*)sn and (Eu/Eu*)cn positive anomalies are also displayed by C2-1 uncontaminated luminescent replacive calcite on volcanic clasts (Tables 6.4 and 6.7). Being BC-C24 calculated palaeotemperatures related to a mixture of luminescent and non-luminescent calcite phases, temperatures higher than 100°C (≈ 200°-250°C) for luminescent replacive calcite phases cannot be excluded, even though deduced on the base of only one analysis point (C2-1). Along the Infierno fault, the recognised circulation events were instead three: a Mn-rich reducing deep phreatic fluid precipitating luminescent calcite rims and calcite in clasts phases (1), followed by oxygenated fluids precipitating non-luminescent calcite in clasts and fibrous cement calcite phases (2) and calcite filling veins cross-cutting fibrous cement calcite (3). As previously suggested, disagreements between (Ce/Ce*)sn and (Ce/Ce*)cn anomaly values and calcite in clasts phases luminescence character in sample BC-C14 (positive (Ce/Ce*)sn and (Ce/Ce*)cn anomalies in non-luminescent phases) are possibly related to Ce contamination linked to the silicate-contaminated nature of the analysed calcite phases. Nevertheless, available data could still indicate a change in redox conditions during fluid migration, supported by the presence of positive (Ce/Ce*)sn and negative (Eu/Eu*)sn anomalies in some luminescent calcite in clasts analysed spots (Bau and Möller, 1992), in analogy to what stated for the Azufre fault. However, contrarily to the Azufre fault system, the occurrence of contemporaneously positive (Ce/Ce*)sn, (Ce/Ce*)cn and (Eu/Eu*)sn and (Eu/Eu*)cn anomalies is strongly dependent on the type of normalization applied. Therefore, no suggestions of high temperature fluids (≈ 200°-250°C) circulating along the Infierno fault can be made for the first circulation event depositing luminescent calcite in clasts and rim calcite. Generally speaking, temperatures higher than 100°C for the first fluid circulation event along the Azufre fault are in line with the geothermal contribution highlighted by stable isotope signatures and with the up to 275°C temperature (at reservoir conditions) of geothermal fluids circulating through the area (Lopez et al., 1995). In the case of the Azufre fault system the high temperature (at least 100°C) of fluids depositing luminescent calcite derives from the proximity to the hydrothermal fluid heating source (the 7-9 km deep Tres Vírgenes feeding system, Macias and Jimenez, 2012, 2013; Avellán et al., 2018; Pellicioli et al., submitted, a). In the case of fluids circulating along the Infierno fault heating to a lower degree (temperatures of fault-related fluids up to

100°C) could have been provided by the nowadays quiescent (Garcia-Sánchez et al., 2019) La Reforma caldera complex.

6.7 Conclusions

The use of various multi-scale petrographic and geochemical techniques allowed obtaining novel results regarding the origin, characteristics and temperatures of fluids circulating along two of the most relevant regional structures running across the Tres Vírgenes active geothermal region, the Azufre and Infierno fault systems. This work also contributed to improve the hydrochemical characterization of the region and provided insights on the nature of Las Tres Vírgenes geothermal reservoir recharge mechanisms. The outcomes of this study set the basis for future applications of these multi-scale petrographic and geochemical techniques on other regional lineaments across the Tres Vírgenes area and to any other volcanic area of geothermal proven or prospective potential. Detailed results of this study can be summarized as follows:

a) A marine origin of fluids circulating along the Azufre and Infierno fault systems inferred by along-fault precipitated calcite phases is excluded based on negative $\delta^{13}C$ and $\delta^{18}O$ isotopic signatures, Y/Ho, Zr/Hf, Sm/Nd ratios, average ∑REE abundances and shale- and chondrite-normalized REY trends. These parameters rather support a mixed meteoric-hydrothermal (Azufre fault) to meteoric (Infierno fault) fluid origin, in agreement with the predominant meteoric (Holocene to Pleistocene fossil water) recharge of Las Tres Vírgenes geothermal reservoir stated by Portugal et al. (2000).

b) In addition to the presence or absence of a geothermal component, fluids circulating along regional faults across the Tres Vírgenes region display supplementary different characteristics, including rather distinct $\delta^{13}C$ values, calcite precipitation palaeotemperatures and Fe and Mn concentrations. A deeper and mixed hydrothermal-meteoric origin of reducing hotter fluids circulating along Azufre fault system was inferred, in agreement with the closer proximity of this fault system to the Tres Vírgenes feeding system, representing the heating source of hydrothermal fluids. A direct influence of palaeosoils-derived organic carbon on meteoric circulating fluids is instead suggested for the Infierno fault.

c) Multiple fluid circulation events depositing distinct calcite phases often under different temperature and redox conditions have been recognised both along the Azufre and Infierno fault systems. Reducing fluids precipitating luminescent replacive calcite on volcanic clasts (1) are followed by mixed meteoric-hydrothermal fluids precipitating non-luminescent replacive calcite on

volcanic clasts, mixed plagioclase-quartz-calcite veins, drusy vein calcite and ground mass microsparite (2) along the Azufre fault system, whilst a first Mn-rich reducing deep phreatic fluid precipitating luminescent calcite rims and calcite in within clasts (1) is followed by oxygenated fluids precipitating non-luminescent calcite in clasts and fibrous cement calcite phases (2) and calcite filling veins cross-cutting fibrous cement calcite (3) along the Infierno fault.

d) Surface to near-surface temperatures of fault-related fluids depositing calcite generally do not exceed 100°C, as derived from measured $\delta^{18}O$ on calcites and confirmed by field occurrence of clinotptilolite and (Ce/Ce*)sn, (Ce/Ce*)cn and (Eu/Eu*)sn and (Eu/Eu*)sn anomalies**.** Nevertheless, interesting insights regarding a change of redox conditions during fluid migration and a possibly higher than 100°C (≈200°-250°C) precipitation temperature for luminescent calcite phases (not properly isolated during stable isotope analyses) along the Azufre fault system are suggested by local variability of (Ce/Ce*)sn, (Ce/Ce*)cn and (Eu/Eu*)sn and (Eu/Eu*)cn anomalies.

6.8 Acknowledgements

This study benefited from CeMIE Geo project P15 of SENER-CONACyT to Josè Luis Macias and UNAM (Universidad National Autónoma de México, Instituto de Geofísica, Morelia, Michoacán, México) to support 2015-2017 field trips to Santa Rosalía-Tres Vírgenes, and from Italgas S.p.a. funds issued by former CNR-IDPA of Milan (now CNR-IGAG) to sponsor C. Pellicioli in her PhD research activity. We are thankful to UNAM also for managing logistic aspects of field trips, including employing local guides from UMA and Ecoturismo Borrego Cimarrón, Bonfil, B.C.S., who took care of people working in the field. Among UMA members, we are especially grateful to Francisco, for having led us to any site that could (and could not) be reached in the fastest way possible and for always patiently waiting for us to finish all of our measurements. Special thanks go to Josè Luis Macias, Laura García-Sánchez, Susana Osorio-Ocampo, Reyna-Marcela Lira-Beltran, Antonio Pola-Villaseñor, Pedro Martin Pacheco and Vincenzo Parisi for their support during fieldwork activity, post-field technical discussions and for hospitality in Morelia. Thanks also to Monica Dapiaggi, Elena Ferrari and Andrea Risplendente for their support during X-ray diffraction, IRMS and electron microprobe analyses and to Curzio Malinverno for thin section preparation.

6.9 References

Alibo, D.S., Nozaki, Y., 1999. Rare earth elements in seawater: particle association, shale-normalization, and Ce oxidation. Geochimica et Cosmochimica Acta, 63, 363-372.

Azmy, K., Brand, U., Sylvester, P., Gleeson, S. A., Logan, A., Bitner, M. A., 2011. Biogenic and abiogenic low-Mg calcite (bLMC and aLMC): Evaluation of seawater-REE composition, water masses and carbonate diagenesis. Chemical Geology, 280, 180-190.

Angelier, J., Colletta, B., Chorowicz, J., Ortlieb, L., Rangin, C., 1981. Fault tectonics of the Baja California Peninsula and the opening of the Sea of Cortez, Mexico. Journal of Structural Geology, *3*, 347-357.

Antayhua-Vera, Y., Lermo-Samaniego, J., Quintanar-Robles, L., Campos-Enríquez, O., 2015. Seismic activity and stress tensor inversion at Las Tres Vírgenes Volcanic and Geothermal Field (México). Journal of Volcanology and Geothermal Research, 305, 19-29.

Aquilina, L., Ladouche, B., Dörfliger, N., Seidel, J. L., Bakalowicz, M., Dupuy, C., Le Strat, P., 2002. Origin, evolution and residence time of saline thermal fluids (Balaruc springs, southern France): implications for fluid transfer across the continental shelf. Chemical Geology, 192, 1-21.

Arango-Galván, C., Prol-Ledesma, R. M., Torres-Vera, M. A., 2015. Geothermal prospects in the Baja California peninsula. Geothermics, 55, 39-57.

Aragón-Arreola, M., Morandi, M., Martín-Barajas, A., Delgado-Argote, L., González-Fernández, A., 2005. Structure of the rift basins in the central Gulf of California: Kinematic implications for oblique rifting. Tectonophysics, 409, 19-38.

Arthur, M., Anderson, T., Kaplan, I., Veizer, J., Land, L., 1983. Stable Isotopes in Sedimentary Geology, SEPM Short Course No 10. SEPM.

Avellán, D. R., Macías, J. L., Arce, J. L., Jiménez-Haro, A., Saucedo-Girón, R., Garduño-Monroy, V. H., Sosa-Ceballos, G., Bernal, J. P., Lopez-Loera, H., Cisneros, G., Layer, P. W., Garcia-Sanchez, L., Reyes-Aguston, G., Rocha, V.S., Rangel, E., 2018. Eruptive chronology and tectonic context of the late Pleistocene Tres Vírgenes volcanic complex, Baja California Sur (México). Journal of Volcanology and Geothermal Research, 360, 100-125.

Barbier, E., 2002. Geothermal energy technology and current status: an overview. Renewable and sustainable energy reviews, 6, 3-65.

Barker, S. L., Bennett, V. C., Cox, S. F., Norman, M. D., Gagan, M. K., 2009. Sm–Nd, Sr, C and O isotope systematics in hydrothermal calcite–fluorite veins: implications for fluid–rock reaction and geochronology. Chemical Geology, 268, 58-66.

Barnaby, R. J., Rimstidt, J. D., 1989. Redox conditions of calcite cementation interpreted from Mn and Fe contents of authigenic calcites. Geological Society of America Bulletin, 101, 795-804.

Barrat, J. A., Boulegue, J., Tiercelin, J. J., Lesourd, M., 2000. Strontium isotopes and rare-earth element geochemistry of hydrothermal carbonate deposits from Lake Tanganyika, East Africa. Geochimica et Cosmochimica Acta, 64, 287-298.

Bau, M., 1991. Rare-earth element mobility during hydrothermal and metamorphic fluid-rock interaction and the significance of the oxidation state of europium. Chemical Geology, 93, 219-230.

Bau, M., 1996. Controls on the fractionation of isovalent trace elements in magmatic and aqueous systems: evidence from Y/Ho, Zr/Hf, and lanthanide tetrad effect. Contributions to Mineralogy and Petrology, 123, 323-333.

Bau, M., Dulski, P., 1999. Comparing yttrium and rare earths in hydrothermal fluids from the Mid-Atlantic Ridge: implications for Y and REE behaviour during near-vent mixing and for the Y/Ho ratio of Proterozoic seawater. Chemical Geology, 155, 77-90.

Bau, M., Dulski, P. E. T. E. R., Möller, P., 1995. Yttrium and holmium in South Pacific seawater: vertical distribution and possible fractionation mechanisms. Oceanographic Literature Review, 11, 955.

Bau, M., Möller, P., 1992. Rare earth element fractionation in metamorphogenic hydrothermal calcite, magnesite and siderite. Mineralogy and Petrology, 45, 231-246.

Benedicto, A., Plagnes, V., Vergély, P., Flotté, N., Schultz, R. A., 2008. Fault and fluid interaction in a rifted margin: integrated study of calcite-sealed fault-related structures (southern Corinth margin). Geological Society, London, Special Publications, 299, 257-275.

Bignall, G., Rae, A., Rosenberg, M., 2010. Rationale for targeting fault versus formation-hosted permeability in high-temperature geothermal systems of the Taupo Volcanic Zone, New Zealand. In Proceedings of the World Geothermal Congress 2010, Bali, Indonesia, 25-29 April 2010, pp. 1-7.

Birkle, P., Marín, E. P., Pinti, D. L., Castro, M. C., 2016. Origin and evolution of geothermal fluids from Las Tres Vírgenes and Cerro Prieto fields, Mexico–Co-genetic volcanic activity and paleoclimatic constraints. Applied geochemistry, 65, 36-53.

Boles, J. R., Grivetti, M., 2000. Calcite cementation along the Refugio/Carneros fault, Coastal California: a link between deformation, fluid movement and fluid–rock interaction at a basin margin. Journal of Geochemical Exploration, 69, 313-316.

Brown, G., 1982. Crystal structures of clay minerals and their X-ray identification (Vol. 5). The Mineralogical Society of Great Britain and Ireland.

Budd, D. A., Hammes, U., Ward, W. B., 2000. Cathodoluminescence in calcite cements: new insights on Pb and Zn sensitizing, Mn activation, and Fe quenching at low trace-element concentrations. Journal of Sedimentary Research, 70, 217-226.

Caine, J. S., Evans, J. P., Forster, C. B., 1996. Fault zone architecture and permeability structure. Geology, 24, 1025-1028.

Carroll, D., 1970. Clay minerals: a guide to their X-ray identification (Vol. 126). Printed by the Geological Society of America.

Chiodini, G., Caliro, S., Cardellini, C., Avino, R., Granieri, D., Schmidt, A., 2008. Carbon isotopic composition of soil CO_2 efflux, a powerful method to discriminate different sources feeding soil CO2 degassing in volcanic-hydrothermal areas. Earth and Planetary Science Letters, 274, 372-379.

Conly, A. G., Beaudoin, G., Scott, S. D., 2006. Isotopic constraints on fluid evolution and precipitation mechanisms for the Boléo Cu–Co–Zn district, Mexico. Mineralium Deposita, 41, 127.

Coplen, T. B., Kendall, C., Hopple, J., 1983. Intercomparison of stable isotope reference samples. Nature 302, 236–238.

Coplen, T. B., 2007. Calibration of the calcite–water oxygen-isotope geothermometer at Devils Hole, Nevada, a natural laboratory. Geochimica et Cosmochimica Acta, 71, 3948-3957.

Costa, A., 2006. Permeability-porosity relationship: A reexamination of the Kozeny-Carman equation based on a fractal pore-space geometry assumption. Geophysical research letters, 33.

Craig, H., 1965. Measurement of oxygen isotope paleotemperatures, p. 162–182. Tongiorgi, E. ed., Stable Isotopes in Oceanographic Studies and Paleotemperatures. Consiglio Nazionale Delle Ricerche, Spoleto, Italy.

David, K., Schiano, P., Allegre, C.J., 2000. Assessment of the Zr/Hf fractionation in oceanic basalts and continental materials during petrogenetic processes. Earth and Planetary Science Letters, 178, 285-301.

Delaney, M. L., Boyle, E.A., 1983. Uranium and thorium isotope concentrations in foraminiferal calcite. Earth and Planetary Science Letters, 62, 258-262.

Della Porta, G., Webb, G. E., McDonald, I., 2015. REE patterns of microbial carbonate and cements from Sinemurian (Lower Jurassic) siliceous sponge mounds (Djebel Bou Dahar, High Atlas, Morocco). Chemical Geology, 400, 65-86.

Eberl, D.D., 2003. User guide to RockJock-A program for determining quantitative mineralogy from X-ray diffraction data, No. 2003-78. US Geological Survey.

Elderfield, H., 1988. The oceanic chemistry of the rare-earth elements. Philosophical Transactions of the Royal Society of London. Series A, Mathematical and Physical Sciences, 325, 105-126.

Elderfield, H., Sholkovitz, E.T., 1987. Rare earth elements in the pore waters of reducing nearshore sediments. Earth and Planetary Science Letters, 82, 280-288.

Elderfield, H., Upstill-Goddard, R., Sholkovitz, E. R., 1990. The rare earth elements in rivers, estuaries, and coastal seas and their significance to the composition of ocean waters. Geochimica et Cosmochimica Acta, 54, 971-991.

Epstein, S., Mayeda, T., 1953. Variation of O-18 content of water from natural sources. Geochim. Cosmochim. Acta 4, 213–224.

Evensen, N. M., Hamilton, P. J., O'nions, R.K., 1978. Rare-earth abundances in chondritic meteorites. Geochimica et Cosmochimica Acta, 42, 1199-1212.

Ferrari, L., López-Martínez, M., Orozco-Esquivel, T., Bryan, S. E., Duque-Trujillo, J., Lonsdale, P., Solari, L., 2013. Late Oligocene to Middle Miocene rifting and synextensional magmatism in the southwestern Sierra Madre Occidental, Mexico: The beginning of the Gulf of California rift. Geosphere, 9, 1161-1200.

Ferrari, L., Orozco-Esquivel, T., Bryan, S. E., Lopez-Martinez, M., Silva-Fragoso, A., 2018. Cenozoic magmatism and extension in western Mexico: Linking the Sierra Madre Occidental silicic large igneous province and the Comondú Group with the Gulf of California rift. Earth-Science Reviews, 183, 115-152.

Fleet, A. J., 1984. Aqueous and sedimentary geochemistry of the rare earth elements. Developments in Geochemistry, Vol. 2, pp. 343-373, Elsevier.

Frank, J. R., Carpenter, A. B., Oglesby, T.W., 1982,. Cathodoluminescence and composition of calcite cement in the Taum Sauk Limestone (Upper Cambrian), southeast Missouri. Journal of Sedimentary Research, 52, 631-638.

Freeman, K. H., Hayes, J. M., Trendel, J. M., Albrecht, P., 1990. Evidence from carbon isotope measurements for diverse origins of sedimentary hydrocarbons. Nature, 343, 254.

Friedman I. and O'Neil J.R., 1977. Compilation of stable isotope fractionation: Factors of geochemical interest. In Data of Geochemistry 6th ed. Geology Survey Prof. Paper, Vol. 440, ed. M. Fleischer. USGS.

García-Sánchez, L., Macías, J.L., Sulpizio, R., Osorio-Ocampo, L.S., Pellicioli, C., Pola, A., Avellán, D., Cisneros, G., García, F., Ocampo-Díaz, Y.Z.E, Lira-Beltran, R.M., Saucedo, R., Sánchez-Nuñez, J.M., Arce, J.L., Corona-Chávez, P., Reyes-Augustin, G., Cardona, M., Layer, P.W., Benowitz, J., Solari, L., Groppelli, G., 2019. Geology of La Reforma caldera complex, Baja California, Mexico. Journal of Maps, 15, 487-498.

Garduño-Monroy, V. H., Vargas-Ledezma, H., Campos-Enriquez, J.O., 1993. Preliminary geologic studies of Sierra El Aguajito (Baja California, Mexico): a resurgent-type caldera. Journal of Volcanology and Geothermal Research, 59, 47-58.

Gastil, R. G., Phillips, R. P., Allison, E.C., 1975. Reconnaissance geology of the state of Baja California (Vol. 140). Geological Society of America.

Gifkins, C. C., Herrmann, W., Large, R. R., 2005. Altered volcanic rocks: A guide to description and interpretation. Published by the Centre for Ore Deposit Research, University of Tasmania.

Gutiérrez-Negrín, L. C., Maya-González, R., Quijano-León, J.L., 2010. Current status of geothermics in Mexico. In Proceedings World Geothermal Congress 2010, Bali, Indonesia, 25-29 April 2010, pp. 25-29.

Habermann, D., Neuser, R. D., Richter, D. K., 1998. Low limit of Mn2+-activated cathodoluminescence of calcite: state of the art. Sedimentary Geology, 116, 13-24.

Haley, B. A., Klinkhammer, G. P., McManus, J., 2004. Rare earth elements in pore waters of marine sediments. Geochimica et Cosmochimica Acta, 68, 1265-1279.

Hanawalt, J. D., Rinn, H. W., Frevel, L.K., 1938. Chemical analysis by X-ray diffraction. Industrial & Engineering Chemistry Analytical Edition, 10, 457-512.

Harris, W., White, G. N., Ulery, A. L., Drees, L.R., 2008. X-ray diffraction techniques for soil mineral identification. Methods of soil analysis. Part, 5, 81-115.

Hemming, N. G., Meyers, W. J., Grams, J. C., 1989. Cathodoluminescence in diagenetic calcites; the roles of Fe and Mn as deduced from electron probe and spectrophotometric measurements. Journal of sedimentary research, 59, 404-411.

Henley, R.W., Truesdell, A.H., Barton Jr., P.B., 1984. Fluid–Mineral Equilibria in Hydrothermal Systems. Reviews in Economic Geology 1, 267 pp.

Hiatt, E. E., Pufahl, P. K., 2014. Cathodoluminescence petrography of carbonate rocks: a review of applications for understanding diagenesis, reservoir quality and pore system evolution. Short Course, 45, 75-96.

Hinojosa, E. T., Verma, M. P., Partida, E. G., 2005. Geochemical Characteristics of Reservoir Fluids in the Las Tres Virgenes, BCS, Mexico. In Proceedings of World Geothermal Congress 2005 Antalya, Turkey, 24–29 April 2005, p. 11.

Hoefs, J., 1980. Stable isotope geochemistry (Vol. 9, No. 1980). Berlin: springer.

Hopf, S., Freeston, D. H., Browne, P. R. L., Scott, G. L., 1991. A comparison of REE trends in geothermal/epithermal systems—Modern and ancient. In Proceedings of the 13th New Zealand geothermal workshop, University of Auckland, 1991, Vol. 100, pp. 75-80.

Hudson, J. D., Anderson, T.F., 1989. Ocean temperatures and isotopic compositions through time. Transactions of the Royal Society of Edinburgh: Earth Sciences, 80, 183-192

Iijima, A., 1980. Geology of natural zeolites and zeolitic rocks. Pure and Applied Chemistry, 52, 2115-2130. Pergamon Press Ltd., 1980, printed in Great Britain.

Kamber, B. S., Greig, A., Collerson, K. D., 2005. A new estimate for the composition of weathered young upper continental crust from alluvial sediments, Queensland, Australia. Geochimica et Cosmochimica Acta, 69, 1041-1058.

Kim, S.T., O'Neil, J.R., 1997. Equilibrium and nonequilibrium oxygen isotope effects in synthetic carbonates. Geochimica et Cosmochimica Acta 61, 3461–3475.

Kolditz, O., Clauser, C., 1998. Numerical simulation of flow and heat transfer in fractured crystalline rocks: application to the hot dry rock site in Rosemanowes (UK). Geothermics, 27, 1-23.

Kump, L.R., Arthur, M. A., 1999. Interpreting carbon-isotope excursions: carbonates and organic matter. Chemical Geology, 161, 181-198.

Lajtha, K., Michener, R. H., 1994. Stable Isotopes in Ecology and Environmental Science. Blackwell publishing Ltd, printed in Singapore.

Lawrence, M. G., Greig, A., Collerson, K. D., Kamber, B.S., 2006. Rare earth element and yttrium variability in South East Queensland waterways. Aquatic Geochemistry, 12, 39-72.

Lewicki, J. L., Evans, W. C., Hilley, G. E., Sorey, M. L., Rogie, J. D., Brantley, S. L., 2003. Shallow soil CO2 flow along the San Andreas and Calaveras faults, California. Journal of Geophysical Research: Solid Earth, 108.

Liotta, D., Ruggieri, G., Brogi, A., Fulignati, P., Dini, A., Nardini, I., 2010. Migration of geothermal fluids in extensional terrains: the ore deposits of the Boccheggiano-Montieri area (southern Tuscany, Italy). International Journal of Earth Sciences, 99, 623-644.

Liu, Y. G., Miah, M. R. U., Schmitt, R. A., 1988. Cerium: a chemical tracer for paleo-oceanic redox conditions. Geochimica et Cosmochimica Acta, 52, 1361-1371.

López, A. C., Casarrubias, U. Z. Z., Leal, R., 1993. Estudio geológico regional de la zona geotérmica de Las Tres Vírgenes. Report Interno OGL-BC-002/93, GPG-CFE.

López, H. A., Robin, C., Vincent, O., 1989. Estudio geoquímico, mineralógico y edades radiométricas de la zona de Las Tres Vírgenes BCS Implicaciones geotérmicas. Rep. Interno 5/89, GPG-*CFE*.

López, H. A., García, G. H., Arellano, F. G., 1995. Geothermal exploration at Las Tres Vírgenes, BCS, Mexico. In Proceedings of the 1995 World Geothermal Congress, Florence, Italy, 18-31 May 1995, pp. 707-712.

Machel, H. G., 1985. Cathodoluminescence in calcite and dolomite and its chemical interpretation. Volume 12, number 4. Published by Geoscience Canada in 1985.

Macías, J.L., Jiménez, S., 2012. Actualización vulcanológica del complejo de Las Tres Vírgenes, BCS. Memorias del XX Congreso Anual de la Asociación Geotérmica Mexicana, Morelia, Mich., México, 26-28 September 2012.

Macías, J.L., Jiménez, S., 2013. Estudio de Estratigrafía y Geología del Complejo Volcánico Tres Vírgenes. B.C.S. Geotermia 26, 14–23.

Maskenskaya, O. M., Drake, H., Åström, M. E., 2013. Geochemistry of calcite veins: records of fluid mixing and fluid- rock interaction. Procedia Earth and Planetary Science, 7, 566-569.

Mason, R. A., Mariano, A. N., 1990. Cathodoluminescence activation in manganese-bearing and rare earth-bearing synthetic calcites. Chemical Geology, 88, 191-206.

McCrea J. M., 1950. On the isotopic chemistry of carbonates and a paleotemperatures scale. Journal of Chemical Physics, 18, 163–171.

McLean, H., 1988. Reconnaissance geologic map of the Loreto and part of the San Javier quadrangles, Baja California Sur, Mexico. U.S. Geological Survey Miscellaneous Field Studies Map, Report No. MF-2000, p. 10, 1 mapa, escala 1:50,000.

McLennan, S. M., 2001. Relationships between the trace element composition of sedimentary rocks and upper continental crust. Geochemistry, Geophysics, Geosystems, 2, 4, 1-24.

Minissale, A., Kerrick, D. M., Magro, G., Murrell, M. T., Paladini, M., Rihs, S., Sturchio, N.C., Tassi, F. Vaselli, O., 2002. Geochemistry of Quaternary travertines in the region north of Rome (Italy): structural, hydrologic and paleoclimatic implications. Earth and Planetary Science Letters, 203, 709-728.

Möller, P., 2000. Rare earth elements and yttrium as geochemical indicators of the source of mineral and thermal waters. In Hydrogeology of crystalline rocks, pp. 227-246. Springer, Dordrecht.

Möller, P., 2002. Rare earth elements and yttrium in geothermal fluids. Water Science and Technology Library, 40, 97-125.

Möller, P., Dulski, P., Morteani, G., 2003. Partitioning of rare earth elements, yttrium, and some major elements among source rocks, liquid and vapor of Larderello-Travale geothermal field, Tuscany (Central Italy). Geochimica et Cosmochimica Acta, 67, 171-183.

Möller, P., Dulski, P., Savascin, Y., Conrad, M., 2004. Rare earth elements, yttrium and Pb isotope ratios in thermal spring and well waters of West Anatolia, Turkey: a hydrochemical study of their origin. Chemical Geology, 206, 97-118.

Morad, S., Al-Aasm, I. S., Sirat, M., Sattar, M. M., 2010. Vein calcite in cretaceous carbonate reservoirs of Abu Dhabi: Record of origin of fluids and diagenetic conditions. Journal of Geochemical Exploration, 106, 156-170.

Mulitza S., Donner B., Fischer G., Paul A., Patzold J., Ruhlemann C. Segl M., 2003. The South Atlantic oxygen isotope record of planktic foraminifera. In The South Atlantic in the Late Quaternary: Reconstruction of Material budgets and Current Systems, eds. G. Wefer, S. Mulitza and V. Ratmeyer. Springer-Verlag, Berlin, pp. 121–142.

Nava-Sánchez, E.H., Gorsline, D.S., Molina-Cruz, A., 2001. The Baja California peninsula borderland: structural and sedimentological characteristics. Sedimentary Geology, 144, 63-82.

Norman, M. D., Pearson, N. J., Sharma, A., Griffin, W. L., 1996. Quantitative analysis of trace elements in geological materials by laser ablation ICPMS: instrumental operating conditions and calibration values of NIST glasses. Geostandards Newsletter, 20, 247-261.

Nozaki, Y., Alibo, D. S., 2003. Importance of vertical geochemical processes in controlling the oceanic profiles of dissolved rare earth elements in the northeastern Indian Ocean. Earth and Planetary Science Letters, 205, 155-172.

Ogihara, S., 2000. Composition of clinoptilolite formed from volcanic glass during burial diagenesis. Clays and Clay Minerals, 48, 106-110.

O'Neil J. R., Clayton R. N. Mayeda T. K., 1969. Oxygen isotope fractionation in divalent metal carbonates. Journal of Chemical Physics, 51, 5547–5558.

O'Sullivan, M.J., Pruess, K., Lippmann, M.J., 2001. State of the art of geothermal reservoir simulation. Geothermics, 30, 395-429.

Pagel, M., Barbin, V., Blanc, P., Ohnenstetter, D., 2000. Cathodoluminescence in geosciences: an introduction. In Cathodoluminescence in Geosciences (pp. 1-21). Springer, Berlin, Heidelberg.

Panichi, C., Tongiorgi, E., 1976. Carbon isotopic composition of CO_2 from springs, fumaroles, mofettes and travertines of central and southern Italy: a preliminary prospection method of geothermal area. Proceedings 2nd UN Symosium on the Develop and Use of Geothermal Energy, 20– 29 May 1975, San Francisco, U.S.A., pp. 815– 825.

Paquette, J., Reeder, R.J., 1990. New type of compositional zoning in calcite: Insights into crystal-growth mechanisms. Geology, 18, 1244.

Paul, D., Skrzypek, G., Fórizs, I., 2007. Normalization of measured stable isotopic compositions to isotope reference scales–a review. Rapid Communications in Mass Spectrometry: An International Journal Devoted to the Rapid Dissemination of Up-to-the-Minute Research in Mass Spectrometry, 21, 3006-3014.

Pearce, N. J., Perkins, W. T., Westgate, J. A., Gorton, M. P., Jackson, S. E., Neal, C. R., Chenery, S. P., 1997. A compilation of new and published major and trace element data for NIST SRM 610 and NIST SRM 612 glass reference materials. Geostandards Newsletter, 21, 115-144.

Pellicioli, C., Groppelli, G., Macías, J.L., Sulpizio, R., submitted (a). Control of regional structures on the evolution of Pleistocene La Reforma caldera complex: implications on caldera collapse and resurgence. Submitted to the GSA Bulletin in June 2019.

Pellicioli, C., Zucali, M., Groppelli, G., submitted (b). Kinematics and deformation patterns from micro-structural and image analysis on fault-rock samples in volcanic regions: the example of the Tres Vírgenes active geothermal region, Baja California, Mexico. Submitted to the Journal of Structural Geology in August 2019.

Périnet, G., 1964. Determination par diffraction X de la temperature de cuisson dun ossement calcine. Application au materiel prehistorique. Comptes Rendus Hebdomadaires Des Seances De L. Academie Des Sciences, 258, 4115.

Pili, E., Poitrasson, F., Gratier, J. P., 2002. Carbon–oxygen isotope and trace element constraints on how fluids percolate faulted limestones from the San Andreas Fault system: partitioning of fluid sources and pathways. Chemical Geology, 190, 231-250.

Piper, D. Z., and Bau, M., 2013. Normalized rare earth elements in water, sediments, and wine: identifying sources and environmental redox conditions. American Journal of Analytical Chemistry, 4, 69-83.

Portugal, E., Barragan, R.M., Bautista, J., 1998a. Estudio isotopico de fluidos de pozos productores, de reinyeccion y manantiales del campo geotermico de Las Tres Vırgenes, B.C.S. Instituto de Investigaciones Electricas, Cuernavaca, Report IIE/11/10933/I01/F, 35pp.

Portugal, E., Birkle, P., Tello, E., Tello, M., 2000. Hydrochemical–isotopic and hydrogeological conceptual model of the Las Tres Vırgenes geothermal field, Baja California Sur, México. Journal of Volcanology and Geothermal Research, 101, 223-244.

Richter, D. K., Götte, T., Götze, J., Neuser, R.D., 2003. Progress in application of cathodoluminescence (CL) in sedimentary petrology. Mineralogy and Petrology, 79, 127-166.

Rocholl, A. B., Simon, K., Jochum, K. P., Bruhn, F., Gehann, R., Kramar, U., Luecke, W., Molazan, M., Pernicka, E., Seufert, M., Stummeier, J., 1997. Chemical Characterisation of NIST Silicate Glass Certified Reference Material SRM 610 by ICP-MS, TIMS, LIMS, SSMS, INAA, AAS and PIXE. Geostandards Newsletter, 21, 101-114.

Romanek, C. S., Grossman, E. L., Morse, J. W., 1992. Carbon isotopic fractionation in synthetic aragonite and calcite: effects of temperature and precipitation rate. Geochimica et cosmochimica acta, 56, 419-430.

Savard, M. M., Veizer, J., Hinton, R., 1995. Cathodoluminescene at low Fe and Mn concentrations; a SIMS study of zones in natural calcites. Journal of Sedimentary Research, 65, 208-213.

Schmidt, E. K., 1975. Plate tectonics, volcanic petrology, and ore formation in the Santa Rosalía area, Baja California, Mexico. Master Degree Thesis, Department of Geosciences, University of Arizona, 1975.

Schmitt, A. K., Stockli, D. F., Hausback, B. P., 2006. Eruption and magma crystallization ages of Las Tres Vírgenes (Baja California) constrained by combined 230Th/238U and (U–Th)/He dating of zircon. Journal of Volcanology and Geothermal Research, 158, 281-295.

Sharp Z., 2007. Principles of Stable Isotope Geochemistry. Pearson Prentice Hall, Upper Saddle River, New Jersey.

Shields, G. A., Webb, G. E., 2004. Has the REE composition of seawater changed over geological time?. Chemical Geology, 204, 103-107.

Sibson, R.H., 1981. Fluid flow accompanying faulting: field evidence and models. Earthquake prediction: an international review, Simpson and Richards ed., 4, 593-603.

Schwarcz, H. P., Latham, A.G., 1989. Dirty calcites 1. Uranium-series dating of contaminated calcite using leachates alone. Chemical Geology: Isotope Geoscience section, 80, 35-43.

Swart, P. K., 2015. The geochemistry of carbonate diagenesis: The past, present and future. Sedimentology, 62, 1233-1304.

Sweatman, T. R., Long, J.V.P., 1969. Quantitative electron-probe microanalysis of rock-forming minerals. Journal of Petrology, 10, 332-379.

Tarutani T., Clayton R. N., Mayeda T. K., 1969. The effect of polymorphism and magnesium substitution on oxygen isotope fractionation between calcium carbonate and water. Geochimica et Cosmochimica Acta 33, 987–996.

Taylor, S. R., McLennan, S. M., 1985. The continental crust: its composition and evolution. Blackwell Scientific Publications, Oxford, 1985, 312+XV pp.

Travé, A., Calvet, F., Soler, A., Labaume, P., 1998. Fracturing and fluid migration during Palaeogene compression and Neogene extension in the Catalan Coastal Ranges, Spain. Sedimentology, 45, 1063-1082.

Tucker, M.E., Wright, V.P., 1990. Carbonate Sedimentology. Blackwell Science. 482 pp.

Truesdell, A. H., Hulston, J. R., 1980. Isotopic evidence on environments of geothermal systems. In Handbook of environmental isotope geochemistry. Vol. 1, published in Netherlands.

Umhoefer, P. J., Dorsey, R. J., Willsey, S., Mayer, L., Renne, P., 2001. Stratigraphy and geochronology of the Comondu Group near Loreto, Baja California Sur, Mexico. Sedimentary Geology, 144, 125-147.

Uysal, I. T., Golding, S. D., 2003. Rare earth element fractionation in authigenic illite–smectite from Late Permian clastic rocks, Bowen Basin, Australia: implications for physico-chemical environments of fluids during illitization. Chemical Geology, 193, 167-179.

Uysal, I. T., Zhao, J. X., Golding, S. D., Lawrence, M. G., Glikson, M., Collerson, K. D., 2007. Sm–Nd dating and rare- earth element tracing of calcite: implications for fluid-flow events in the Bowen Basin, Australia. Chemical Geology, 238, 63-71.

Uysal, I. T., Feng, Y. X., Zhao, J. X., Isik, V., Nuriel, P., Golding, S. D., 2009. Hydrothermal CO_2 degassing in seismically active zones during the late Quaternary. Chemical Geology, 265, 442-454.

Uysal, I. T., Feng, Y. X., Zhao, J. X., Bolhar, R., Işik, V., Baublys, K. A., Yago, A., Golding, S. D., 2011. Seismic cycles recorded in late Quaternary calcite veins: geochronological, geochemical and microstructural evidence. Earth and Planetary Science Letters, 303, 84-96.

van Achterbergh, E., Ryan, C. G., and Griffin, W. L., 2001. GLITTER user's manual: on-line interactive data reduction for the LA-ICP-MS microprobe. GEMOC Version, 4, 72.

Verma, S. P., Pandarinath, K., Santoyo, E., González-Partida, E., Torres-Alvarado, I. S., Tello-Hinojosa, E., 2006. Fluid chemistry and temperatures prior to exploitation at the Las Tres Vírgenes geothermal field, Mexico. Geothermics, 35, 156-180.

Veizer, J., Hoefs, J., 1976. The nature of O18/O16 and C13/C12 secular trends in sedimentary carbonate rocks. Geochimica et Cosmochimica Acta, 40, 1387-1395.

Wilson, S. A., 1997. The collection, preparation, and testing of USGS reference material BCR-2, Columbia River. Basalt US Geological Survey Open-File Report.

Wong, V., Munguía, L., 2006. Seismicity, focal mechanisms, and stress distribution in the Tres Vírgenes volcanic and geothermal region, Baja California Sur, Mexico. Geofísica internacional, 45, 23-37.

Yamaguchi, A., Cox, S. F., Kimura, G., Okamoto, S. Y., 2011. Dynamic changes in fluid redox state associated with episodic fault rupture along a megasplay fault in a subduction zone. Earth and Planetary Science Letters, 302(3-4), 369-377.

Zanchi, A., 1994. The opening of the Gulf of California near Loreto, Baja California, Mexico: from basin and range extension to transtensional tectonics. Journal of Structural Geology, 16, 1619-1639.

Zhang, J., Amakawa, H., Nozaki, Y., 1994. The comparative behaviors of yttrium and lanthanides in the seawater of the North Pacific. Geophysical Research Letters, 21, 2677-2680.

Zhang, J., Nozaki, Y., 1996. Rare earth elements and yttrium in seawater: ICP-MS determinations in the East Caroline, Coral Sea, and South Fiji basins of the western South Pacific Ocean. Geochimica et Cosmochimica Acta, 60, 4631-4644.

Zhang, J., Nozaki, Y., 1998. Behavior of rare earth elements in seawater at the ocean margin: a study along the slopes of the Sagami and Nankai troughs near Japan. Geochimica et Cosmochimica Acta, 62, 1307-1317.

Zhang, X., Sanderson, D. J., 1996. Numerical modelling of the effects of fault slip on fluid flow around extensional faults. Journal of Structural Geology, 18, 109-119.

6.10 Appendix

Table 6.10 Complete set of electron microprobe analysis results on sample BC-C24.

	Major elements mass abundance from WDS analysis (ppm)													
Analysis point	**Na**	**Cl**	**Mn**	**K**	**Mg**	**Si**	**Sr**	**Fe**	**Ca**	**Al**	**Ti**	**Ba**	**O**	**composition**
1	0	0	111	36	1518	262	0	0	563900	493	0	0	0	calcite
2	0	0	6641	16	4804	169	255	0	566200	18	153	0	0	calcite
3	135	25	589	0	2847	128	507	0	560200	320	844	0	0	calcite
4	0	94	906	90	943	15	1264	0	545500	90	123	456	0	calcite
5	0	95	5888	0	5366	26	2159	0	568100	209	444	0	0	calcite
6	0	174	0	0	6510	275	1143	168	541200	0	0	605	0	calcite
7	186	39	0	0	1287	100	0	0	571900	90	0	642	0	calcite
8	377	0	162	0	654	326	2405	4	549700	187	0	0	0	calcite
9	225	0	928	0	1797	105	0	798	539700	0	384	0	0	calcite
10	0	134	317	0	4395	176	0	65	567000	40	0	0	0	calcite
11	0	0	0	12	2212	790	0	0	542300	3102	0	229	0	calcite
12	199	203	0	54	1574	366	758	560	541600	181	430	0	0	calcite
13	32	163	0	0	3835	627	0	181	555600	36	0	769	0	calcite
14	0	40	0	34	1219	330	1517	0	546600	113	138	535	0	calcite
15	186	109	0	0	2783	305	0	0	561200	0	0	567	0	calcite
16	226	119	4905	0	1424	0	634	0	563600	0	383	254	0	calcite
17	97	0	391	79	399	281	0	353	565000	201	276	83	0	calcite
18	81	0	8	0	1485	355	0	240	561100	0	323	381	0	calcite
19	0	0	4251	34	2491	0	379	0	546100	0	0	386	0	calcite
20	0	114	0	81	311	272	0	0	551800	0	92	289	0	calcite
21	0	0	4901	0	1024	436	0	259	558100	56	92	0	0	calcite
22	62	0	0	59	1286	0	0	0	551700	260	169	36	0	calcite
23	81	0	0	4	4390	0	0	921	540800	54	0	0	0	calcite
24	49	148	37	35	2073	228	0	158	559400	0	476	457	0	calcite

25	283	0	0	66	1774	173	0	366	549100	0	139	21	0	calcite
26	315	139	155	135	1973	338	0	393	560500	131	0	0	0	calcite
27	26	50	494	35	4906	557	380	0	539500	10	0	151	0	calcite
28	260	138	81	35	1043	0	0	181	538200	0	0	716	0	calcite
29	646	184	0	26	8260	510	0	141	547000	0	0	271	0	calcite
30	0	40	162	8	2880	929	1	10	539500	372	323	146	0	calcite
31	167	198	280	30	2229	43	0	0	541300	38	77	436	0	calcite
32	0	69	0	0	1951	0	0	0	570000	127	0	555	0	calcite
33	254	39	0	0	1862	7	0	29	546900	346	0	0	0	calcite
34	135	45	0	38	1076	236	507	9	567200	137	0	176	0	calcite
35	0	0	450	48	2673	118	0	302	542300	40	0	335	0	calcite
36	186	119	96	0	1686	0	0	0	543900	0	169	166	0	calcite
37	9	5	125	0	7876	288	1144	0	552200	501	0	0	0	calcite
38	152	0	0	0	2439	124	0	0	544200	0	0	119	0	calcite
39	242	188	191	0	3359	200	20	0	563900	9	108	398	0	calcite
40	0	20	420	114	4951	533	634	60	551900	259	15	0	0	calcite
41	0	0	0	0	1763	241	506	161	563200	0	169	342	0	calcite
42	0	0	37	155	3202	0	0	0	553500	137	0	99	0	calcite
43	0	124	0	0	1152	211	1517	7	563500	54	0	0	0	calcite
44	0	0	0	161	6500	210	0	0	552300	0	0	328	0	calcite
45	353	0	0	62	4323	457	0	0	551800	54	399	381	0	calcite
46	0	25	177	0	2650	90	761	0	566400	215	292	401	0	calcite
47	176	69	0	35	3991	73	0	283	544600	80	215	591	0	calcite
48	0	65	37	0	5325	129	252	0	545800	42	0	0	0	calcite
49	324	0	8	43	2130	31	253	0	556100	0	230	94	0	calcite

Table 6.11 Complete set of electron microprobe analysis results on sample BC-C14.

Major elements mass abundance from WDS analysis (ppm)

Analysis point	Na	Cl	Mn	K	Mg	Si	Sr	Fe	Ca	Al	Ti	Ba	O	composition
1	49	228	0	22	5107	0	1777	142	573100	60	0	215	0	calcite
2	126	44	0	0	1497	218	0	164	569500	0	0	209	0	calcite

3	600	0	0	0	2885	115	0	219	566000	137	0	516	0	calcite
4	0	139	133	5	4020	113	128	0	544800	368	0	402	0	calcite
5	0	178	251	3	5026	541	380	129	566300	293	338	0	0	calcite
6	131	0	133	19	1807	0	0	126	574000	0	0	0	0	calcite
7	0	94	0	0	2859	0	0	539	547200	0	31	0	0	calcite
8	195	0	221	9	4302	238	379	0	552100	0	0	897	0	calcite
10	0	0	258	65	4572	732	760	203	543600	317	62	0	0	calcite
11	459	315	0	95	14922	9643	126	565	520400	1884	0	0	0	calcite
14	0	65	162	54	6517	2387	0	628	538600	375	461	2	0	calcite
15	0	20	0	5	5106	175	759	620	567000	143	522	213	0	calcite
16	543	32	324	604	66400	96500	0	1638	390700	15107	242	359	0	silicate+calcite
17	865	196	649	175	84000	21051	0	359	455300	3951	501	67	0	silicate+calcite
19	0	264	0	207	5029	10296	633	2421	540000	2853	505	365	0	calcite
20	703	1039	420	398	89200	38300	1857	2189	406800	6494	0	452	0	silicate+calcite
21	323	180	74	107	9297	7938	255	1147	529700	1467	751	765	0	calcite
22	83	95	0	105	6904	2841	1142	647	546800	385	0	131	0	calcite
23	0	0	251	3	4919	490	0	60	536400	0	0	186	0	calcite
24	94	35	243	85	8694	830	887	0	565200	0	61	367	0	calcite
25	571	89	184	117	9171	3741	0	495	554500	613	521	427	0	calcite
26	0	0	0	212	2894	554	0	734	550700	76	138	0	0	calcite
27	0	114	0	240	5673	5289	0	1480	547500	1201	138	0	0	calcite
28	74	119	0	16	7911	100	0	266	552500	0	0	0	0	calcite
29	599	0	96	448	44200	21400	258	749	489100	4040	168	815	0	silicate+calcite
30	373	105	560	61	15118	14516	383	114	524700	2574	490	255	0	calcite
31	0	0	376	82	6052	13549	0	599	539300	2547	0	0	0	calcite
32	541	0	140	848	3604	7082	0	166	548200	2946	0	633	0	calcite
33	318	0	280	150	7020	423	0	266	550300	0	0	0	0	calcite
34	0	54	0	0	4817	101	0	0	557700	171	445	360	0	calcite
35	174	0	280	256	20300	15119	639	631	531700	2842	122	0	0	calcite
36	925	197	398	248	93400	67500	1065	3064	393500	13659	0	214	0	silicate+calcite
37	408	176	88	181	24100	17499	384	466	521800	3635	92	97	0	calcite
38	336	104	66	0	4489	253	1016	111	564700	28	630	226	0	calcite
39	102	51	656	123	34700	24800	2581	1305	494600	4928	274	0	0	calcite

40	960	238	449	0	89300	9543	1723	887	448400	1480	0	174	0	silicate+calcite
41	1061	1036	0	4	93400	27800	789	1444	398300	4819	0	338	0	silicate+calcite
42	1258	252	663	67	78300	11019	394	310	469400	2184	0	367	0	silicate+calcite
43	813	265	597	0	63800	10192	260	353	492800	1721	152	694	0	silicate+calcite
44	98	0	0	158	5797	1975	125	70	541900	662	261	4	0	calcite
45	369	61	221	3695	14919	33200	768	3666	504500	8921	473	358	0	calcite
46	308	153	118	0	2160	158	0	0	559600	0	0	22	0	calcite

Chapter 7

Paper V

Determination of porosity and permeability of undeformed and faulted volcanic rocks and related challenges: a case study on the Tres Vírgenes geothermal region (Baja California, Mexico)

C. Pellicioli [a, b], M. Zucali [a, c], N. Fusi [d], R. Castellanza [d], G.B. Crosta [d] and G. Groppelli [b].

[a] Dipartimento di Scienze della Terra "Ardito Desio", Università degli Studi di Milano, Milano, Italia;
[b] C.N.R. - Istituto di Geologia Ambientale e Geoingegneria– sezione di Milano, Milano, Italia;
[c] Department of Earth and Atmospheric Sciences, University of Houston, Texas-USA;
[d] Dipartimento di Scienze dell'Ambiente e della Terra, Università degli Studi di Milano-Bicocca, Milano, Italia.

SUBMITTED TO THE ENGINEERING GEOLOGY JOURNAL IN SEPTEMBER 2019,
REF: MANUSCRIPT NUMBER ENGEO_2019_1637.

Sample collection in the field: ***C. Pellicioli.***

Sample preparation and laboratory tests (triaxial tests and X-ray computerized tomography): ***C. Pellicioli*** under the supervision of *N. Fusi*.

Data processing and results interpretation: ***C. Pellicioli*** under the supervision of *M. Zucali, R. Castellanza, G.B. Crosta*.

PhD tutoring: *G. Groppelli.*

Manuscript writing: ***C. Pellicioli.***

Manuscript Details

Manuscript number	ENGEO_2019_1637
Title	Determination of porosity and permeability of un-deformed and faulted volcanic rocks and related challenges: a case study on the Tres Vírgenes geothermal region (Baja California, Mexico)
Article type	Research Paper

Abstract

The assessment of porosity and permeability is fundamental for fluid extraction purposes (i.e. oil and gas and geothermal industries). Contrarily to the conventional oil and gas industry, geothermal industry has to face the challenges deriving from the extremely low porosity and permeability values of volcanic rocks, often resulting in structurally-controlled migration of hydrothermal fluids, rather difficult to model. The Tres Vírgenes volcanic region (Baja California, Mexico) represents no exception to this, as several studies demonstrated the key role of faults in sustaining geothermal fluids circulation. Nevertheless, an adequate quantitative characterization of physical properties of fault-rocks and exposed succession is still lacking. This study aims to fill this gap, determining porosity and permeability of un-deformed and faulted rocks with two different techniques: triaxial tests and X-ray computerized tomography (CT) and coupled permeability simulations. Results confirm the hydraulically non-conductive character of the exposed volcanic rocks and for the first time quantify porosity and permeability variations linked to faulting and fluid circulation processes along regional fault systems linked to the Gulf of California geodynamic setting. In addition to providing novel characterization of the Tres Vírgenes region, this work also adds a case study to the existing poor literature regarding physical properties of faulted ignimbrites and provides insights on fault-related permeability with implications in both volcanic and non-volcanic settings, including: lithological control on the formation of fault-permeability; issues and challenges affecting the determination of fault-permeability (i.e. dynamic and transient nature, scale, time); the presence of an important size effect affecting results of permeability simulations based on X-ray (CT) images. The approach used in this study to quantify fault-related porosity and permeability variations can be applied to any type of fault and geological setting.

Keywords	interconnected pore space; fault-rock permeability; fluid migration.
Corresponding Author	Claudia Pellicioli
Order of Authors	Claudia Pellicioli, Michele Zucali, Nicoletta Fusi, Riccardo Castellanza, Giovanni Crosta, Gianluca Groppelli
Suggested reviewers	Domenico Liotta, Fabio Luca Bonali, Antonio Pola

Submission Files Included in this PDF

File Name [File Type]

Cover Letter_EG.docx [Cover Letter]

Highlights_EG.docx [Highlights]

Manuscript_EG.docx [Manuscript File]

Figures_EG.pdf [Figure]

To view all the submission files, including those not included in the PDF, click on the manuscript title on your EVISE Homepage, then click 'Download zip file'.

Research Data Related to this Submission

There are no linked research data sets for this submission. The following reason is given:
Data will be made available on request

7.1 Abstract

The assessment of porosity and permeability is fundamental for fluid extraction purposes (i.e. oil and gas and geothermal industries). Contrarily to the conventional oil and gas industry, geothermal industry has to face the challenges deriving from the extremely low porosity and permeability values of volcanic rocks, often resulting in structurally-controlled migration of hydrothermal fluids, rather difficult to model. The Tres Vírgenes volcanic region (Baja California, Mexico) represents no exception to this, as several studies demonstrated the key role of faults in sustaining geothermal fluids circulation. Nevertheless, an adequate quantitative characterization of physical properties of fault-rocks and exposed succession is still lacking. This study aims to fill this gap, determining porosity and permeability of undeformed and faulted rocks with two different techniques: triaxial tests and X-ray computerized tomography (CT) and coupled permeability simulations. Results confirm the hydraulically non-conductive character of the exposed volcanic rocks and for the first time quantify porosity and permeability variations linked to faulting and fluid circulation processes along regional fault systems linked to the Gulf of California geodynamic setting. In addition to providing novel characterization of the Tres Vírgenes region, this work also adds a case study to the existing poor literature regarding physical properties of faulted ignimbrites and provides insights on fault-related permeability with implications in both volcanic and non-volcanic settings, including: lithological control on the formation of fault-permeability; issues and challenges affecting the determination of fault-permeability (i.e. dynamic and transient nature, scale, time); the presence of an important size effect affecting results of permeability simulations based on X-ray (CT) images. The approach used in this study to quantify fault-related porosity and permeability variations can be applied to any type of fault and geological setting.

Keywords: *interconnected pore space, fault-rock permeability, fluid migration*.

7.2 Introduction

Both geothermal and oil and gas industries focus on fluid extraction from the subsurface. In geothermal regions, the identification of fluid migration patterns is somehow easier than in the oil and gas industry, and is linked to the several surficial manifestations of hydrothermal fluid migration

processes (i.e. fumaroles, hot soils, warm springs, hydrothermal alteration of rock masses). This derives from the fact that geothermal systems are "living" thermal systems, whilst in conventional oil and gas reservoirs the thermal phase responsible for kerogene maturation is by far finished at the time of the oil and gas extraction, although this does not prevent hydrocarbons migration up to surface in rare cases. As fluid extraction from the subsurface is the main concern, assessing permeability is the key, and often the most difficult, task in both industries (Ehrlich et al. 1991; Aydin 2000). Contrarily to conventional hydrocarbon reservoirs, geothermal reservoir rocks usually display a very low permeability (comparable to unconventional oil and gas reservoirs), linked to their magmatic nature. Intrusive and volcanic rocks in fact quite often exhibit the two most common factors inhibiting permeability: the abundance of isolated (i.e. pumice) and small pores (i.e. clay minerals resulting from alteration of magmatic minerals like feldspars). As a result, in most cases faults and other structures account for most of fluid flow (Moeck, 2014) across geothermal regions, rendering permeability assessment often more complicate and challenging than in the conventional oil and gas industry.

This is the case of the Tres Vírgenes geothermal region, lying inside the Baja California peninsula (Mexico) and characterized by Quaternary volcanic manifestations and currently active exploitation of geothermal resources (10 MW_e of operating net capacity; Gutierrez-Negrin et al., 2010). Here, the primary role of faults in supporting hydrothermal fluid circulation was identified by a series of studies performed by Pellicioli et al. (submitted, a, b and c), who in their structural model argue that the intersection between regional and volcanic structures enhances permeability, similarly to what occurring in other important geothermal areas (Taupo volcanic zone, Rowland and Sibson, 2004). Migration of hydrothermal fluids along regional and volcanic structures across the Tres Vírgenes region is testified by the presence of hydrothermal alteration (i.e. zeolite minerals) and calcite and oxides precipitation along fault planes following fluid circulation processes (Pellicioli et al., submitted, b and c). Nevertheless, adequate quantitative characterization of physical properties (i.e. porosity and permeability) of undeformed and faulted rocks exposed across the Tres Vírgenes regions is still lacking. Available information only refer to well-bore samples of Cretaceous granitic rocks (97.8 Ma, Garcia-Sanchez et al., 2019) representing the reservoir for geothermal fluids. No other study concerning vertical and/or lateral fluid migration through the volcanic succession (i.e. ignimbrite flows) exposed across the region has ever been performed, and their impermeable character has been simply assumed (Contreras and Garcia, 1998; Portugal et al., 2000). Similarly, along-fault and cross-fault permeability throughout the Tres Vírgenes regions has never been investigated.

This study aims to compensate these gaps, by determining for the first time porosity and permeability of undeformed (intact) and faulted volcanic rocks exposed across the Tres Vírgenes region, and to provide a further case study for permeability estimate in geothermal regions and for ignimbrite rocks,

representing so far one of the least studied lithotypes (Soden and Shipton, 2013). Results are of high importance for regional fluid flow modelling purposes given the active character of the Tres Vírgenes geothermal region. Based on the pervasive structural control exerted on Quaternary volcanic processes by regional lineaments belonging to the Gulf of California (Pellicioli et al., submitted, a) and the fractal nature of Gulf-related deformation patterns (Pellicioli et al., submitted, b), the outcomes of this study can give insights on porosity and permeability variations in response to faulting mechanisms acting across this sector of the Gulf of California. Furthermore, the approaches and techniques used in this work to quantify porosity and permeability changes following faulting and fluid circulation processes can be applied to any fault in any geological setting.

Interconnected porosity and permeability were estimated using two techniques working at different scales: the triaxial system and the X-ray computerized tomography (CT). 6 samples collected from the exposed volcanic succession (protolith samples) and 10 samples from the main deformations zones mapped through the region (fault-rock samples) were analysed. All samples were collected at surface or near-surface conditions. In three cases changes in interconnected pore space, interconnected porosity and permeability following fluid circulation and synchronous faulting processes could be captured and quantified on fault-rock samples.

7.3 Geodynamic and geological setting

The Tres Vírgenes geothermal region is located about 33 km NW of the Santa Rosalía town, on eastern side of the Baja California peninsula, facing the Gulf of California (Mexico, Fig. 7.1a). The region is strongly influenced by the complex tectonics linked to the Gulf of California opening and lies within the NW-SE trending Santa Rosalía half graben basin, developed from oblique divergence following Cenozoic subduction ceasing between the Farallon and North America plates (Ferrari et al., 2018). Following stress reorganization occurred at 3.5 Ma (Angelier et al., 1981; Zanchi, 1994; Aragón-Arreola et al., 2005) the Santa Rosalía basin has been displaying a normal right-lateral oblique faulting style and a seismically active character (Nava-Sanchez et al., 2001; Aragón-Arreola et al., 2005; Wong and Munguia, 2006). Inside the Santa Rosalía basin Quaternary siliciclastic volcanism commenced at 1.35 Ma with La Reforma caldera complex (Garcia-Sánchez et al., 2019) and was followed by the Sierra Aguajito (1.17 Ma, Schmitt et al., 2006) and Tres Vírgenes (Holocene, Avellán et al., 2018) volcanic complexes. Exploitation of geothermal energy started in the 1980s with CFE (*Comisión Federal de Electricidad*) in the Tres Vírgenes geothermal plant (Fig. 7.1a). Following recent dramatic increase in water and electricity demand linked to tourism growth (Arango-Galván et

al., 2015) renewed interest in the region has led the Mexican authorities to sponsor a series of studies to assess geothermal prospectivity beyond the Las Tres Vírgenes field borders, to include nearby volcanic complexes of La Reforma and Aguajito. Among these studies is the CeMIE Geo P15 project of SENER-CONACyT awarded to the UNAM (*Universidad Nacional Autónoma de México*), from which this and previous studies (Garcia-Sanchez et al., 2019; Pellicioli et al., submitted, a, b and c) have benefited from.

Recent work in the Tres Vírgenes region contributed to improve geological, stratigraphic and geochemical characterization of La Reforma caldera complex and summarize its evolution in a pre-, syn- and post-caldera phases. Additionally, a structural model for the Tres Vírgenes area was provided, and the fractal geometry affecting this sector of the Gulf of California and responsible for the regular repetition at different scales of pull-apart basins bounded by right-lateral normal oblique large-scale NW-SE trending gulf-related structures (i.e. the Azufre and Santa Ana fault systems, Fig. 7.1b) and NE-SW oriented conjugate structures (i.e. the Infierno fault, Fig. 7.1b) was identified Pellicioli et al (submitted, a and b). These authors also highlighted the control exerted by Gulf-related structures on the location and the style of Quaternary volcanic processes (i.e. caldera collapse and resurgence) and on hydrothermal fluids migration patterns. Furthermore, the non-marine but mixed hydrothermal-meteoric to meteoric origin of fault-circulating fluids, previously suggested by Portugal et al., (2000), was clarified based on multi-technique and multi-scale petrographic and geochemical investigations, that also led to estimate surface precipitation temperatures of calcite along fault planes up to 100°C (Pellicioli et al., submitted, c).

7.4 Sample collection and type

The nineteen samples analysed in this study divide into the following two categories: i) samples (9) collected away from main deformation zones mapped across the study area (Garcia-Sanchez et al.; 2019; Pellicioli et al., submitted, a) and labelled protoliths in this study, as considered representative of physical properties intrinsic to the lithotype; ii) samples (10) collected along some of the major structures fault planes or within their damage zone, labelled fault-rocks in this study. They all represent volcanic rocks: mainly ignimbrites or local PDCs, andesitic and basaltic lava flows and intrusions and were collected at surface to near-surface conditions during a series of field surveys conducted through the Tres Vìrgenes area between 2014 and 2017. Information regarding the lithostratigraphic units, composition and age is summarized in Table 7.1, whilst information regarding

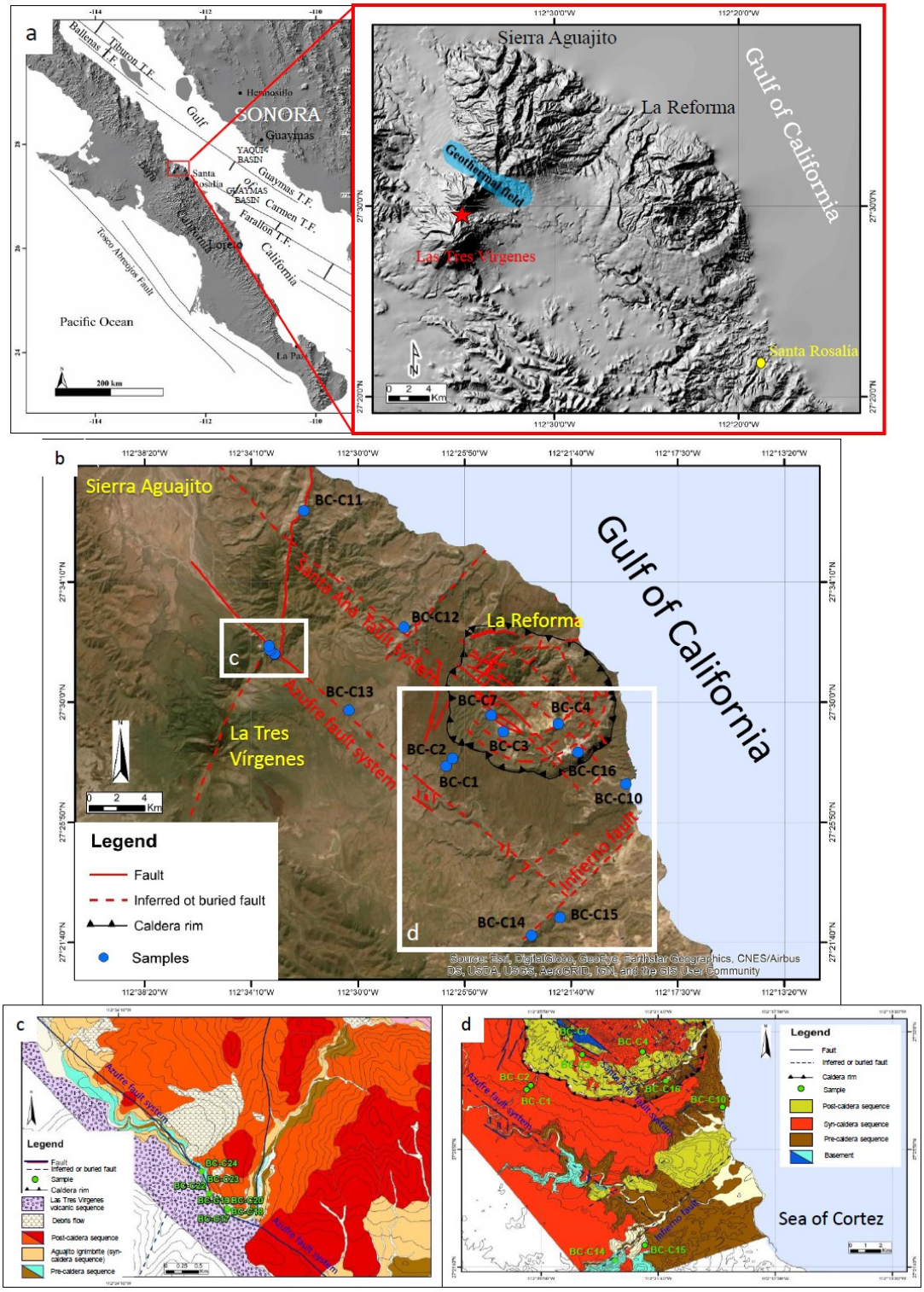

Figure 7.1 Location of the study area and of the Tres Vírgenes geothermal field (shaded in light blue, a) and collection sites of samples analysed in the study (b, c and d). Figures modified after Garcia-Sanchez et al. (2019) and Pellicioli et al., (submitted, b and c).

the collection sites is reported in Figures 7.1b to 7.1d. In detail, fault-rock samples were collected along both regional (the Azufre, Santa Ana fault and Infierno fault systems; Pellicioli et al., submitted, a) and volcanic structures (i.e. BC-C4 along La Reforma caldera complex ring faults, Fig. 7.1b) or at their crossing points (i.e. BC-C16, Fig. 7.1b).

Table 7.1 List of samples and analyses performed in this study.

Sample Coordinates	Sample type	Lithostratigraphic Unit	Description	Performed analysis
BC-C1 112°26'31.867"W 27°27'47.435"N	Protolith	La Reforma ignimbrite – pumice-rich facies (1.29 Ma [a]) - rhyolite	Up to 40 thick, basal welded reddish facies with fiammae overlain by brownish to dark-grey deposits ([a]).	Triaxial test; X-ray (CT); permeability simulation
BC-C2 112°26'17.661"W 27°28'2.841"N	Protolith	Los Balcones ignimbrite (1.35 Ma [a]) - rhyolite	Up to 30 m thick grey welded pyroclastic deposit with grey pumices, fiammae and abundant lithics ([a]).	Triaxial test; X-ray (CT); permeability simulation
BC-C3 112°24'19.277"W 27°28'59.324"N	Protolith	Punta Arena ignimbrite – fiammae-rich facies (0.96 Ma [a])	Up to 200 m thick white loose pyroclastic deposit with grey and white pumices and lava and scoria lithics. Local greenish matrix when hydrothermally altered ([a]).	Triaxial test; X-ray (CT); permeability simulation
BC-C4 112°22'9.845"W 27°29'16.127"N	Protolith	Punta Arena ignimbrite – greenish altered facies (0.96 Ma [a])	Up to 200 m thick white loose pyroclastic deposit with grey and white pumices and lava and scoria lithics. Local greenish matrix when hydrothermally altered ([a]).	Sample lost during cutting and coring
BC-C7 112°24'47.588"W 27°29'33.192"N	Fault-rock – Santa Ana fault system / La Reforma ring faults	Punta Arena ignimbrite – greenish altered facies (0.96 Ma [a])	Up to 200 m thick white loose pyroclastic deposit with grey and white pumices and lava and scoria lithics. Local greenish matrix when hydrothermally altered ([a]).	X-ray (CT); permeability simulation
BC-C10 112°19'30.949"W 27°27'9.618"N	Protolith	Cueva Amarilla ignimbrite (2.4 Ma [a])	Up to 30 m thick greenish grey pyroclastic deposit with white pumice at bottom and black scoriae at top ([a]).	Sample lost during cutting and coring
BC-C11 112°32'7.548"W 27°36'38.825"N	Protolith	pre-Aguajito ignimbrite PDC* (>1.17 Ma [b])	Up to 10 m thick white welded pyroclastic deposit with black scoriae and grey pumice.	Sample lost during cutting and coring
BC-C12 112°28'11.835"W 27°32'36.312"N	Protolith	Carrizo ignimbrite (1.89 Ma [a]) – rhyolite	Up to 10 m thick red welded pyroclastic deposit with yellow and grey pumice and abundant lithics ([a]).	Triaxial test; X-ray (CT); permeability simulation
BC-C13 112°30'21.793"W 27°29'44.131"N	Protolith	Aguajito ignimbrite – welded facies (1.17 Ma [b]) - rhyolite	Up to 40 m thick non-welded light brown facies with white pumice overlain by pinkish welded lithic rich facies with brown fiammae and lithics ([a]).	Triaxial test; X-ray (CT); permeability simulation
BC-C14 112°23'12.894"W 27°21'54.19"N	Fault-rock – Infierno fault	Santa Lucia formation (19.25 Ma [a]) – andesitic and basaltic lava	Up to 80 m thick lava flows and domes associated with dykes ([a]).	X-ray (CT); permeability simulation
BC-C15 112°22'5.636"W 27°22'32.183"N	Protolith	La Reforma ignimbrite – fiammae-rich facies (1.29 Ma [a]) – rhyolite	Up to 40 thick, basal welded reddish facies with fiammae overlain by brownish to dark-grey deposits ([a]).	Triaxial test; X-ray (CT); permeability simulation
BC-C16 112°21'23.773"W 27°28'15.673"N	Fault-rock - La Reforma ring fault	Cueva del Diablo formation (0.46 – 0.28 Ma [a]) – basaltic-andesitic and andesitic intrusion	Up to 50 m thick lava flows, domes and scoria cones sometimes associated with dykes and intrusive bodies ([a]).	X-ray (CT); permeability simulation
BC-C17 112°33'15.934"W 27°31'39.999"N	Fault-rock – Azufre fault damage zone	Aguajito ignimbrite (1.17 Ma [b]) - rhyolite	Up to 40 m thick non-welded light brown facies with white pumice overlain by pinkish welded lithic rich facies with brown fiammae and lithics ([a]).	X-ray (CT); permeability simulation
BC-C18 112°33'16.026"W 27°31'40.064"N	Fault-rock – Azufre fault damage zone	Aguajito ignimbrite (1.17 Ma [b]) - rhyolite	Up to 40 m thick non-welded light brown facies with white pumice overlain by pinkish welded lithic rich facies with brown fiammae and lithics ([a]).	X-ray (CT); permeability simulation

BC-C19 112°33'16.075"W 27°31'40.553"N	Fault-rock – Azufre fault damage zone	Aguajito ignimbrite (1.17 Ma [b]) - rhyolite	Up to 40 m thick non-welded light brown facies with white pumice overlain by pinkish welded lithic rich facies with brown fiammae and lithics ([a]).	X-ray (CT); permeability simulation
BC-C20 112°33'16.007"W 27°31'40.571"N	Fault-rock – Azufre fault damage zone	Aguajito ignimbrite (1.17 Ma [b]) - rhyolite	Up to 40 m thick non-welded light brown facies with white pumice overlain by pinkish welded lithic rich facies with brown fiammae and lithics ([a]).	X-ray (CT); permeability simulation
BC-C22 112°33'24.864"W 27°31'47.133"N	Fault-rock – Azufre fault damage zone	Aguajito ignimbrite (1.17 Ma [b]) - rhyolite	Up to 40 m thick non-welded light brown facies with white pumice overlain by pinkish welded lithic rich facies with brown fiammae and lithics ([a]).	X-ray (CT); permeability simulation
BC-C23 112°33'27.842"W 27°31'50.046"N	Fault-rock – Azufre fault damage zone	Aguajito ignimbrite (1.17 Ma [b]) - rhyolite	Up to 40 m thick non-welded light brown facies with white pumice overlain by pinkish welded lithic rich facies with brown fiammae and lithics ([a]).	X-ray (CT); permeability simulation
BC-C24 112°33'28.869"W 27°31'57.057"N	Fault-rock – Azufre fault system	pre-Aguajito ignimbrite PDC (>1.17 Ma [b])	Up to 10 m thick welded pinkish pyroclastic flow with pumices.	X-ray (CT); permeability simulation

(*) PDC: pyroclastic density current.
[a] Garcia-Sánchez et al. (2019).
[b] Schmitt et al. (2006).

7.5 Materials and methods

Collected protolith and fault-rock samples underwent porosity and permeability determinations using two different techniques: i) collocation inside a triaxial system at unconfined conditions; ii) X-ray computerized tomography (CT) coupled with permeability simulations (Table 7.1). The triaxial system allowed to derive interconnected porosity and hydraulic conductivity, from which permeability was derived, whilst X-ray (CT) and coupled permeability simulations determined total and interconnected porosity and permeability. Only protolith rocks, following appropriate coring and cutting operations, could be allocated in the triaxial cell, whose geometry prevented the analysis of the smaller and irregularly shaped fault-rock samples. To overcome this issue, porosity of fault-rock samples was determined with the X-ray (CT) technique, reconstructing the internal structure of samples based on the distribution of the X-ray linear absorption coefficient deduced from the projection of X-rays through a sample (Ohtani et al., 2000). Then, simulations through the 3D pore space volume isolated from X-ray (CT) images were run to determine permeability. The X-ray (CT) and permeability simulation techniques were also applied to protolith samples, previously analysed with the triaxial system, in order to derive independent porosity and permeability estimates for comparison purposes. Both triaxial and X-ray (CT) analyses were performed at the Department of Earth and Environmental Sciences of the Milano-Bicocca University (Milan), deploying the WYKEHAM FARRANCE's TRITECH 50kN triaxial cell by Controls © and the GE-D600 medical CT hybrid scanner and a BIR Actis 130/150 Micro CT/DR system to obtain X-ray (CT) images of the samples (5 to 650 μm of

resolution). The software package used to process images, extract and analyse data, perform volume calculations and permeability simulations on X-ray (CT) images is the Thermo Scientific ™ Avizo ™ Software 9 fitted with the XLab extension suite, specifically designed for simulation of materials physical properties.

7.5.1 The triaxial system

Protolith samples were tested with the triaxial system in unconfined pressure conditions and without reaching failure. Unconfined pressure conditions were chosen to re-create the surface or near-surface conditions at which the samples were collected in the field, whilst the integrity of the cores was preserved for following X-ray (CT) analyses. During preparatory cutting and coring operations samples BC-C4, BC-C10 and BC-C11 were lost, as too soft and poorly consolidated and thus triaxial testing was performed on the 6 remaining protolith samples (Table 7.1). Following the collocation of 37-mm diameter protolith cores inside the triaxial cell, this was filled with distilled water and cores left until saturation conditions were reached. Back and cell pressures were risen in alternate steps to favour the (generally difficult) achievement of saturated conditions, always paying attention to deploy a delta pressure in line with unconfined conditions. Whenever saturation revealed a rather time-consuming process, cores were flushed with CO_2 before undergoing the water saturation process, in order to facilitate air escape from tight pores. In all cases, protoliths could not reach complete saturation due to the high percentage of isolated pores that in ignimbrites are usually represented by pumice vesiculation (Klug and Cashmann, 1996; Srouga et al., 2004). Following partial saturation, a top to bottom (or vice versa) flow of distilled water was induced inside the core, by applying a delta pressure between the sample top and bottom. The water flow was measured at regular time intervals (30 seconds) by an automatic volume change device connected to the triaxial system. Volume measures were ceased when volume variations became stable in the set time interval. By simple knowledge of the core dimensions, dry and wet weights (prior to and following saturation) the interconnected (or effective) porosity was computed (Table 7.2) for each sample based on the standard test procedure by IRMS (1972), using the following equation (Eq.1):

$$\varphi_i = V_v / V_T \quad (1)$$

where φ_i is interconnected porosity, V_v is the volume of voids and V_T is the total volume. Following saturation, pores are filled by water and V_v thus represents the volume of water. V_T instead represents the sum of the volume of water (V_v) and the volume or the solid (or dry volume of the sample prior to saturation). All volumes were back-calculated from measured dry and wet weights and from core densities. The interconnected (or effective) character of the porosity derived from triaxial tests is given

by the fact that during these tests water is forced into the existing interconnected pores, and no new connections are established between isolated pores. Hydraulic conductivity (*Hc*, Table 7.2) in m/s was calculated by means of the Darcy equation (Eq. 2):

$$Hc = Q \cdot 10^{-2} / 60 \cdot i \cdot \delta t \cdot A_C \quad (2)$$

where Q is the volume variation (cm^3) measured by the volume change device during the δt time interval (30 s), i is the hydraulic gradient, or the ratio between the applied hydraulic load and the height of the core, and A_C the core section (cm^2). Hydraulic conductivity relates to the ease with which water passes through a porous material and therefore is a property of the whole system including both the porous medium and the flowing fluid. On the contrary, permeability (k) specifically relates to the innate properties of the porous material itself, and was thus calculated by taking into consideration the fluid (distilled water) density (997 kg/m^3) and viscosity ($8.9 \cdot 10^{-4}$ Pa.s) and g (9.8 m/s^2, Table 7.2). Being fluid viscosity pressure-independent, no correction was needed in regards to the application of hydraulic loads during the measurement of the core volume variations. According to the geometry of the flow induced through the sample (top to bottom and vice versa, Fig. 7.2a), hydraulic conductivity and derived permeability refer to the z direction (kz in Table 7.2).

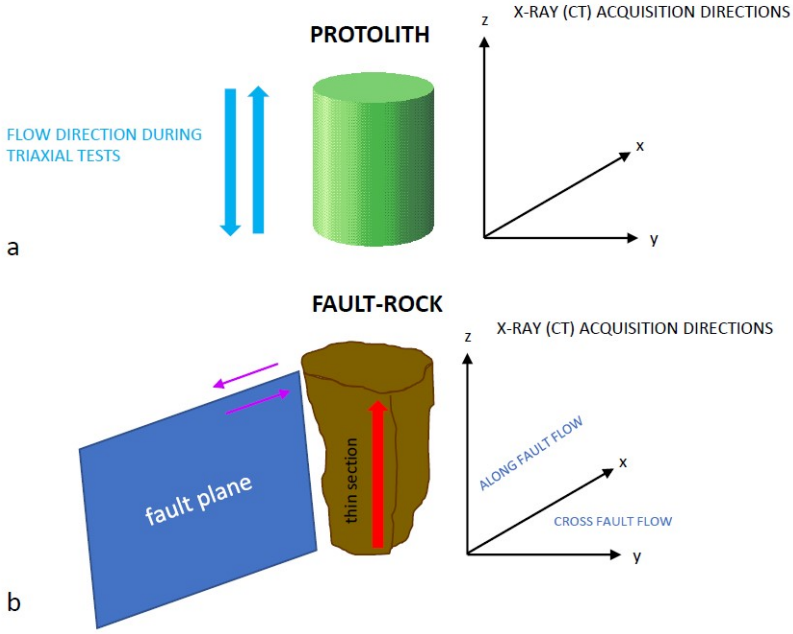

Figure 7.2 Scheme illustrating the geometrical relationship between the X-ray (CT) acquisition directions (x, y and z) used to simulate permeability with the Avizo software and the direction of the flow induced inside the triaxial cell on protolith samples (a) or the orientation of fault-rock samples in respect to the fault shear direction (b). Notice that permeability obtained through triaxial tests on protolithes should be compared with permeability along the z direction derived from

permeability simulations. In fault-rock samples permeabilities along the z and x directions resulting from simulations represent along-fault permeabilities, while permeability along the y direction is cross-fault permeability.

7.5.2 X-ray computerized tomography (CT)

Protolith and fault-rock samples were scanned with a Bir/Actis X-ray computerized tomography (CT) instrument, using the same resolution (voxel size=0.026 mm) in the x, y and z scanning directions. A variable number of slices (images) per sample, usually between 900 and 2600, was obtained based on sample dimensions. These slices were then loaded into the Thermo Scientific ™ Avizo ™ Software 9 for processing, porosity computation and permeability simulation. In many cases it was necessary to crop the most external portion of the scanned slices before any computation, to avoid including regions falling outside the core and to remove beam hardening artefacts. A threshold was interactively applied to the 3D scanned volume to derive the core 3D total volume, pore volume and related statistics, from which total porosity of the core was computed. In addition to total porosity, interconnected porosity (φi) of the core was derived following plotting of 3D pore volume distributions and identification of the volume and percentage of interconnected pores. Interconnected pores were distinguished from isolated pores by means of the 3D pore volume distribution and based on the evidence that interconnected pores are seen by the Avizo software as a single large pore displaying a rather high 3D volume. 3D scanned images of three fault-rock samples (BC-C14, BC-C16 and BC-C24) highlighted the presence of volumetrically consistent quantities of calcite and oxides precipitated inside some fault-related micro-fractures, revealing partial sealing of the open pore space following fluid circulation processes along the fault plane. Additional computation of 3D volume statistics and interconnected porosity was performed on pore space filled by oxides (BC-C16) and calcite (BC-C14 and BC-C24) for these samples. Original porosity displayed by these samples before any partial occlusion of the open pore space by mineral precipitation ('pre-sealing conditions') was determined by summing the 3D volumetric information regarding the open pore space ('actual conditions') and the calcite or oxides-filled pore space. The difference between interconnected porosity determined in pre-sealing and actual conditions allowed to estimate the interconnected porosity reduction following fluid circulation along the fault plane.

Permeability of protoliths and fault rock samples was derived using a trial version of the XLabSuite extension of the Avizo software, able to provide numerical simulation capabilities to calculate physical properties of materials from the 3D image of a sample. The algorithm chosen to estimate permeability is the Absolute Permeability Experiment Simulation, based on Stokes equations resolution and simulating an experiment along the x, y and z axis. The boundary conditions for this algorithm imply the following: no slip conditions at fluid-solid interfaces; the isolation of the sample from outside allowing no flow out of the system; the user can choose two among the following three conditions, the

third being estimated from the chosen two: input pressure, output pressure, flow rate. In this study the input and output pressures were respectively set at 130 and 100 kPa, while the flow rate left free to be computed by the software. The chosen pressure values imply a delta pressure of 30 kPa, comparable with the hydraulic load applied during the triaxial tests (Table 7.2) and representative of surface or near-surface conditions. Fluid viscosity during the simulation was set at 0.001 Pa.s, representing the viscosity of water. For each sample, the input volume for the Absolute Permeability Experiment Simulation was the 3D pore space volume derived from the interactive thresholding processes performed during porosity calculations from X-ray (CT) images. Before running the Absolute Permeability Experiment Simulation isolated void spaces were removed with the Axis Connectivity tool. 50 was the maximum number of slices used to obtain results in a reasonable time given the available CPU equipment. In order to test the reliability of obtained permeability results and the eventual presence of a size effect, a set of permeability simulations using 20 slices was also run and results were compared (Table 7.3). Given the geometry of the X-ray (CT) acquisition directions in respect to protolith and fault-rock samples (Fig. 7.2a and b), permeability was simulated along all direction (x, y and z) for fault-rock samples and only along the z direction for protolith samples for comparison purposes with triaxial tests results along the same direction. As done for porosity estimation through X-ray (CT) images, double permeability simulations were performed on samples BC-C14, BC-C16 and BC-C24: a first simulation for the actual conditions (flow through the open pore space) and a second one for the pre-sealing conditions (flow through the open plus mineral-filled pore space).

7.6 Results

7.6.1 Porosity

Interconnected porosity (φ_i) of protoliths obtained deploying the triaxial system is summarized in Table 7.2, while total (φ_T) and interconnected porosity (φ_i) of protoliths and fault-rocks derived from the X-ray (CT) technique are illustrated in Tables 7.4 and 7.5. Values obtained for total and interconnected porosity for both protoliths and fault-rock samples with the use of the two different techniques are overall rather low, and do not exceed 5% (Fig. 7.3). Triaxial tests and the use of X-ray (CT) images provided consistent values of interconnected porosity for protoliths, defining narrow ranges: from 0.21 (BC-C15) to 5.18% (BC-C13) in the case of triaxial tests (Table 7.2) and from 0.12 (BC-C15) to 4.12% (BC-C3) for X-ray (CT, Table 7.4 and Figure 7.3). Protoliths total porosity derived from X-ray (CT) defined a similarly tight range, from 0.14 (BC-C15) to 4.34% (BC-C3, Table

7.4 and Figure 7.3), thus indicating that the interconnected pore space volume (V_{Pi}) composes the majority (83-95%) of the total pore space volume (Table 7.4), despite the percentage of interconnected pores in protoliths is rather low (3 to 10%, Table 7.4) as indicated by 3D pore space volume frequency distributions (Figs. 7.7 to 7.9 Appendix). Such low abundance of interconnected pores (3-10%) justifies the achievement of only partial saturation conditions inside the triaxial cell. Similarly narrow ranges for total and interconnected porosity were obtained for fault-rock samples analysed with the X-ray (CT) technique (Fig. 7.3b). Actually, total porosity ranges from 1.39 (BC-C14) to 4.63% (BC-C18) while interconnected porosity from 1.34 (BC-C14) to 4.58% (BC-C18, Table 7.4 and Figure 7.3). Also in fault-rock samples the interconnected pore space volume (V_{Pi}) composes the majority (88-99%) of the total pore space volume (Table 7.4), even though the percentages of interconnected pores reach higher values than in protoliths (up to 25%, Table 7.4 and Figures 7.7 to 7.9 Appendix). Values up to 45% of total (φ_{Tf}) and interconnected (φ_{if}) porosity instead characterized samples BC-C14, BC-C16 and BC-C24 before any oxides and/or calcite precipitation occurred along the fault plane (Table 7.5 and Figure 7.4) causing partial seal of the open pore space. By comparing X-ray (CT)-derived pre-sealing values of interconnected porosity (Table 7.5) with those referring to the actual conditions (Table 7.4) a reduction up to 43% in interconnected porosity was estimated for these samples (Fig. 7.4). Despite the higher values of interconnected porosity and the volumetric predominance of interconnected pores (97-99% of the total pore space volume), the percentage of interconnected pores in pre-sealing conditions only reached values up to 10%.

Porosity values from 0.1 to 5% obtained for protolith and fault-rock samples of rhyolitic ignimbrites and basaltic to andesitic intrusive rocks are in line with porosities of silicic samples from published sources (Eichelberger et al., 1986; Klug and Cashman; 1996; Jouniaux et al., 2000; Melnik and Sparks, 2002; Rust and Cashman, 2004) and with lower values found by Srouga et al. (2004) and Srouga and Rubinstein (2007) in welded rhyolites of the Austral and Neuquen basins (Argentina), displaying pumice fragments and vitric shards that also occur in some of the analysed samples (Pellicioli et al., submitted, b). Less than 5% porosity has also been found in vesicular basalts by Saar and Manga (1999) and in granitic protolith rocks (< 1%, Evans et al., 1997). For what specifically concerns fault-rock porosity, values lower than 4% have been measured by Evans et al. (1997) in a fault zone cutting through granitic rocks in Wyoming (USA) by inducing a steady flow field through 5.2 centimetres diameter cores. Previous works discussing porosity across the study area (Portugal et al., 2000) report values of 1.1 to 5% effective porosity from petrophysical laboratory analysis performed on well-bore samples of Cretaceous granodioritic rocks (97.8 Ma, Garcia-Sanchez et al., 2019), not tested in this study and representing the geothermal reservoir rocks (Contreras and Garcia, 1998). The relatively good porosity assumed by Portugal et al. (2000) for the andesitic lavas of the Santa Lucia fm. (19.25

Ma, Garcia-Sanchez et al., 2019) was not confirmed by X-ray (CT) results on sample BC-C14, collected along a fault-zone cross-cutting this unit (Table 7.1). On the contrary, the low porosity of ignimbrite flows from La Reforma and Sierra Aguajito volcanic complexes, hypothesized by Portugal et al. (2000) in the absence of any laboratory testing, is confirmed by both triaxial and X-ray (CT) analyses results (Table 7.2 and 7.4) on protoliths.

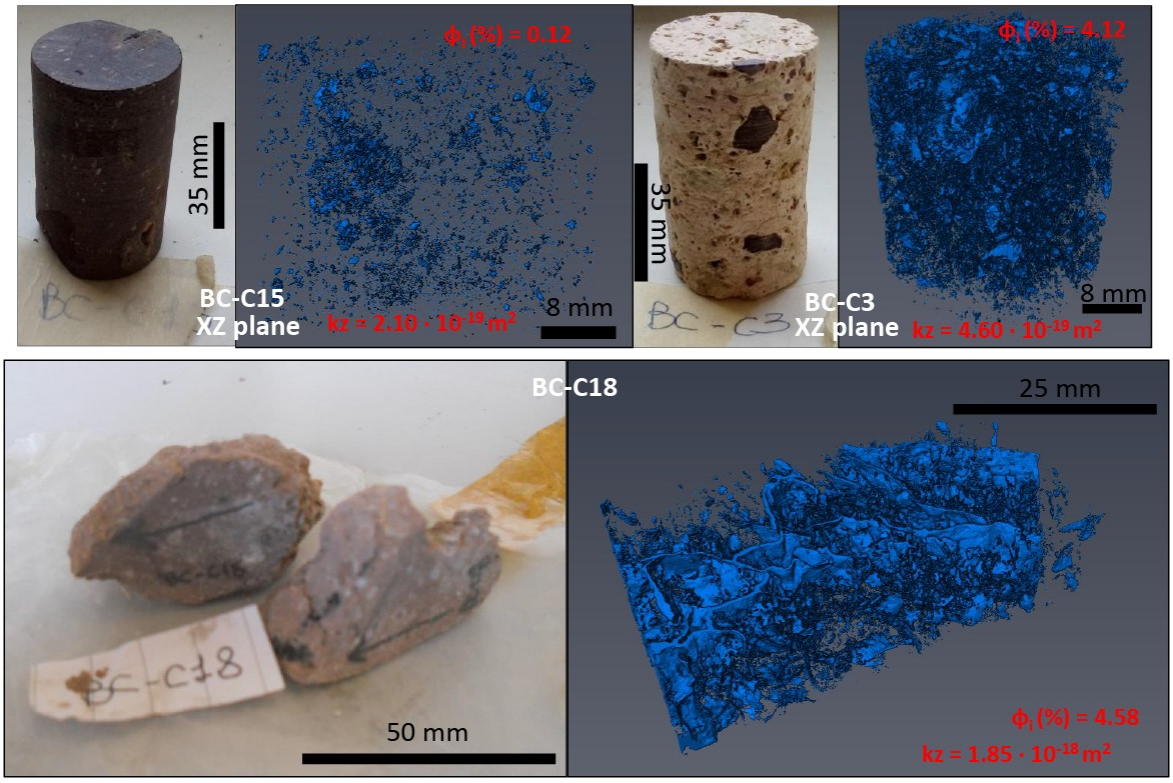

Figure 7.3 3D Pore space volume (highlighted in blue) from X-ray (CT) analysis on protolith samples BC-C15 (a) and BC-C3 (b) and on fault-rock sample BC-C18 (c). Interconnected porosity (φ_i) and protolith or along-fault permeability (kz) values derived from permeability simulations based on X-ray (CT) images are reported in red. Notice how open pore space in fault-rock samples focuses along fracture networks.

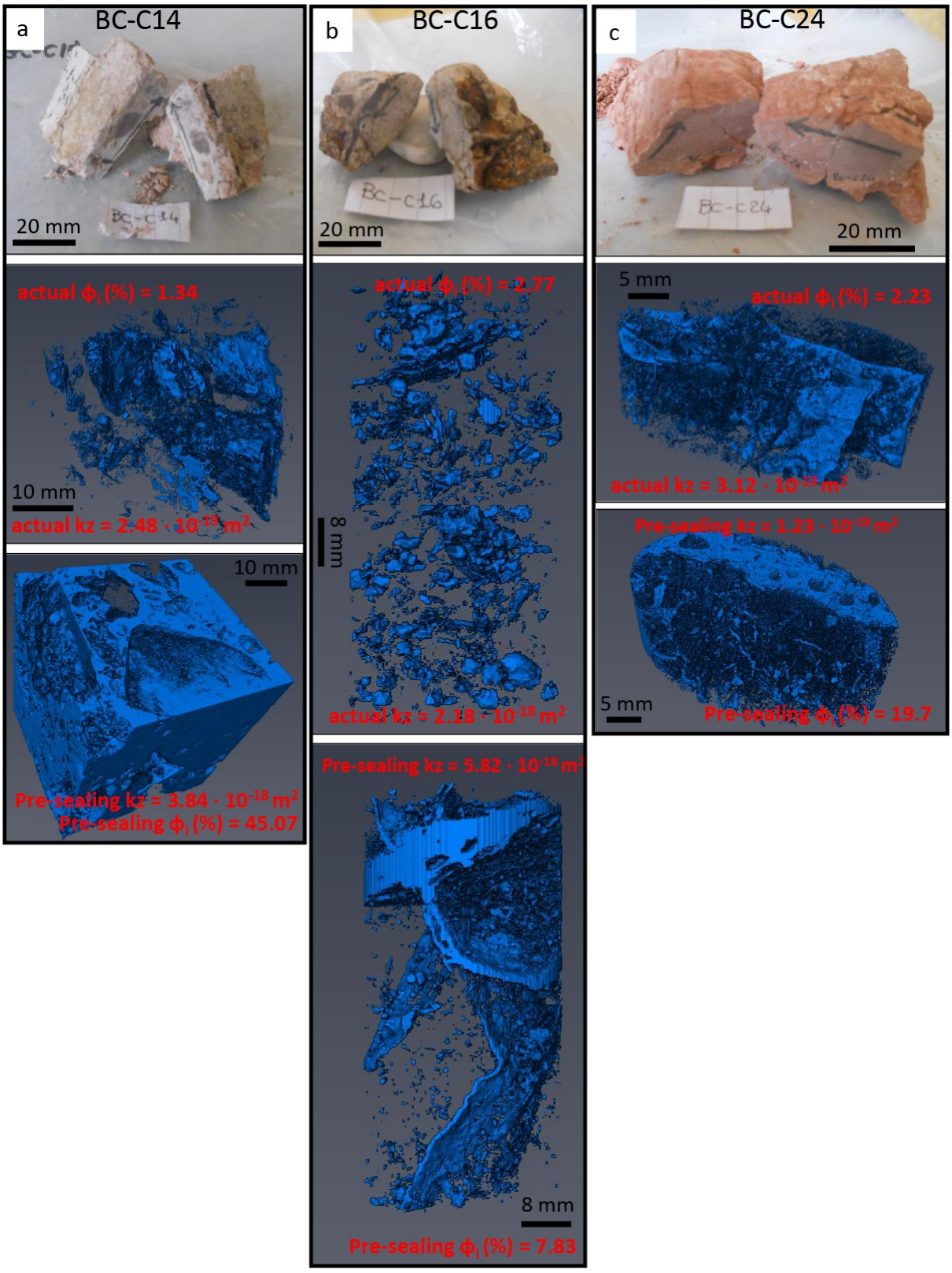

Figure 7.4 3D Pore space volume (highlighted in blue) from X-ray (CT) analysis in actual and pre-sealing conditions for fault-rock samples BC-C14 (a), BC-C16 (b) and BC-C24 (c). Interconnected porosity (φ_i) and along-fault permeability (kz)

values derived from permeability simulations based on X-ray (CT) images are reported in red. Notice the reduction in interconnected porosity (φ_i) and the small variation in along-fault permeability (kz) from pre-sealing to actual conditions.

7.6.2 Permeability

Permeability of protoliths obtained from triaxial tests (kz) is summarized in Table 7.2, while permeability of protoliths and fault-rocks derived from permeability simulations using X-ray (CT) images is illustrated in Tables 7.3 to 7.5. Table 7.3 in particular highlights how permeability resulting from simulations on protoliths and fault-rocks using a different number of slices (either 50 or 20) displays a size effect. The shift in protoliths kz (the only direction tested for protoliths) when a different number of slices is used is acceptable, and up to one order of magnitude, as in the case of the size effect found by Alarcon-Ruiz et al. (2010) on concrete samples. Given the generally low resulting permeability values for protoliths (Table 7.3 to 7.5), the identified size effect (up to one order of magnitude difference) is negligible under the hydraulic and geological point of view. The same regards permeability simulations on fault-rock samples performed along the z and y axes using a different number of X-ray (CT) images. Resulting kz and ky values are quite stable, and similarly to protoliths display up to one order of magnitude permeability differences. Rather fluctuating values (up to six orders of magnitude difference) instead resulted from permeability simulations with a different number of slices along the x direction (kx, Table 7.3). Being both kx and kz representative of along-fault fluid flow conditions (Fig. 7.2) and given the unstable nature of kx simulation results, only kz was considered for the purposes of this study as the along-fault permeability, keeping however in mind that generally higher, although unstable, permeability values were reached along the analysed faults (kx, Table 7.3). Furthermore, minor attention was paid to cross-fault permeability (ky, Table 7.3), being the main aim of this work to determine the fluid flow potential of faults within the Tres Vírgenes region.
Protoliths kz varies between $1.93 \cdot 10^{-18}$ m^2 (BC-C15) and $6.27 \cdot 10^{-15}$ m^2 (BC-C13) based on triaxial test results, while between $2.10 \cdot 10^{-19}$ m^2 (BC-C15) and $1.93 \cdot 10^{-18}$ m^2 (BC-C1) according to X-ray (CT) analysis result (Tables 7.2 and 7.4 and Figure 7.3a). A shift in interconnected porosity from 0.2 to 5% is accompanied by a variation over three orders of magnitude of kz obtained from triaxial tests, while X-ray (CT)-derived kz only varies of one order of magnitude roughly over the same porosity interval (0.1 to 4%). Fault-rock samples kz obtained from permeability simulations performed using 50 X-ray (CT) slices ranges between $2.48 \cdot 10^{-19}$ m^2 (BC-C14) and $4.40 \cdot 10^{-18}$ m^2 (BC-C19) for interconnected porosities spanning from 1.34 to 4.58% (Table 7.4 and Fig. 7.3b). Surprisingly, kz derived from permeability simulations referring to pre-sealing conditions along faults BC-C14, BC-C16 and BC-C24 display rather low values (around 10^{-18} m^2, Table 7.5 and Figure 7.4), comparable to or just one order of magnitude higher than those obtained for the actual conditions (Table 7.4), where mineral precipitation has occluded most of the originally open pore space. This happens despite the

substantially higher interconnected porosity (up to 45%) determined from X-ray (CT) images in pre-sealing conditions (Table 7.5 and Fig. 7.4).

Table 7.2 Interconnected porosity (φ_i), hydraulic conductivity (Hc) and permeability (kz) of protolith samples derived from testing inside the triaxial cell. Dry and net weights of cores and applied hydraulic loads used for porosity and permeability calculations are also reported.

Sample	Dry weight (g)	Wet Weight (g)	Hydraulic load (kPa)	φ_i (%)	Hc (m/s)*	kz (m^2)
BC-C1	81.83	98.34	20 - 30	3.43	$1.93 \cdot 10^{-8}$	$1.76 \cdot 10^{-15}$
BC-C2	124.14	140.83	30	2.42	$1.79 \cdot 10^{-9}$	$1.63 \cdot 10^{-16}$
BC-C3	97.49	126.13	50	3.72	$2.19 \cdot 10^{-10}$	$2.00 \cdot 10^{-17}$
BC-C12	152.79	169.3	30	2.14	$5.11 \cdot 10^{-10}$	$4.65 \cdot 10^{-17}$
BC-C13	106.01	143.81	10 - 20	5.18	$6.88 \cdot 10^{-8}$	$6.27 \cdot 10^{-15}$
BC-C15	143.74	144.91	50	0.21	$2.12 \cdot 10^{-11}$	$1.93 \cdot 10^{-18}$

(*) reported Hc values are average values for the analysed samples.

Table 7.3 Comparison between permeability values in the x, y and z directions obtained from permeability simulations using a different number of X-ray (CT) slices (20 or 50). Notice how variation is acceptable (up to one order of magnitude difference) for kz and ky, while rather high (up to six orders of magnitude) for kx.

Sample	kz (m^2) 20 slices	kz (m^2) 50 slices	kx (m^2) 50 slices	kx (m^2) 20 slices	ky (m^2) 50 slices	ky (m^2) 20 slices
BC-C1	$5.30 \cdot 10^{-19}$	$1.93 \cdot 10^{-18}$	-	-	-	-
BC-C2	$5.22 \cdot 10^{-19}$	$6.67 \cdot 10^{-19}$	-	-	-	-
BC-C3	$5.43 \cdot 10^{-19}$	$4.60 \cdot 10^{-19}$	-	-	-	-
BC-C7	$1.50 \cdot 10^{-19}$	$1.91 \cdot 10^{-18}$	$8.52 \cdot 10^{-14}$	$4.13 \cdot 10^{-12}$	$7.83 \cdot 10^{-16}$	$3.05 \cdot 10^{-15}$
BC-C12	$4.46 \cdot 10^{-19}$	$6.06 \cdot 10^{-19}$	-	-	-	-
BC-C13	$5.37 \cdot 10^{-19}$	$9.38 \cdot 10^{-19}$	-	-	-	-
BC-C14	$1.30 \cdot 10^{-19}$	$2.48 \cdot 10^{-19}$	$2.01 \cdot 10^{-14}$	$3.74 \cdot 10^{-11}$	$4.20 \cdot 10^{-15}$	$9.26 \cdot 10^{-14}$
BC-C15	$5.17 \cdot 10^{-19}$	$2.10 \cdot 10^{-19}$	-	-	-	-
BC-C16	$1.60 \cdot 10^{-19}$	$2.18 \cdot 10^{-18}$	$6.21 \cdot 10^{-15}$	$1.81 \cdot 10^{-13}$	$7.75 \cdot 10^{-16}$	$4.43 \cdot 10^{-16}$
BC-C17	$1.56 \cdot 10^{-19}$	$2.31 \cdot 10^{-18}$	$2.98 \cdot 10^{-14}$	$2.85 \cdot 10^{-11}$	$8.64 \cdot 10^{-16}$	$8.77 \cdot 10^{-16}$
BC-C18	$1.88 \cdot 10^{-19}$	$1.85 \cdot 10^{-18}$	$3.51 \cdot 10^{-14}$	$1.17 \cdot 10^{-11}$	$1.71 \cdot 10^{-15}$	$3.07 \cdot 10^{-15}$
BC-C19	$3.74 \cdot 10^{-19}$	$4.40 \cdot 10^{-18}$	$3.82 \cdot 10^{-15}$	$7.19 \cdot 10^{-15}$	$1.44 \cdot 10^{-15}$	$1.73 \cdot 10^{-15}$
BC-C20	$2.95 \cdot 10^{-19}$	$1.96 \cdot 10^{-18}$	$6.19 \cdot 10^{-14}$	$9.12 \cdot 10^{-10}$	$1.92 \cdot 10^{-15}$	$3.38 \cdot 10^{-15}$
BC-C22	$4.92 \cdot 10^{-19}$	$2.77 \cdot 10^{-18}$	$3.15 \cdot 10^{-14}$	$2.64 \cdot 10^{-13}$	$6.57 \cdot 10^{-16}$	$9.50 \cdot 10^{-16}$
BC-C23	$2.54 \cdot 10^{-19}$	$2.95 \cdot 10^{-18}$	$1.85 \cdot 10^{-14}$	$1.65 \cdot 10^{-13}$	$9.46 \cdot 10^{-16}$	$1.12 \cdot 10^{-15}$

BC-C24	$8.40 \cdot 10^{-20}$	$3.12 \cdot 10^{-19}$	$5.40 \cdot 10^{-14}$	$9.68 \cdot 10^{-8}$	$4.12 \cdot 10^{-15}$	$6.21 \cdot 10^{-15}$

Permeability values between 10^{-19} and 10^{-15} m^2 found in protoliths and in fault-rock samples (in the along-fault direction) are in line with values reported by several authors for crystalline faulted and undeformed rocks: 10^{-22} to 10^{-19} m^2 permeabilities typically characterize fault gouges due to gran size reduction and/or mineral precipitation (Morrow et al., 1981, 1984; Chester and Logan, 1986; Morrow and Byerlee, 1988; Chu and Wang, 1988; Antonellini and Aydin, 1994; Goddard and Evans, 1995; Faulkner and Rutter, 1996), still representing conduits for vertical fluid flow during low-flow conditions based on capillarity attraction (Dinwiddie et al., 2006) but rarely sustaining cross-fault fluid flow (Caine et al., 1996); 10^{-16} to 10^{-14} m^2 are found within damage zones (Evans et al., 1997); 10^{-20} to 10^{-17} m^2 refer to fault cores (Evans et al., 1997); and 10^{-18} to 10^{-16} m^2 to protoliths (Evans et al., 1997). Kz values derived for protoliths from both triaxial tests and permeability simulations based on X-ray (CT) images agree with Evans et al. (1997) ranges for undeformed rocks, while along-fault permeability (kz) seems to fall within the fault core range defined by (Evans et al., 1997), even though substantial overlap exists the intervals identified by this author. Obtained protoliths permeabilities also partly overlap with published data regarding silicic volcanic samples resumed by Rust and Cashman (2004; between 10^{-9} and 10^{-16} m^2). Analogously, permeabilities computed on well-bore ignimbrite cores inside the Cerro Norte region (Argentina, Srouga et al., 2004) are similar to the ones derived for protoliths and the same is also true for the nearby Oceano field (Argentina, Srouga et al., 2004), displaying overall permeability values lower than 10^{-17} m^2. Interestingly, permeability values between 10^{-18} and 10^{-16} m^2 , similar to those derived for protoliths in this study, were specifically computed by Saar and Manga (1999) for micropores in vesicular basalts, whose structure and geometry could resemble the one of the isolated pores constituting the great majority of pore space inside the analysed samples (7.7 to 7.9 Appendix). Along-fault permeability ranges derived from Avizo simulations (kz: from 10^{-19} to 10^{-18} m^2) well agree with fault-rocks permeability intervals defined by Evans et al. (1997) for low confining pressure conditions (10^{-20} to 10^{-15} m^2). On the contrary, resulting cross-fault permeability values (ky) are higher (10^{-16} to 10^{-15} m^2) than those found by Evans et al. (1997) for samples oriented perpendicular to the fault plane (10^{-20} to 10^{-17} m^2). Overall, the fact that similar along-fault permeability values were obtained on structures running up to 30 km apart is indicative of results strenght, and agrees with the generalized deformation style affecting regional structures across the Tres Vírgenes region identified by Pellicioli et al. (submitted, b).

Table 7.4 Total (φ_T) and interconnected (φ_i) porosity and permeability (kz) of protolith and fault-rock samples in actual conditions from X-ray (CT) and coupled permeability simulations using 50 slices. Voxel size of the scanned 3D volume and volume statistics are also reported, including: total volume (V_T), pore space volume (V_P), volume of interconnected pore space (V_{Pi}) and percentage of interconnected pores (Ip). Notice the rather low percentages of interconnected pores (Ip) in all samples.

Sample	Voxel size (mm)	V_T (mm^3)	V_P (mm^3)	φ_T (%)	V_{Pi} (mm^3)	V_{Pi} (%)	Ip (%)	φ_i (%)	kz (m^2)
BC-C1	0.0256	16624.7	328.53	1.98	306.27	93	6	1.84	$1.93 \cdot 10^{-18}$
BC-C2	0.0256	41236.8	519.41	1.26	463.27	89	3	1.12	$6.67 \cdot 10^{-19}$
BC-C3	0.0256	51046.4	2217.42	4.34	2108.78	95	5	4.12	$4.60 \cdot 10^{-19}$
BC-C7	0.0175	1574.49	56.41	3.58	49.80	88	7	3.16	$1.91 \cdot 10^{-18}$
BC-C12	0.0256	45922.6	1777.88	3.87	1665.08	94	7	3.63	$6.06 \cdot 10^{-19}$
BC-C13	0.0257	29016.20	809.04	2.79	739.50	91	10	2.55	$9.38 \cdot 10^{-19}$
BC-C14	0.0138	3506.02	50.20	1.39	48.60	97	5	1.34	$2.48 \cdot 10^{-19}$
BC-C15	0.0257	15143.2	21.82	0.14	18.04	83	3	0.12	$2.10 \cdot 10^{-19}$
BC-C16	0.0145	1082.91	24.86	2.79	24.60	99	12	2.77	$2.18 \cdot 10^{-18}$
BC-C17	0.0174	810.37	19.16	2.36	18.42	96	8	2.27	$2.31 \cdot 10^{-18}$
BC-C18	0.0174	1460.57	67.58	4.63	66.86	99	12	4.58	$1.85 \cdot 10^{-18}$
BC-C19	0.0174	347.10	10.51	3.03	10.41	99	18	3.00	$4.40 \cdot 10^{-18}$
BC-C20	0.0185	4477.17	68.11	1.52	63.98	94	20	1.43	$1.96 \cdot 10^{-18}$
BC-C22	0.0185	1637.00	28.41	1.74	27.32	96	22	1.67	$2.77 \cdot 10^{-18}$
BC-C23	0.0185	1877.70	38.26	2.04	37.96	99	25	2.02	$2.95 \cdot 10^{-18}$
BC-C24	0.0146	1222.13	30.72	2.47	27.43	90	2	2.23	$3.12 \cdot 10^{-19}$

Table 7.5 Total (φ_{Tf}) and interconnected (φ_{if}) porosity and permeability (kz) of fault-rock samples BC-C14, BC-C16 and BC-C24 in pre-sealing conditions from X-ray (CT) and coupled permeability simulations using 50 slices. Volume statistics are also reported, including: pore space volume (V_{Pf}), volume of interconnected pore space (V_{Pif}), and percentage of interconnected pores (Ip). Notice the rather low percentage of interconnected pores for all samples. Interconnected porosity decrease from pre-sealing to actual conditions (Table 7.4) is indicated by $\Delta\varphi$, while 'kz extrapolated' indicates permeability estimated from the porosity-permeability relationship fitting fault-rock data determined with the X-ray (CT) technique.

Sample	V_{Pf} (mm^3)	φ_{Tf} (%)	V_{Pif} (mm^3)	V_{Pif} (%)	Ip (%)	φ_{if} (%)	$\Delta\varphi$ (%)	kz (m^2)	kz (m^2) extrapolated
BC-C14	1581.13	45.27	1574.41	99	4	45.07	43.73	$3.84 \cdot 10^{-18}$	$7.56 \cdot 10^{-17}$
BC-C16	54.99	7.89	54.48	99	10	7.83	5.06	$5.82 \cdot 10^{-18}$	$1.14 \cdot 10^{-17}$
BC-C24	240.22	20.27	233.02	97	3	19.7	17.47	$1.23 \cdot 10^{-18}$	$3.19 \cdot 10^{-17}$

7.6.3 Porosity-permeability relationships

Interconnected porosity (φ_i) vs permeability (kz) of protoliths and fault-rocks resulting from triaxial tests and permeability simulations based on X-ray (CT) images are plotted in Figures 7.5 and 7.6. Equations for porosity-permeability relationships have been extrapolated: for protoliths based on triaxial tests results (Fig. 7.5) and for fault-rocks based on permeability simulations conducted along the z direction (along-fault flow, Fig. 7.6). No reliable porosity-permeability relationship could be extrapolated from permeability simulations on protoliths, exhibiting too scattered results to be fitted by a single regression line (Fig. 7.6). The scattering characterising the resulting porosity-permeability distributions (Figs. 7.5 and 7.6) is not surprising for volcanic rocks, as previously found by Saar and Manga (1999) who argued that a series of factors influencing the geometry of pores can result in a range of permeabilities for a given porosity. Similar scattering to the one found in this study was encountered in porosity-permeability distributions related to various volcanic materials, including: ignimbrites, lava flows and vitrophyres (Srouga et al., 2004); pumice, breadcrust bombs and dome material (Mueller et al., 2005); vesicular basalts (Saar and Manga, 1999). In order to double-check the low along-fault permeability values (kz) obtained for pre-sealing conditions from permeability simulations on samples BC-C14, BC-C16 and BC-C24 (Table 7.5), expected permeability was calculated based on the identified porosity-permeability relationship fitting fault-rock samples exhibiting porosity values up to 4.58% (Fig. 7.6). Results, illustrated in last column of Table 7.5, cluster around 10^{-17} m^2 and are in agreement with kz values derived from permeability simulations, or just one order of magnitude higher (Table 7.5). This thus indicates that, despite the higher interconnected porosity values (up to 45%) displayed by fault-rock samples before calcite and/or oxide minerals precipitation along fault planes, overall permeability was rather low, and comparable to the one shown in the actual conditions. In addition, we estimated BC-C14, BC-C16 and BC-C24 pre-sealing conditions permeability based on the porosity-permeability relationship extrapolated for protoliths from triaxial tests (Fig. 7.5), which proved more sensible to porosity variations over a small interval (three order of magnitude increase in permeability passing from 0.2 to 5% interconnected porosity, Table 7.2). Maximum resulting fault-rock permeability for pre-sealing conditions calculated using the porosity-permeability relationship fitting triaxial tests results on protoliths is around 10^{-14} m^2. Despite this is a higher absolute value than the one extrapolated using the porosity-permeability relationship fitting fault-rock samples, its meaning is similar when compared to the highest permeability values found in protolith rocks by triaxial tests ($6.27 \cdot 10^{-15}$ m^2, BC-C13, Table 7.2): in both cases, permeability of the analysed volcanic rocks does not exponentially increase by increasing the interconnected porosity up to 43%. No other published porosity-permeability relationship was used

to independently estimate and double-check permeability values obtained in this study, firstly due to the scarcity of reliable published data regarding ignimbrites and volcanic rocks in general, and secondly because the few attempts done using simplified relationships (Costa, 2006) fitting silicic samples porosity-permeability distributions (Saar and Manga, 1999; Melnik and Sparks, 2002; Rust and Cashman, 2004) revealed inadequate for volcanic rocks displaying interconnected porosities greater than 1%.

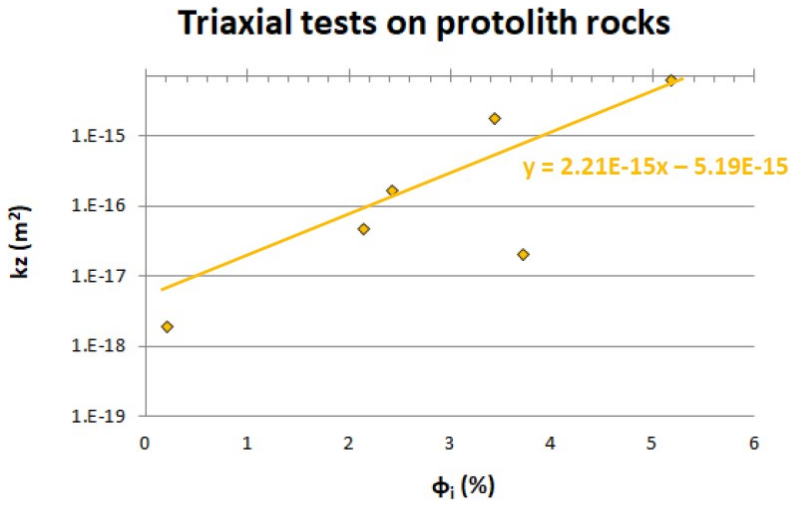

Figure 7.5 Interconnected porosity (φ_i) vs permeability (kz) relationship (yellow line fitting the data) derived for protoliths from triaxial tests.

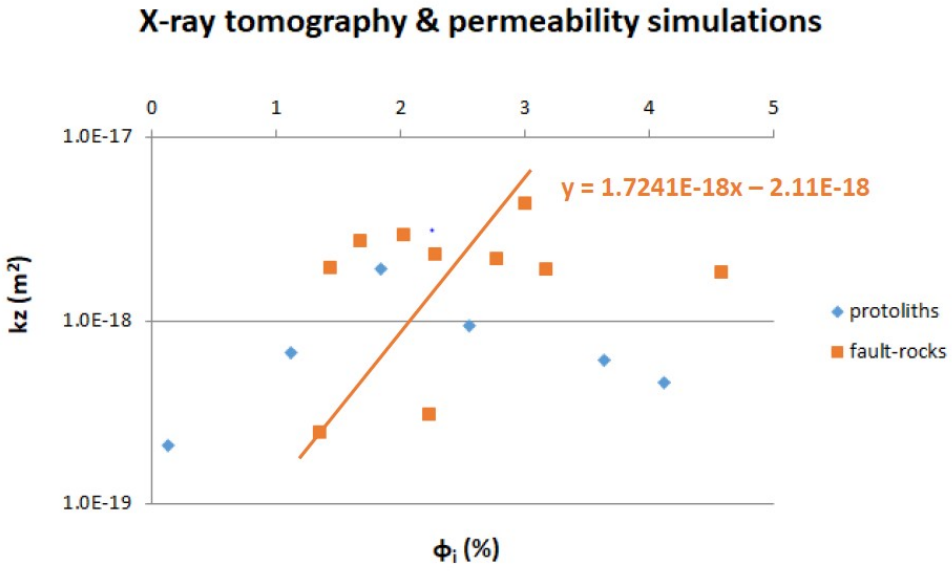

Figure 7.6 Interconnected porosity (φ_i) vs permeability (kz) values derived for protolith (in blue) and fault-rock (in orange) samples from permeability simulations based on X-ray (CT) images. kz values plotted in the diagram for fault-rocks represents the along-fault permeability. The orange line represents the porosity-permeability relationship fitting results on fault-rock samples.

7.7 Discussions

7.7.1 Porosity and permeability variations during synchronous faulting and circulation processes

Maximum total and interconnected porosity of protoliths (in actual conditions) derived from triaxial tests and X-ray (CT) analyses appear rather low (around 5%) to envisage vertical and/or lateral sustained fluid migration through volcanic succession exposed across the Tres Vìrgenes region, as previously assumed by Contreras and Garcia (1998) and Portugal et al. (2000) despite the lack of laboratory test results. Overall less than 5% protolith porosities resulting from this study would not justify any further large-scale investigation aimed to quantify fluid migration inside rock succession, contrarily to what performed by Bignall et al. (2010) in the Mokai-Taupo geothermal field, where ignimbrites exposed through the area displayed up to 25-30% porosity. On the other hand, fault-rock porosities estimated with the X-ray (CT) technique are equally low. In both cases the 3D pore space volume reconstructed with X-ray (CT) analysis appears as composed of a myriad of isolated pores (90-97% in protoliths and up to 85% in fault-rocks) displaying volumes as low as 10^{-6} mm^3 and only minimally contributing to the overall measured porosity, that is instead controlled by a small percentage (3 to 10% in protoliths and up to 25% in fault-rocks) of interconnected pores that define most the 3D pore space volume (83-95% in protoliths and 88-99% in fault-rock samples). Fault-rock samples thus display a higher percentage of interconnected pores (up to 25%) covering a higher volumetric portion (up to 99%) in respect to protoliths. This however refers to fault-rock samples in actual conditions, whilst in pre-sealing conditions (samples BC-C14, BC-C16 and BC-C24) interconnected pores still cover the majority of pore space volume (97-99%), but display abundances minor than in the actual conditions and comparable to the one shown by protoliths (3-10%). This happens regardless the overall higher interconnected porosity values computed for pre-sealing conditions, up to 45%. To a closer look, the percentage of interconnected pores varies from 4 to 5% passing from pre-sealing to actual conditions in sample BC-C14, and from 10 to 12% for BC-C16 and from 3 to 2% in sample BC-C24 (Tables 7.4 and 7.5), indicating an increase in the abundance of interconnection between pores in two out of three cases. Such increase following pure mineral precipitation processes that seal the interconnected pore space is not realistic, unless fluid circulation processes involve hydraulic fracturing and/or are accompanied by synchronous faulting mechanisms. In the case of hydraulic fracturing, a drusy breccia porosity type may form (Srouga and Rubinstein, 2007), depending on the amount of secondary minerals precipitated in hydraulic fractures and on hydrothermal flow conditions. This could cause an up to 5 orders of magnitude increase in

permeability (up to 10^{-13} m^2), as found by Srouga and Rubinstein (2007) in welded ignimbrites and andesites in the Austral and Neuquen basins (Argentina). Despite there are indications of pressurized fluids along fault planes across the Tres Vírgenes region, Pellicioli et al. (submitted, b) demonstrated that hydrofracturing processes are not dominant, nor permeability values found in this study resemble those found by Srouga and Rubinstein (2007). Thus synchronous faulting mechanisms, already suggested in previous studies focusing on the same fault planes (Pellicioli et al., submitted, b), appear as the most likely process responsible for the increasing in the interconnected pore space of 1 to 2%, based on the analysed samples. The fact that other analysed fault-rocks display a higher percentage of interconnected pores in actual conditions (i.e. above 20% in samples BC-C20, BC-C22 and BC-C23, Table 7.4) suggests that the increase in the interconnected pore space following synchronous faulting and fluid circulation processes could be significantly higher. The local and conservative character of the 1-2% increase in the interconnected pore space following faulting and fluid circulation processes found in this study is even more clear when considering the scale of the analysed fault-rock samples: few cm^3 volume rock slices collected in the surficial portion of one of the several fault planes constituting the damage zone associated to the investigated regional fault systems. Despite new interconnections between pores during faulting, these were mostly sealed by mineral precipitation following fluid circulation, resulting in overall sensibly lower interconnected porosity values (<5%) compared to pre-sealing conditions (reduction up to 43%). If we now consider variations in along-fault (kz) permeability of fault-rocks from the pre-sealing to the actual conditions, we should bear in mind that permeability is by definition an intrinsic characteristic of the porous material itself, depending on the size, shape and connection between the pores. It is thus reasonable to assume that permeability obtained by simulating a flow through 100% of a given pore space is the same obtained if the flow is simulated through a minor percentage of the same pore space, if connections between pores are regular. This is in fact the principle based on which permeability is routinely tested in laboratory without specific concern regarding core dimensions, such that recent studies began to test this assumption by searching for a possible size effect implying permeability variations when the dimensions of cores derived from the same material are reduced or increased (Alarcon-Ruiz et al., 2010). Based on these considerations, permeability along faults should not change if simulated through the pre-sealing open pore space or through the same and partially sealed pore space following fluid circulation (actual conditions), except that in our case two things differ from this ideal scenario: i) interconnected pore space varies following faulting and synchronous fluid circulation processes; ii) interconnected pore space in rocks (and in especially volcanic rocks) is not regularly distributed, as in artificial materials (i.e. concrete), and the selection of different fractions of the same pore space during permeability simulations may result in locally different permeabilities (up to 1 order of magnitude

difference, Mueller et al., 2005) simply based on changes in sample orientation or on the involuntary selection of fractions richer or poorer in interconnected pores For these reasons along-fault permeability is expected to change passing from pre-sealing to actual conditions, and it does. This detected change is however of small significance under the hydraulic and geological point of view: up to 1 order of magnitude difference based on permeability simulation results (Tables 7.4 and 7.5) or 2 orders of magnitude if extrapolated from the porosity-permeability relationship defined for fault-rock samples (Fig. 7.6). Furthermore, in two out of three cases along-fault permeability decreases following faulting and synchronous fluid circulation processes, as previously found by Morrow et al. (1984) for both clay-rich and non-clay fault gouges following shearing. Along-fault permeability obtained from simulations based on X-ray (CT) images (kz) falls indeed into the overlapping filed between the intervals identified by Evans et al. (1997) for fault gouges and fault cores, and is in agreement with field observations (Pellicioli et al., submitted, b) regarding the lack or the poor development of a damage zone and the presence of local displacements (Class A and B fault zones, Gray et al., 2005). Such faults, according to Gray et al. (2005), would represent localized conduits for fluids (A) and fluid conduits at the time of their formation converting to barriers to cross-fluid flow (B) after an unspecified amount of time. Hence, the up to 2 orders of magnitude variation in along-fault permeability resulting from a 1 to 2% change in the interconnected pore space following faulting and synchronous fluid circulation processes could be explained in this perspective, and the analysed fault-rocks thus be interpreted as localized conduits for fluids. Concerning cross-fault fluid flow, the analysed faults should represent barriers, both according to Portugal et al. (2000) and Gray et al. (2005), the first arguing tectonic sealing preventing the communication between the regions separated by a system of NW-SE trending faults including the Azufre fault (Fig. 7.1b) based on the variable geochemical characteristics of spring waters sampled around the Sierra Aguajito and La Reforma volcanic complexes. However, cross-fault permeability (ky) resulting from simulations based on X-ray (CT) images is up to 4 orders of magnitude higher (10^{-16} – 10^{-15} m^2, Table 7.3) than along-fault permeability (kz, Tables 7.3 to 7.5). This raises doubts on the sealing potential of the Azufre fault system analysed in this study (samples BC-C17 to BC-C24) and of parallel NW-SE trending structures suggested by Portugal et al. (2000). More likely, the difference in chemical and isotopic composition of spring waters found by Portugal et al. (2000) across the Tres Vírgenes region can be explained in terms of closer proximity of some of the sampled water springs to the Tres Vírgenes volcanic complex feeding system (Macias and Jimenez, 2012, 2013; Avellán et al., 2018), as also indicated by the hydrothermal to meteoric origin of fluids circulating and depositing calcite along regional faults (Pellicioli et al., submitted, c). The higher values obtained for cross-fault permeability (ky) in respect to along-fault permeability (kz) should not surprise when considering that kz only represents one

component of the along-fault permeability. This in fact derives from the combination of kz and kx, even though only kz is discussed in this study due to size effects affecting kx results (Table 7.3). Although unstable, kx average values are several orders of magnitude higher than kz and hence the along-fault permeability values discussed in this study (kz) are conservative. This might thus imply an overall along-fault permeability (resulting from the combination of kz and kx) higher than cross-fault permeability (ky), as expected for faults in most cases.

7.7.2 Lithological control in the formation of fault-related permeability

Although this study highlights changes in the interconnected pore space and in the along-fault permeability following faulting and synchronous fluid circulation processes, the overall measured fault-rock permeability in both actual and pre-sealing conditions across the Tres Vírgenes region remains rather low, and comparable to, or even smaller than, the one displayed by protoliths. This is not rare in magmatic-volcanic settings, as indicated by Evans et al. (1997) and Dinwiddie et al (2006), who found comparable permeabilities (up to 1 order of magnitude difference) in granitic or non-welded ignimbrite host-rocks and within their damage zones. Primary porosity and permeability of ignimbrites and volcanic rocks is generally associated to vesiculation formed by bubble coalescence that ends in melt phase disruption (Srouga et al., 2004). Secondary porosity instead develops during cooling history and is strongly controlled by welding degree, even though deuteric, hydrothermal and tectonic processes can still induce secondary porosity and permeability (Srouga et al. 2004; Srouga and Rubinstein, 2007). When a protolith is deformed inside a shear zone, its primary porosity and permeability, linked to the rock texture and origin, and its eventual secondary permeability, formed in response to cooling and deuteric processes, are modified by faulting and fluid circulation processes that furtherly create and occlude secondary permeability. Thus, finding comparable permeability in fault-rock and protoliths is not unreasonable, and could be indicative of either locally limited effectiveness of faulting and/or fluid circulation processes in bringing additional secondary permeability or of the intrinsic control exerted by lithology during deformation and fluid circulation processes (Caine et al., 1996; Lin et al., 2007; Paul et al., 2009) and in the formation of faulting-related secondary permeability. The presence of a lithological control on deformation processes is supported by many authors, including Smith et al. (1990) who argues that the broad range (approximately 10 orders of magnitude, from 10^{-22} to 10^{-12} m^2) of laboratory-determined permeabilities of natural fault core materials suggests that permeability depends, in part, on lithology and on the degree to which that lithology has been chemically altered. Additionally, Soden and Shipton (2013) link faults growth and architecture to the precursory joint density, depending on variations in mechanical strength linked to rock texture and lithology. Dinwiddie et al. (2006) argue that although faulting, fracturing and relative

matrix deformation produce additional heterogeneity beyond those of the host rock, secondary permeability heterogeneity is still sensitive to host rock lithology, and Caine et al. (1996) suggest that the 'conduit-barrier systematics' of faults may be predicted based on the correlation between the protolith rock type and resulting types of fault core materials developing in a given deformation environment.

7.7.3 Challenges in determining fault-rock permeability and relevance of the study results

Given that results of this study indicate fault-rock permeabilities comparable to those exhibited by protoliths, which are interpreted as incapable of sustaining vertical and/or lateral fluid migration through volcanic succession, how can these faults support fluid migration across the Tres Vírgenes region? On the other hand, we have proofs that along-fault fluid circulation occurred through the study area, based on evidences collected both at the meso- (field evidences; Garcia-Sánchez et al., 2019; Pellicioli et al., submitted, a) and the micro-scales (i.e. microstructural studies; Pellicioli et al., submitted, b), and as also suggested by the results of this study which recognize the potential of the analysed faults to represent localized conduits for fluids (Gray et al., 2005). The answer probably resides in the transient and dynamic nature of fault-related permeability, and in the challenges linked to its determination. The dynamic and transient nature of fault-related permeability (Sibson, 1981; Pili et al., 2002) is well-known in both the geothermal and oil and gas industries. Actually, in these settings production tests still reveal essential to ascertain reservoir flows, despite several techniques are used to model permeability through whole and faulted reservoir rock cores. The dynamic and transient nature of fault-related permeability was originally described by Sibson (1981) in his 'valve system model', that well suits faulting mechanisms across the Tres Vírgenes region (Pellicioli et al., submitted, b). This model implies that fluid pressure rise induces slip along faults, creating new fractures systems and interconnections between the existing pore space, together with a temporary fracture permeability that allows partial draining of the reservoir. As fluid pressure drops, self-sealing of the fracture systems occurs by mineral deposition and the whole cycle can be repeated (Sibson, 1981; Robert et al., 1995). Capturing this temporary fracture permeability maintained by a fault during, and at least temporarily after, an earthquake and its variation through time, due to progressive sealing of veins and deformation zones (Pili et al. 2002), is very challenging indeed. Another issue that makes the determination of fault-rock permeability such a challenge is scale. Scale issue are somehow linked to the above-mentioned possibility of having locally limited faulting and /or fluid circulation processes justifying an overall low along-fault permeability. As discussed above, permeability varies in response to variations of the interconnected pore space, and this is exactly what happens when we change the

scale of the investigated fault-rock volume, given the uneven distribution of pore space typical of volcanic rocks and natural material in general. This is the case of the selected fault-rock samples, collected inside regional large-scale fault damage zones that display variable fluid flow properties along the fault plane (Caine et al., 1996), depending both on the morphological position of the sample (i.e., core, damage zone, or protolith, Evans, 1990; Caine, 1996) and on depth-related variations of rheology and stress field (Teufel, 1987). Time further complicates scale issues, as deformation along faults is a multi-stage process, and thus physical properties derived for samples from any fault zone do only represent one stage of the fault evolution (Evans et al. 1997), and this is particularly true for structures displaying a complex history of re-activation under different stress regimes and geodynamic settings, like the ones analysed in this study (Ferrari et al., 2018). One thing is measuring permeability along a restricted volume portion (i.e. few cm^3) of a single fault plane within a decametric wide damage zone at a single instant in time, another one is measuring cumulative permeability resulting from the sum of the conduits developing alongside and between different structures belonging to the same damage zone at different depths over a certain time interval, impossible to reproduce at the laboratory scale.

Considering the above-discussed challenges in determining fault-rock permeability, the up to 2 orders of magnitude decrease in along-fault permeability associated with the 1-2% increase in interconnected porosity detected in a few cm^3 fault-rock sample could turn into a several orders of magnitude permeability increase when considering larger volumes within the same damage zone. The same might happen sampling structures displaying a better developed local damage zone than the one shown by BC-C14, BC-C16 and BC-C24 samples, able to justify a fracture-dominated flow of hydrothermal fluids. In addition to suggestions brought by this study regarding the role of analysed faults in acting as local conduits for fluids, several are the other evidences that testify fluid flow along fault zones (Garcia-Sánchez et al., 2019; Pellicioli et al., submitted, a and b). It is therefore clear that, despite providing novel characterization of the physical properties across the Tres Vírgenes region, the analyses performed in this study could not properly capture fault-sustained fluid migration processes occurring at the meso-scale. On the other hand, the identification of pore space (up to 2% increase) and along-fault permeability (up to 2 orders of magnitude) variations following faulting and synchronous fluid circulation processes still represents an important and novel outcome, useful to quantify variations of physical properties along faults at a rather small and detailed scale (few cm^3), but also possibly to a larger scale if used as input parameters in simulation models. Furthermore, this can be applied to any typology of fault regardless its origin, kinematics, age and cross-cut successions, and any to geological setting, even though fluid migration remains a key focus of the hydrocarbons (sedimentary) and geothermal (volcanic) industries. What also arises from this study is that a good

chance of improving the rather poor physical properties commonly exhibited by exposed volcanic rocks is inside or in proximity of fault zones, that induce changes in the interconnected pore space and networks. This especially regards the Tres Vírgenes region, where no processes other than tectonics (i.e. deuteric processes) are in fact likely to develop significant secondary permeability in a such a desert climate environment.

7.8 Methodological note

The good agreement between interconnected porosity values determined on protoliths by collocations inside the triaxial system and through the use of the X-ray (CT) technique is remarkable, and indicates robustness of the methodology and results (Tables 7.2 and 7.4). Nevertheless, minor discrepancies can be recognized, as the up to 2.63% difference in porosity of sample BC-C13 (Tables 7.2 and 7.4). These are linked to the fact that the two deployed analysis techniques work at different scales and resolutions and base their porosity estimates on different principles and experimental apparatus. Under the geological point of view however, this difference is insignificant. Also, the up to four orders of magnitude difference (from 10^{-19} to 10^{-15} m^2, Tables 7.2 and 7.4) in protoliths permeability obtained using these two different techniques is acceptable when considering its geological meaning, overall indicating rather difficult fluid flowing conditions through these rocks. The good correspondence of outputs obtained with these two techniques on protolith samples renders fault-rocks porosity and permeability values determined with the X-ray (CT) technique trustworthy, as on the other hand independently confirmed by previous studies on fault-rock samples (Morrow et al., 1981, 1984; Morrow and Byerlee, 1988; Chu and Wang, 1988; Faulkner and Rutter, 1996; Evans et al., 1997). Nevertheless, a size effect in along-fault permeability resulting from simulations performed on X-ray (CT) images has been highlighted in the course of this study (Table 7.3). This size effect is in some cases far greater (kx) that the one found by other studies (cf. Alarcon-Ruiz et al., 2010). One possible reason for this could be that using a different number of slices (20 or 50 in the case of this study), or in other words cutting the 3D pore space volume at different coordinates in space, modifies the connectivity character of pores seen by the Avizo software by means of the Axis Connectivity tool, that automatically removes isolated pore spaces before running the *Absolute Permeability Experiment Simulation*. In this way pores that are interconnected in a 50 slices 3D volume may be seen as isolated objects when considering a smaller (20 slices) volume and vice versa, especially pores display a highly irregular geometry, like in the case of volcanic rocks. Also, as pores in natural media are not organized networks of void spaces like in artificial materials, the selection of one portion of the 3D volume in

respect to another could represent an a-priori involuntary selection of volume fractions that are either richer or poorer in interconnected pores. For the above mentioned reasons, one important side result of this study is to highlight the need for further investigation on size effects linked to use of the X-ray (CT) technique and related Avizo software *Absolute Permeability Experiment Simulation* tool.

7.9 Conclusions

The regional implications of this study, the first to directly quantify physical properties of undeformed and faulted rocks exposed across the Tres Vírgenes region, are the followings:

1) Interconnected porosity (<5%) and permeability (10^{-19} – 10^{-15} m^2) of volcanic rocks exposed through the Tres Vírgenes region is too low to envisage vertical and/or lateral sustained fluid migration.
2) Despite exhibiting low porosity and permeability values (comparable to those found for protoliths) fault-rock samples analysed in this study allowed to quantify an up to 2% increase in interconnected pore space linked to an up to 2 orders of magnitude variation in along-fault permeability following synchronous faulting and fluid circulation processes. This outcome represents a novel quantification of variations of physical properties along faults at a rather small and detailed scale (few cm3), that could also have larger scale implications if used as an input parameters in simulation models.
3) The overall low values of along-fault permeability (10^{-19} – 10^{-18} m^2) and of the detected along-fault permeability change following faulting processes (up to 2 orders of magnitude) may be linked to the intrinsic nature of the sampled fault-zones, which exhibit a poorly developed damage zone accommodating centimetre to few metres displacements and a permeability decrease with shearing (Morrow et al., 1984), typically displayed by fault gouges and fault cores, whose permeability values are rather similar (Evans et a., 1997) to those determined along fault in this study.
4) Cross-fault permeability obtained from this study contrasts with Portugal et al. (2000) hydrological conceptual model indicating tectonic sealing provided by some of the analysed faults (i.e. the Azufre fault system) as responsible for variable geochemical characteristics of spring waters across the region, that could be instead explained in terms of proximity to the Tres Vírgenes feeding system (Pellicioli et al., submitted, c).

Further and more general implications of this study regarding determination of fault-related porosity and permeability and related challenges in volcanic (and also non-volcanic) settings include:

1) The lithological control in the formation of fault-related permeability can explain comparable permeability values found in undeformed and faulted rocks, especially when primary porosity and permeability are rather low (i.e. volcanic rocks).
2) Several important issues render the determination of fault-permeability a challenge, including: the dynamic and transient nature of fault-related permeability, scale and time.
3) Under the methodological point of view, this study highlighted the presence of a rather significant size effect affecting permeability simulations conducted with the Avizo software XLab extension on a different number of X-ray (CT) images, which indicates the need for further investigation linked to use of the X-ray (CT) analysis technique.
4) The approaches and techniques used in this work to quantify porosity and permeability changes following faulting and fluid circulation processes can be applied to any fault in any geological setting.

7.10 Acknowledgements

This study benefited from the CeMIE Geo project P15 of SENER-CONACyT awarded to Jose Luis Macías and UNAM (Universidad National Autónoma de México, Instituto de Geofísica, Morelia, Michoacán, México) to support 2014-2017 field trips to Santa Rosalía-Tres Vírgenes, and from Italgas S.p.a. funds issued by former CNR-IDPA of Milan (now CNR-IGAG) to sponsor C. Pellicioli in her PhD research activity. We are thankful to UNAM also for managing logistic aspects of field trips, including employing local guides from UMA and Ecoturismo Borrego Cimarrón, Bonfil, B.C.S., who took care of people working in the field. Among UMA members, we are especially grateful to Francisco, for having led us to any site that could (and could not) be reached in the fastest way possible and for always patiently waiting for us to finish all of our measurements. Special thanks go to Josè Luis Macias, Laura García-Sánchez, Susana Osorio-Ocampo, Reyna-Marcela Lira-Beltran, Antonio Pola-Villaseñor, Pedro Martin Pacheco and Vincenzo Parisi for their support during fieldwork activity, post-field technical discussions and for hospitality in Morelia.

7.11 References

Alarcon-Ruiz, L., Brocato, M., Dal Pont, S., Feraille, A., 2010. Size effect in concrete intrinsic permeability measurements. Transport in porous media, 85(2), 541-564.

Angelier, J., Colletta, B., Chorowicz, J., Ortlieb, L., Rangin, C., 1981. Fault tectonics of the Baja California Peninsula and the opening of the Sea of Cortez, Mexico. Journal of Structural Geology, 3, 347-357.

Antonellini, M., Aydin, A., 1994. Effect of faulting on fluid flow in porous sandstones: petrophysical properties. AAPG bulletin, *78*(3), 355-377.

Aragón-Arreola, M., Morandi, M., Martín-Barajas, A., Delgado-Argote, L., González-Fernández, A., 2005. Structure of the rift basins in the central Gulf of California: Kinematic implications for oblique rifting. Tectonophysics, 409, 19-38.

Arango-Galván, C., Prol-Ledesma, R. M., Torres-Vera, M. A., 2015. Geothermal prospects in the Baja California peninsula. Geothermics, 55, 39-57.

Avellán, D. R., Macías, J. L., Arce, J. L., Jiménez-Haro, A., Saucedo-Girón, R., Garduño-Monroy, V. H., Sosa-Ceballos, G., Bernal, J. P., Lopez-Loera, H., Cisneros, G., Layer, P. W., Garcia-Sanchez, L., Reyes-Aguston, G., Rocha, V.S., Rangel, E., 2018. Eruptive chronology and tectonic context of the late Pleistocene Tres Vírgenes volcanic complex, Baja California Sur (México). Journal of Volcanology and Geothermal Research, 360, 100-125.

Aydin, A., 2000. Fractures, faults, and hydrocarbon entrapment, migration and flow. Marine and petroleum geology, 17(7), 797-814.

Bignall, G., Rae, A., Rosenberg, M., 2010. Rationale for targeting fault versus formation-hosted permeability in high-temperature geothermal systems of the Taupo Volcanic Zone, New Zealand. In Proceedings of the World Geothermal Congress 2010, Bali, Indonesia, 25-29 April 2010, pp. 1-7.

Caine, J.S., Evans, J.P., Forster, C.B., 1996. Fault zone architecture and permeability structure. Geology, 24(11), 1025-1028.

Chester, F. M., Logan, J. M., 1986. Implications for mechanical properties of brittle faults from observations of the Punchbowl fault zone, California. Pure and Applied Geophysics, 124(1-2), 79-106.

Chu, C.L., Wang, C.Y., Lin, W., 1988. Permeability and frictional properties of San Andreas fault gouges. Geophysical Research Letters, 8(6), 565-568.

Contreras, E., Garcıa, P., 1998. Mediciones petrofısicas en muestras de los fragmentos de núcleos de perforación LV-5, LV-8A y LV-8B. Instituto de Investigaciones Ele´ctricas, Mexico. Internal report, Contract no. GPG/LIR/CPS/006/98, 15 pp.

Costa, A., 2006. Permeability-porosity relationship: A reexamination of the Kozeny-Carman equation based on a fractal pore-space geometry assumption. Geophysical research letters, 33(2).

Dinwiddie, C. L., Bradbury, K. K., McGinnis, R. N., Fedors, R. W., Ferrill, D. A., 2006. Fault zone deformation overprints permeability of nonwelded ignimbrite: Chalk Cove fault, Bishop Tuff, Bishop, California. Vadose Zone Journal, 5(2), 610-627.

Ehrlich, R., Etris, E. L., Brumfield, D., Yuan, L. P., CRABTREE, S. J., 1991. Petrography and reservoir physics III: Physical models for permeability and formation factor (1). AAPG Bulletin, 75(10), 1579-1592.

Eichelberger, J.C., Carrigan, C.R., Westrich, H.R., Price, R.H., 1986. Non-explosive silicic volcanism. Nature, 323(6089), 598.

Evans, J. P., 1990. Thickness-displacement relationships for fault zones. Journal of structural geology, 12(8), 1061-1065.

Evans, J. P., Forster, C. B., Goddard, J. V., 1997. Permeability of fault-related rocks, and implications for hydraulic structure of fault zones. Journal of structural Geology, 19(11), 1393-1404.

Faulkner, D. R., Rutter, E. H., 1996. The permeability anisotropy of clay-bearing fault gouge and its implications for earthquake source mechanisms. EOS, Transactions American Geophysical Union77, F736.

Ferrari, L., Orozco-Esquivel, T., Bryan, S. E., Lopez-Martinez, M., Silva-Fragoso, A., 2018. Cenozoic magmatism and extension in western Mexico: Linking the Sierra Madre Occidental silicic large igneous province and the Comondú Group with the Gulf of California rift. Earth-Science Reviews, 183, 115-152.

García-Sánchez, L., Macías, J.L., Sulpizio, R., Osorio-Ocampo, L.S., Pellicioli, C., Pola, A., Avellán, D., Cisneros, G., García, F., Ocampo-Díaz, Y.Z.E, Lira-Beltran, R.M., Saucedo, R., Sánchez-Nuñez, J.M., Arce, J.L., Corona-Chávez, P., Reyes-Augustin, G., Cardona, M., Layer, P.W., Benowitz, J., Solari, L., Groppelli, G., 2019. Geology of La Reforma caldera complex, Baja California, Mexico. Journal of Maps, 15, 487-498.

Goddard, J. V., Evans, J. P., 1995. Fluid-rock interactions in faults of crystalline thrust sheets, northwestern Wyoming, USA Inferences from geochemistry of fault-related rocks. J. Struct. Geol, 17, 533-549.

Gray, M. B., Stamatakos, J. A., Ferrill, D. A., Evans, M. A., 2005. Fault-zone deformation in welded tuffs at Yucca Mountain, Nevada, USA. Journal of Structural Geology, 27, 1873-1891.

Jouniaux, L., Bernard, M. L., Zamora, M., Pozzi, J. P., 2000. Streaming potential in volcanic rocks from Mount Pelée. Journal of Geophysical Research: Solid Earth, 105(B4), 8391-8401.

Klug, C., Cashman, K.V., 1996. Permeability development in vesiculating magmas: implications for fragmentation. Bulletin of Volcanology, 58(2-3), 87-100.

Lin, A., Maruyama, T., Kobayashi, K., 2007. Tectonic implications of damage zone-related fault-fracture networks revealed in drill core through the Nojima fault, Japan. Tectonophysics, 443, 161-173.

Macías, J.L., Jiménez, S., 2012. Actualización vulcanológica del complejo de Las Tres Vírgenes, BCS. Memorias del XX Congreso Anual de la Asociación Geotérmica Mexicana, Morelia, Mich., México, 26-28 September 2012.

Macías, J.L., Jiménez, S., 2013. Estudio de Estratigrafía y Geología del Complejo Volcánico Tres Vírgenes. B.C.S. Geotermia 26, 14–23.

Melnik, O., Sparks, R. S. J., 2002. Dynamics of magma ascent and lava extrusion at Soufrière Hills Volcano, Montserrat. Geological Society, London, Memoirs, 21(1), 153-171.

Moeck, I. S., 2014. Catalog of geothermal play types based on geologic controls. Renewable and Sustainable Energy Reviews, 37, 867-882.

Morrow, C., Byerlee, J., 1988. Permeability of rock samples from Cajon Pass, California. Geophysical Research Letters, 15(9), 1033-1036.

Morrow, C., Shi, L. Q., Byerlee, J., 1981. Permeability and strength of San Andreas fault gouge under high pressure. Geophysical Research Letters, 8(4), 325-328.

Morrow, C. A., Shi, L. Q., Byerlee, J. D., 1984. Permeability of fault gouge under confining pressure and shear stress. Journal of Geophysical Research: Solid Earth, 89(B5), 3193-3200.

Mueller, S., Melnik, O., Spieler, O., Scheu, B., Dingwell, D. B., 2005. Permeability and degassing of dome lavas undergoing rapid decompression: an experimental determination. Bulletin of Volcanology, 67(6), 526-538.

Nava-Sánchez, E.H., Gorsline, D.S., Molina-Cruz, A., 2001. The Baja California peninsula borderland: structural and sedimentological characteristics. Sedimentary Geology, 144, 63-82.

Ohtani, T., Nakashima, Y., Muraoka, H., 2000. Three-dimensional miarolitic cavity distribution in the Kakkonda granite from borehole WD-1a using X-ray computerized tomography. Engineering Geology, 56(1-2), 1-9.

Paul, P. K., Zoback, M. D., Hennings, P. H., 2009. Fluid flow in a fractured reservoir using a geomechanically constrained fault-zone-damage model for reservoir simulation. SPE Reservoir Evaluation & Engineering, 12, 562-575.

Pellicioli, C., Groppelli, G., Macías, J.L., Sulpizio, R., submitted (a). Control of regional structures on the evolution of Pleistocene La Reforma caldera complex: implications on caldera collapse and resurgence. Submitted to the GSA Bulletin in June 2019.

Pellicioli, C., Zucali, M., Groppelli, G., submitted (b). Kinematics and deformation patterns from micro-structural and image analysis on fault-rock samples in volcanic regions: the example of the Tres Vírgenes active geothermal region, Baja California, Mexico. Submitted to the Journal of Structural Geology in August 2019.

Pellicioli, C., Della Porta, G., Langone, A., Groppelli, G., Zucali, M., submitted (c). Insights on fluid origin from multi-scale petrographic and geochemical investigation of fault-related calcites in volcanic-geothermal regions (Tres Vírgenes area, Baja California, Mexico). Submitted to the Journal of Volcanology and Geothermal Research in September 2019.

Pili, E., Poitrasson, F., Gratier, J. P., 2002. Carbon–oxygen isotope and trace element constraints on how fluids percolate faulted limestones from the San Andreas Fault system: partitioning of fluid sources and pathways. Chemical Geology, 190, 231-250.

Portugal, E., Birkle, P., Tello, E., Tello, M., 2000. Hydrochemical–isotopic and hydrogeological conceptual model of the Las Tres Vırgenes geothermal field, Baja California Sur, México. Journal of Volcanology and Geothermal Research, 101(3-4), 223-244.

Robert, F., Boullier, A. M., Firdaous, K., 1995. Gold-quartz veins in metamorphic terranes and their bearing on the role of fluids in faulting. Journal of Geophysical Research: Solid Earth, 100, 12861-12879.

Rowland, J. V., and Sibson, R. H., 2004, Structural controls on hydrothermal flow in a segmented rift system, Taupo Volcanic Zone, New Zealand: Geofluids, 4(4), 259-283.

Rust, A. C., Cashman, K. V., 2004. Permeability of vesicular silicic magma: inertial and hysteresis effects. Earth and Planetary Science Letters, 228(1-2), 93-107.

Saar, M. O., Manga, M., 1999. Permeability-porosity relationship in vesicular basalts. Geophysical Research Letters, 26(1), 111-114.

Schmitt, A. K., Stockli, D. F., Hausback, B. P., 2006. Eruption and magma crystallization ages of Las Tres Vírgenes (Baja California) constrained by combined 230Th/238U and (U–Th)/He dating of zircon. Journal of Volcanology and Geothermal Research, 158, 281-295.

Sibson, R. H., 1981. Fluid flow accompanying faulting: field evidence and models. Earthquake prediction: an international review, 4, 593-603.

Smith, L., Forster, C. B., Evans, J. P., 1990. Interaction between fault zones, fluid flow and heat transfer at the basin scale.

Soden, A. M., Shipton, Z. K., 2013. Dilational fault zone architecture in a welded ignimbrite: The importance of mechanical stratigraphy. Journal of Structural Geology, 51, 156-166.

Sruoga, P., Rubinstein, N., 2007. Processes controlling porosity and permeability in volcanic reservoirs from the Austral and Neuquén basins, Argentina. AAPG bulletin, 91(1), 115-129.

Sruoga, P., Rubinstein, N., Hinterwimmer, G., 2004. Porosity and permeability in volcanic rocks: a case study on the Serie Tobífera, South Patagonia, Argentina. Journal of Volcanology and Geothermal Research, 132(1), 31-43.

Teufel, L. W., 1987. Permeability changes during shear deformation of fractured rock (No. SAND-86-2522C; CONF-870625-4). Sandia National Labs., Albuquerque, NM (USA).

Wong, V., Munguía, L., 2006. Seismicity, focal mechanisms, and stress distribution in the Tres Vírgenes volcanic and geothermal region, Baja California Sur, Mexico. Geofísica internacional, 45, 23-37.

Zanchi, A., 1994. The opening of the Gulf of California near Loreto, Baja California, Mexico: from basin and range extension to transtensional tectonics. Journal of Structural Geology, 16, 1619-1639.

7.12 Appendix

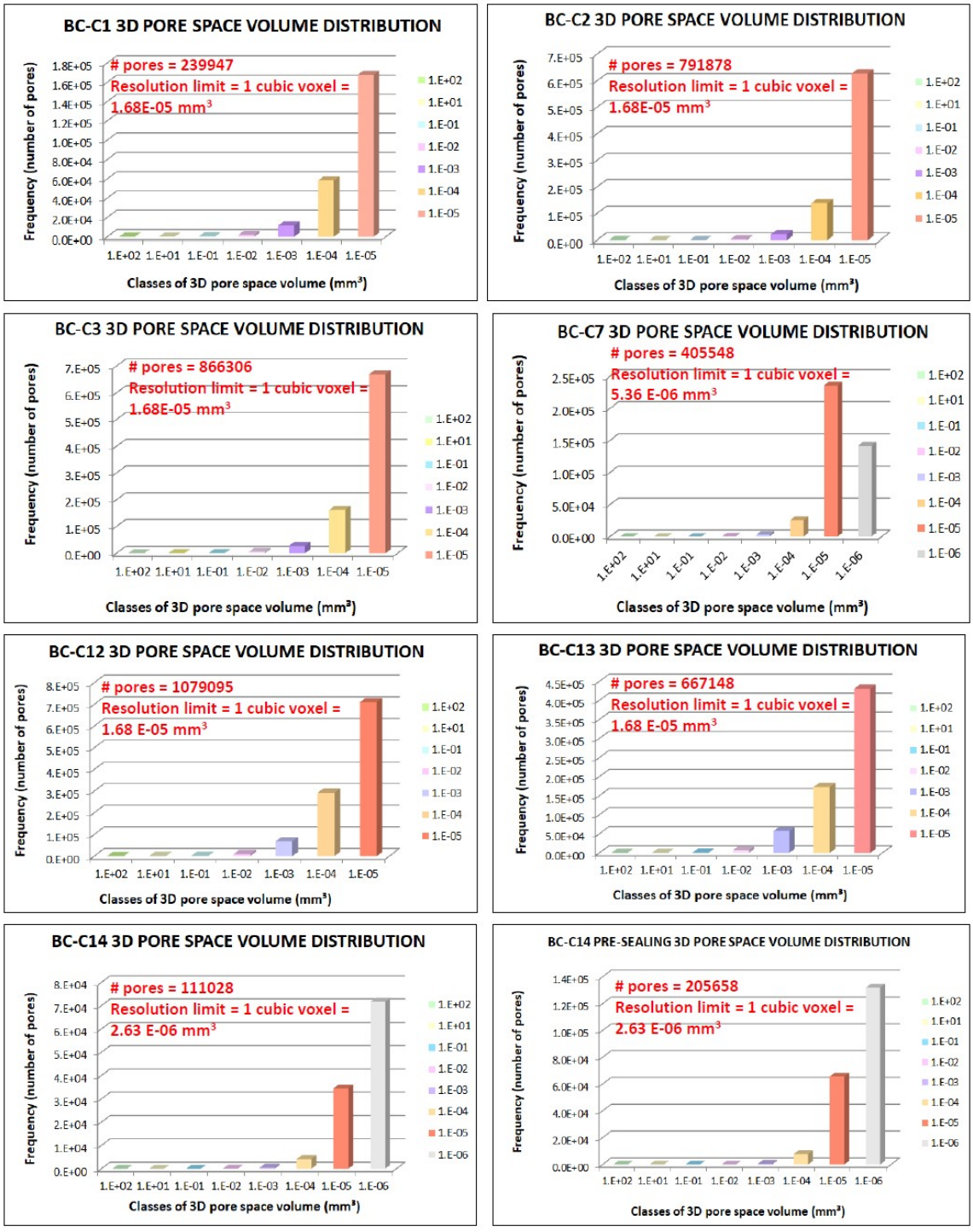

Figure 7.7 3D pore space volume frequency distributions for samples from BC-C1 to BC-C14 derived from X-ray (CT) analysis. Interconnected pores are larger ones (volume up to E-03 mm^3), while isolated pores are smallest ones (from E-04 to E-06 mm^3). Notice the large abundance of isolated pores over interconnected pores.

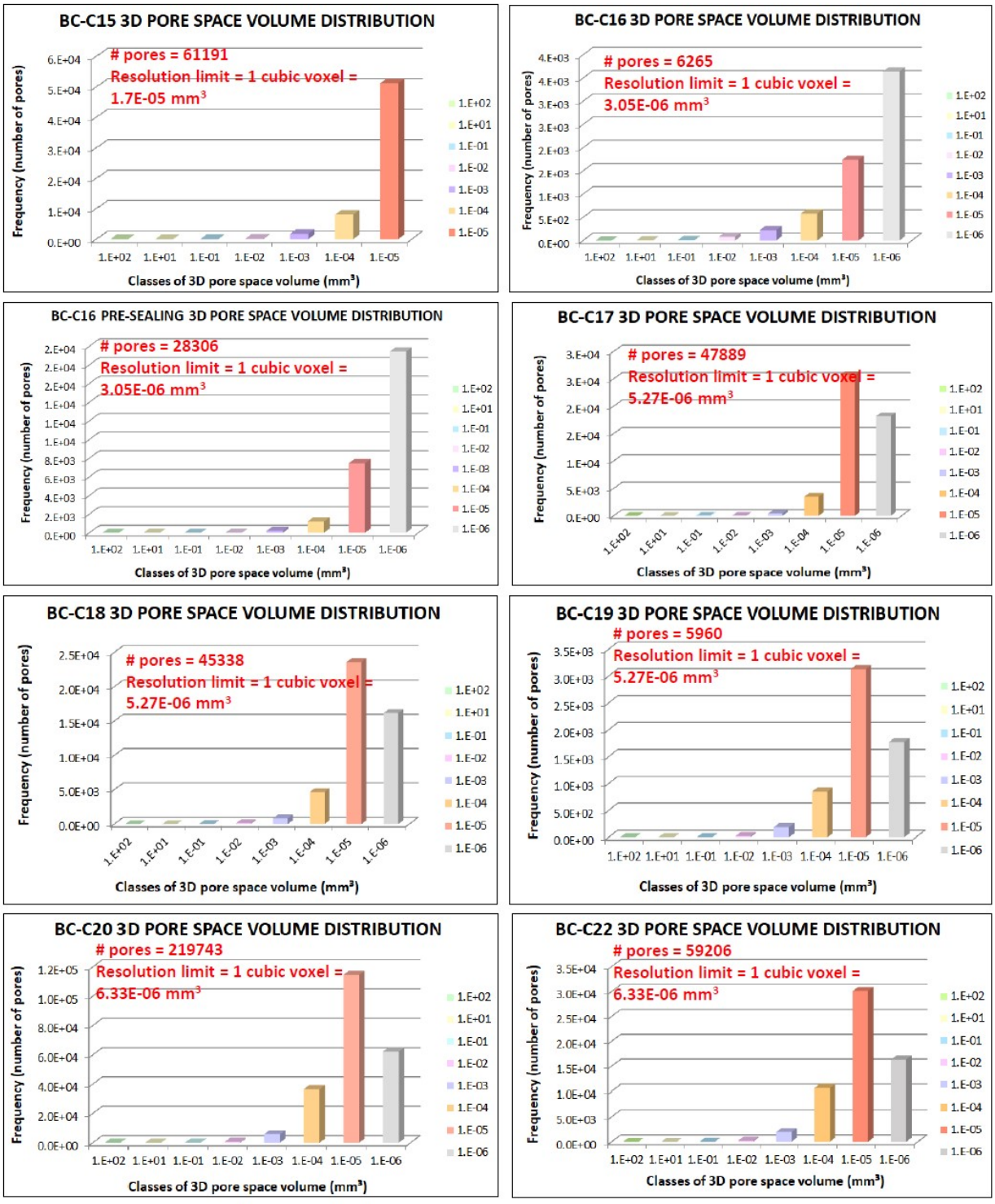

Figure 7.8 3D pore space volume frequency distributions for samples from BC-C15 to BC-C22 derived from X-ray (CT) analysis. Interconnected pores are larger ones (volume up to E-03 mm^3), while isolated pores are smallest ones (from E-04 to E-06 mm^3). Notice the large abundance of isolated pores over interconnected pores.

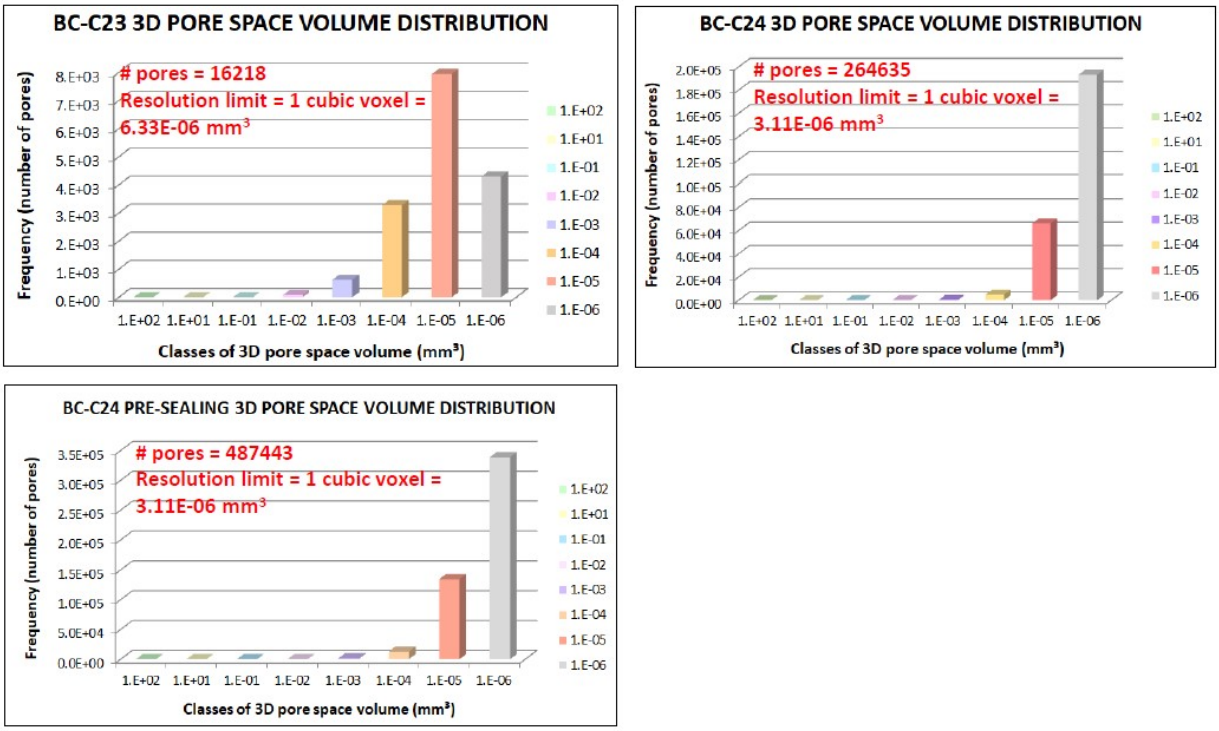

Figure 7.9 3D pore space volume frequency distributions for samples BC-C23 and BC-C24 derived from X-ray (CT) analysis. Interconnected pores are larger ones (volume up to E-03 mm^3), while isolated pores are smallest ones (from E-04 to E-06 mm^3). Notice the large abundance of isolated pores over interconnected pores.

Chapter 8
Concluding remarks

This chapter summarizes the main findings of the PhD research activity (Chapters 3 to 7) and highlights the relevance of each step of the research in fulfilling the objectives of this Thesis.

The main objectives of the Thesis, in line with the aims of the CeMIE Geo project, are recalled below:
1) providing a structural model for the Tres Vírgenes region;
2) demonstrating and quantifying the dominant role of structures in controlling hydrothermal fluids migration.

To provide a structural model for the Tres Vírgenes region (objective 1), geological surveys (Paper I) were coupled with the analysis of structural data collected at the meso-scale (Paper II) and with micro-structural and image analyses of samples collected along major faults mapped across the Tres Vírgenes region (Paper III). These studies show that deformation patterns, inside the Tres Vírgenes region, are strongly controlled by regional-scale strike-slip oblique structures. These structures are linked to the Gulf of California, and develop pull-apart basins at km to tens of km scales. These regional features guide Quaternary volcanic processes, like caldera collapse and resurgence in the case of La Reforma caldera complex, and strongly interfere with volcanic structures in exhuming Cretaceous basement across the region. Regional patterns are self-similar (fractal) at the scale of the Tres Vírgenes region, suggesting the presence of a generalized deformation trend affecting this sector of the Gulf of California.
To demonstrate the dominant role of structures in controlling hydrothermal fluids migration (objective 2), in-depth analyses of fault-related alteration facies mapped in the field (Paper II) and of mineral phases precipitated along fault planes (Paper III) were undertaken. Furthermore, a novel methodology using different techniques working at different scales was applied for the first time in a volcanic-geothermal setting (Paper IV). These studies reveal the presence of a geothermal-hydrothermal component in fluids circulating and depositing calcite along regional fault planes; they also provide insights on temperatures reached during fault-sustained multiple circulation events. They identify the Tres Vírgenes feeding system as the heating source for hydrothermal fluids circulating through the region, thus indicating the areas where fault-sustained hydrothermal circulation is more likely to occur.

To quantify hydrothermal fluids migration across the Tres Vírgenes region (objective 2) determination of physical properties of undeformed and faulted volcanic rocks was performed and results compared (Paper V). The study highlights very low porosity and permeability of undeformed Quaternary volcanic rocks exposed in the Tres Vírgenes region, discouraging further investigation concerning vertical and lateral migration across the volcanic succession. However, once involved into regional deformation zones these volcanic rocks experience significant changes in their physical properties, as a consequence of faulting and synchronous circulation processes which vary the interconnected pore space and fault-permeability.

The scenario reconstructed for the Tres Vírgenes region during the PhD research is rich of novel and quantitative results, which bear multifaceted implications: regional implications directly affecting the Tres Vírgenes region and the Gulf of California setting; industry-related implications concerning modelling of geothermal potential and fluid flow through the Tres Vírgenes and other geothermal regions worldwide; broader implications regarding deformation processes involving the upper-crust in volcanic and non-volcanic settings.

Regional implications include the reconstruction of the different geological processes affecting the Tres Vírgenes region and this sector of the Gulf of California and of their interplay. The suggested reconstruction provides a sound basis for any further detailed study, as future prospecting of geothermal and ore resources in the region or natural hazard assessment (i.e. seismic hazard of the active faults identified in Paper II).

Industry-related implications mainly consist in the identification of mechanisms driving hydrothermal fluids circulation throughout the Tres Vírgenes region and in the computation of a series of associated quantitative physical characteristics.

The geothermal potential across the Tres Vírgenes region is clearly:

i) focused along faults, as indicated by field data (Paper II), the link between active faulting and fluid circulation processes (Papers III and V), the origin of fluids circulating along faults (Paper IV);

ii) absent inside volcanic rocks, which cannot support any lateral or vertical fluid flow migration across the region (Paper V);

iii) generally higher along regional faults linked to the Gulf of California setting and maximum where these large-scale structures intersect volcano-tectonic structures (Paper II);

iv) more prone to be active and exploitable close to the current location of the magmatic feeding system (Paper IV), as testified by the ‘fossil and exhumed’ character of La Reforma caldera complex geothermal system lying on the farthest point from the current focus of magmatic activity;

v) characterized by the presence of low temperature fluids (up to 100°C, Papers II and IV) of non-marine origin (Paper IV).

Quantitative physical characteristics computed in this Thesis can represent input parameters for different kinds of models, either producing statistically based predictions of crustal deformation patterns beyond the scale of observation or simulating fluid flow for extraction purposes across any region of active geothermal potential, like Tres Vírgenes.

Some of these quantitative results are:

i) fault-related micro-fractures maximum and minimum lengths, length frequency distributions and fractal dimension (Paper III);

ii) porosity and permeability of undeformed volcanic rocks (Paper V);

iii) along-fault and cross-fault permeability of regional structures (Paper V);

iv) changes in fault-related interconnected pore space and permeability following deformation of volcanic rocks within regional fault zones (Paper V).

Concerning upper-crustal deformation processes in volcanic settings, some of the implications of this Thesis can be extended outside the investigated region and geodynamic setting, and applied globally to other volcanic-geothermal areas. This is for example the case of regional control exerted on the geometry of the caldera collapse and on the asymmetrical shape of the resurgent block within La Reforma caldera complex (Paper II) and also regards the novel methodology applied for the first time in a volcanic-geothermal setting to gain insights on the origin and temperature of fluids circulating along structures (Paper IV). The quantification of uplift in resurgent calderas (La Reforma caldera complex), useful for explaining the dynamics of some of the most catastrophic processes modelling the Earth surface (Paper II), represents a further example. Finally, the broader implications of this Thesis regard crustal deformation processes occurring in a wide range of geological settings, which could be of great interest for the Scientific Community.

These mainly include:

i) a case study for the application of the ‘fault-valve system model’ (Sibson, 1981) and related dynamics, where fluids overpressure generates a temporary fracture permeability allowing partial drainage of the reservoir (Paper III);

ii) the investigation of the chronological and geometrical relationships between faulting and fluid circulation processes through the analysis of fault-related micro-fractures and veins, based on the Riedel model in an actively deforming geological setting (Paper III);

iii) a new case study for evaluating and testing of the concept of fractal nature of faults and fracture systems, a topic that has encountered growing attention since the 1980s (Paper III);

iv) a new case study for porosity and permeability of faulted ignimbrites and faulted rocks in general, poorly covered by available literature (Paper V);
v) the quantification of changes in the interconnected pore space and fault-permeability following faulting processes along structures of regional importance, useful for understating the variation of physical properties at the sub-millimetre scale (Paper V);
vi) a case study for investigating the not yet fully understood general issues affecting the determination of fault-permeability (Paper V);
vii) a new case study for size effects affecting permeability of natural materials (rocks), for the first time obtained from simulations using 3D images acquired with the X-ray (CT) methodology (Paper V).

Clearly, some issues still remain open, due to the wide range of problematics addressed by this Thesis. The uneven distribution and quality of data collected across the remote and logistically difficult study area, where Pleistocene volcanic products cover most of the structures, and some experimental and methodological issues encountered during the PhD research prevented drawing univocal conclusions on some of the covered aspects.
Among the points that deserve future and further investigation are:
i) the volumes of ignimbrites erupted by La Reforma caldera complex, of high relevance for classifying the eruption magnitude for hazard assessment purposes (Papers I and II);
ii) the geothermal potential intrinsic to volcanic structures, only partially constrained based on the occurrence of alteration phases along ring-faults (i.e. clinoptilolite), which can also result from volcanic glass alteration in submarine depositional settings (Papers II and IV);
iii) the regional control on the location and shifting of Quaternary magmatism through the Tres Vírgenes region (i.e. from SE in La Reforma to NW in Sierra Aguajito and Tres Vírgenes), needing further investigation on magma rise and emplacement dynamics (Paper II), also in the light of newly disclosed results from seismic tomography surveys performed in the region (Garcia et al., 2019; Sena-Lozoya et al., 2020);
iv) the uneven occurrence of calcite mineralization along regional fault planes, possibly linked to the lithological control on fault-related deformation including the size of the damage zone (Papers III and V);
v) the occurrence of temperatures higher than those indicated by the oxygen stable isotope (100°C) for fluids circulating along regional fault planes, as suggested by LA-ICP-MS analysis results (i.e. Ce and Eu anomalies, Paper IV);

vi) the obstacles in capturing fluid circulation within fault damage zones and the methodological issues (i.e. size effect) affecting the determination of fault-rock permeability, of crucial importance for a correct assessment of fluid flow migration processes through the upper crust (Paper V);
vii) the use of well-bore data, never disclosed during the course of this PhD research, for comparison and integration purposes and to develop a 3D subsurface model, rarely produced for volcanic regions.

This Thesis covers complex and challenging topics and receives contributions from several branches of the Earth Sciences, including volcanology, structural geology, geochemistry and geo-engineering. The main strength points of this Thesis are the multi-disciplinary approach used to investigate different problematics and the multifaceted character of the results, of great importance for the industry at the regional scale and engaging the Scientific Community at a worldwide scale. Hopefully, the findings of this Thesis will help achieving a more complete understanding of processes and dynamics affecting volcanic-geothermal regions situated in tectonically active and complex geodynamic settings.

8.1 References

Garcia, V.V., Calò, M., & Samaniego, J.F.L. (2019). Imaging of the magmatic system feeding Las Tres Vírgenes Geothermal field (Baja California Sur, Mexico) using Enhanced Seismic Tomography. Journal of Volcanology and Geothermal Research, 106710.

Sena-Lozoya, E.B., González-Escobar, M., Goméz-Arias, E., González-Fernández, A., & Gómez-Ávila, M. (2020). Seismic exploration survey northeast of the Tres Vírgenes Geothermal Field, Baja California Sur, Mexico: A new Geothermal prospect. Geothermics, 84, 101743.

Sibson, R. H., 1981. Fluid flow accompanying faulting: field evidence and models. Earthquake prediction: an international review, 4, 593-603.

Chapter 9

Appendix

Appendix 1: Fractals and fractal statistics (Pellicioli et al., submitted, b; Chapter 5)

Fractal statistics, or fractal analysis, is the analysis of fractals. The term "fractal" was first used by the mathematician Benoit Mandelbrot in 1975, based on the latin word *fractus,* meaning "broken" or "fractured". Fractals are objects that tend to appear nearly the same at different levels and are ubiquitous in nature (i.e. coastlines, ice crystals, craters, river networks, ocean waves, fault patterns, leaves, trees and plants). Fractals are not limited to geometric patterns, but can also describe processes in time (i.e. images, sounds). The characteristic of fractals to exhibit similar patterns at increasingly small scales is called *self-similarity*. Fractals are different from finite geometric figures in the way they scale: if a fractal's one dimensional lengths are all doubled, the spatial content of the fractal scales by a power that is not necessarily an integer. This power is called *fractal dimension* of the fractal. The fractal dimension represents a statistical index of complexity, comparing how detail in a pattern changes with the scale at which it is measured. Figure 9.1 (left image) illustrates that if we measure a line using a 1 unit long stick (l=1) stick and then another stick which is 1/3 its size (l=1/3) in the second case we obtain that the total length of the line is three times as many sticks long as with the first. The same applies in two dimensions. If we measure the area of a square and then measure it again

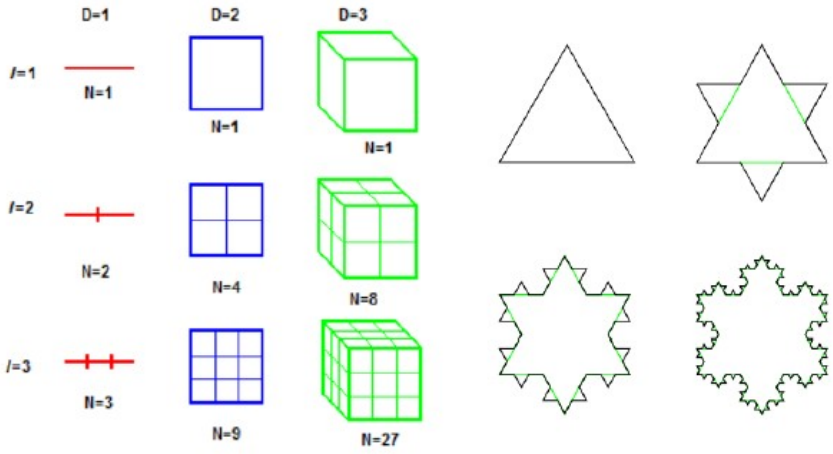

Figure 9.1 On the left are traditional notions of geometry for defining scaling and dimension; on the right the first four iterations of the Koch snowflake, which has an approximate fractal dimension of 1.2619. Image source: public domain.

with a box of side length 1/3 the size of the original, we will find 9 times as many squares as with the first measure. This can be mathematically expressed by the following equation:

$$N \approx s^{-D}$$

where N is the number of sticks, s the scaling factor, D the fractal dimension and ≈ means proportional. The same rule applies to fractals but less intuitively. A fractal line measured at first to be 1 length, when re-measured using a stick scaled by 1/3 of the old stick may not be the expected 3 but instead 4 times as many scaled sticks long. In this case, N = 4 when s = 1/3 and the value of D can be found rearranging the previous equation to:

$$\log_s N = -D = \log N / \log s$$

D thus equals 1.2619, which is a non-integer dimension suggesting the fractal has a dimension not equal to the space it resides in. The scaling used in this example is the same scaling of the *Koch curve* and *snowflake*, illustrated in Figure 9.1 (right image).

In practice, fractal dimensions (D) can be determined using techniques that approximate scaling and detail from regression lines over log-log plots of size vs scale:

$$D = \log N(s) / \log (1/s)$$

where N is the number of parts in which a fractal can be scaled down by the factor s. Figure 9.2 illustrates an example of this. If we consider the *Koch curve*, the object in image b is formed by 4 segments each one displaying a 1/3 length of the object in image a. The fractal dimension is then *log (4) / log (3)*, that again equals 1.2619.

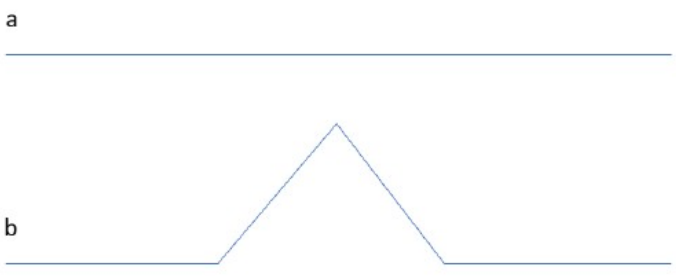

Figure 9.2 Example of application of the Koch curve.

If *N(s)* and *1/s* can be fitted by a linear regression line (y = ax + b) in a log-log plot, then the fractal dimension *D* can be simplified to the angular coefficient (a) of the regression line.

Appendix 2: IRMS analysis (Pellicioli et al., submitted, c; Chapter 6)

Table 9.1 Slot configuration during IRMS analysis.

Row	Position	Sample	Net weight (10^{-3} mg)
1	A1	MAMI	188
2	A2	MAMI	175
3	A3	NB518	156
4	A4	IAEA603	265
5	A5	BC-C24A	314
6	A6	BC-C24A	378
7	A7	BC-C24B	374
8	A8	BC-C24C	446
9	A9	BC-C24D	368
10	A10	BC-C24E	375
11	B1	NB518	194
12	B2	BC-C24F	388
13	B3	BC-C24G	411
14	B4	BC-C24H	346
15	B5	BC-C24H	393
16	B6	BC-C24I	388
17	B7	BC-C24J	360
18	B8	BC-C14A	264
19	B9	BC-C14B	371
20	B10	BC-C14C	408
21	C1	IAEA603	317
22	C2	BC-C14D	409
23	C3	BC-C14E	409
24	C4	BC-C14F	303
25	C5	BC-C14G	333
26	C6	BC-C14H	425
27	C7	BC-C14H	394
28	C8	BC-C14I	350
29	C9	IAEA603	207
30	C10	NB518	366
31	D1	MAMI	252
32	D2	MAMI	237
33	D3	MAMI	222
34	D4	NB518	251
35	D5	NB518	234
36	D6	IAEA603	254

Table 9.2 IAEA official and average measured standard values used for IRMS raw data normalization.

Value	Standard	Name	$^{13}C/^{12}C$ (‰)	stdevC (‰)	$^{18}O/^{16}O$ (‰)	stdevO (‰)
IAEA official	ST1	NBS18	-5.014	0.035	-23.2	0.1
IAEA official	ST2	IAEA603	2.46	0.01	-2.37	0.04
Average measured	ST1	NBS18	-4.58	0.05	-23.01	0.07
Average measured	ST2	IAEA603	2.81	0.03	-2.51	0.05

Appendix 3: X-ray (CT) (Pellicioli et al., submitted, d; Chapter 7)

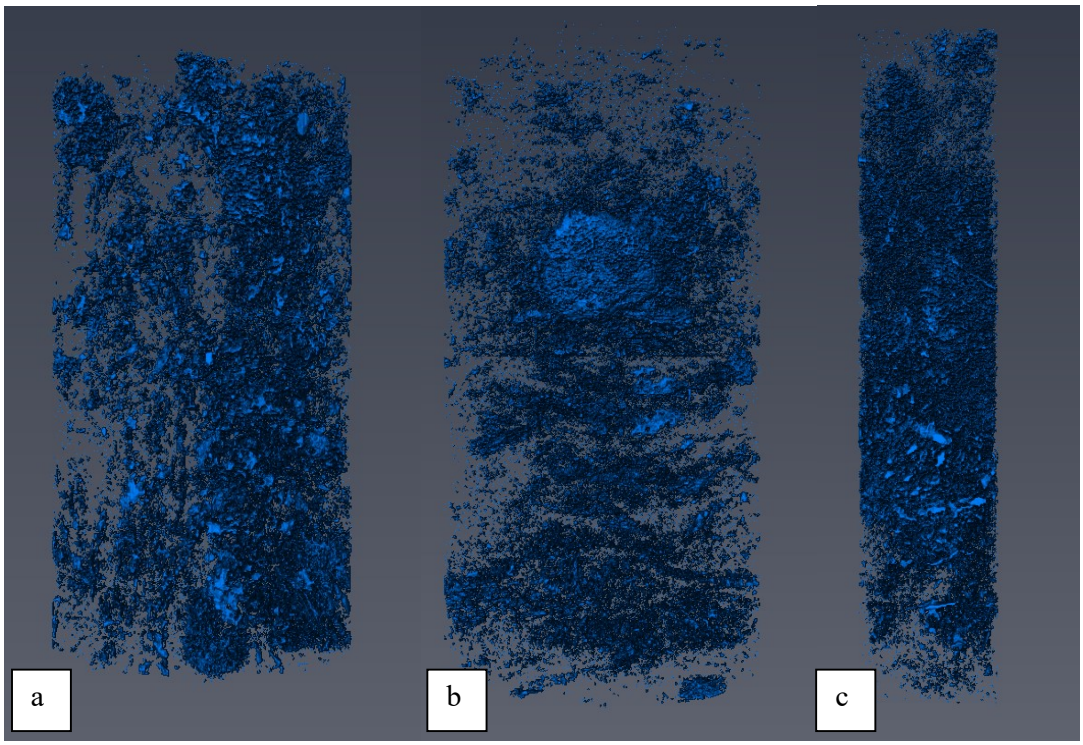

Figure 9.3 XZ view of pore space volume (highlighted in blue) from X-ray (CT) analysis on protolith samples BC-C1 (a) and BC-C2 (b) and on fault-rock sample BC-C7 (c).

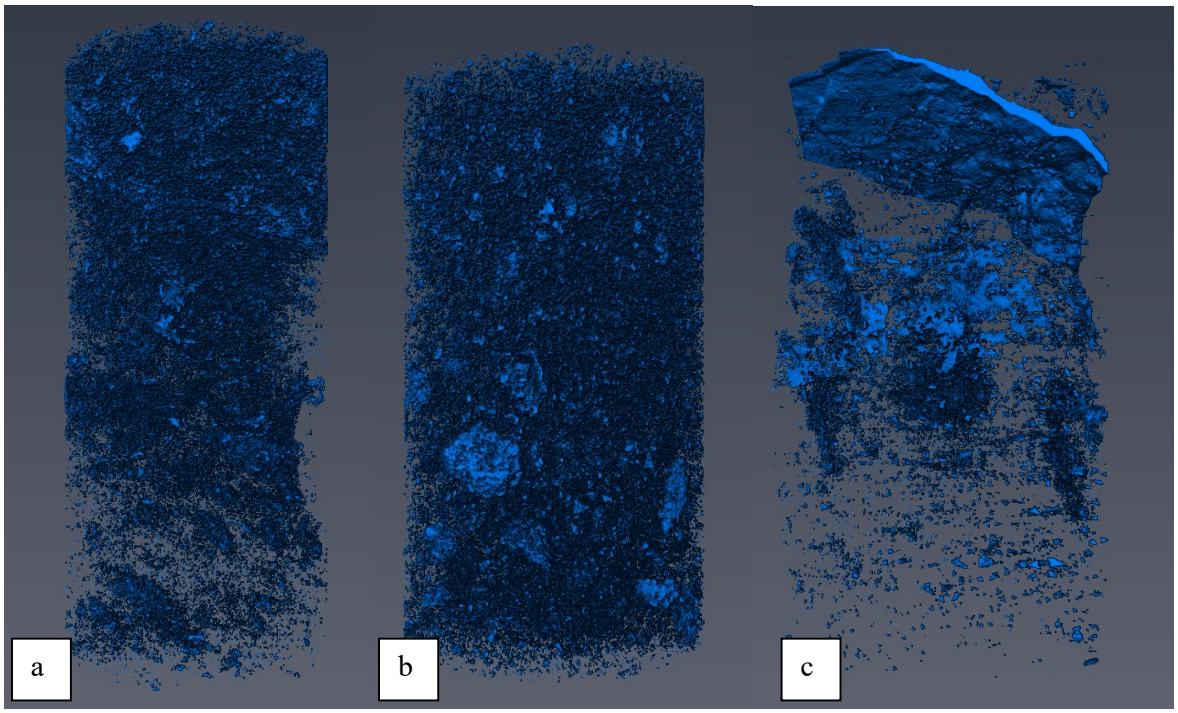

Figure 9.4 XZ view of pore space volume (highlighted in blue) from X-ray (CT) analysis on protolith samples BC-C12 (a) and BC-C13 (b) and on fault-rock sample BC-C17 (c).

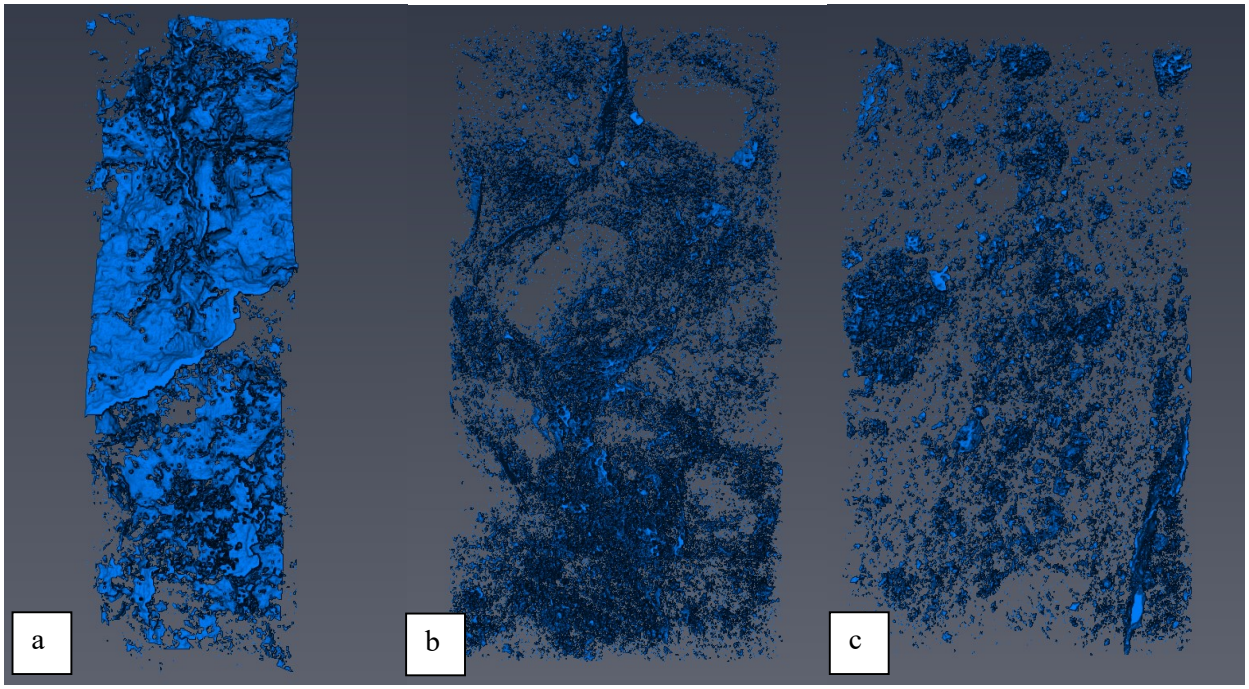

Figure 9.5 XZ view of pore space volume (highlighted in blue) from X-ray (CT) analysis on fault-rock samples BC-C19 (a) and BC-C20 (b) and BC-C22 (c).

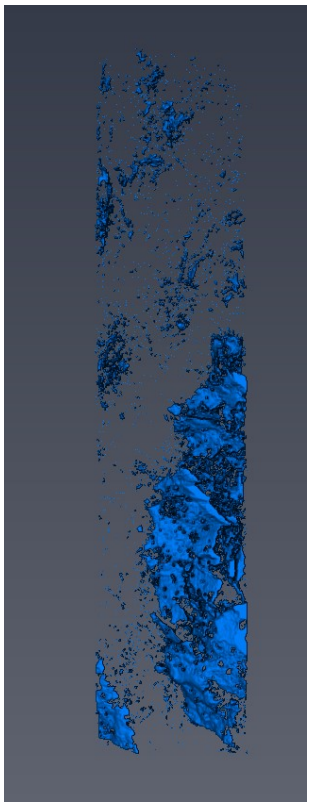

Figure 9.6 XZ view of pore space volume (highlighted in blue) from X-ray (CT) analysis on fault-rock sample BC-C23.